Durability and Damage Tolerance of High Temperature Polymeric Composites

Scott W. Case and Kenneth L. Reifsnider
Materials Response Group
Virginia Tech
Blacksburg, VA 24061-0219

Contract # NAG1-1608
NASA Langley Research Center

Key Words: composite materials, durability, damage tolerance, micromechanical models, fatigue, life prediction, strength prediction

Durability and Damage Tolerance of High Temperature Polymeric Composites

by

Scott W. Case and Kenneth L. Reifsnider

(ABSTRACT)

Modern durability and damage tolerance predictions for composite material systems rely on accurate estimates of the local stress and material states for each of the constituents, as well as the manner in which the constituents interact. In this work, an number of approaches to estimating the stress states and interactions are developed. First, an elasticity solution is presented for the problem of a penny-shaped crack in an N-phase composite material system opened by a prescribed normal pressure. The stress state around such a crack is then used to estimate the stress concentrations due to adjacent fiber fractures in a composite materials. The resulting stress concentrations are then used to estimate the tensile strength of the composite. The predicted results are compared with experimental values.

In addition, a cumulative damage model for fatigue is presented. Modifications to the model are made to include the effects of variable amplitude loading. These modifications are based upon the use of remaining strength as a damage metric and the definition of an equivalent generalized time. The model is initially validated using results from the literature. Also, experimental data from APC-2 laminates and IM7/K3B laminates are used in the model. The use of such data for notched laminates requires the use of an effective hole size, which is calculated based upon strain distribution measurements. Measured remaining strengths after fatigue loading are compared with the predicted values for specimens fatigued at room temperature and 350°F (177°C).

Table of Contents

1. INTRODUCTION AND LITERATURE REVIEW 1

1.1 MICROMECHANICAL MODELING OF TENSILE STRENGTH 2
1.2 ESTIMATION OF RESIDUAL STRENGTH DURING FATIGUE AND FATIGUE LIFE 10

2. STRENGTH PREDICTION IN UNIDIRECTIONAL COMPOSITE MATERIALS 15

2.1 BASIC EQUATIONS AND THEIR SOLUTION 15
2.2 FORMULATION OF THE PROBLEM 21
2.3 REDUCTION OF THE PROBLEM TO THE SOLUTION OF A FREDHOLM INTEGRAL EQUATION OF THE SECOND KIND 21
2.4 REPRESENTATION OF THE BROKEN FIBER PROBLEM 30
2.5 NUMERICAL RESULTS 32
2.6 MULTIPLE FIBER FRACTURES 41
2.7 APPLICATION TO COMPOSITE TENSILE STRENGTH 44
2.8 MODEL REFINEMENTS 56

3. DURABILITY AND DAMAGE TOLERANCE ANALYSIS IN COMPOSITE MATERIALS 71

3.1 DAMAGE ACCUMULATION CONCEPTS 71
3.2 CONCEPTS OF THE CRITICAL ELEMENT MODEL 78
3.3 VALIDATION EXAMPLES 80

4. QUASI-STATIC AND FATIGUE BEHAVIOR OF NOTCHED $[0/90]_{4S}$ APC-2 90

4.1 EXPERIMENTAL TECHNIQUES 90
4.1.1 Specimen Preparation 90
4.1.2 Quasi-Static Testing 90
4.1.3 Fatigue Tests 91
4.1.4 Penetrant Enhanced Radiography 91
4.1.5 Strip Strain Gages and Residual Strength Testing 92
4.2 EXPERIMENTAL RESULTS AND DISCUSSION 94
4.2.1 Quasi-Static Testing 94
4.2.2 Fatigue Testing 94
4.2.3 Penetrant Enhanced Radiography 98
4.2.4 Strip Gage Results 102
4.2.5 Residual Strength Results 102
4.3 ANALYSIS TECHNIQUES 106
4.3.1 Notched Quasi-Static Strength 106
4.3.2 Notched Residual Strength Analysis 107

5. ROOM TEMPERATURE AND ELEVATED TEMPERATURE CHARACTERIZATION OF IM7/K3B 120

5.1 PHASE I TESTING 122
5.1.1 Room Temperature Testing 122
5.1.2 Elevated Temperature Testing 126
5.2 PHASE II TESTING 128
5.2.1 Room Temperature Testing of Notched $[0/\pm45]_{2s}$ Specimens 128
5.2.2 Elevated Temperature (350°F—177°C) Testing of Notched $[0/\pm45]_{2s}$ Specimens 129
5.3 PHASE III TESTING OF UNNOTCHED AND NOTCHED $[45/0/-45/90]_{2S}$ SPECIMENS 130
5.3.1 Quasi-Static Testing 130

5.3.2 Fatigue Testing *130*
5.4 EXPERIMENTAL RESULTS 130
5.4.1 Phase I Tests *130*
5.4.2 Phase II Tests *137*
5.4.3 Phase III Tests *162*

6. SUMMARY AND CONCLUSIONS 205

6.1 INTRODUCTION AND LITERATURE REVIEW 205
6.1.1 Micromechanical Modeling of Tensile Strength *205*
6.1.2 Estimation of Residual Strength and Fatigue Life *205*
6.2 STRENGTH PREDICTION IN UNIDIRECTIONAL COMPOSITE MATERIALS 206
6.3 DURABILITY AND DAMAGE TOLERANCE ANALYSIS IN COMPOSITE MATERIALS 207
6.4 QUASI-STATIC AND FATIGUE BEHAVIOR OF NOTCHED $[0/90]_{4S}$ APC-2 208
6.5 ROOM TEMPERATURE AND ELEVATED TEMPERATURE CHARACTERIZATION OF IM7/K3B 208
6.6 RECOMMENDATIONS 209

7. REFERENCES 211

List of Illustrations

Figure 2.1. Penny-shaped crack surrounded by multiple concentric cylinders having different elastic constants. 16
Figure 2.2. Composite material having hexagonal packing which contains a single broken fiber. The shaded area is selected as a representative volume element for the analysis. 31
Figure 2.3. Representation of the hexagonal arrangement as an axisymmetric one having the same fiber volume fraction. 33
Figure 2.4. Variation of the $\sigma_{zz}(0,z) / p_0$ stress (at the center of the broken fiber) as a function of distance above the crack plane for various fiber to matrix stiffness ratios. 35
Figure 2.5. Variation of the $\sigma_{zz}(r_1,z)$stress (at the inside edge of the fiber annular ring) as a function of distance above the crack plane for various fiber to matrix stiffness ratios. 36
Figure 2.6. Variation of the $\sigma_{zz}(r_{1/2},z) / p_0$stress (at the center of the fiber annular ring) as a function of distance above the crack plane for various fiber to matrix stiffness ratios. 38
Figure 2.7. Variation of the stress $\sigma_{zz}(0,z) / p_0$ (at the center of the broken fiber) as a function of distance from the crack plane for various fiber volume fractions. 39
Figure 2.8. Variation of the $\sigma_{zz}(r_{1/2},z) / p_0$stress (at the center of the fiber annular ring) as a function of distance above the crack plane for various fiber volume fractions. 40
Figure 2.9. Variation of the $\sigma_{zz}^{(i)}(r,0)$stress (in the plane of the crack) for the three inner concentric cylinders (i = 2, 3, 4). 42
Figure 2.10. Hexagonally-packed composite material showing regions selected for geometry approximation. 43
Figure 2.11. Batdorf-type Q-plot. Composite failure occurs at the point of instability. 49
Figure 2.12. Maximum stress concentration as a function of number of broken fibers and fiber volume fraction. 52
Figure 2.13. Center stress concentration as a function of fiber volume fraction and number of broken fibers. 53
Figure 2.14. Ineffective lengths for glass/epoxy composites of different fiber volume fractions as a function of number of adjacent broken fibers. 54
Figure 2.15. Predicted composite strengths as a function of fiber volume fraction and Weibull modulus using the maximum stress concentration values. 55
Figure 2.16. Predicted composite strengths as a function of fiber volume fraction and Weibull modulus using the center stress concentration values. 57
Figure 2.17. Schematic illustration of approach employed to determine stress concentrations using Pagano's [26] axisymmetric damage model. 58
Figure 2.18. Comparison between the predicted stress concentrations using the axisymmetric model [26] and the analysis of Hedgepeth and Van Dyke [20]. 62
Figure 2.19. Center stress concentration on adjacent fibers as a function of number of broken fibers and matrix stiffness for a graphite/polymeric composite material. 64
Figure 2.20. Center stress concentration on adjacent fibers as a function of number of broken fibers and matrix stiffness for a graphite/polymeric composite material. 65
Figure 2.21. Ineffective length as a function of number of broken fibers and matrix stiffness for a graphite/polymeric composite material. 66
Figure 2.22. Predicted composite strength based on maximum stress concentration as a function of matrix stiffness and fiber Weibull modulus for a 60% fiber volume fraction graphite/polymeric composite material 67

Figure 2.23. Predicted composite strength based on center stress concentration as a function of matrix stiffness and fiber Weibull modulus for a 60% fiber volume fraction graphite/polymeric composite material 68
Figure 2.24. Comparison of predicted strength based on maximum stress concentration and experimentally measured values for composites containing four different graphite fibers. 69
Figure 2.25. Comparison of predicted strength based on center stress concentration and experimentally measured values for composites containing four different graphite fibers. 70
Figure 3.1.The use of remaining strength as a damage metric. 73
Figure 3.2. Calculation of equivalent ("pseudo") cycles for block loading. 77
Figure 3.3. Illustration of the concepts involved in the critical element model. 79
Figure 3.4. Flowchart of the approach used to calculate remaining strength. 82
Figure 3.5. Comparison between measured and fitted fatigue lives for unidirectional APC-2 based on the data of Picasso and Priolo [54]. 84
Figure 3.6. Comparison between predicted and measured fatigue lives for cross-ply APC-2 based on the data of Curtis [55]. 85
Figure 3.7. Comparison between predicted and measured fatigue lives for quasi-isotropic APC-2 based on the data of Simonds and Stinchcomb [56] 87
Figure 3.8. Comparison between predicted and measured remaining strength for quasi-isotropic APC-2 based on the data of Simonds and Stinchcomb [56]. 88
Figure 4.1. Strip strain gage placement along hole axis 93
Figure 4.2. Failed cross-ply APC-2 quasi-static specimens. 95
Figure 4.3. Normalized compliance meaured across the hole using an extensometer for APC-2 specimens fatigue at 87.5% and 80% of ultimate tensile strength. 97
Figure 4.4. Radiographs of specimens fatigued at 80% of ultimate strength for 100, 10000, and 100000 cycles. 99
Figure 4.5. Radiographs of specimens fatigued at 87.5% of ultimate strength for 100, 10000, and 100000 cycles. 100
Figure 4.6. Longitudinal split length as a function of cycles for APC-2 laminates fatigued at 80% and 87.5% of ultimate tensile strength. 101
Figure 4.7. Cross-ply APC-2 specimens after residual strength testing exhibiting the three different failure modes. 105
Figure 4.8. Comparison of predicted and measured axial strain as a function of position along the hole axis. 108
Figure 4.9. Comparison between the strip-strain gage measurements and the predictions based on the effective hole size for specimens fatigued 100 cycles at 80% of the ultimate strength. 111
Figure 4.10. Comparison between the strip-strain gage measurements and the predictions based on the effective hole size for specimens fatigued 10000 cycles at 80% of the ultimate strength. 112
Figure 4.11. Comparison between the strip-strain gage measurements and the predictions based on the effective hole size for specimens fatigued 100000 cycles at 80% of the ultimate strength. 113
Figure 4.12. Comparison between the strip-strain gage measurements and the predictions based on the effective hole size for specimens fatigued 100 cycles at 87.5% of the ultimate strength. 114
Figure 4.13. Comparison between the strip-strain gage measurements and the predictions based on the effective hole size for specimens fatigued 10000 cycles at 87.5% of the ultimate strength. 115
Figure 4.14. Comparison between the strip-strain gage measurements and the predictions based on the effective hole size for specimens fatigued 100000 cycles at 87.5% of the ultimate strength. 116
Figure 4.15. Comparison between predicted and measured remaining strength of cross-ply APC-2 laminates as a function of number of cycles. 119
Figure 5.1. Bridge wiring for +/- 45 tensile specimens. 125
Figure 5.2. Failed $[0]_{12}$ tensile specimens from room temperature (left) and 350°F (177°C) tests (right). 133
Figure 5.3. Stress-strain curves for $[0]_{12}$ laminates of IM7/K3B at room temperature and 350°F (177°C). 134
Figure 5.4. Failed $[90]_{12}$ tensile specimens from room temperature (left) and 350°F (177°C) tests (right). 135

Figure 5.5. Stress-strain curves for $[90]_{12}$ laminates of IM7/K3B at room temperature and 350°F (177°C).136
Figure 5.6. Failed $[\pm45]_{3s}$ tensile specimens from room temperature (left) and 350°F (177°C) tests (right).138
Figure 5.7. Shear stress-shear strain curves for $[\pm45]_{3s}$ laminates of IM7/K3B at room temperature and 350°F (177°C) 139
Figure 5.8. Failed notched $[0/\pm45]_{2s}$ tensile specimens from room temperature (left) and 350°F (177°C) (right) tests 140
Figure 5.9. Stress-strain curves based on extensometer measurements for room temperature $[0/\pm45]_{2s}$ IM7/K3B laminates containing a center hole 141
Figure 5.10. Stress-strain curves based on stroke measurements at 350°F (177°C) for $[0/\pm45]_{2s}$ IM7/K3B laminates containing a center hole. 142
Figure 5.11. Fatigue stiffness reduction curves based on extensometer measurements at room temperature for $[0/\pm45]_{2s}$ IM7/K3B laminates containing a center hole 143
Figure 5.12. Fatigue stiffness reduction curves based on stroke measurements at room temperature for $[0/\pm45]_{2s}$ IM7/K3B laminates containing a center hole. 145
Figure 5.13. Fatigue stiffness reduction curves based on stroke measurements at 350°F (177°C) for $[0/\pm45]_{2s}$ IM7/K3B laminates containing a center hole. 146
Figure 5.14. Penetrant-enhanced radiographs of $[0/\pm45]_{2s}$ laminates of IM7/K3B fatigued at room temperature at 70% of ultimate tensile strength after 10000 cycles (left), 260000 cycles (center) and 1430515 cycles (right) 147
Figure 5.15. Penetrant-enhanced radiographs of $[0/\pm45]_{2s}$ laminates of IM7/K3B fatigued at room temperature at 80% of ultimate tensile strength after 10000 cycles (left), 280000 cycles (center) and 1560401 cycles (right) 148
Figure 5.16. Penetrant-enhanced radiographs of $[0/\pm45]_{2s}$ laminates of IM7/K3B fatigued at 350°F (177°C) at 70% of ultimate tensile strength after 10000 cycles (left) and 224500 cycles (right). 149
Figure 5.17. Penetrant-enhanced radiographs of $[0/\pm45]_{2s}$ laminates of IM7/K3B fatigued at 350°F (177°C) at 80% of ultimate tensile strength after 10000 cycles (left), 75000 cycles (center) and 224500 cycles (right) 150
Figure 5.18. Comparison of predicted and measured axial strain as a function of position along the hole axis before fatigue. 152
Figure 5.19. Comparison between the strip-strain gage measurements and the predictions based on the effective hole size for a specimen fatigued 10000 cycles at room temperature at 70% of ultimate strength 153
Figure 5.20. Comparison between the strip-strain gage measurements and the predictions based on the effective hole size for a specimen fatigued 260000 cycles at room temperature at 70% of ultimate strength 154
Figure 5.21. Comparison between the strip-strain gage measurements and the predictions based on the effective hole size for a specimen fatigued 10000 cycles at room temperature at 80% of ultimate strength 155
Figure 5.22. Comparison between the strip-strain gage measurements and the predictions based on the effective hole size for a specimen fatigued 280000 cycles at room temperature at 80% of ultimate strength 156
Figure 5.23. Comparison between the strip-strain gage measurements and the predictions based on the effective hole size for a specimen fatigued 10000 cycles at 350°F (177°C) at 70% of ultimate strength 157
Figure 5.24. Comparison between the strip-strain gage measurements and the predictions based on the effective hole size for a specimen fatigued 10000 cycles at 350°F (177°C) at 80% of ultimate strength 158
Figure 5.25. Comparison between the strip-strain gage measurements and the predictions based on the effective hole size for a specimen fatigued 10000 cycles at 350°F (177°C) at 80% of ultimate strength 159

Figure 5.26. Comparison between measured and predicted remaining strength as a function of fatigue cycles and applied stress level at room temperature for $[0/\pm45]_{2s}$ laminates of IM7/K3B containing a center hole. 161
Figure 5.27. Comparison between measured and fitted stress relaxation modulus for $[\pm45]_{3s}$ IM7/K3B at 350°F (177°C) 163
Figure 5.28. Comparison between measured and predicted remaining strength as a function of fatigue cycles and applied stress level 350°F (177°C) for $[0/\pm45]_{2s}$ laminates of IM7/K3B containing a center hole 164
Figure 5.29. Representative stress-strain curve based on extensometer measurements for room temperature tests of $[45/0/-45/90]_{2s}$ IM7/K3B laminates without a center hole 166
Figure 5.30. Representative stress-strain curve based on stroke measurements for room temperature tests $[45/0/-45/90]_{2s}$ IM7/K3B laminates without a center hole. 167
Figure 5.31. Representative stress-strain curve based on stroke measurements for 350°F (177°C) tests of $[45/0/-45/90]_{2s}$ IM7/K3B laminates without a center hole. 168
Figure 5.32. Representative stress-strain curve based on extensometer measurements for room temperature tests of $[45/0/-45/90]_{2s}$ IM7/K3B laminates with a center hole 169
Figure 5.33. Representative stress-strain curve based on stroke measurements for room temperature tests of $[45/0/-45/90]_{2s}$ IM7/K3B laminates with a center hole 170
Figure 5.34. Representative stress-strain curve based on stroke measurements for 350°F (177°C) tests of $[45/0/-45/90]_{2s}$ IM7/K3B laminates with a center hole 171
Figure 5.35. Normalized dynamic storage modulus measurements for room temperature fatigue tests at 65% of ultimate strength for $[45/0/-45/90]_{2s}$ IM7/K3B laminates without a center hole. 173
Figure 5.36. Phase lag measurements for room temperature fatigue tests at 65% of ultimate strength for $[45/0/-45/90]_{2s}$ IM7/K3B laminates without a center hole. 174
Figure 5.37. Normalized dynamic storage modulus measurements for room temperature fatigue tests at 70% of ultimate strength for $[45/0/-45/90]_{2s}$ IM7/K3B laminates without a center hole. 175
Figure 5.38. Phase lag measurements for room temperature fatigue tests at 70% of ultimate strength for $[45/0/-45/90]_{2s}$ IM7/K3B laminates without a center hole. 176
Figure 5.39. Normalized dynamic storage modulus measurements for 350°F (177°C) fatigue tests at 65% of ultimate strength for $[45/0/-45/90]_{2s}$ IM7/K3B laminates without a center hole. 177
Figure 5.40. Phase lag measurements for room temperature fatigue tests at 65% of ultimate strength for $[45/0/-45/90]_{2s}$ IM7/K3B laminates without a center hole. 178
Figure 5.41. Normalized dynamic storage modulus measurements for 350°F (177°C) fatigue tests at 70% of ultimate strength for $[45/0/-45/90]_{2s}$ IM7/K3B laminates without a center hole. 179
Figure 5.42. Phase lag measurements for 350°F (177°C) fatigue tests at 70% of ultimate strength for $[45/0/-45/90]_{2s}$ IM7/K3B laminates without a center hole. 180
Figure 5.43. Normalized dynamic storage modulus measurements for room temperature fatigue tests at 70% of ultimate strength for $[45/0/-45/90]_{2s}$ IM7/K3B laminates with a center hole. 182
Figure 5.44. Phase lag measurements for room temperature fatigue tests at 70% of ultimate strength for $[45/0/-45/90]_{2s}$ IM7/K3B laminates with a center hole 183
Figure 5.45. Normalized dynamic storage modulus measurements for room temperature fatigue tests at 80% of ultimate strength for $[45/0/-45/90]_{2s}$ IM7/K3B laminates with a center hole. 184
Figure 5.46. Phase lag measurements for room temperature fatigue tests at 80% of ultimate strength for $[45/0/-45/90]_{2s}$ IM7/K3B laminates with a center hole 185
Figure 5.47. Normalized dynamic storage modulus measurements for 350°F (177°C) fatigue tests at 70% of ultimate strength for $[45/0/-45/90]_{2s}$ IM7/K3B laminates with a center hole. 186
Figure 5.48. Phase lag measurements for350°F (177°C) fatigue tests at 70% of ultimate strength for $[45/0/-45/90]_{2s}$ IM7/K3B laminates with a center hole 187
Figure 5.49. Normalized dynamic storage modulus measurements for 350°F (177°C) fatigue tests at 80% of ultimate strength for $[45/0/-45/90]_{2s}$ IM7/K3B laminates with a center hole. 188

Figure 5.50. Phase lag measurements for 350°F (177°C) fatigue tests at 70% of ultimate strength for $[45/0/-45/90]_{2s}$ IM7/K3B laminates with a center hole. 189
Figure 5.51. Penetrant-enhanced radiographs of unnotched $[45/0/-45/90]_{2s}$ laminates of IM7/K3B fatigued at room temperature at 65% of ultimate tensile strength after 10000 cycles (left) and 20000 cycles (right). 190
Figure 5.52. Penetrant-enhanced radiograph of an unnotched $[45/0/-45/90]_{2s}$ laminate of IM7/K3B fatigued at room temperature at 70% of ultimate tensile strength after 10000 cycles. 191
Figure 5.53. Penetrant-enhanced radiograph of an unnotched $[45/0/-45/90]_{2s}$ laminate of IM7/K3B fatigued at 350°F (177°C) at 65% of ultimate tensile strength after 8160 cycles. 193
Figure 5.54. Penetrant-enhanced radiographs of unnotched $[45/0/-45/90]_{2s}$ laminates of IM7/K3B fatigued at 350°F (177°C) at 70% of ultimate tensile strength after 3500 cycles (left) and 5200 cycles (right). 194
Figure 5.55. Penetrant-enhanced radiographs of notched $[45/0/-45/90]_{2s}$ laminates of IM7/K3B fatigued at room temperature at 70% of ultimate tensile strength after 1000 cycles (left), 10000 cycles (center) and 100000 cycles (right). 195
Figure 5.56. Penetrant-enhanced radiographs of notched $[45/0/-45/90]_{2s}$ laminates of IM7/K3B fatigued at room temperature at 80% of ultimate tensile strength after 10000 cycles (left) and 100000 cycles (right). 196
Figure 5.57. Penetrant-enhanced radiographs of notched $[45/0/-45/90]_{2s}$ laminates of IM7/K3B fatigued at 350°F (177°) at 70% of ultimate tensile strength after 10000 cycles (left) and 100000 cycles (right). 197
Figure 5.58. Penetrant-enhanced radiograph of an notched $[45/0/-45/90]_{2s}$ laminate of IM7/K3B fatigued 350°F (177°C) at 80% of ultimate tensile strength after 38500 cycles. 198
Figure 5.59. Comparison of predicted and measured remaining strength for unnotched $[45/0/-45/90]_{2s}$ specimens fatigued at room temperature. 203
Figure 5.60. Comparison of predicted and measured remaining strength for unnotched $[45/0/-45/90]_{2s}$ specimens fatigued at 350°F (177°C). 204

List of Illustrations

Table 2.1. Stress concentrations due to multiple fiber fractures for a glass/epoxy composite material at various fiber volume fractions. 45
Table 2.2. Fiber mechanical properties used in the stress concentration analysis. 59
Table 2.3. Stress concentrations and ineffective lengths obtained using Pagano's [26] axisymmetric model as a function of matrix stiffness and number of broken fibers for a graphite/polymeric composite material 61
Table 3.4. Mechanical properties of APC-2 composites [53]. 81
Table 4.1. Notched quasi-static test results for APC-2 laminates having different cooling rates. 96
Table 4.2. Strip strain gage results for APC-2 laminates. 103
Table 4.3. Residual strength results for APC-2 laminates. 104
Table 5.1. Nominal specimen dimensions for IM7/K3B material. 121
Table 5.2. Results of Phase I tests on IM7/K3B laminates at room temperature and 350°F (177°C). 132
Table 5.3. Residual strength results for $[0/\pm45]_{2s}$ IM7/K3B laminates containing a center hole. 160
Table 5.4. Residual strength results for unnotched $[45/0/-45/90]_{2s}$ laminates of IM7/K3B. 200
Table 5.5. Residual strength results for notched $[45/0/-45/90]_{2s}$ laminates of IM7/K3B. 201

1. Introduction and Literature Review

Modern durability and damage tolerance predictions for composite material systems rely on accurate estimates of the local stress and material states for each of the constituents, as well as the manner in which the constituents interact. It is possible to make estimates of the local stress state, even in the presence of complex damage modes, using either closed-form analyses or detailed numerical methods. However, the manner in which the evolution of the material states during component life contributes to the final failure is less well understood. In particular, there are many different damage modes that may develop and interact before a final failure occurs. These damage modes make it possible to design components from composite materials that are extremely damage tolerant. To use this damage tolerance to its fullest, we must have some method to predict the stiffness, strength, and life of these materials in variable environmental conditions. For engineering applications, the ability to evaluate the evolution of *fiber-controlled* properties under various long-term thermo-mechanical loading conditions is of particular importance. Under these loading conditions, it is necessary to have accurate depictions of changes in stress state due to damage development. Damage development may include matrix cracking, fiber fracture, fiber-matrix separation, delamination, and environmental degradation. A coherent rationale for combining these effects to evaluate the material state at any point during the service life is required.

In order to approach the problem of fiber-controlled failure of composite materials, there are a number of methods that can be employed. These include empirical methods, laminate-level models, and micromechanical models. Each of these methods has its own particular advantages and disadvantages. The empirical methods typically require a great deal of experimental work and are reliable only within ranges for which data are available. Also, when parameters such as the laminate stacking sequence are changed, additional experimental characterization is required. Laminate-level models have the advantage of being sensitive to stacking sequence variations, although they lack sensitivity to fiber-matrix interphase

variations which have been shown [1-4] to have a great influence on composite strength and durability. Micromechanical models have the advantage of being sensitive to variations at the fiber/matrix/interphase level. However, many of the quantities necessary for these models may be difficult (or nearly impossible) to measure. It is the author's opinion that the best approach to modeling the fiber-controlled behavior is a "building-block" approach in which laminate-level models are able to make use of information from micromechanical models of the composite behavior, but not to the exclusion of known data. For example, it would be of questionable benefit to use a micromechanical model for tensile strength when that strength has already been characterized experimentally. In cases in which some data are missing, however, the micromechanical models are invaluable. In order to understand how such a building-block approach may be achieved, it is useful to review previous work that has been done in the area of fiber-controlled behavior of composite materials. This review will begin with micromechanical modeling and will then consider the estimation of residual strength during fatigue and fatigue life for the case of laminates dominated by the fiber behavior. As the area of compression-controlled micromechanical modeling has recently been considered by Lesko [5], the present review of micromechanical modeling will consider only tensile strength.

1.1 Micromechanical Modeling of Tensile Strength

For continuous fiber reinforced polymeric composite materials, the tensile strength is controlled by the stress distributions surrounding fiber fractures (Gao, et al. [6]). In particular, the stress concentrations in fibers adjacent to the fractured ones and the distance over which the perturbed stress field acts (the *ineffective length*) are required for tensile strength predictions such as that presented by Batdorf [7]. The understanding of these stress concentrations and the resulting ineffective lengths may be better achieved by reviewing some of the previous work which has been done in the area of "penny-shaped" cracks (circular disk cracks), as a simple fiber fracture falls into this class of problems.

Sneddon [8] was among the first to consider the penny-shaped crack problem. His analysis concerned a crack created in the interior of an infinite elastic medium occupying the circle $r^2 = x^2 + y^2 = c^2$ in the plane $z = 0$. Sneddon was able to obtain exact expressions for the stresses at any point in the body. In addition, he applied a Griffith-type criterion for the condition of crack growth.

Collins [9] also considered the case of a penny-shaped crack subjected to shear as well as normal loading. His approach was based on the use of two harmonic potential functions to represent the stresses and displacements. To illustrate the solution procedure, Collins determined the solution for four different penny-shaped crack problems:

(i) the opening of the crack by a point force acting at an interior point of the infinite solid

(ii) two parallel cracks in an infinite solid

(iii) an infinite row of parallel cracks in an infinite solid

(iv) and a crack in a thick plate with stress-free faces.

In all cases except for *(i)*, approximate solutions to the resulting integral equations were presented. Collins presented expressions for the work of the crack and the maximum displacement of the crack faces.

Keer [10] was the first to consider non-symmetrical loading of the penny-shaped crack. He used cylindrical polar coordinates (r, θ, z) where the crack, with radius a, is given by $z = 0, 0 \leq r \leq a$. The crack was assumed to be opened by an arbitrary distribution of normal pressure. The problems were solved using a stress function technique similar to that employed by Green and Zerna [11]. Having obtained the solution for the problem of a crack in an infinite medium being opened by a non-symmetrical normal pressure, Keer next considered two other problems: a crack symmetrically loaded within a stress-free, thick elastic plate and a crack embedded in a beam exposed to pure bending. In the case of the crack

in a thick plate, Keer derived a Fredholm integral equation of the second kind for the solution. The resulting equation must be solved by iteration or numerically.

Smith et al. [12] developed an expression for the stress intensity factor of a penny-shaped crack in a infinite elastic solid subjected to non-axisymmetric normal loading. Their analysis began as Keer [10] did by assuming that, in the absence of body forces, the complete solution for a restricted class of problems in which the shear stresses on the plane $z = 0$ can be represented by a single harmonic function, $\phi(r, \theta, z)$. They also expressed the loading on the crack surface as a Fourier series. By considering the general solution in the vicinity of the crack tip, the authors developed an expression for the stress intensity factor for the opening mode of fracture. Additionally, they showed that the state of stress becomes that of plane strain at the tip of a penny-shaped crack for any non-axisymmetric continuous distribution of loading on the crack surface. To illustrate the applicability of their results, Smith et al. considered two particular cases: that of two concentrated forces at equal radial distances on the crack surface and that of a penny-shaped crack in a large beam subjected to pure bending.

Guidera and Lardner [13] used the Somigliana formula from dislocation theory to solve the problem of a crack whose deformation is caused by the action of prescribed tractions on the crack surface. They obtained expressions for the stress intensity factors for two cases of loading of the crack plane, normal and shear.

Lardner and Tupholme [14] considered much the same problem as that considered by Guidera and Lardner—only for a hexagonal crystal. By appropriately replacing certain isotropic constants by the appropriate elastic constants for the hexagonal material, they were able to obtain the stress intensity factors for a penny-shaped crack in a hexagonal medium. The resulting forms of the integral equations for the hexagonal medium are the same as those solved by Guidera and Lardner for the isotropic case.

Lardner and Tupholme arrived at the stress intensity factors by direct substitution into the previous results. Using the results from the previous study by Guidera and Lardner for a constant unidirectional shear traction, Lardner and Tupholme studied the effect of the anisotropy on the distribution of stress in the vicinity of the crack.

Each of the above solutions considered the radial dimension of the body (the direction perpendicular to the crack) to be infinite. Sneddon and Tait [15] considered the case of a very long (taken to be infinite) cylinder containing a crack with the center of the crack lying on the axis of the cylinder with the plane of the crack perpendicular to that axis. They assumed that the cylindrical surface is free from shear and is supported in such a way that the radial component of the displacement vector vanishes on the surface. Such a situation would arise physically if the elastic cylinder were resting in a hollow cylinder in a rigid body of exactly the same radius, and if the cylinder were then deformed by the application of a known pressure to the surfaces of the crack. Sneddon and Tait presented the derivation of two solutions to the problem: one based on an integral-type solution and the other based on a series-type solution. The second is simpler, although it cannot be generalized to cover the case in which the cylinder surface is free from stress. Sneddon and Tait obtained an approximate solution for the case in which the crack is opened by a constant pressure.

The problems considered previously have dealt with a penny shaped crack in a homogenous material. Dhaliwal et al. [16] considered the state of stress in a long elastic cylinder with a concentric penny-shaped crack, bonded to an infinite elastic medium. They assumed the crack to be opened by an internal pressure and that the plane of the crack was perpendicular to the axis of the cylinder, and allowed the elastic constants of the cylinder and the semi-infinite medium to be different. They then reduced the problem to the solution of a Fredholm integral equation of the second kind and obtained closed-form expressions for the stress intensity factor and the crack energy.

Cox [17] was one of the first to study the stress redistribution which occurs in the vicinity of a fiber fracture in a unidirectional composite material. Rosen [18] later presented an nearly identical model. Rosen's analysis (a shear lag model) assumed that the fibers support only tensile loading, the matrix supports (and transmits) only shear loading, and that the shear transfer between the broken fiber and adjacent fibers is limited to the matrix between those fibers. This analysis suggests that the stress terms increase exponentially as axial distance increases along the fractured fiber. In addition, by making use of an efficiency parameter which relates the stresses in the vicinity of the fiber fracture to those far removed, it was possible to predict an *ineffective length*—the axial distance over which the stress field is perturbed.

Whitney and Drzal [19] considered the case of a single fractured fiber embedded in an infinite matrix. Their analysis extended the shear lag concepts to include axial loading in the matrix and shearing stresses in the fractured fiber. By using the equilibrium equations in conjunction with constitutive relations, and an assumed functional dependence of the stresses on the radial and axial coordinates, they were able to formulate an approximate solution to the ineffective length problem. This solution does not satisfy all of the compatibility conditions. The ineffective lengths calculated using this analysis were compared with experimentally determined values using a single fiber fracture test for on composite systems to validate the micromechanical model.

Hedgepeth and Van Dyke [20] considered the stress concentrations on neighboring fibers due to single and multiple adjacent fiber fractures. Their analysis used an influence function approach along with shear lag concepts. Results were presented for both three-dimensional square and hexagonal arrays where specified fibers were broken, and for the stress concentration factor in a fiber adjacent to a broken fiber in a two-dimensional array where the shear stress in the matrix is restricted by a limiting stress value. Due to the inherent shear lag assumptions, however, the model does not include the effects of the fiber and

matrix stiffness values or fiber volume fraction. Therefore, it is applicable to high fiber modulus, low matrix modulus, high fiber volume fraction systems.

Carman et al. [21] attempted to include the effect of fiber volume fraction, material properties, crack size, and fiber eccentricity on the resulting stress concentrations in the vicinity of a fiber fracture. Their analysis represented the fibers adjacent to a fractured fiber by a ring of material. Using an assumed functional dependence of strains in the vicinity of the fractured fiber in conjunction with a mechanics of materials approach and elasticity concepts, an approximate stress field was developed in each of the constituent materials. They presented numerical results for stress concentrations with variables such as fiber volume fraction, stiffness values, crack size, and fiber eccentricity. In addition, the analytical predictions were compared with direct experimental measurements obtained from a macro-model composite system. The results were shown to be in good agreement with the analytical predictions.

Fajardo [22] performed an experimental study of fiber fracture in a glass/epoxy composite using a macro-model composite. In particular, the effects of fiber volume fraction and crack size on stress concentration and ineffective length due to a single fiber fracture were studied. The experimental results were compared with theoretical predictions made using the annular ring model proposed by Carman et al. [21] and the shear lag model [18]. It was shown that the annular ring model provided closer agreement with the experimental results, although both models still over predicted the ineffective length.

Case et al. [23] expanded on the axisymmetric model of Carman et al. [21] and included the effects of multiple fiber fractures by using a linear superposition technique. In addition, a series solution model was used in conjunction with the assumed radial decay from Carman et al. [21] to obtain predictions of stress concentration as a function of axial distance from a broken fiber. These analytical results were compared to experimental measurements from a model composite system and were found to be in good agreement

for the case in which only a fiber fracture was present. However, poor agreement was achieved for the case in which a matrix crack, as well as a broken fiber, was present.

Recently, Kaw and Jadhav [24] considered the axisymmetric response of a cracked fiber in a matrix. The problem considered was almost identical to that considered by Dhaliwal et al. [10] with two exceptions: the matrix was taken to be of finite radial dimension, and the bonding between the fiber and the matrix was not taken to be perfect. Rather, the interface shear stress was assumed to be proportional to the difference between the axial displacement in the fiber and the axial displacement in the matrix. The problem was reduced to the solution of a Cauchy singular integral equation which was solved numerically. This analysis has the advantage of allowing researchers to consider the effects of imperfect bonding on the stress state surrounding a broken fiber. However, it is somewhat limited in that the effect of this imperfect bonding on the adjacent fibers cannot be analyzed.

McCartney [25] presented an approximate analysis of a more general class of fracture problems than those previously considered. This solution was based upon the assumption that the shear stress, σ_{rz}, in each of the constituents can be expressed as a product of an unknown function of z, and a linear variation in the radial direction. By making algebraic simplifications, he reduced the problem to the solution of a system of fourth order simultaneous ordinary differential equations which were solved numerically. The resulting stress state was compared with finite element models with good agreement.

Another approximate approach has been presented by Pagano [26], who used Reissner's variational theorem in conjunction with an equilibrium stress field in which the radial dependence was assumed to study the axisymmetric response of a concentric cylindrical body. The interfaces between adjacent cylinders were permitted to be either continuous or subjected to mixed boundary conditions. The external

surfaces were also permitted to be exposed to mixed boundary conditions. An example thermal stress problem was compared with an elasticity solution to examine details of the model accuracy.

The ultimate goal in modeling the stress concentrations and ineffective length surrounding a fiber fracture in the present context is to obtain accurate lamina level tensile strength predictions. Harlow and Phoenix [27] used a statistical analysis in conjunction with an assumed load sharing rule for a single ply tape to predict composite strength for this idealized problem. They considered both the case of the usual Weibull distribution and what they considered to be a more realistic double version which has the effect of putting an upper bound on fiber strength. They found that for typical cases the use of the double Weibull distribution for fiber strength does not affect the behavior of the probability distribution for the strength of composite materials and therefore its use may not be justified. The difficulty in calculating the probability distribution for the two-dimensional case suggests that it would be extremely difficult to extend the analysis to include three-dimensional effects.

Batdorf [7] has presented a somewhat simpler approach to the tensile strength of composite materials. The analysis is based on that proposed by Harlow and Phoenix [27], but through many simplifications the analysis may be used to predict the tensile strength of three-dimensional composite materials. The analysis uses theoretically determined stress concentrations and ineffective lengths due to multiple fiber fractures to estimate the fiber load level at which an instability occurs. This load level corresponds to the load at which the composite itself experiences catastrophic failure. To study the effects of the simplifications on the predicted strength, a comparison was made to the results published by Harlow and Phoenix [27]. It was shown that the failure stresses predicted by both methods differ by only a few percent, suggesting that the simplifying assumptions did not significantly affect the predictions made by the model.

A similar approach to modeling and predicting the tensile strength of polymer composites has been given by Reifsnider [28]. Rather than using the instability condition suggested by Batdorf, this analysis is based upon assuming that global composite failure (characterized by unstable fiber fracture) is characterized by the condition in which all fibers immediately adjacent to a single broken fiber fail due to the stress concentration. By making an assumption of the functional relationship between the ineffective length and the stress concentrations, they were able to suggest that an optimum stress concentration (an hence ineffective length) exists.

Gao et al. [6] conducted a study of strength prediction and optimization of composites. Their analysis used a modified shear lag approach in conjunction with the statistical analysis of Batdorf [7] to achieve tensile strength predictions. As part of their shear lag analysis, they showed that there was a direct relationship between stress concentrations due to fractured fibers and ineffective length. In addition, they considered the effects of irregular fiber spacing and the ratio of fiber to matrix stiffness values on the predictions for composite tensile strength. Their analysis also suggests that there may be an optimum ineffective length which maximizes the tensile strength.

1.2 Estimation of Residual Strength During Fatigue and Fatigue Life

The prediction of fatigue damage and fatigue life for composite materials has been the subject of many investigations during recent years. Hwong and Han [29] suggested four requirements for a universal fatigue damage model:

1. It should explain fatigue phenomena at an applied stress level.
2. It should explain fatigue phenomena for an overall applied stress range
    a) During a cycle at a high applied stress level the material should be more damaged than that at a low applied stress level.

b) If it is true that failure occurs at each maximum applied stress level, then the final damage (damage just before failure) at a low applied stress level should be larger than that of a high applied stress level.

3. It should explain multi-stress level fatigue phenomena.
4. It is desirable to establish the fatigue damage model without an S-N curve.

An excellent review of work in this area of fatigue life predictions has been given by Liu and Lessard [30]. In this paper, they divided the models used to predict fatigue life into three classes: residual strength degradation, modulus degradation, and damage tolerance approaches. According to Huston [31], most of the life prediction methods for polymeric composite materials are based on the residual strength degradation. However, he suggested that theories for fatigue failure based on the reduction of stiffness have one significant advantage over the remaining strength theories: remaining life can be assessed by non-destructive techniques. Also, Huston suggested that less testing needs to be conducted for stiffness-degradation-based models.

One such analysis based upon stiffness degradation has been proposed by Poursartip et al. [32]. In their analysis, it was assumed that the stiffness reduction could be related in a linear manner to the "damage" that was present due to fatigue. By making arguments based upon the global stiffness reduction due to cracks in composite materials, they were able to relate the measured stiffness reduction in a linear fashion to the damage (for a low concentration of cracks). The damage parameter could then be integrated from its initial value to some final (critical) value using the experimentally measured stiffness reduction. Failure was predicted to occur at the point where the damage parameter reached the critical value.

In the residual strength degradation approach, fatigue failure is typically assumed to occur when the residual strength becomes equal to the applied maximum stress amplitude. Such an approach was used by Broutman and Sahu [33], who proposed a cumulative damage theory based on a linear strength

degradation approach to explain the fatigue damage of fiberglass reinforced composites. Using this approach, they were able to make predictions for the residual strengths of laminates which were subjected to high-low stress tests and of laminates which were subjected to low-high stress tests. These predictions were compared with the experimentally measured residual strengths.

Hashin and Rotem [34] proposed a cumulative fatigue damage theory in which the damage during cyclic loading may be represented by the residual lifetime under subsequent constant amplitude cycling. The theory was based on the concept of damage curve families which are defined in terms of residual lifetimes for two-stage loading. The damage in two components due to two different loading histories was considered to be equivalent if it gave the same remaining life under subsequent loading at the same stress level. The authors considered procedures of lifetime prediction for piecewise constant cycle amplitude variation (multi-stage loading) as well as for the case of continuous variation of cycle amplitude with number of cycles. For the second case, the solution of initial value problems for first order nonlinear differential equations was required. The authors compared their analytical results to that of Miner's rule for multi-stage loading programs and found there to be considerable difference. In addition, they compared their analytical results to the experimental data obtained on both soft and hard steels with good agreement.

The modeling approaches presented previously dealt with phenomenological representations of fatigue life and residual strength predictions. Reifsnider and his coworkers [35-38] proposed a mechanistic non-linear residual strength prediction based on the critical element model. In this approach, a representative volume was selected which was typical of the material in question. This representative volume may contain damage, such as matrix cracks, delaminations, microbuckles, or fiber fractures, but some part of it still retains the ability to carry load. It is the failure of this part of the representative volume, the so-called "critical element", which determines the fracture of the entire representative volume. The remaining strength of the critical element was calculated by using a non-linear damage evolution equation which

accounts for the changing stress amplitude in the critical element. The predictions of the model were compared with laboratory data for polymeric as well as ceramic composite systems.

The general approach given a by Reifsnider et al. was extended by Subramanian et al. [39] to include the effects of an interphase region on the tensile fatigue behavior of composite laminates. The effect of this interphase region was modeled by the inclusion of an "efficiency" parameter which was taken to be a measure of displacement transfer between the fiber and the matrix. The effect of this efficiency parameter on the tensile strength was assessed using a micromechanical tensile strength model. Changes in the interphase property were used in conjunction with a maximum strain criterion to determine the fatigue life of the laminate. The results were compared with the experimentally measured lives.

The goal of the present study is to develop and validate a method to predict the residual strength and life of a polymeric composite component subjected to cyclic and sustained thermomechanical conditions. Conditions to be considered include elevated temperature (in air) and cyclic (fatigue) loading at various stress levels. As this area, in itself, is so broad, particular emphasis will be given to fiber-controlled-tensile failure in the context of the critical element model. The approach employed will be one which incorporates micromechanical, ply-level, and laminate-level modeling. To accomplish the goals of the proposal, the work will undertake a natural progression:

- Micromechanical tensile strength modeling which includes the role of the mechanical properties of the constituents, the interphase region, as well as the fiber volume fraction.
- Fatigue damage modeling in the context of the critical element model, including initial validation of the critical element model for laminates with "simple" damage development patterns using available data from the literature. This will concentrate on residual strength as well as lifetime prediction.

- Identification of damage processes and development of modeling techniques for unnotched and notched laminates at room temperature
- Identification of damage processes and development of modeling techniques for unnotched and notched laminates at elevated temperature

2. Strength Prediction in Unidirectional Composite Materials

In this section, an analytical model is developed which provides an approximate stress state in the region surrounding a fiber fracture in a unidirectional composite material. The stress state is approximate in that the adjacent fibers have been smeared together to form a ring, making the resulting problem axisymmetric. Using an additional smearing technique in conjunction with this approach, it is possible to determine the stress state in the neighborhood of multiple fiber fractures. This stress state is then be used in strength prediction models such as that described by Batdorf [7] to arrive at the desired macro-level strength predictions.

2.1 Basic Equations and Their Solution

The present analysis is an extension of that employed by Dhaliwal et al. [16] with modifications made to the potential functions to allow the body to include any number of concentric cylinder elements. We begin by considering the problem of a penny-shaped crack of radius r_c in an infinitely long elastic cylinder of radius r_1. This cylinder is surround by $N-1$ concentric elastic cylinders of radius r_i $(i=2, N-1)$, as shown in Figure 2.1. The crack surface $(0 \le r < r_c)$ is subjected to a prescribed normal loading. The assumption of perfect bonding requires continuity of displacements and tractions at each interface $(r = r_1, r_2, \ldots r_{N-1})$. Since the geometry of the problem is symmetric about the plane $z = 0$, the problem reduces to a mixed boundary value problem for the region $z \ge 0$, $r \ge 0$. By assuming appropriate solutions for the regions of interest, the problem is reduced to the solution of a Fredholm integral equation of the second kind. This equation may be solved numerically. Once this solution has been obtained, it may be used to calculate the stress and displacement components in each of the constituent materials. By using a geometry

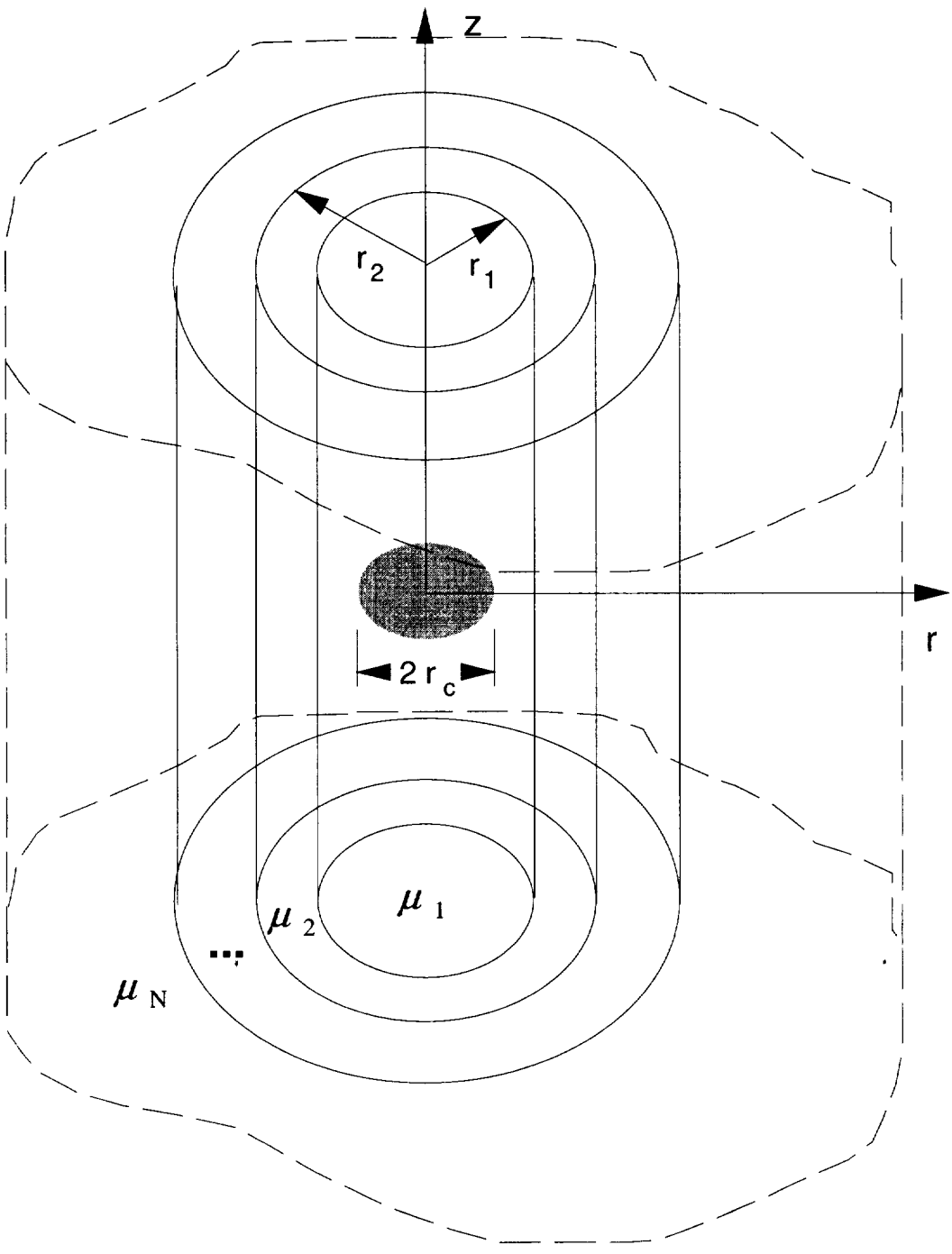

Figure 2.1. Penny-shaped crack surrounded by multiple concentric cylinders having different elastic constants.

approximation, it is then possible to use these stresses to determine the stress concentrations in unidirectional composite materials due to a single fiber fracture.

For the case of axisymmetric loading and boundary conditions, the displacement vector **U** assumes the form (u_r, 0, u_z) in a cylindrical coordinate system (r, θ, z). The equations of equilibrium in terms of displacement are given by

$$\mu\nabla\mathbf{U}+(\lambda+\mu)\nabla(\nabla\cdot\mathbf{U})=0 \tag{2.1}$$

The corresponding stresses are given by

$$\begin{aligned}
\sigma_{rr}(r,z)&=(\lambda+2\mu)\frac{\partial u_r}{\partial r}+\lambda\left(\frac{u_r}{r}+\frac{\partial u_z}{\partial z}\right)\\
\sigma_{zz}(r,z)&=(\lambda+2\mu)\frac{\partial u_z}{\partial z}+\lambda\left(\frac{u_r}{r}+\frac{\partial u_r}{\partial r}\right)\\
\sigma_{rz}(r,z)&=\mu\left(\frac{\partial u_r}{\partial z}+\frac{\partial u_z}{\partial r}\right)
\end{aligned} \tag{2.2}$$

where λ and μ are Lamé's constants.

Following Dhaliwal et al. [16], we may take the solution of the system of partial differential equations given by Equation (2.1) in the form of

$$\begin{aligned}
u_r(r,z)&=(1-2\nu)\frac{\partial\chi}{\partial r}+z\frac{\partial^2\chi}{\partial r\partial z}+\frac{\partial\phi}{\partial r}+(3-4\nu)\psi-r\frac{\partial\psi}{\partial r}\\
u_z(r,z)&=-2(1-\nu)\frac{\partial\chi}{\partial z}+z\frac{\partial^2\chi}{\partial z^2}+\frac{\partial\phi}{\partial z}-r\frac{\partial\psi}{\partial z}
\end{aligned} \tag{2.3}$$

where ν is Poisson's ratio and the functions χ, ϕ, and ψ satisfy the following relations

$$\left(\frac{\partial^2}{\partial r^2}+\frac{1}{r}\frac{\partial}{\partial r}+\frac{\partial^2}{\partial z^2}\right)\chi=0$$
$$\left(\frac{\partial^2}{\partial r^2}+\frac{1}{r}\frac{\partial}{\partial r}+\frac{\partial^2}{\partial z^2}\right)\phi=0 \qquad (2.4)$$
$$\left(\frac{\partial^2}{\partial r^2}+\frac{1}{r}\frac{\partial}{\partial r}+\frac{\partial^2}{\partial z^2}-\frac{1}{r^2}\right)\psi=0$$

Solution of Equations (2.4) for the regions R_i, $1 \le i \le N$, are taken in the form of

$$\chi^{(1)}(r,z)=\int_0^\infty \frac{1}{\xi^2}F(\xi)J_0(\xi r)\mathrm{e}^{-\xi z}\,d\xi$$
$$\phi^{(1)}(r,z)=\int_0^\infty \frac{1}{\xi}A(\xi)\left[I_0(\xi r)\cos(\xi z)-1\right]d\xi, \qquad (r, z) \in R_1$$
$$\psi^{(1)}(r,z)=\int_0^\infty B(\xi)I_1(\xi r)\cos(\xi z)d\xi$$

(2.5)

$$\chi^{(i)}(r,z)=0$$
$$\phi^{(i)}(r,z)=\int_0^\infty \frac{1}{\xi}\left[C^{(i)}(\xi)K_0(\xi r)+E^{(i)}(\xi)I_0(\xi r)\right]\cos(\xi z)d\xi, \qquad (r, z) \in R_i,\ 2 \le i \le N\text{-}1$$
$$\psi^{(i)}(r,z)=\int_0^\infty \left[D^{(i)}(\xi)K_1(\xi r)+G^{(i)}(\xi)I_1(\xi r)\right]\cos(\xi z)d\xi$$

(2.6)

$$\chi^{(N)}(r,z)=0$$
$$\phi^{(N)}(r,z)=\int_0^\infty \frac{1}{\xi}C^{(N)}(\xi)K_0(\xi r)\cos(\xi z)d\xi, \qquad (r, z) \in R_N$$
$$\psi^{(N)}(r,z)=\int_0^\infty D^{(N)}(\xi)K_1(\xi r)\cos(\xi z)d\xi$$

(2.7)

where the superscript i ($i = 1, 2...N$) denote quantities for the regions R_i and $J_i(\xi r)$, $I_i(\xi r)$, and $K_i(\xi r)$ denote Bessel functions of the first kind and modified Bessel functions of the first and second kind, respectively, of orders j ($j = 0, 1$). From Equations (2.2), (2.3), (2.5), (2.6), and (2.7), we obtain the following expressions for the stress and displacement components in the regions R_i, $i = 1, 2, \ldots N$:

$$u_r^{(1)} = \int_0^\infty \left[\frac{1}{\xi}(2\nu_1 - 1 + \xi z)F(\xi)J_1(\xi r)e^{-\xi z} + \left\{ A(\xi)I_1(\xi r) + B(\xi)\left[4(1-\nu_1)I_1(\xi r) - \xi r I_0(\xi r)\right]\right\}\cos(\xi z)\right] d\xi \tag{2.8}$$

$$u_z^{(1)} = \int_0^\infty \left[\frac{1}{\xi}(2 - 2\nu_1 + \xi z)F(\xi)J_0(\xi r)e^{-\xi z} - \left\{ A(\xi)I_0(\xi r) - \xi r B(\xi)I_1(\xi r)\right\}\sin(\xi z)\right] d\xi \tag{2.9}$$

$$\sigma_{rr}^{(1)} = \int_0^\infty 2\mu_1 [\left\{ (\xi z - 1)J_0(\xi r) + (1 - 2\nu_1 - \xi z)\frac{1}{\xi r}J_1(\xi r)\right\} F(\xi)e^{-\xi z} - \frac{1}{r}\left\{ A(\xi)\left[I_1(\xi r) - \xi r I_0(\xi r)\right] + B(\xi)\left[(4 - 4\nu_1 + \xi^2 r^2)I_1(\xi r) - (3 - 2\nu_1)\xi r I_0(\xi r)\right]\right\}\cos(\xi z)] d\xi \tag{2.10}$$

$$\sigma_{zz}^{(1)}(r,z) = -2\mu_1 \int_0^\infty \left[(1 + \xi z)F(\xi)J_0(\xi r)e^{-\xi z} + \xi\left\{ A(\xi)I_0(\xi r) - B(\xi)\left[2\nu_1 I_0(\xi r) + \xi r I_1(\xi r)\right]\right\}\cos(\xi z)\right] d\xi \tag{2.11}$$

$$\sigma_{rz}^{(1)}(r,z) = -2\mu_1 \int_0^\infty \left[\xi z F(\xi)J_1(\xi r)e^{-\xi z} + \xi\left\{ A(\xi)I_1(\xi r) + B(\xi)\left[2(1-\nu_1)I_1(\xi r) - \xi r I_0(\xi r)\right]\right\}\sin(\xi z)\right] d\xi \tag{2.12}$$

$$u_r^{(i)}(r,z) = \int_0^\infty \{ -C^{(i)}(\xi)K_1(\xi r) + E^{(i)}(\xi)I_1(\xi r) + D^{(i)}(\xi)\left[4(1-\nu_i)K_1(\xi r) + \xi r K_0(\xi r)\right] + G^{(i)}(\xi)\left[4(1-\nu_i)I_1(\xi r) - \xi r I_0(\xi r)\right]\}\cos(\xi z) d\xi \tag{2.13}$$

$$u_z^{(i)}(r,z) = \int_0^\infty \left\{ -C^{(i)}(\xi)K_0(\xi r) - E^{(i)}(\xi)I_0(\xi r) + D^{(i)}(\xi)\xi r K_1(\xi r) + G^{(i)}(\xi)\xi r I_1(\xi r)\right\}\sin(\xi z) d\xi \tag{2.14}$$

$$\sigma_{rr}^{(i)}(r,z)=\frac{2\mu_i}{r}\int_0^\infty\{C^{(i)}(\xi)\left[\xi rK_0(\xi r)+K_1(\xi r)\right]-D^{(i)}(\xi)\left[\left(4-4\nu_i+\xi^2r^2\right)K_1(\xi r)+(3-2\nu_i)\xi rK_0(\xi r)\right]$$
$$+E^{(i)}(\xi)\left[\xi rI_0(\xi r)-I_1(\xi r)\right]-G^{(i)}(\xi)\left[\left(4-4\nu_i+\xi^2r^2\right)I_1(\xi r)-(3-2\nu_i)\xi rI_0(\xi r)\right]\}\cos(\xi z)d\xi$$

(2.15)

$$\sigma_{rz}^{(i)}(r,z)=2\mu_i\int_0^\infty\xi\{C^{(i)}(\xi)K_1(\xi r)-D^{(i)}(\xi)\left[2(1-\nu_i)K_1(\xi r)+\xi rK_0(\xi r)\right]$$
$$-E^{(i)}(\xi)I_1(\xi r)-G^{(i)}(\xi)\left[2(1-\nu_i)I_1(\xi r)+\xi rI_0(\xi r)\right]\}\sin(\xi z)d\xi$$

(2.16)

$$\sigma_{zz}^{(i)}(r,z)=-2\mu_i\int_0^\infty\xi\{C^{(i)}(\xi)K_0(\xi r)+D^{(i)}(\xi)\left[2\nu_iK_0(\xi r)-\xi rK_1(\xi r)\right]$$
$$+E^{(i)}(\xi)I_1(\xi r)-G^{(i)}(\xi)\left[2\nu_iI_0(\xi r)+\xi rI_1(\xi r)\right]\}\cos(\xi z)d\xi$$

(2.17)

$$u_r^{(N)}(r,z)=\int_0^\infty\{-C^{(N)}(\xi)K_1(\xi r)+D^{(N)}(\xi)\left[4(1-\nu_N)K_1(\xi r)+\xi rK_0(\xi r)\right]\}\cos(\xi z)d\xi$$

(2.18)

$$u_z^{(N)}(r,z)=\int_0^\infty\left\{-C^{(N)}(\xi)K_0(\xi r)+D^{(N)}(\xi)\xi rK_1(\xi r)\right\}\sin(\xi z)d\xi$$

(2.19)

$$\sigma_{rr}^{(N)}(r,z)=\frac{2\mu_N}{r}\int_0^\infty\{C^{(N)}(\xi)\left[\xi rK_0(\xi r)+K_1(\xi r)\right]-D^{(N)}(\xi)\left[\left(4-4\nu_N+\xi^2r^2\right)K_1(\xi r)+(3-2\nu_N)\xi rK_0(\xi r)\right]\}\cos(\xi z)d\xi$$

(2.20)

$$\sigma_{rz}^{(N)}(r,z)=2\mu_N\int_0^\infty\xi\left\{C^{(N)}(\xi)K_1(\xi r)-D^{(N)}(\xi)\left[2(1-\nu_N)K_1(\xi r)+\xi rK_0(\xi r)\right]\right\}\sin(\xi z)d\xi$$

(2.21)

$$\sigma_{zz}^{(N)}(r,z)=-2\mu_N\int_0^\infty\xi\left\{C^{(N)}(\xi)K_0(\xi r)+D^{(N)}(\xi)\left[2\nu_NK_0(\xi r)-\xi rK_1(\xi r)\right]\right\}\cos(\xi z)d\xi$$

(2.22)

where μ_i and ν_i denote the shear modulus and Poisson's ratio for the region R_i (i = 1, 2, ... N).

2.2 Formulation of the Problem

The problem of a penny shaped-crack of radius r_c in a long elastic cylinder of radius r_1 ($r_1 > r_c$) is considered. We assume that there is perfect bonding between each of the constituents. All of the materials are assumed to be homogenous and isotropic. Since the geometry of the problem is symmetric about the crack plane, we consider a semi-infinite elastic cylinder subjected to the following boundary conditions:

$$\sigma_{zz}^{(1)}(r,0) = p(r), \qquad 0 < r < r_c \tag{2.23}$$

$$u_z^{(1)}(r,z) = 0, \qquad r_c < r < r_1 \tag{2.24}$$

$$\sigma_{rz}^{(1)}(r,0) = 0, \qquad 0 < r < r_1 \tag{2.25}$$

$$u_z^{(i)}(r,z) = 0, \qquad r_{i-1} < r < r_i \tag{2.26}$$

$$\sigma_{rz}^{(i)}(r,0) = 0, \qquad r_{i-1} < r < r_i \tag{2.27}$$

The continuity conditions for displacements and tractions are given by

$$\begin{aligned} u_z^{(i)}(r_i,z) &= u_z^{(i+1)}(r_i,z) \\ u_r^{(i)}(r_i,z) &= u_r^{(i+1)}(r_i,z) \\ \sigma_{rr}^{(i)}(r_i,z) &= \sigma_{rr}^{(i+1)}(r_i,z) \\ \sigma_{rz}^{(i)}(r_i,z) &= \sigma_{rz}^{(i+1)}(r_i,z) \end{aligned} \tag{2.28}$$

2.3 Reduction of the Problem to the Solution of a Fredholm Integral Equation of the Second Kind

Due to the functional forms chosen for χ, ϕ, and ψ in each of the constituents, it is apparent that the boundary conditions given by Equations (2.24)-(2.27) are identically satisfied by the stresses and displacements given in Equations (2.12), (2.14), (2.16), (2.19), and (2.21). Substituting Equations (2.11) and (2.9) into the boundary conditions given by Equations (2.23) and (2.24), we arrive at the following dual integral equations:

$$\int_0^\infty F(\xi)J_0(\xi r)d\xi + \int_0^\infty \xi\left\{A(\xi)I_0(\xi r) - B(\xi)\left(2\nu_1 I_0(\xi r) + \xi r I_1(\xi r)\right)\right\}d\xi = \frac{-p(r)}{2\mu_1} \tag{2.29}$$

$$0 < r < r_c$$

$$\int_0^\infty \frac{1}{\xi} F(\xi)J_0(\xi r) = 0 \tag{2.30}$$

$$r_c < r < r_1$$

Equation (2.30) is identically satisfied if the solution for $F(\xi)$ is taken as

$$F(\xi) = \xi\int_0^{r_c} h(t)\sin(\xi t)dt \tag{2.31}$$

regardless of the form of $h(t)$.

Substituting Equation (2.31) into Equation (2.29), we see that the function $h(t)$ must satisfy

$$h(t) + \frac{2}{\pi}\int_0^\infty \xi\left\{\left[A(\xi) - 2\nu_1 B(\xi)\right]\int_0^t \frac{rI_0(\xi r)dr}{\sqrt{(t^2 - r^2)}} - \xi B(\xi)\int_0^t \frac{r^2 I_1(\xi r)dr}{\sqrt{(t^2 - r^2)}}\right\}d\xi = -\frac{1}{\pi\mu_1}\int_0^t \frac{rp(r)dr}{\sqrt{(t^2 - r^2)}} \tag{2.32}$$

Making use of the fact that

$$\int_0^t \frac{rI_0(\xi r)d\xi}{\sqrt{(t^2 - r^2)}} = \frac{\sinh(\xi t)}{\xi}$$

$$\int_0^t \frac{r^2 I_1(\xi r)d\xi}{\sqrt{(t^2 - r^2)}} = \frac{\xi t\cosh(\xi t) - \sinh(\xi t)}{\xi^2} \tag{2.33}$$

and substituting into Equation (2.32) we find that

$$h(t)+\frac{2}{\pi}\int_0^\infty\left\{\left[A(\xi)-2\nu_1 B(\xi)\right]\sinh(\xi t)-\left(\xi t\cosh(\xi t)-\sinh(\xi t)\right)B(\xi)\right\}d\xi=-\frac{1}{\pi\mu_1}\int_0^t\frac{rp(r)dr}{\sqrt{\left(t^2-r^2\right)}}$$

(2.34)

Using the Fourier inversion theorem along with the boundary conditions given by Equations (2.28) and the stress and displacements given by Equations (2.8)-(2.10) and (2.12)-(2.16), we obtain the following relations at $r = r_1$:

$$-I_0(r_1s)A(s)+r_1sI_1(r_1s)B(s)+K_0(r_1s)C^{(2)}(s)-r_1sK_1(r_1s)D^{(2)}(s)$$
$$+I_0(r_1s)E^{(2)}(s)-r_1sI_1(r_1s)G^{(2)}(s)=\frac{-2}{\pi}\int_0^\infty\frac{1}{u}\left(2(1-\nu_1)f_1+uf_2\right)J_0(r_1u)F(u)du=X_1$$

(2.35)

$$I_1(r_1s)A(s)+\left[4(1-\nu_1)I_1(r_1s)-r_1sI_0(r_1s)\right]B(s)+K_1(r_1s)C^{(2)}(s)-I_1(r_1s)E^{(2)}(s)$$
$$-\left[4(1-\nu_2)K_1(r_1s)+r_1sK_0(r_1s)\right]D^{(2)}(s)-\left[4(1-\nu_2)I_1(r_1s)-r_1sI_0(r_1s)\right]G^{(2)}(s)$$
$$=\frac{-2}{\pi}\int_0^\infty\frac{1}{u}\left((2\nu_1-1)f_3+uf_4\right)J_1(r_1u)F(u)du=X_2$$

(2.36)

$$\mu_2\{C^{(2)}(s)\left[r_1sK_0(r_1s)+K_1(r_1s)\right]-D^{(2)}(s)\left[\left(4-4\nu_2+r_1^2s^2\right)K_1(r_1s)+(3-2\nu_2)r_1sK_0(r_1s)\right]$$
$$+E^{(2)}(s)\left[r_1sI_0(r_1s)-I_1(r_1s)\right]-G^{(2)}(s)\left[\left(4-4\nu_2+r_1^2s^2\right)I_1(r_1s)-(3-2\nu_2)r_1sI_0(r_1s)\right]\}$$
$$+\mu_1\{-A(s)\left[r_1sI_0(r_1s)-I_1(r_1s)\right]+B(s)\left[\left(4-4\nu_2+r_1^2s^2\right)I_1(r_1s)-(3-2\nu_2)r_1sI_0(r_1s)\right]\}$$
$$=\frac{2}{\pi}r_1\mu_1\int_0^\infty F(u)\left[\left(-f_3+uf_4\right)J_0(r_1u)+\left\{(1-2\nu_1)f_3-uf_4\right\}\frac{J_1(r_1u)}{r_1u}\right]du=X_3\mu_1$$

(2.37)

$$\mu_2s\{C^{(2)}(s)K_1(r_1s)-D^{(2)}(s)\left[2(1-\nu_2)K_1(r_1s)+r_1sK_0(r_1s)\right]-E^{(2)}(s)I_1(r_1s)$$
$$-G^{(2)}(s)\left[2(1-\nu_2)I_1(r_1s)-r_1sI_0(r_1s)\right]\}+\mu_1s\{A(s)I_1(r_1s)$$
$$+B(s)\left[2(1-\nu_1)I_1(r_1s)-r_1sI_0(r_1s)\right]\}=-\frac{2}{\pi}\mu_1\int_0^\infty uF(u)f_2J_1(r_1u)du=X_4\mu_1$$

(2.38)

where, using the notation of Dhaliwal et al.,

$$f_1 = \int_0^\infty \sin(sz)e^{-uz}dz = \frac{s}{\left(s^2+u^2\right)}$$

$$f_2 = \int_0^\infty z\sin(sz)e^{-uz}dz = \frac{2su}{\left(s^2+u^2\right)^2} \tag{2.39}$$

$$f_3 = \int_0^\infty \cos(sz)e^{-uz}dz = \frac{u}{\left(s^2+u^2\right)}$$

$$f_4 = \int_0^\infty z\cos(sz)e^{-uz}dz = \frac{u^2-s^2}{\left(s^2+u^2\right)^2}$$

Imposing the boundary conditions given by Equations (2.28) along with Equations (2.13)-(2.16) and (2.18)-(2.21) and using the Fourier inversion theorem, we arrive at the following relations for $3 \le i \le N-1$:

$$\begin{aligned}
&-C^{(i-1)}(s)K_1(r_{i-1}s) + E^{(i-1)}(s)I_1(r_{i-1}s) + D^{(i-1)}(s)\left[4(1-\nu_{i-1})K_1(r_{i-1}s) + r_{i-1}sK_0(r_{i-1}s)\right] \\
&\qquad +G^{(i-1)}(s)\left[4(1-\nu_{i-1})I_1(r_{i-1}s) - r_{i-1}sI_0(r_{i-1}s)\right] \\
&= -C^{(i1)}(s)K_1(r_{i-1}s) + E^{(i)}(s)I_1(r_{i-1}s) + D^{(i1)}(s)\left[4(1-\nu_{i-1})K_1(r_{i-1}s) + r_{i-1}sK_0(r_{i-1}s)\right] \\
&\qquad +G^{(i)}(s)\left[4(1-\nu_{i-1})I_1(r_{i-1}s) - r_{i-1}sI_0(r_{i-1}s)\right]
\end{aligned} \tag{2.40}$$

$$\begin{aligned}
&-C^{(i-1)}(s)K_0(r_{i-1}s) + D^{(i-1)}(s)r_{i-1}sK_1(r_{i-1}s) - E^{(i-1)}(s)I_0(r_{i-1}s) + G^{(i-1)}(s)r_{i-1}sI_1(r_{i-1}s) \\
&= -C^{(i1)}(s)K_0(r_{i-1}s) + D^{(i1)}(s)r_{i-1}sK_1(r_{i-1}s) - E^{(i1)}(s)I_0(r_{i-1}s) + G^{(i)}(s)r_{i-1}sI_1(r_{i-1}s)
\end{aligned} \tag{2.41}$$

$$\frac{2\mu_{i-1}}{r_{i-1}}\{C^{(i-1)}(s)\left[r_{i-1}sK_0(r_{i-1}s)+K_1(r_{i-1}s)\right]-D^{(i-1)}(s)\left[\left(4-4\nu_{i-1}+r_{i-1}{}^2s^2\right)K_1(r_{i-1}s)+(3-2\nu_{i-1})r_{i-1}sK_0(r_{i-1}s)\right]$$
$$+E^{(i-1)}(s)\left[r_{i-1}sI_0(r_{i-1}s)-I_1(r_{i-1}s)\right]-G^{(i-1)}(s)\left[\left(4-4\nu_{i-1}+r_{i-1}{}^2s^2\right)I_1(r_{i-1}s)-(3-2\nu_{i-1})r_{i-1}sI_0(r_{i-1}s)\right]\}$$
$$=\frac{2\mu_i}{r_{i-1}}\{C^{(i)}(s)\left[r_{i-1}sK_0(r_{i-1}s)+K_1(r_{i-1}s)\right]-D^{(i)}(s)\left[\left(4-4\nu_i+r_{i-1}{}^2s^2\right)K_1(r_{i-1}s)+(3-2\nu_i)r_{i-1}sK_0(r_{i-1}s)\right]$$
$$+E^{(i)}(s)\left[r_{i-1}sI_0(r_{i-1}s)-I_1(r_{i-1}s)\right]-G^{(i)}(s)\left[\left(4-4\nu_i+r_{i-1}{}^2s^2\right)I_1(r_{i-1}s)-(3-2\nu_i)r_{i-1}sI_0(r_{i-1}s)\right]\} \tag{2.42}$$

$$2\mu_{i-1}\{C^{(i-1)}(s)K_1(r_{i-1}s)-D^{(i-1)}(s)\left[2(1-\nu_{i-1})K_1(r_{i-1}s)+r_{i-1}sK_0(r_{i-1}s)\right]$$
$$-E^{(i-1)}(s)I_1(r_{i-1}s)-G^{(i-1)}(s)\left[2(1-\nu_{i-1})I_1(r_{i-1}s)+r_{i-1}sI_0(r_{i-1}s)\right]\}$$
$$=2\mu_i\{C^{(i)}(s)K_1(r_{i-1}s)-D^{(i)}(s)\left[2(1-\nu_i)K_1(r_{i-1}s)+r_{i-1}sK_0(r_{i-1}s)\right]$$
$$-E^{(i)}(s)I_1(r_{i-1}s)-G^{(i)}(s)\left[2(1-\nu_i)I_1(r_{i-1}s)+r_{i-1}sI_0(r_{i-1}s)\right]\} \tag{2.43}$$

and at the last interface ($r = r_{N-1}$)

$$-C^{(N-1)}(s)K_1(r_{N-1}s)+E^{(N-1)}(s)I_1(r_{N-1}s)+D^{(N-1)}(s)\left[4(1-\nu_{N-1})K_1(r_{N-1}s)+r_{N-1}sK_0(r_{N-1}s)\right]$$
$$+G^{(N-1)}(s)\left[4(1-\nu_{N-1})I_1(r_{N-1}s)-r_{N-1}sI_0(r_{N-1}s)\right]$$
$$=C^{(N)}(s)K_1(r_{N-1}s)+D^{(N)}(s)\left[4(1-\nu_N)K_1(r_{N-1}s)+r_{N-1}sK_0(r_{N-1}s)\right] \tag{2.44}$$

$$-C^{(N-1)}(s)K_0(r_{N-1}s)+D^{(N-1)}(s)r_{N-1}sK_1(r_{N-1}s)-E^{(N-1)}(s)I_0(r_{N-1}s)+G^{(N-1)}(s)r_{N-1}sI_1(r_{N-1}s)$$
$$=-C^{(N)}(s)K_0(r_{N-1}s)+D^{(N)}(s)r_{N-1}sK_1(r_{N-1}s) \tag{2.45}$$

$$\frac{2\mu_{N-1}}{r_{N-1}}\{C^{(N-1)}(s)\left[r_{N-1}sK_0(r_{N-1}s)+K_1(r_{N-1}s)\right]$$
$$-D^{(N-1)}(s)\left[\left(4-4\nu_{N-1}+r_{N-1}{}^2s^2\right)K_1(r_{N-1}s)+(3-2\nu_{N-1})r_{N-1}sK_0(r_{N-1}s)\right]$$
$$+E^{(N-1)}(s)\left[r_{N-1}sI_0(r_{N-1}s)-I_1(r_{N-1}s)\right]$$
$$-G^{(N-1)}(s)\left[\left(4-4\nu_{N-1}+r_{N-1}{}^2s^2\right)I_1(r_{N-1}s)-(3-2\nu_{N-1})r_{N-1}sI_0(r_{N-1}s)\right]\}$$
$$=\frac{2\mu_N}{r_{N-1}}\{C^{(N)}(s)\left[r_{N-1}sK_0(r_{N-1}s)+K_1(r_{N-1}s)\right]$$
$$-D^{(N)}(s)\left[\left(4-4\nu_N+r_{N-1}{}^2s^2\right)K_1(r_{N-1}s)+(3-2\nu_N)r_{N-1}sK_0(r_{N-1}s)\right]\} \tag{2.46}$$

$$2\mu_{N-1}\{C^{(N-1)}(s)K_1(r_{N-1}s)-D^{(N-1)}(s)\left[2(1-\nu_{N-1})K_1(r_{N-1}s)+r_{N-1}sK_0(r_{N-1}s)\right]$$
$$-E^{(N-1)}(s)I_1(r_{N-1}s)-G^{(N-1)}(s)\left[2(1-\nu_{N-1})I_1(r_{N-1}s)+r_{N-1}sI_0(r_{N-1}s)\right]\}$$
$$=2\mu_N\{C^{(N)}(s)K_1(r_{N-1}s)-D^{(N)}(s)\left[2(1-\nu_N)K_1(r_{N-1}s)+r_{N-1}sK_0(r_{N-1}s)\right]\} \tag{2.47}$$

Equations (2.35)-(2.38) and (2.40)-(2.47) represent a system of *4(N-1)* equations for the unknown functions *A(s)*, *B(s)*, $C^{(i)}(s)$, $D^{(i)}(s)$, $E^{(i)}(s)$, $F^{(i)}(s)$, $C^{(i)}(s)$, and $D^{(i)}(s)$ at each point in *s*-space. These equations may be solved by inverting the resulting matrix equation. It is then possible to write the functions *A(s)* and *B(s)* in the form

$$\begin{aligned} A(s) &= A_1X_1 + A_2X_2 + A_3X_3 + A_4X_4 \\ B(s) &= B_1X_1 + B_2X_2 + B_3X_3 + B_4X_4 \end{aligned} \tag{2.48}$$

where the coefficients A_i and B_i are determined by the matrix inverse.

Making use of Equation (2.48), we may then write the following expression in the form

$$\left[A(s)-2\nu_1 B(s)\right]\sinh(st)-\left[st\cosh(st)-\sinh(st)\right]B(st)$$
$$= C_1(s,t)X_1 + C_2(s,t)X_2 + C_3(s,t)X_3 + C_4(s,t)X_4 \tag{2.49}$$

where

$$\begin{aligned}
C_1(s,t) &= A_1\sinh(st) + B_1\left[(1-2\nu_1)\sinh(st) - st\cosh(st)\right]\\
C_2(s,t) &= A_2\sinh(st) + B_2\left[(1-2\nu_1)\sinh(st) - st\cosh(st)\right]\\
C_3(s,t) &= A_2\sinh(st) + B_2\left[(1-2\nu_1)\sinh(st) - st\cosh(st)\right]\\
C_4(s,t) &= A_4\sinh(st) + B_4\left[(1-2\nu_1)\sinh(st) - st\cosh(st)\right]
\end{aligned} \tag{2.50}$$

Following the analysis of Dhaliwal et al. [16], and making use of Equations (2.31) and (2.35), we find that the expression for X_1 can be written as

$$X_1 = \frac{-4(1-\nu_1)}{\pi}\int_0^{r_c} h(t)dt\int_0^{\infty}\frac{J_0(r_1u)\sin(ut)du}{s^2+u^2} - \frac{4s}{\pi}\int_0^{r_c} h(t)dt\int_0^{\infty}\frac{u^2J_0(r_1u)\sin(ut)du}{\left(s^2+u^2\right)^2} \tag{2.52}$$

From Erdelyi [40] we find that

$$I = \int_0^{\infty}\frac{J_0(r_1u)\sin(ut)du}{s^2+u^2} = \frac{\sinh(st)K_0(r_1s)}{s}, \qquad t < b. \tag{2.53}$$

and

$$\int_0^{\infty}\frac{u^2J_0(r_1u)\sin(ut)du}{\left(s^2+u^2\right)^2} = I - s^2\int_0^{\infty}\frac{J_0(r_1u)\sin(ut)du}{\left(s^2+u^2\right)^2} \tag{2.54}$$

Differentiating both sides of Equation (2.53) with respect to s, we find that

$$\int_0^\infty \frac{J_0(r_1 u)\sin(ut)du}{\left(s^2+u^2\right)^2} = \frac{1}{2s}\left[\sinh(st)K_0(r_1 s) + r_1 s\sinh(st)K_1(r_1 s) - st\cosh(st)K_0(r_1 s)\right]$$

(2.55)

Substituting Equations (2.53)-(2.55) into Equation (2.52), we find that

$$X_1 = \frac{-2}{\pi}\int_0^{r_c} h(t)\left[(3-2\nu_1)\sinh(st)K_0(r_1 s) - r_1 s\sinh(st)K_1(r_1 s) + st\cosh(st)K_0(r_1 s)\right]dt$$

(2.56)

Following a similar procedure, we find that we may write

$$X_2 = -\frac{2}{\pi}(2\nu_1 - 1)\int_0^{r_c} h(t)dt\int_0^\infty \frac{uJ_1(r_1 u)\sin(ut)du}{s^2+u^2} - \frac{2}{\pi}\int_0^{r_c} h(t)dt\int_0^\infty \frac{u\left(u^2-s^2\right)J_1(r_1 u)\sinh(ut)du}{\left(s^2+u^2\right)^2}$$

(2.57)

The second term in Equation (2.57) may be rewritten as

$$\int_0^\infty \frac{u\left(u^2-s^2\right)J_1(r_1 u)\sinh(ut)du}{\left(s^2+u^2\right)^2} = \int_0^\infty \frac{uJ_1(r_1 u)\sin(ut)du}{s^2+u^2} - 2s^2\int_0^\infty \frac{uJ_1(r_1 u)\sin(ut)du}{\left(s^2+u^2\right)^2}$$

(2.58)

From Erdelyi [40], we find that

$$\int_0^\infty \frac{uJ_1(r_1 u)\sin(ut)du}{s^2+u^2} = \sinh(st)K_1(r_1 s), \qquad t<b. \tag{2.59}$$

Differentiating both sides of Equation (2.59), we obtain:

$$\int_0^\infty \frac{uJ_1(r_1u)\sin(ut)du}{(s^2+u^2)^2} = \frac{1}{2s^2}\left[\sinh(st)\{r_1sK_0(r_1s)+K_1(r_1s)\}-st\cosh(st)K_1(r_1s)\right] \tag{2.60}$$

Making use of Equations (2.59) and (2.60), we find that Equation (2.57) can be written as

$$X_2 = -\frac{2}{\pi}\int_0^{r_c} h(t)\{(2\nu_1-1)\sinh(st)K_1(r_1s)-[r_1s\sinh(st)K_0(r_1s)-st\cosh(st)K_1(r_1s)]\}dt \tag{2.61}$$

Using Equations (2.31), (2.37), (2.39), (2.54), and (2.59), we find that

$$\begin{aligned} X_3 = \frac{2}{\pi}[\ \int_0^{r_c} h(t)\{r_1s[r_1s\sinh(st)K_1(r_1s)-st\cosh(st)K_0(r_1s)] \\ +(1-2\nu_1)\sinh(st)K_1(r_1s)-st\cosh(st)K_1(r_1s)\ \}dt\ ] \end{aligned} \tag{2.62}$$

Similarly, the expression for X_4 may be written as

$$X_4 = -\frac{4}{\pi}s\int_0^\infty h(t)dt\int_0^\infty \frac{u^3J_1(r_1u)\sin(ut)du}{(s^2+u^2)^2} \tag{2.63}$$

The second integral in Equation (2.63) can be written in the following form:

$$\int_0^\infty u\frac{u^2J_1(r_1u)\sin(ut)du}{(s^2+u^2)^2} = \int_0^\infty \frac{uJ_1(r_1u)\sin(ut)du}{s^2+u^2} - s^2\int_0^\infty \frac{uJ_1(r_1u)\sin(ut)du}{(s^2+u^2)^2} \tag{2.64}$$

so that

$$X_4 = -\frac{2}{\pi}\int_0^{r_c} h(t)\left[\sinh(st)K_1(r_1s)+st\cosh(st)K_1(r_1s)-r_1s\sinh(st)K_0(r_1s)\right]dt \tag{2.65}$$

By substituting Equations (2.50), (2.56), (2.61), (2.62), and (2.65) into Equation (2.34) we find the following relation

$$h(t)+\int_0^{r_c} h(u)K(u,t)du=-\frac{1}{\pi\mu_1}\int_0^t \frac{rp(r)dr}{\sqrt{t^2-r^2}}, \qquad 0<t<r_c, \tag{2.66}$$

where

$$\begin{aligned}K(u,t)=-\frac{4}{\pi}\int_0^{\infty}\{&\left[(3-2\nu_1)\sinh(us)K_0(r_1s)-r_1s\sinh(us)K_1(r_1s)+us\cosh(r_1s)K_0(r_1s)\right]C_1(s,t)\\&+\left[(2\nu_1-1)\sinh(us)K_1(r_1s)-\{r_1s\sinh(us)K_0(r_1s)-us\cosh(us)K_1(r_1s)\}\right]C_2(s,t)\\&-\left[r_1^2s^2\sinh(us)K_1(r_1s)-(r_1s)(us)\cosh(us)K_0(r_1s)+(1-2\nu_1)\sinh(us)K_1(r_1s)-us\cosh(us)K_1(r_1s)\right]C_3(s,t)\\&+\left[s\sinh(us)K_1(r_1s)+s(us)\cosh(us)K_1(r_1s)-s(r_1s)\sinh(us)K_0(r_1s)\right]C_4(s,t)\}ds\end{aligned} \tag{2.67}$$

Equation (2.66) is a Fredholm integral equation of the second kind having a kernel given by Equation 65. This equation may be solved numerically for the unknown function *h(t)*.

2.4 Representation of the Broken Fiber Problem

To analyze a single fiber fracture in a unidirectional composite, we separate the problem into a near-field analysis and a far-field analysis. The total solution is then just the superposition of the far-field solution and the near-field solution. The far-field solution for a uniform strain applied in the fiber direction may be easily obtained in a manner such as that detailed by Pagano and Tandon [41]. In posing the near-field problem, we assume a fiber fracture has occurred in a composite with a hexagonal array of fibers, as shown in Figure 2.2. The size of the crack is denoted by r_c, the size of the fiber by r_f, and the distance to

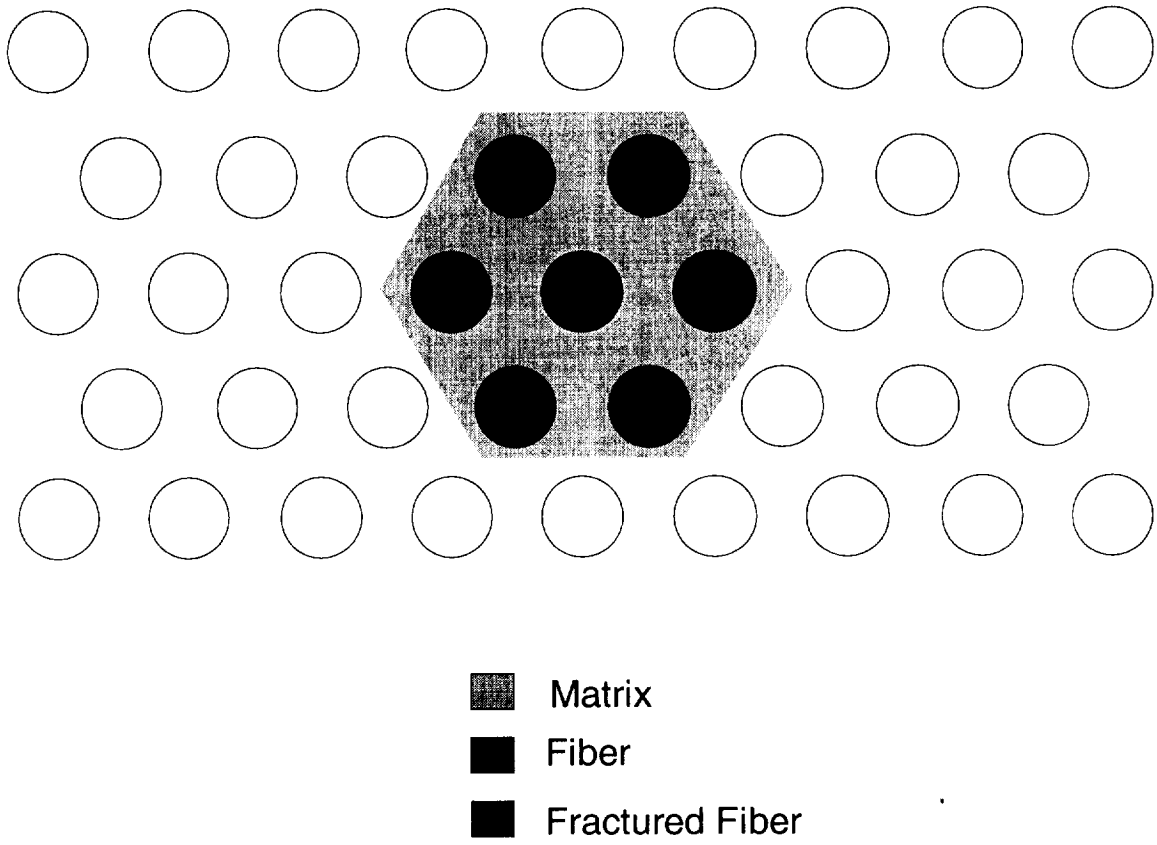

Figure 2.2. Composite material having hexagonal packing which contains a single broken fiber. The shaded area is selected as a representative volume element for the analysis.

the nearest adjacent fiber by r_2 Prior to the formation of the crack, load was carried by this region. The crack is opened by a pressure p_0 which is equal to the negative of the fiber stress determined from the far-field analysis such that the superposition of the near-field solution and the far-field solution produce a traction-free crack face. Following the suggestion of Carman [42], we make the assumption that the fiber immediately adjacent to the fracture fiber may be represented by an annular ring of material (see Figure 2.3). This assumption reduces the near-field problem to an axisymmetric one. While the point-wise stresses determined in such a manner are not the exact solution to the near-field problem, the do accurately depict the trends in the stress variations of interest. The inner radius of the fiber annular ring, r_2, is given by the distance to the adjacent fibers. The outer radius of the fiber annular ring, r_3, is determined from the global fiber volume fraction. For hexagonal packing, we have

$$r_3 = \sqrt{6r_1^2 + r_2^2}$$
$$r_4 = \frac{7r_1^2}{V_f} \tag{2.68}$$

In order to use the analysis developed previously in this paper, we allow the radius of the crack, r_c, to approach the radius of the fiber, r_1. Equation (2.66) is then solved numerically using the Nystrom method [43].

2.5 Numerical Results

To demonstrate the solution, an number of numerical studies were conducted. The first such study was to determine the effect of fiber to matrix stiffness ratio on the resulting stress state. To calculate the effective composite properties we use the following prescribed values

$$\nu_1 = \nu_2 = \nu_3 = \nu_4 = \nu_5 = 0.2$$
$$\mu_5 = \left[\frac{V_f}{\mu_1} + \frac{V_m}{\mu_2}\right] \tag{2.69}$$

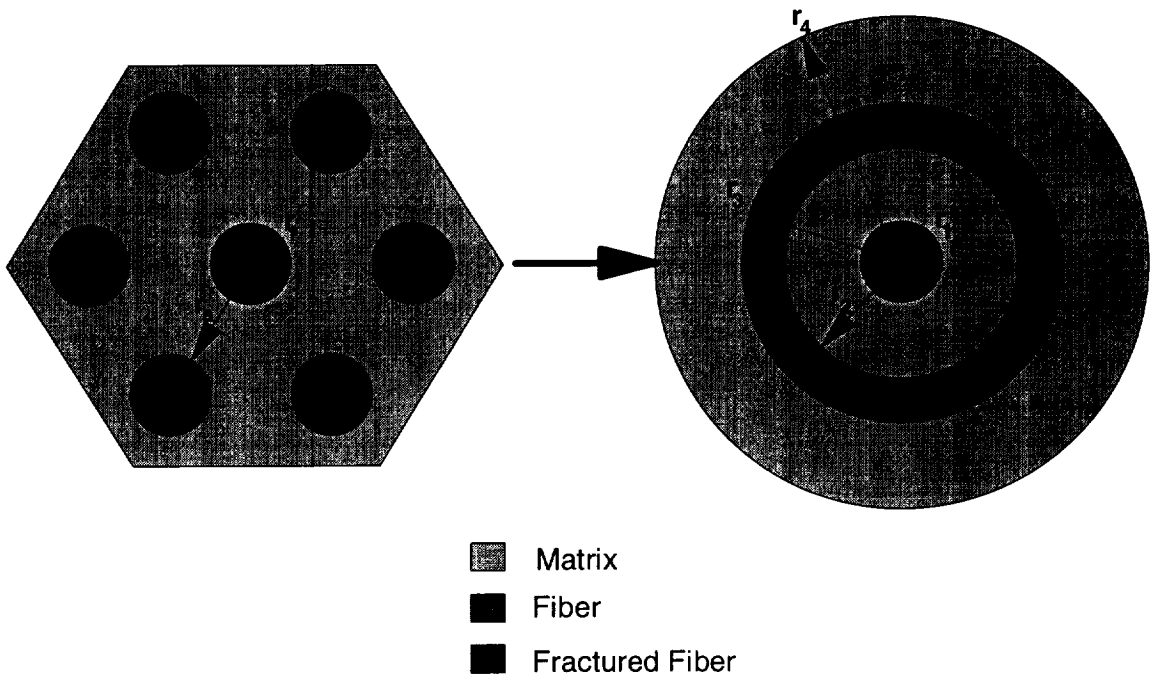

Figure 2.3. Representation of the hexagonal arrangement as an axisymmetric one having the same fiber volume fraction.

While the use of isotropic properties to represent the composite could be questioned, this approximation is certainly not as severe as some of the others used in the model. First we look at the normal stress $\sigma_{zz}^{(1)}(0,z)$ (at the center of the broken fiber) for a 65% fiber volume fraction composite. This is shown graphically in Figure 2.4. A number of interesting features are immediately noticeable. First of all, we see that for high values of the stiffness ratio, the normal stress becomes tensile before asymptotically approaching zero. Even more striking, however, is the distance over which the near-field stress remains compressive (the so-called ineffective length). This distance becomes smaller as the fiber to matrix stiffness ratio is increased. This is exactly the opposite trend from that predicted using a shear-lag analysis.

Of interest for making tensile strength predictions are the stress concentrations on the adjacent fibers and the axial distance over which this increased stress acts. Because there is a strain gradient as a function of r as well as z, it is not possible to speak of a single stress concentration value on the adjacent fiber. Rather this value depends upon position. To illustrate this, we will consider two different radial locations on the adjacent fiber ring: the inner edge of this ring ($r = r_2$) and the center of this ring, denoted $r_{1/2}$ and given by

$$r_{1/2} = \frac{1}{2}(r_3 - r_2) + r_2 \tag{2.70}$$

Such a comparison is shown in Figure 2.5 for the case of a 65% fiber volume fraction composite in which $\mu_1 / \mu_2 = 20$. It will be noted that there is a great difference between the maximum stress values at these two locations. The maximum value at the inner edge is 0.183 while the maximum value at the center is 0.052. Another interesting feature is that the maximum stress concentration at the center of the adjacent ring does not occur in the plane of the crack. Rather, it is located at approximately 0.4 r_c above the plane of the crack. This is not surprising in view of the results given in Figure 2.4, although it is a feature not predicted by the shear lag analysis. The maximum value of the stress concentration at the inner radius of the fiber ring does occur in the plane of the crack (for this particular selection of composite

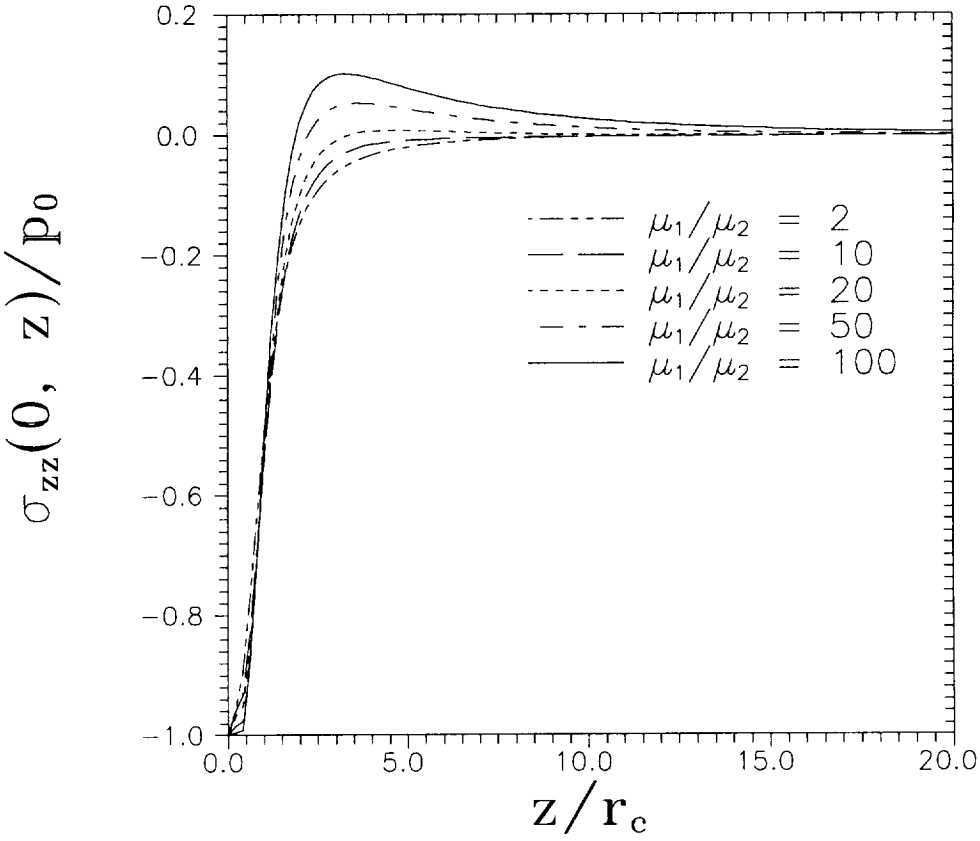

Figure 2.4. Variation of the $\sigma_{zz}(0,z) / p_0$ stress (at the center of the broken fiber) as a function of distance above the crack plane for various fiber to matrix stiffness ratios.

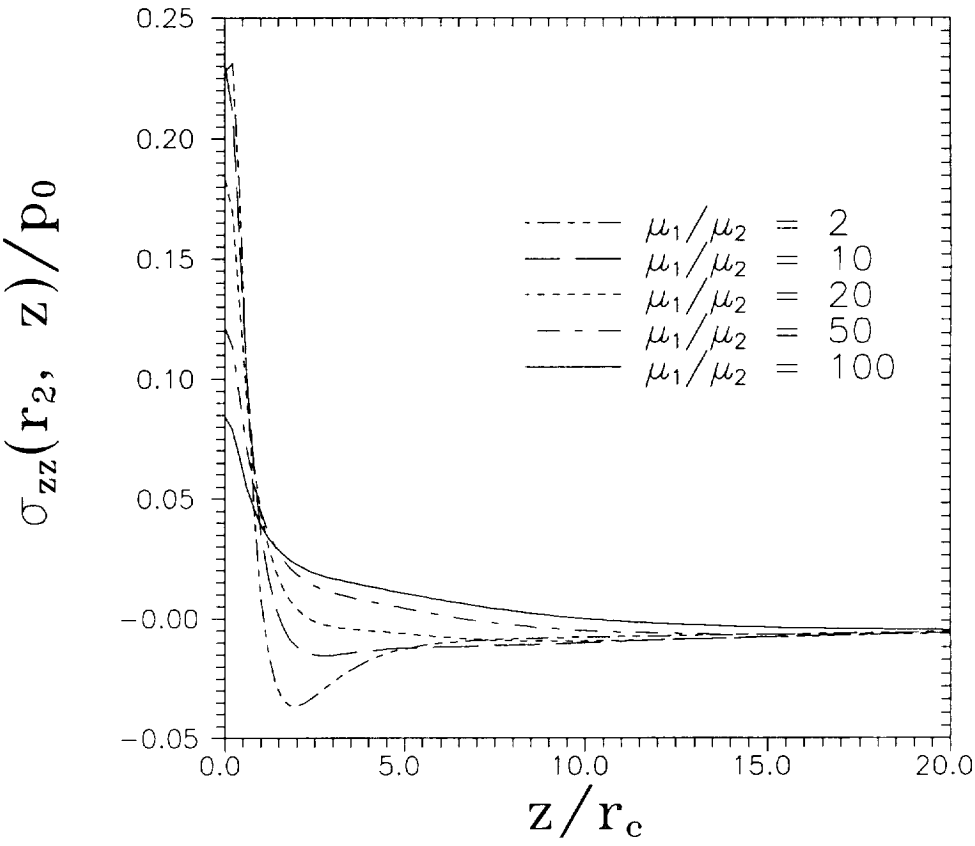

Figure 2.5. Variation of the $\sigma_{zz}(r_2, z)$stress (at the inside edge of the fiber annular ring) as a function of distance above the crack plane for various fiber to matrix stiffness ratios.

properties). To determine whether this was true in general, the stiffness ratio of the constituents was varied once again, and the resulting strain distributions plotted. The variation of the near-field stress as a function of axial distance from the crack plane at the inner edge of the fiber annular ring is shown in Figure 2.5. Once again a fiber volume fraction of 65% was used. In all of the cases except one ($\mu_1 / \mu_2 = 2$), the maximum stress concentration occurs in the plane of the crack. In this one case it occurs at 0.2 r_c above the crack plane. Two stiffness ratios considered, $\mu_1 / \mu_2 = 2$ and $\mu_1 / \mu_2 = 10$ give almost an identical value for the maximum stress concentration. Otherwise, there is a distinct trend: as the stiffness ratio is increased, the stress concentration at the inner radius of the fiber annular ring decreases.

The variation of the near-field stress as a function of distance from the crack plane for different stiffness ratios at the center of the fiber annular ring is illustrated in Figure 2.6. Here the results follow an interesting pattern. As the stiffness is increased, the stress values increase initially and then decrease for higher stiffness values. However, all of these values are much less than would be predicted from a local load sharing rule. Hedgepeth and van Dyke's analysis predicts a stress concentration of 1.104 on the adjacent fiber, which is greater than the values obtained at the center by any of the cases studied. Such a result is not surprising in view of the amount of axial load being carried in the present model.

As a final example of application of the model, we consider the effect of fiber volume fraction on the stress state for composites in which $\mu_1 / \mu_2 = 20$. Four different fiber volume fractions are considered: 20%, 50%, 55%, and 65%. First we consider the effect of those changes in fiber volume fraction have on the normal stress in the broken fiber. The results which are shown in Figure 2.7 suggest that such changes have very little effect on the stress state in the broken fiber. However, if we consider the stress state at the center of the adjacent fiber ring as shown in Figure 2.8 we see that changes in fiber volume

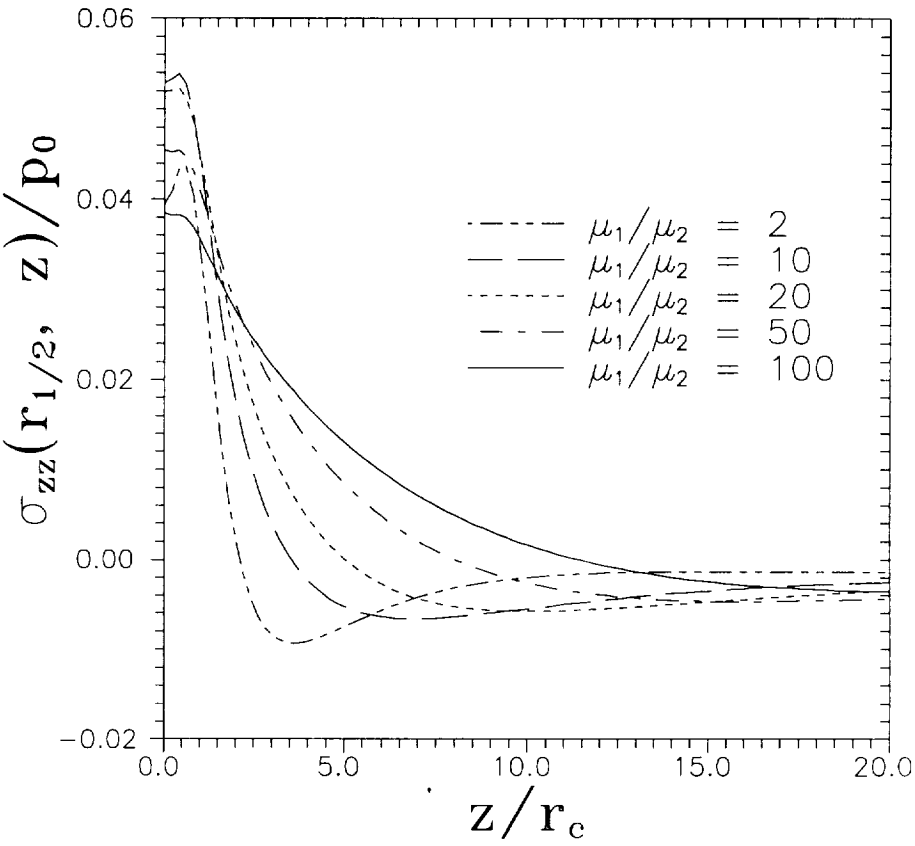

Figure 2.6. Variation of the $\sigma_{zz}(r_{1/2}, z) / p_0$ stress (at the center of the fiber annular ring) as a function of distance above the crack plane for various fiber to matrix stiffness ratios.

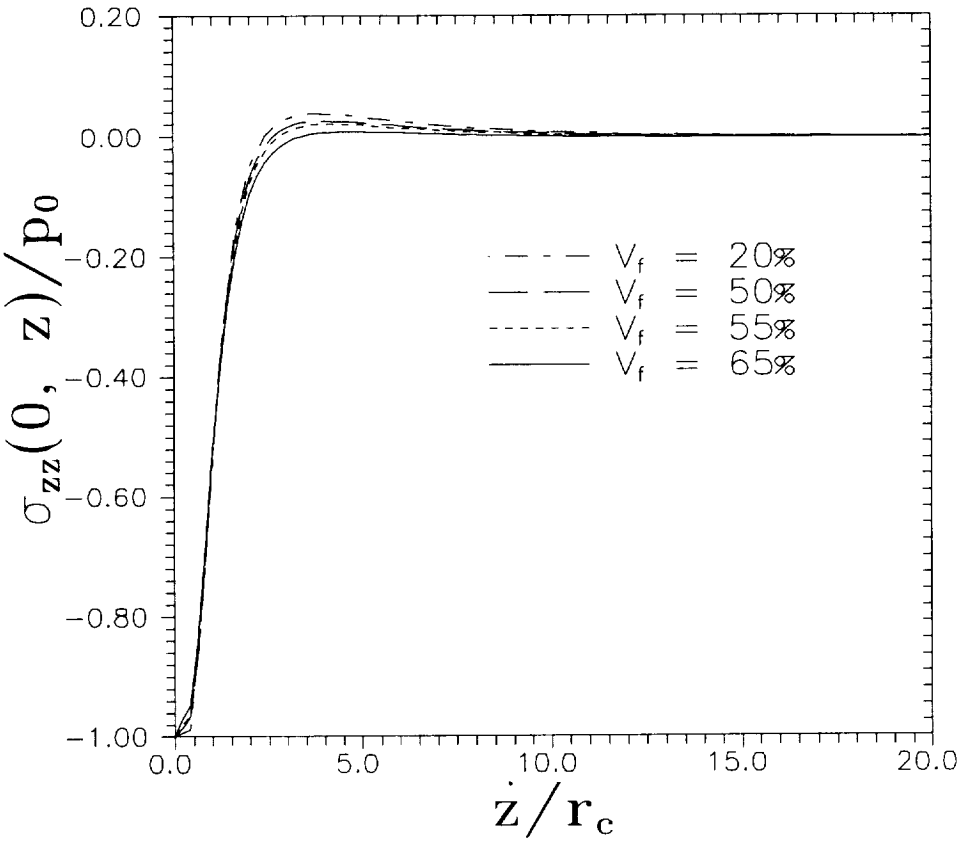

Figure 2.7. Variation of the stress $\sigma_{zz}(0,z) / p_0$ (at the center of the broken fiber) as a function of distance from the crack plane for various fiber volume fractions.

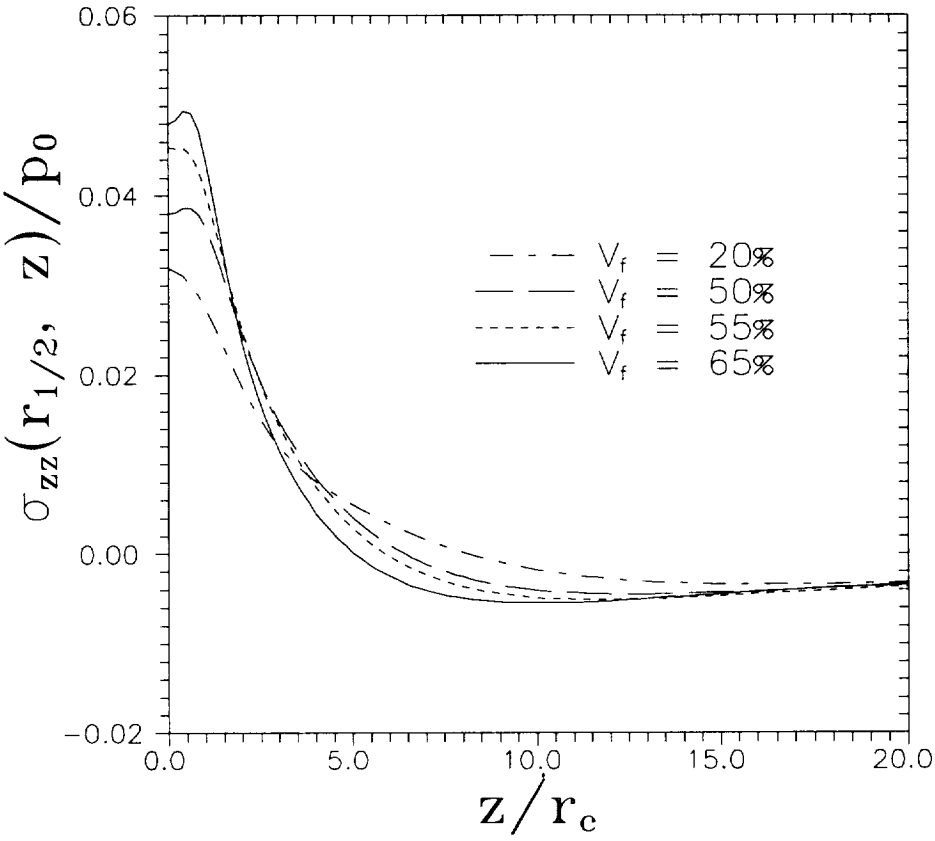

Figure 2.8. Variation of the $\sigma_{zz}(r_{1/2}, z) / p_0$ stress (at the center of the fiber annular ring) as a function of distance above the crack plane for various fiber volume fractions.

fraction have a significant effect on the stress concentration seen here. The reason for these changes (the stress concentration goes up as the fiber volume fraction is increased) is easily understood physically if the geometry of the model is considered. As the fiber volume fraction is increased, the distance from the center of the unbroken fiber to the crack tip is decreased, leading to the larger stress concentration.

There is still one major point to be considered: the magnitude of the tensile stresses carried by the matrix, particularly at the crack tip. The radial variation of the normal stress, $\sigma_{zz}^{(i)}(r,0)$ in the plane of the crack for the $i = 2,3,4$ cylinders is shown in Figure 2.9 for a fiber volume fraction of 65%. The resulting stresses in the matrix adjacent to the crack tip are singular (as expected) with the power of the singularity increasing as the value of μ_1 / μ_2 is increased. We would therefore expect some plasticity in the matrix, which would change the resulting stress state. This case has been recently studied using finite elements by Nedele and Wisnom [44]. Their results suggest that while this plasticity does change the ineffective length, it makes only small changes in the stress concentration.

2.6 Multiple Fiber Fractures

Accounting for the effect of multiple adjacent fiber fractures is somewhat more complex. As pointed out by Batdorf [7], multiple adjacent fiber fractures may have a number of different shapes even for the case of simple packing arrangements such as square and hexagonal. To simplify the analysis somewhat, we use an approach similar to that used by Hedgepeth and van Dyke in which we will consider only arrangements of multiple fiber fractures which are roughly axisymmetric (i.e. the number of breaks is equal to 1, 7, 19,...) as is illustrated in Figure 2.10.

To model such a situation, we use much the same approach as that which was used for the case of a single fractured fiber with a few minor changes. First we calculate the inner radii of the adjacent fiber rings

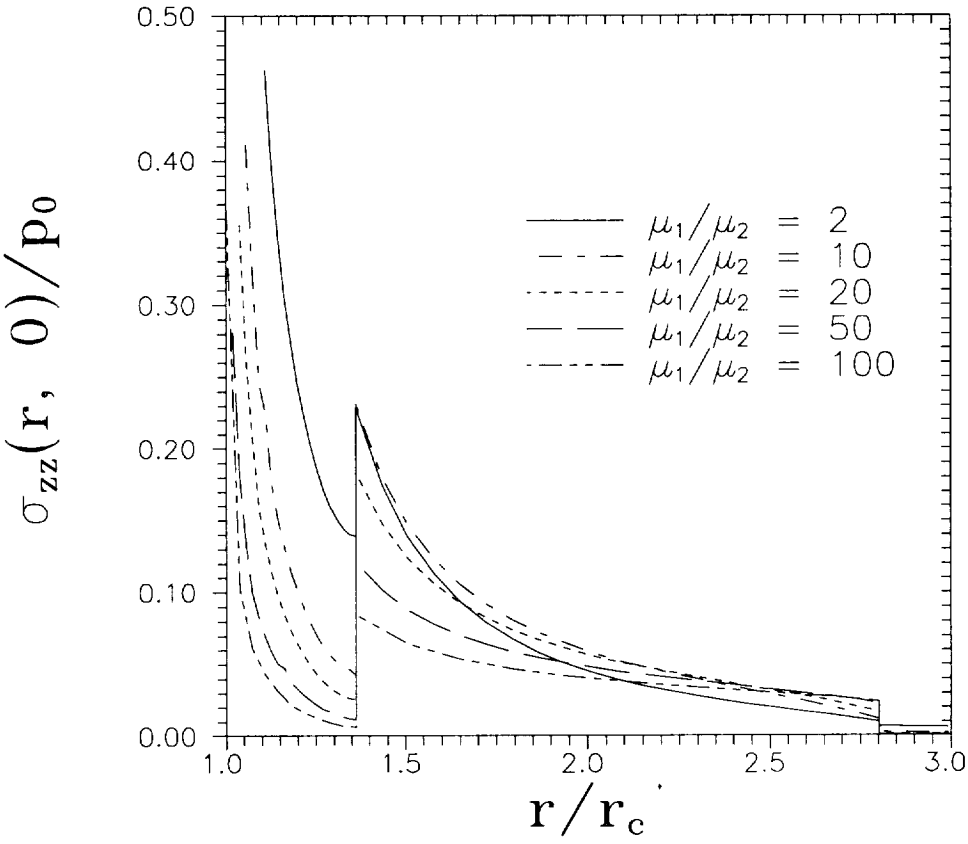

Figure 2.9. Variation of the $\sigma_{zz}^{(i)}(r,0)$ stress (in the plane of the crack) for the three inner concentric cylinders (i = 2, 3, 4).

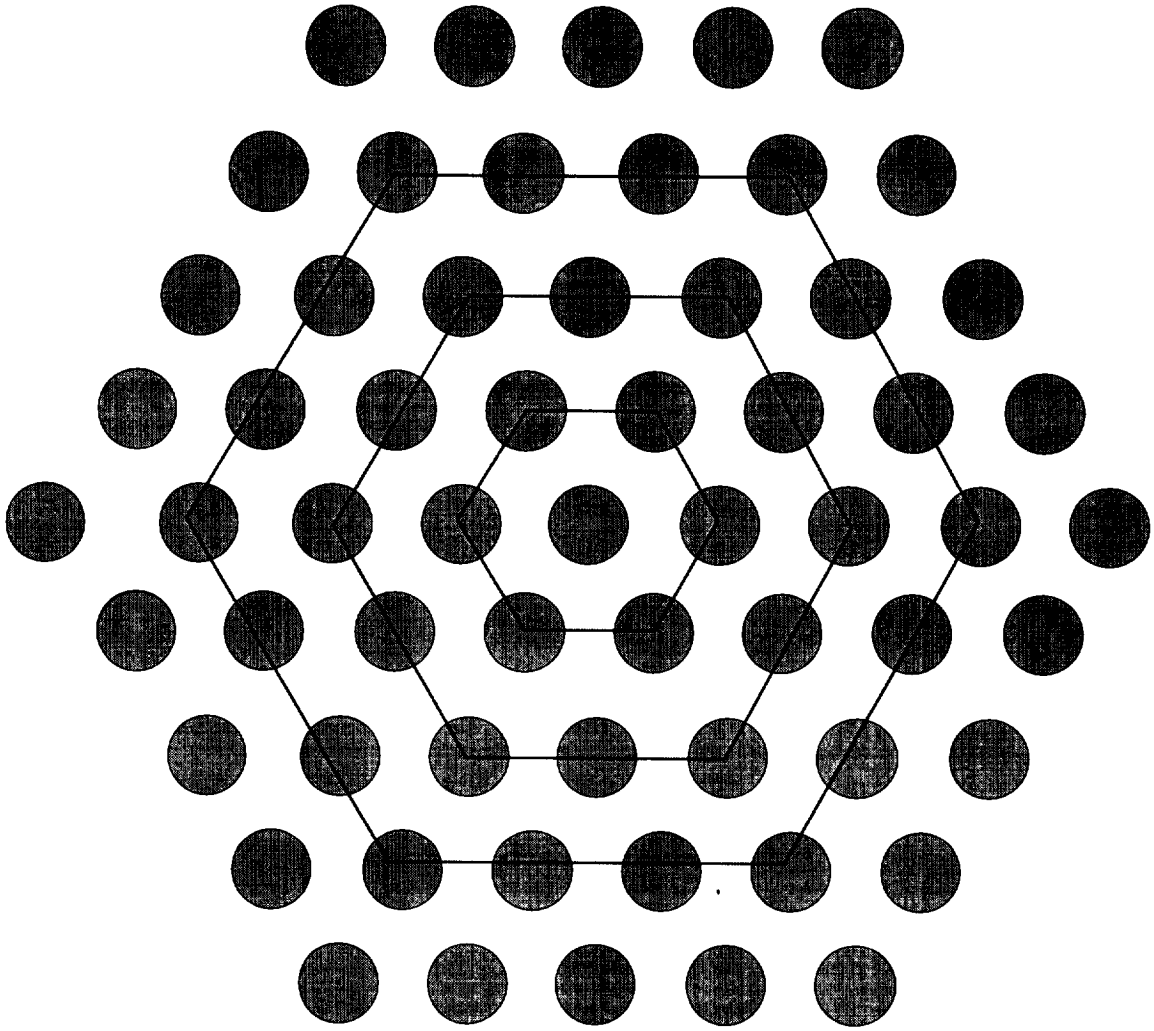

Figure 2.10. Hexagonally-packed composite material showing regions selected for geometry approximation.

based on the geometry for hexagonal packing. Then we calculate the outer radii so that the total area of fibers remains constant. It would be most desirable to represent each of the broken fiber and matrix rings individually, but this is not possible due to the nature of the solution scheme. Rather, it is necessary to represent these broken inner fiber and matrix regions by a single cylinder having effective composite properties. In such a manner, it is possible to calculate the stress concentrations for 1, 7, 19 ... adjacent fiber fractures. The intermediate values may then be estimated by curve fitting between these known values.

As an example, let us consider a composite material in which the fiber-to-matrix shear stiffness ratio is 20. This ratio is typical of glass/epoxy composite materials. The resulting maximum stress concentrations (at the inner edge of the adjacent fiber annular ring), stress concentrations at the center of the adjacent fiber annular ring, and the ineffective lengths (the axial distance over which the stress field is perturbed) are given in Table 2.1 for fiber volume fractions of 30%, 40%, 50% and 60%. The results seen here are not surprising in view of the nature of the model: as the fiber volume fraction is decreased, the distance from the crack tip to the adjacent fiber increases. Since the model predicts singular stresses which decay rapidly as a function of distance from the crack tip, we would expect the stress concentration to vary directly with the fiber volume fraction. This is exactly the trend we see exhibited in Table 2.1. In addition, as the value of the fiber volume fraction increases, the ineffective length decreases for a given number of adjacent fiber fractures.

2.7 Application to Composite Tensile Strength

Once these stress concentrations and ineffective lengths are known, it is then possible to make predictions of composite tensile strength. As discussed previously, one of the classical models of composite tensile strength is that developed by Batdorf [7]. Batdorf considers a composite containing N fibers, each of

Table 2.1. Stress concentrations due to multiple fiber fractures for a glass/epoxy composite material at various fiber volume fractions.

Fiber Volume Fraction (%)	Number of Broken Fibers	Maximum Stress Concentration	Center Stress Concentration	Ineffective Length (Fiber Radii)
30	1	1.043	1.023	15.01
	7	1.151	1.090	25.48
	19	1.312	1.188	30.76
40	1	1.061	1.029	12.67
	7	1.181	1.102	22.78
	19	1.363	1.207	27.55
50	1	1.087	1.036	9.79
	7	1.212	1.114	20.42
	19	1.411	1.224	24.85
60	1	1.130	1.042	4.84
	7	1.251	1.126	18.04
	19	1.453	1.234	21.56

length L, which are held together by a matrix. Damage in the composite due to loading is assumed to consist solely of breaks in the fibers. There will be single isolated breaks *(singlets)*, pairs of breaks *(doublets)*, three adjacent breaks *(triplets)*, and (in general) i adjacent breaks *(i-plets)*. Each *i-plet* is surrounded by n_i nearest neighbors, each of which is subjected to a maximum stress concentration of c_i in the plane of the break. This stress concentration acts over an axial distance of δ_i (the ineffective length). We first assume that the fiber failure conforms to a two-parameter Weibull representation. Therefore, when a stress σ is applied to a fiber of length l, the probability of failure, P_f, is given by

$$P_f(\sigma) = 1 - \exp\left[-\frac{l}{l_0}\left(\frac{\sigma}{\sigma_0}\right)^m\right] \tag{2.71}$$

where σ_0 is the Weibull characteristic value, m is the Weibull modulus, and l_0 is the reference length. For the case in which $P_f << 1$, Batdorf approximates Equation (2.71) by

$$P_f = \frac{l}{l_0}\left(\frac{\sigma}{\sigma_0}\right)^m \tag{2.72}$$

The number of singlets, Q_1, may then be determined by multiplying the probability of failure given by Equation (2.72) so that

$$Q_1 = N P_f = N\frac{l}{l_0}\left(\frac{\sigma}{\sigma_0}\right)^m \tag{2.73}$$

Following Batdorf, we next assume that the stress concentration in the neighboring fibers varies linearly from c_1 to unity over a distance $\delta_1/2$. We may represent such a variation functionally as:

$$f(z) = c_1 + \frac{z}{\delta_1/2}(1 - c_1) \tag{2.74}$$

After Reifsnider [28], we may express the reliability of a fiber having a stress variation of this type may be given by

$$R = \exp\left[-\left(\frac{\sigma}{\sigma_{a0}}\right)^m\right] \tag{2.75}$$

where

$$\sigma_{a0} = \sigma_0\left(\int_0^l [f(z)]^m dz\right)^{\frac{-1}{m}} \tag{2.76}$$

Using this relation, an the variation of the axial stress given by Equation (2.74), we can show that the probability of failure in the overstressed region may be approximated by

$$P_1 \approx \frac{\lambda_1}{l_0}\left(c_1\frac{\sigma}{\sigma_0}\right)^m \tag{2.77}$$

where

$$\lambda_1 = \delta_1\frac{{c_1}^{m+1} - 1}{{c_1}^m(c_1 - 1)(m+1)} \tag{2.78}$$

Because there are n_1 nearest neighbors to each singlet, the probability that a singlet becomes a doublet is given by

$$P_{1\to 2} = n_1\frac{\lambda_1}{l_0}\left(c_1\frac{\sigma}{\sigma_0}\right)^m \tag{2.79}$$

The number of singlets, Q_1, is given by Equation (2.73). Therefore, we may estimate the number of doublets by

$$Q_2 = Q_1 n_1 \frac{\lambda_1}{l_0}\left(c\frac{\sigma}{\sigma_0}\right)^m \tag{2.80}$$

In general, the number of *i-plets* may be given by

$$Q_{i+1} = Q_i n_i \frac{\lambda_i}{l_0}\left(c_i\frac{\sigma}{\sigma_0}\right)^m \tag{2.81}$$

or equivalently,

$$Q_i = N\frac{L}{l_0}\left(\frac{\sigma}{\sigma_0}\right)^{im}\prod_{j=1}^{i-1} {c_j}^m n_j \frac{\lambda_j}{l_0} \tag{2.82}$$

Examining the form of Equation (2.82), it is readily apparent that a log-log plot of Q_i versus σ is a straight line having slope, *im*. A representative schematic diagram of Equation (2.82) is shown in Figure 2.11 for several *i-plets* as a function of the applied stress level. This envelope of intersection points has a special significance in the Batdorf formulation. Over the stress range in which an *i-plet* lies on the envelope, it is unstable (as soon as it is created it will immediately become an *(i+1)-plet*, which will immediately become an *(i+2)-plet* until composite failure occurs). The failure stress is given by the lowest stress at which any unstable *i-plet* is present. This is the stress at which the envelope intersects the horizontal line $Q_i = 1$ (or $ln\ Q_i = 0$).

At this point, we are now ready to estimate the tensile strengths of the glass/epoxy composites considered in the previous section. The necessary inputs to the model are the stress concentrations and the ineffective lengths from Table 1, as well as the Weibull paramters σ_0, *m, and* l_0. Unfortunately accurate measurements of these Weibull parameters are difficult to obtain. Typical values for *m* are approximately

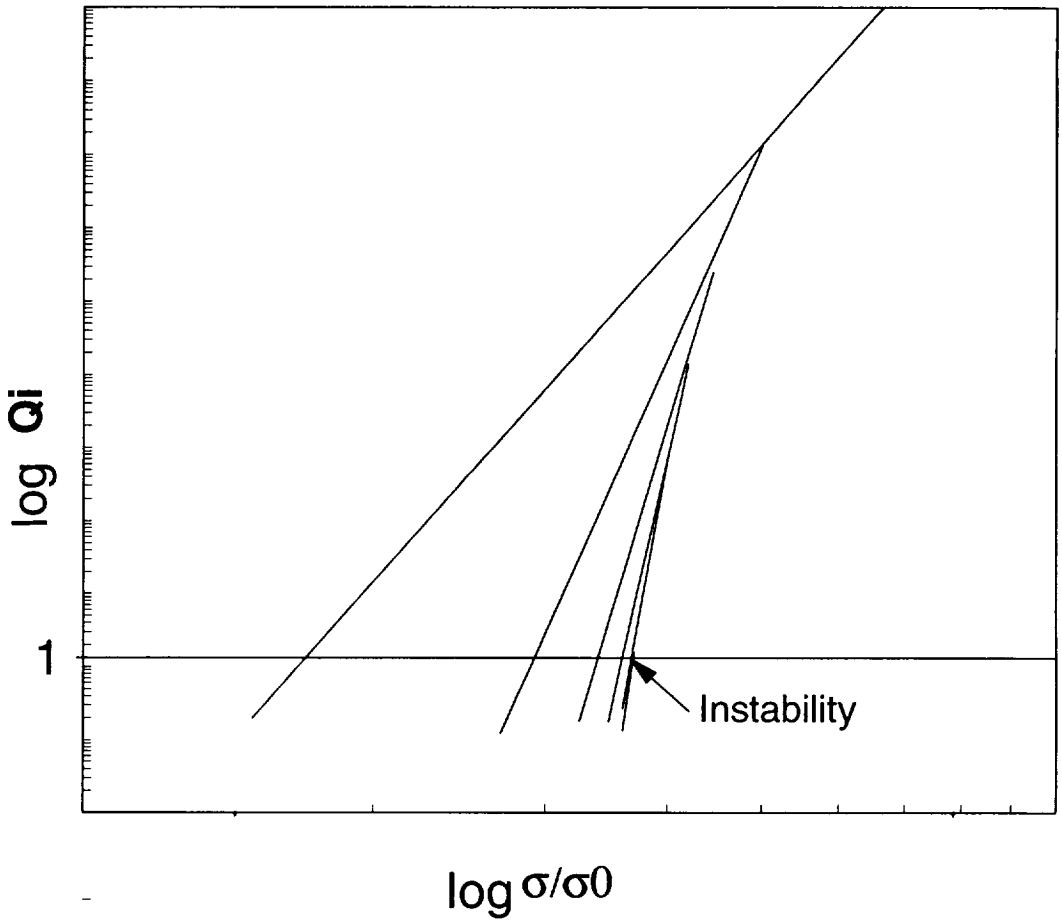

Figure 2.11. Batdorf-type Q-plot. Composite failure occurs at the point of instability.

5-8. The value for σ_0 is more variable depending upon fiber type. For this reason, the predicted values for composite strength will be expressed in terms of the ratio of σ/σ_0 using a reference length, l_0, of 1 cm. If the value of σ_0 is known at a different reference length, it may converted to this reference length using the relation

$$\frac{\sigma_0(l_1)}{\sigma_0(l_2)} = \left(\frac{l_1}{l_2}\right)^{\frac{-1}{m}} \tag{2.83}$$

In addition to these properties of the fibers, we also need to know the number of fibers in the composite, N, and their length, L. For this example, we will consider a component 6" (15 cm) X ½" (1.3 cm) X 6/100" (0.15 cm). If we assume the fibers to initially be continuous, then L may be taken equal to 6" (15 cm) and the number of fibers in the composite may be approximated by

$$N = \frac{\text{Cross Sectional Area of the Composite}}{\text{Area of the Fiber}} V_f \tag{2.84}$$

where V_f is the fiber volume fraction.

The question then becomes how to represent the stress concentrations and ineffective lengths for the values of the stress concentrations and ineffective lengths intermediate to those given in Table 1. Based on the variation of those values given in Table 1, the stress concentrations were fit to a quadratic form over this range of number of broken fibers, while the ineffective lengths were fit to log-linear form. These data, as well as the curve fitting parameters are shown in Figures 12, 13, and 14.

Combining all of this information, the fiber stress at which the instability occurs in the Q-plots may be readily calculated for the two stress concentration fits. The composite strength may be determined using this information and the relation

$$\sigma_c = \frac{E_c}{E_f}\sigma_f \tag{2.85}$$

where σ_f is the fiber stress at which the instability occurs, E_c is the composite modulus, E_f is the fiber modulus, and σ_c is the composite strength. Figure 2.15 shows the results for predicted composite strengths as a function of fiber volume fraction for values of the Weibull modulus ranging from 4 to 8 using the maximum stress concentration values (this should represent a conservative estimate of the composite strength). These values have been normalized to the characteristic value, σ_0, from the Weibull distribution. In addition, the predicted strength using a rule of mixtures type calculation has been shown for comparison. Such as calculation has been made by

$$\sigma_c = V_f \overline{X}_f + \left(1 - V_f\right) X_m \tag{2.86}$$

where X_m is the matrix strength, and $\overline{X}_f$ is the average fiber strength calculated from the Weibull distribution so that

$$\overline{X}_f = \sigma_0 \Gamma\left(\frac{m+1}{m}\right) \tag{2.87}$$

In all cases that have been calculated, the predicted values using the statistical model in conjunction with the local stress concentration analysis are greater than those predicted by the rule of mixtures type analysis. This is an example of the "composite effect" in which the actual behavior cannot be estimated simply by summing the contributions of the constituents.

There is some question as to what value for the stress concentrations should be used in the estimation of the composite strength. Nedele and Wisnom [44] have based their calculations on the average stress concentrations on the adjacent fibers. To investigate this effect, a similar approach has been used in Figure 2.16, although the stress concentration at the center of the adjacent fibers has been used rather than

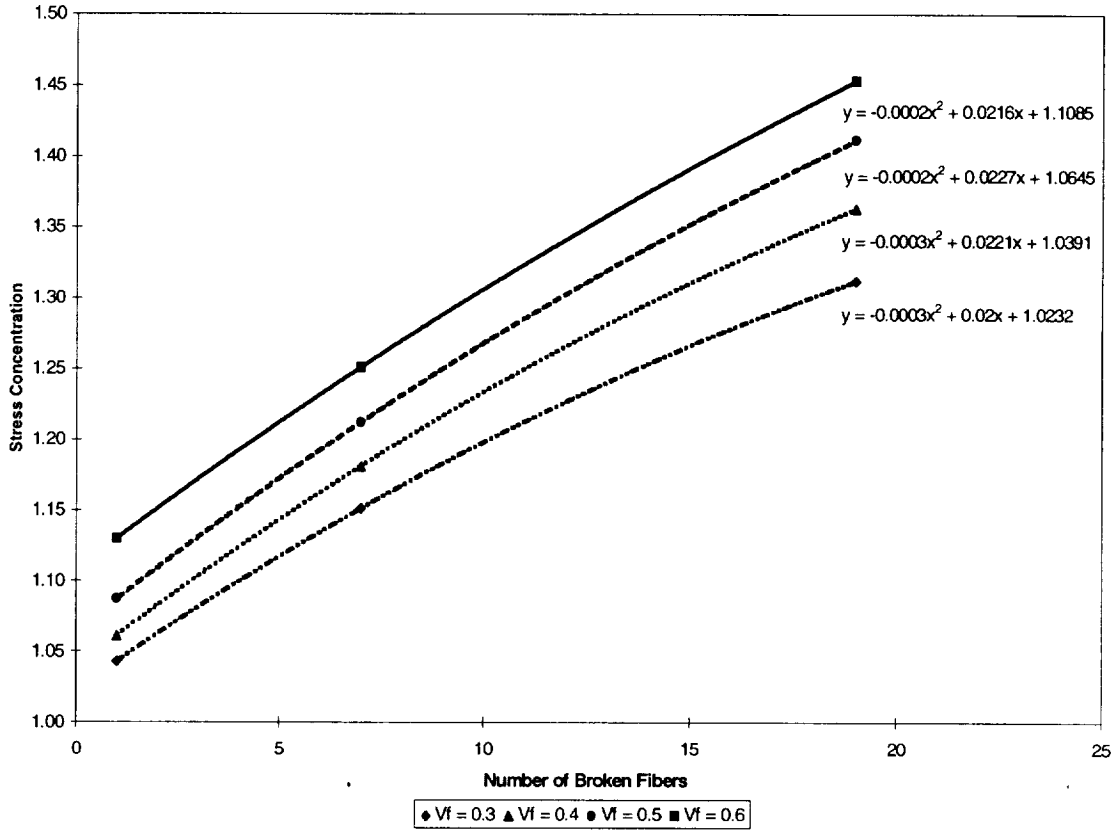

Figure 2.12. Maximum stress concentration as a function of number of broken fibers and fiber volume fraction.

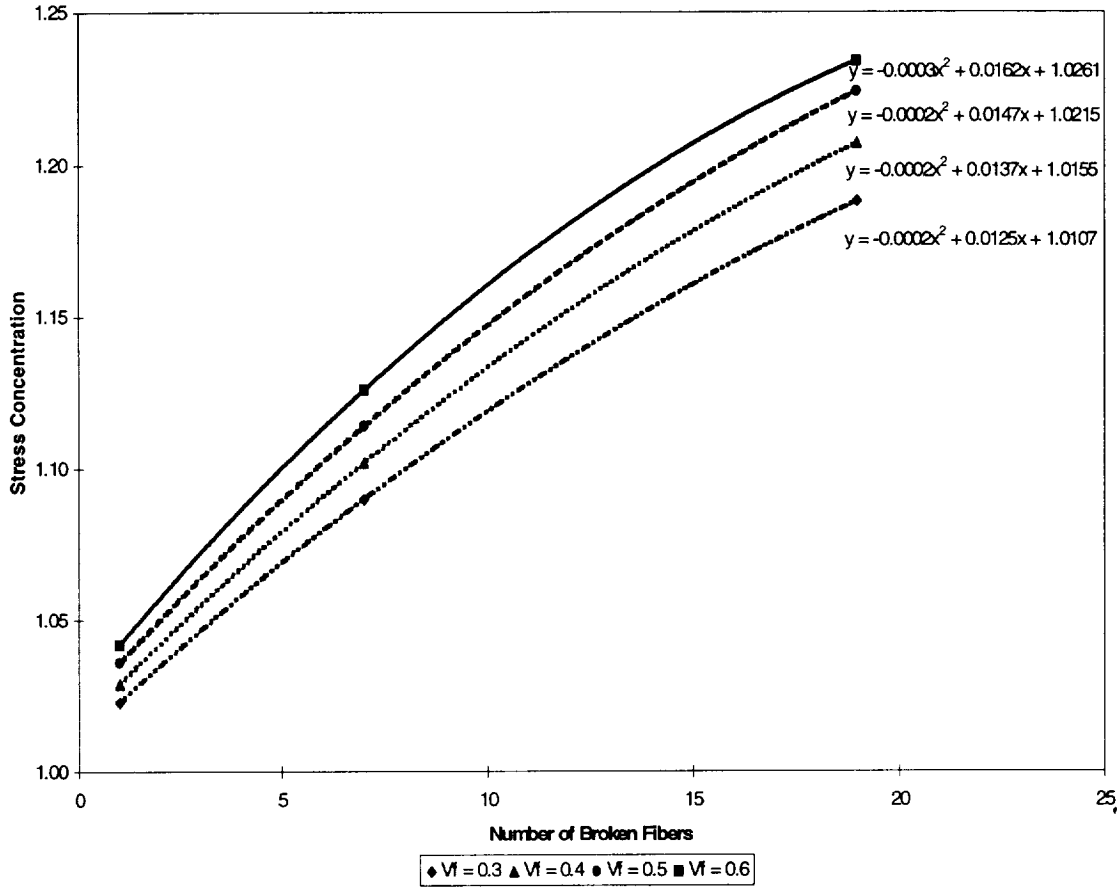

Figure 2.13. Center stress concentration as a function of fiber volume fraction and number of broken fibers.

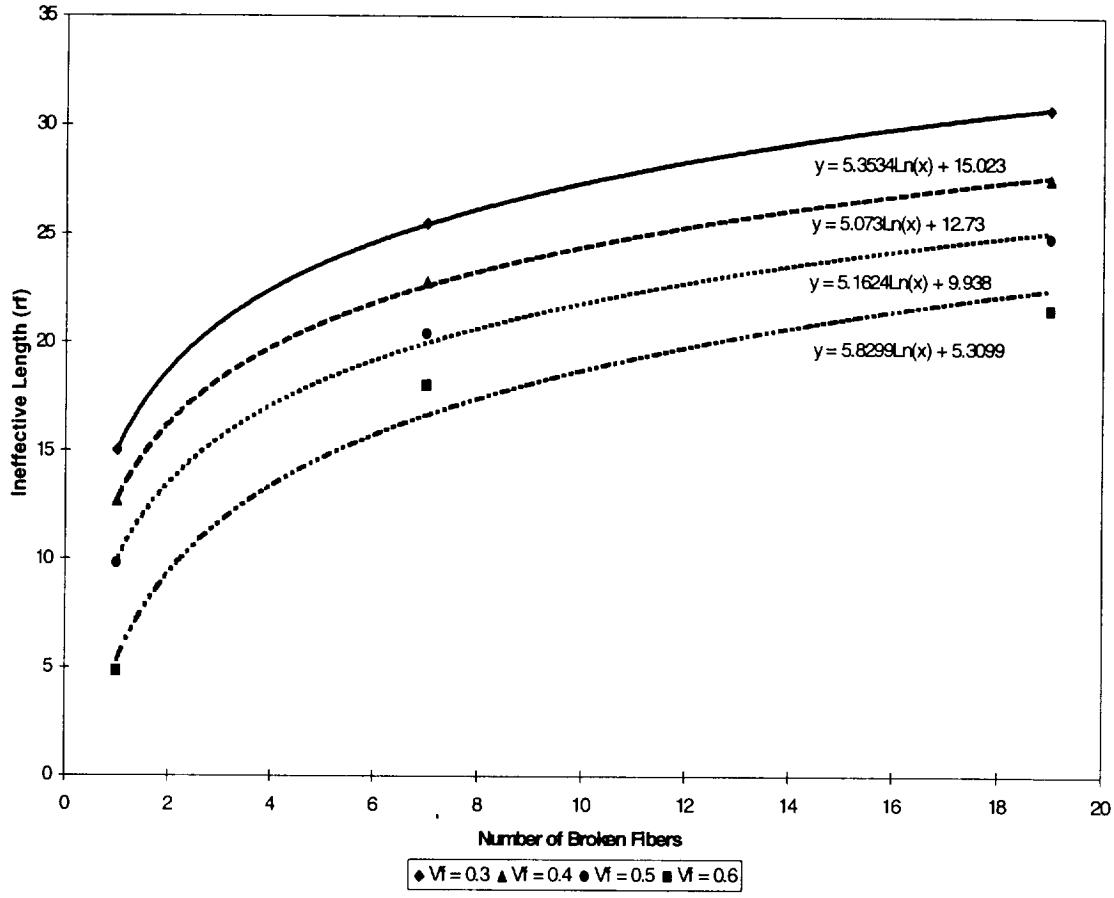

Figure 2.14. Ineffective lengths for glass/epoxy composites of different fiber volume fractions as a function of number of adjacent broken fibers.

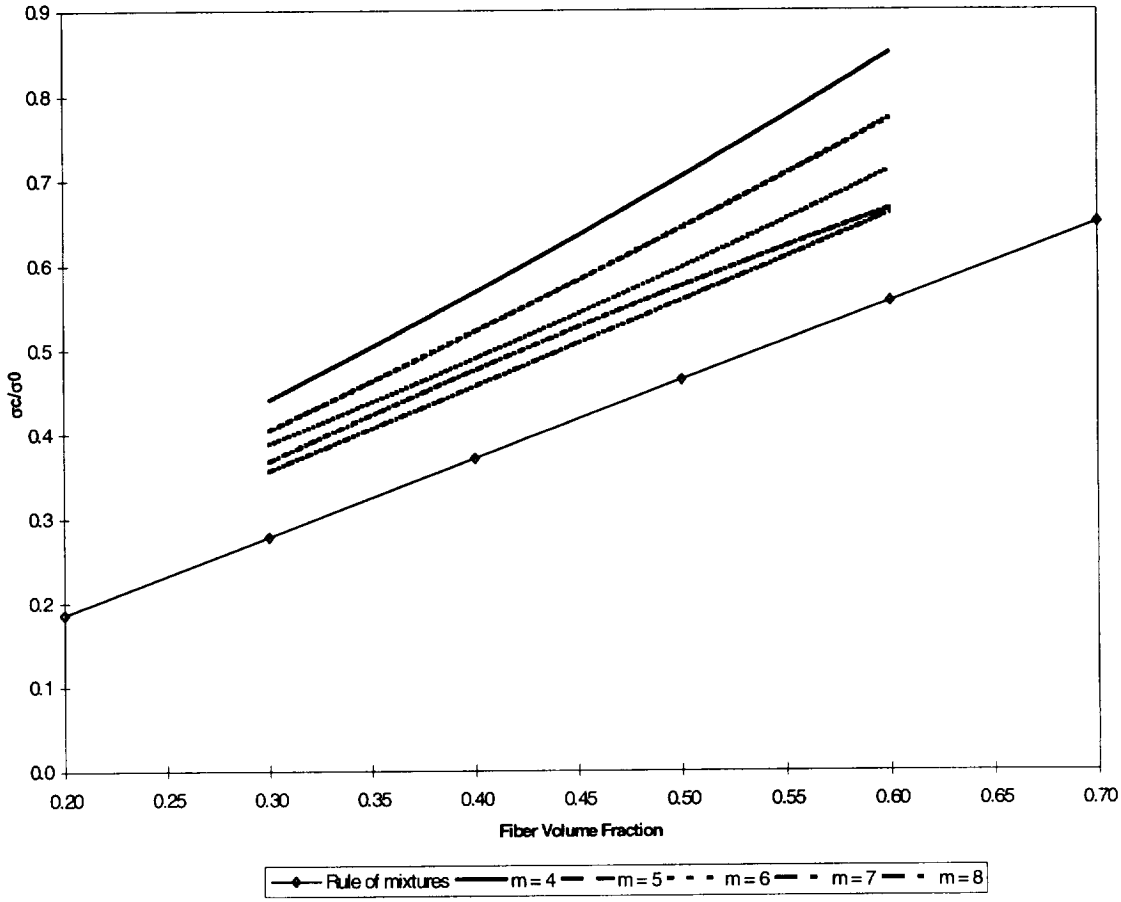

Figure 2.15. Predicted composite strengths as a function of fiber volume fraction and Weibull modulus using the maximum stress concentration values.

the average. This was done in order to simplify the calculations, and in the cases investigated thus far such values do not differ greatly from the average values. In the case of Figure 2.16, the composite effect is even more pronounced—the predicted strengths using the present analysis are always more than 15% greater than the corresponding values using the rule of mixtures calculation.

2.8 Model Refinements

Despite the features of the above stress analysis (it is an exact solution to the problem being solved and solutions may be obtained more rapidly than equivalent finite element models), it is still lacking in many ways. First of all, the solution is limited to a single crack within a single material. Secondly, the solution is presently limited to isotropic constituents. Do to such limitations, it may not be accurately used to represent the stress state in composites containing graphite fibers. A number of approximate solutions have been presented to address these problems. One of the most general is that which has been developed by Pagano [26] for axisymmetric damage in a concentric cylinder assemblage. The solution is quite general, and may readily be applied to the analysis of the stress states surrounding fiber fractures. As an example, we shall consider the strength prediction for a composite which has constituent properties typical of a graphite/polymer composite at a fiber volume fraction of 60%. The procedure employed is similar to that used in the above analysis with one exception: rather than effective properties to represent the broken inner fiber and matrix regions, the fiber rings are broken as illustrated in Figure 2.17.

In this case, rather than varying the fiber volume fraction in the analysis, we will keep the fiber volume fraction constant at 60% in the analysis, and vary the stiffness of the matrix. Such a situation would arise physically if we increased the temperature from room temperature to some elevated temperature. The fiber properties used are given in Table 2.2.

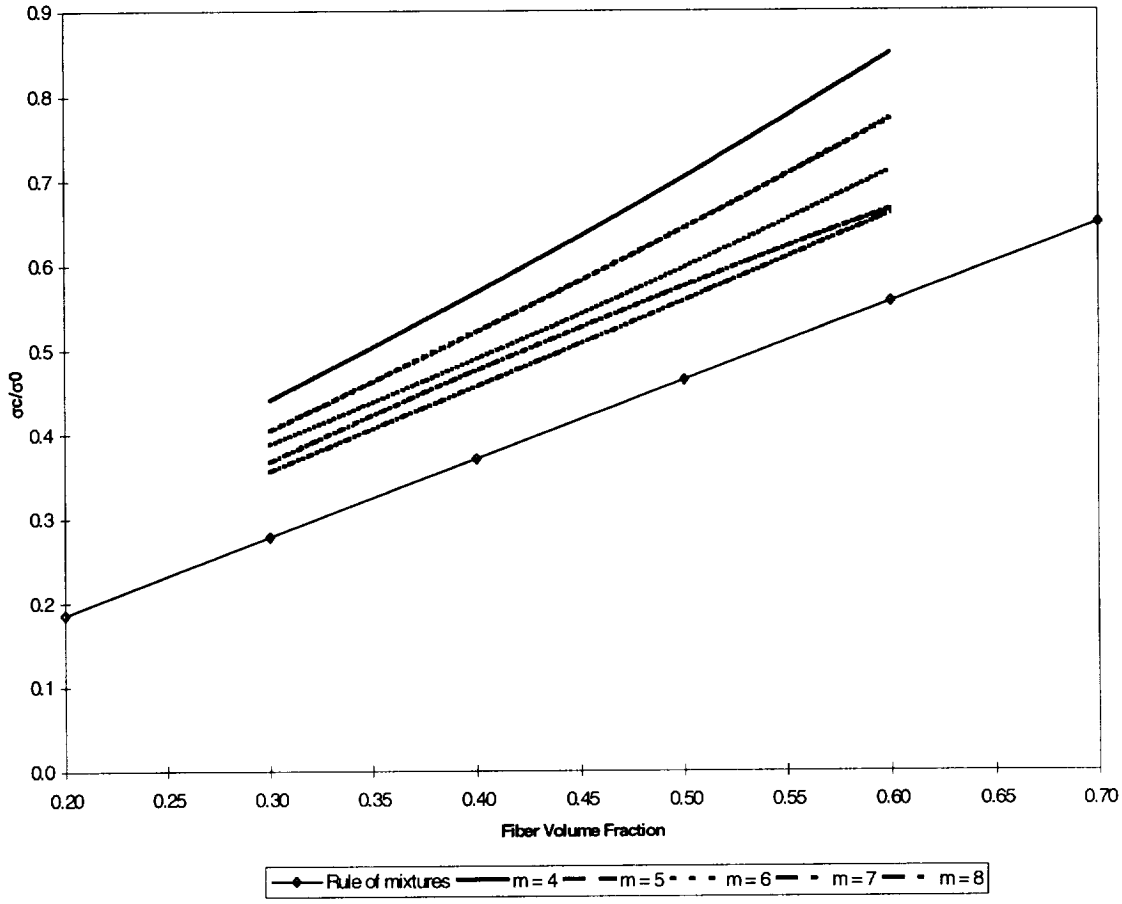

Figure 2.16. Predicted composite strengths as a function of fiber volume fraction and Weibull modulus using the center stress concentration values.

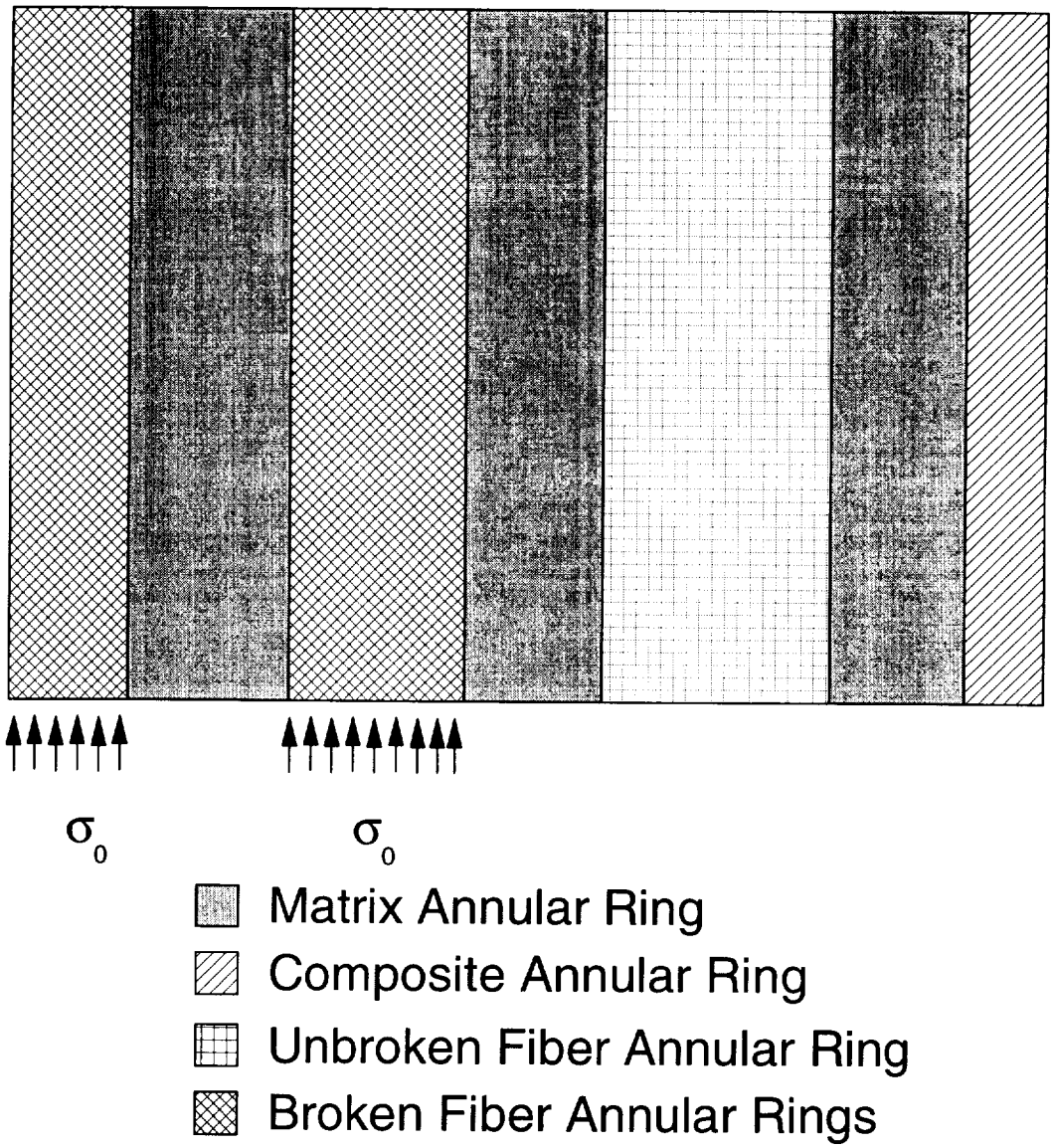

Figure 2.17. Schematic illustration of approach employed to determine stress concentrations using Pagano's [26] axisymmetric damage model.

Table 2.2. Fiber mechanical properties used in the stress concentration analysis.

Property	Value
E_{11}	301 GPa
E_{22}	20.0 GPa
G_{12}	20 GPa
ν_{12}	0.20
ν_{23}	0.25

Three different values for the matrix modulus were employed: 0.75 GPa, 1.50 GPa, and 3.38 GPa (an constant value of the Poisson ratio equal to 0.35 was utilized). The highest stiffness value is typical of a polymeric material at room temperature. The other values are values that could be obtained as the glass transition temperature is approached. Results obtained for the stress concentrations and ineffective lengths are presented in Table 2.3. There are a number of interesting phenomena that occur here. First of all, the stress concentrations do not appear to be greatly influenced by the matrix stiffness values (the greatest difference between corresponding stress concentration values is approximately 6%). However, there is a large difference in the predicted ineffective lengths. As the matrix stiffness is decreased from 3.38 GPa to 0.75 GPa, the ineffective length increases by more than a factor of two for the numbers of fiber fractures considered. An interesting finding may be seen in Figure 2.18 where the stress concentration results from the axisymmetric model for a matrix modulus of 3.38 GPa have been compared to the results of the influence function approach of Hedgepeth and Van Dyke [20]. In their results, Hedgepeth and Van Dyke consider two stress concentrations for the hexagonally packed array: the stress concentration at an adjacent element on a major diagonal and the maximum stress concentration on an adjacent element. For this particular case, the center stress concentration appears to be nearly identical to that of the elements on the major diagonal. This result is not surprising based upon the nature of the two models. In the Hedgepeth and Van Dyke solution, the stress in each of the fibers is assumed to be constant over its cross-section, thus we would expect this stress to represent the average value at a given location.

The final step is to determine the effect of this change in matrix stiffness on the tensile strength of the composite material. To do so, the same approach is employed that was used for the estimation of the tensile strength of the glass/epoxy composite materials. First of all, the maximum and center stress concentrations for the different values of the matrix stiffness are fit to polynomial expressions. The results

Table 2.3. Stress concentrations and ineffective lengths obtained using Pagano's [26] axisymmetric model as a function of matrix stiffness and number of broken fibers for a graphite/polymeric composite material.

Matrix Modulus (GPa)	Number of Broken Fibers	Maximum Stress Concentration	Center Stress Concentration	Ineffective Length (Fiber Radii)
0.75	1	1.226	1.104	44.06
	7	1.482	1.285	93.64
	19	1.837	1.475	149.44
1.50	1	1.254	1.099	29.90
	7	1.503	1.265	63.50
	19	1.852	1.434	96.80
3.38	1	1.288	1.090	17.12
	7	1.520	1.239	41.34
	19	1.885	1.393	63.06

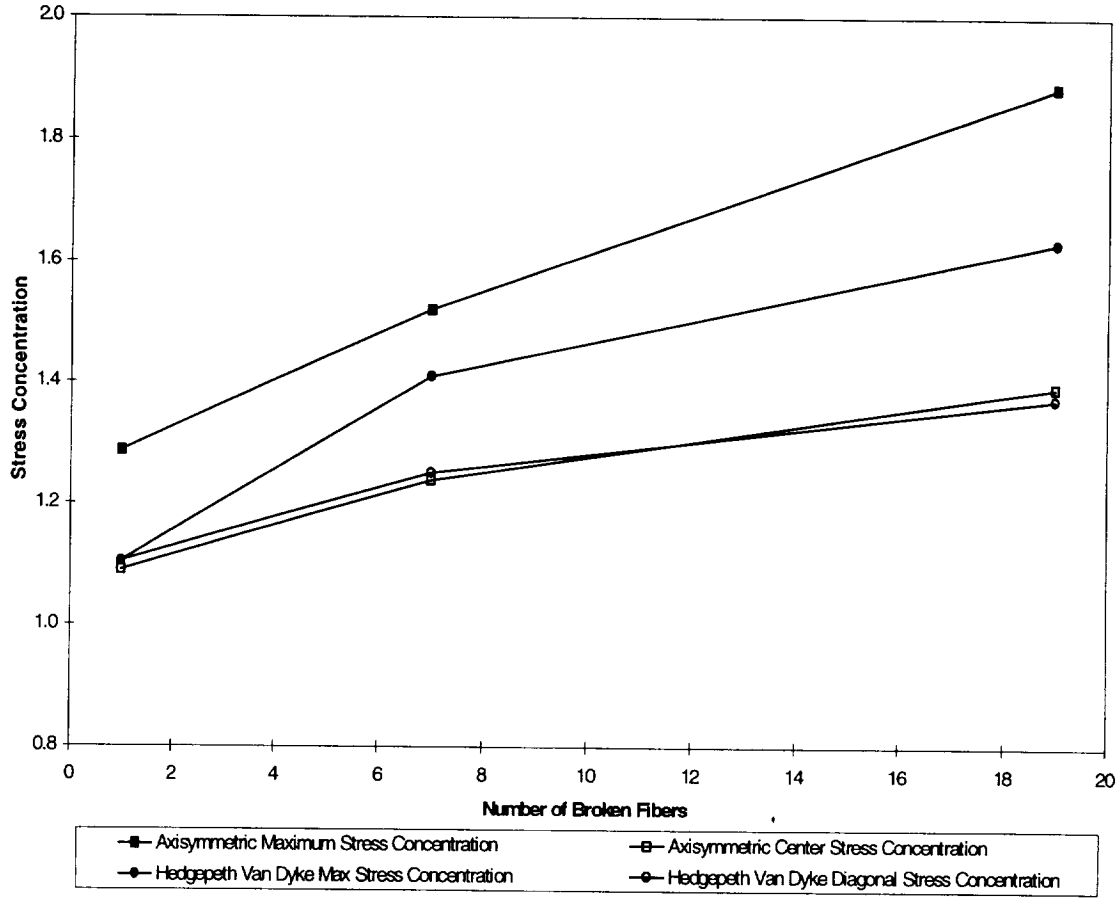

Figure 2.18. Comparison between the predicted stress concentrations using the axisymmetric model [26] and the analysis of Hedgepeth and Van Dyke [20].

of such a fitting process are shown in Figures 2.19 and 2.20. In addition, the ineffective lengths are fit to a power type expression as shown in Figure 2.21. Once such a process is complete, it is then possible to use the Batdorf analysis in the same manner as it was used for the glass/epoxy composite to predict the composite tensile strength. The results for such a prediction using the maximum stress concentration values are shown in Figure 2.22 as a function of Weibull modulus and matrix stiffness. In addition, the results for such a prediction using the center stress concentration values are shown in Figure 2.23. Such results could prove useful for the use of composites at elevated temperatures. By using the appropriate matrix stiffness value at a given temperature, it is possible to use Figures 2.22 and 2.23 to estimate the corresponding tensile strength.

The results presented thus far have been only for parametric studies, without comparison to experimental data. As previously mentioned, complete characterizations of fiber properties to determine the Weibull parameters are difficult to obtain. However, Northrup corporation, as part of the "Development of Ultralightweight Materials" program (Air Force Contract No. F33615-88-C-5452), performed an series of extensive characterizations of four different graphite fibers as well as their composites [45-47]. The results are available on a limited distribution basis. To protect the data results will be presented on a normalized basis (normalized to the maximum experimentally measured average strength value). Figure 2.24 shows a comparison between the predicted strengths for composites made from each of the four fibers, as well as the predicted values based upon the maximum stress concentration. In all cases, the experimental data lie below the prediction (as would be expected). Figure 2.25 shows a comparison between the experimental data and the predictions based upon the center stress concentration value. For these predictions, the model over predicts the strength for all cases except two. However, it is able to give reasonable agreement, except for the composites made from the T1000 fiber.

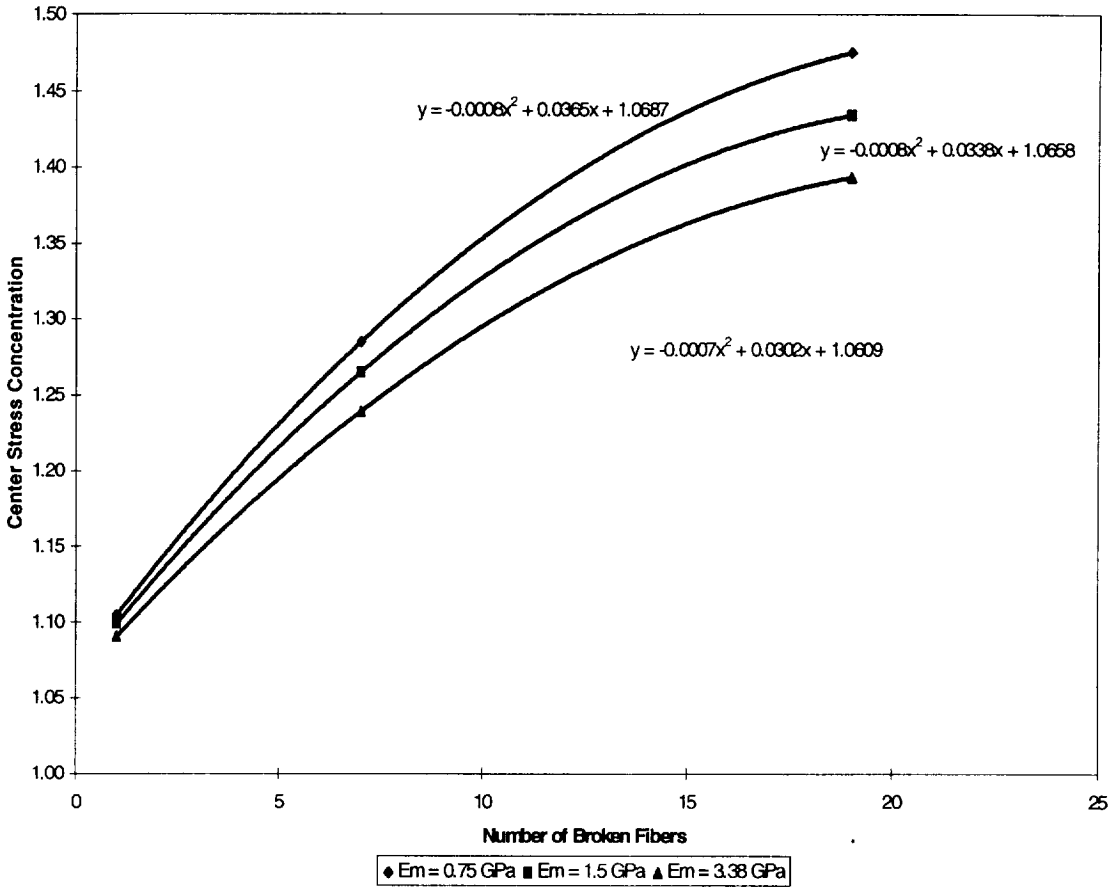

Figure 2.19. Center stress concentration on adjacent fibers as a function of number of broken fibers and matrix stiffness for a graphite/polymeric composite material.

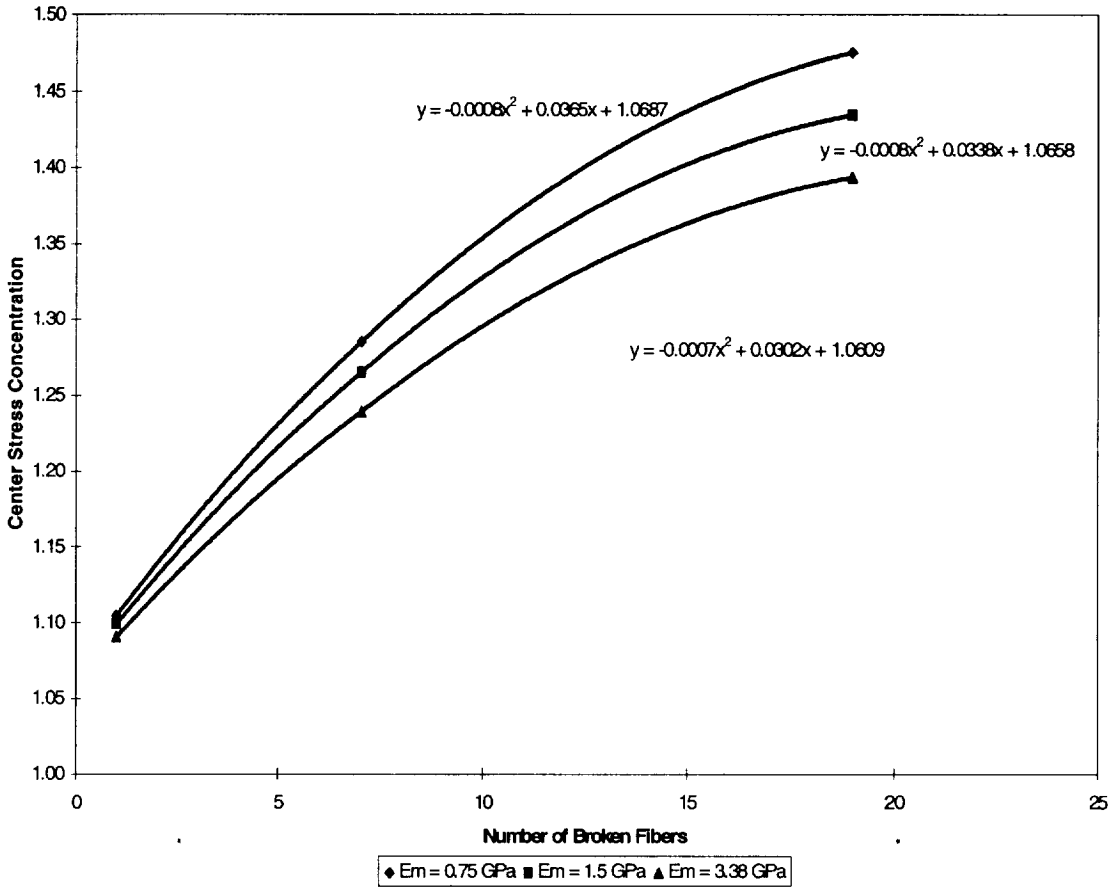

Figure 2.20. Center stress concentration on adjacent fibers as a function of number of broken fibers and matrix stiffness for a graphite/polymeric composite material.

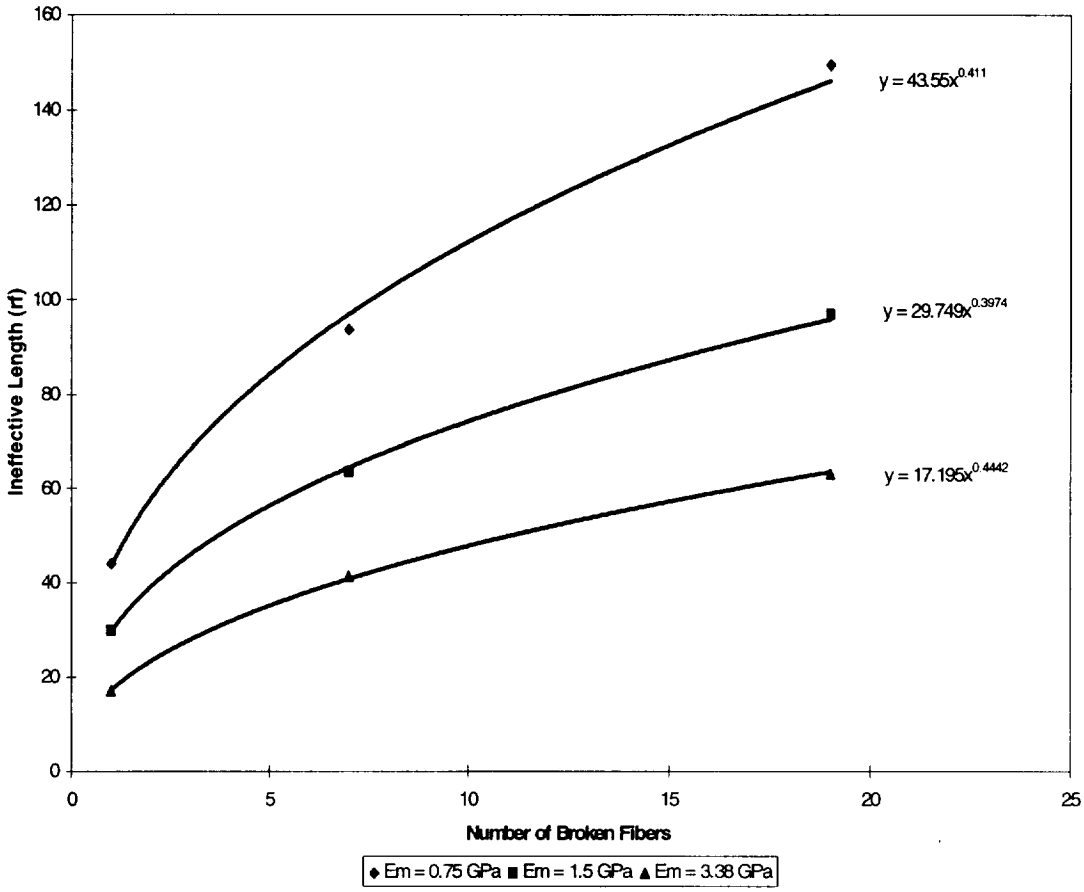

Figure 2.21. Ineffective length as a function of number of broken fibers and matrix stiffness for a graphite/polymeric composite material.

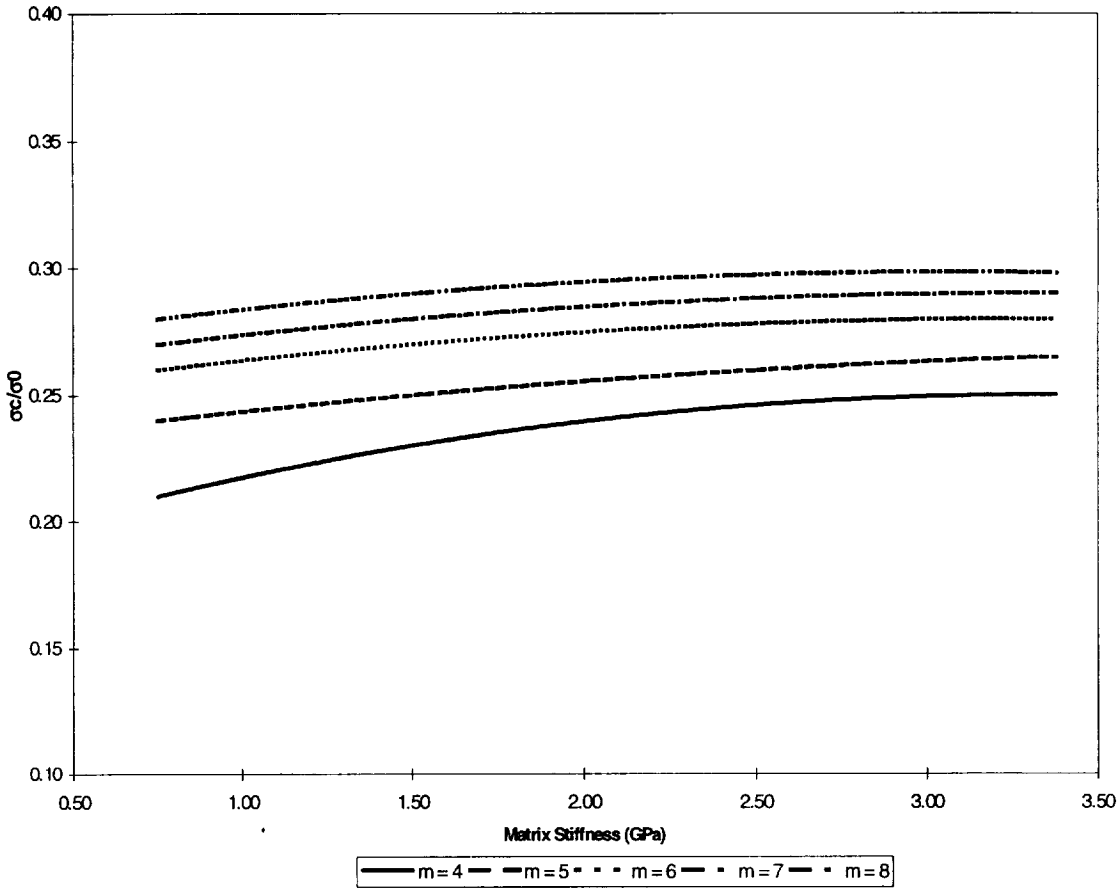

Figure 2.22. Predicted composite strength based on maximum stress concentration as a function of matrix stiffness and fiber Weibull modulus for a 60% fiber volume fraction graphite/polymeric composite material.

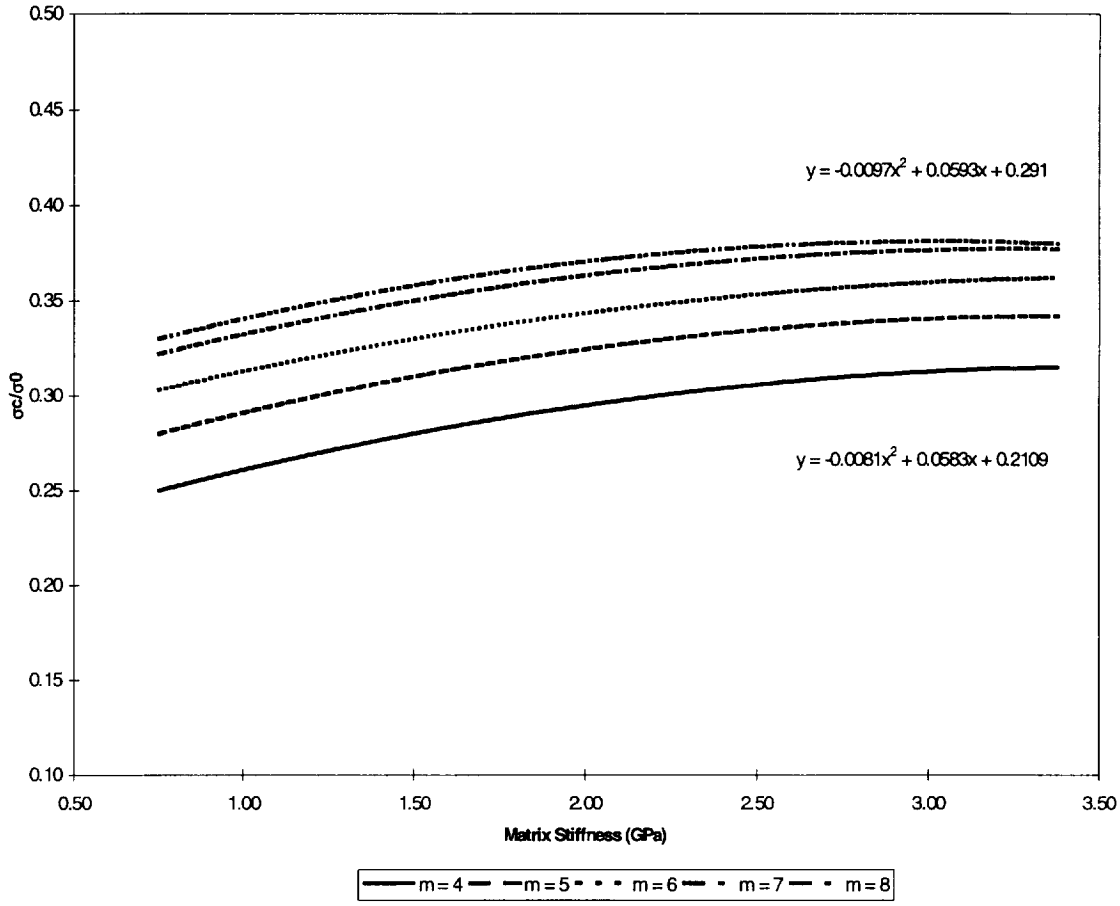

Figure 2.23. Predicted composite strength based on center stress concentration as a function of matrix stiffness and fiber Weibull modulus for a 60% fiber volume fraction graphite/polymeric composite material.

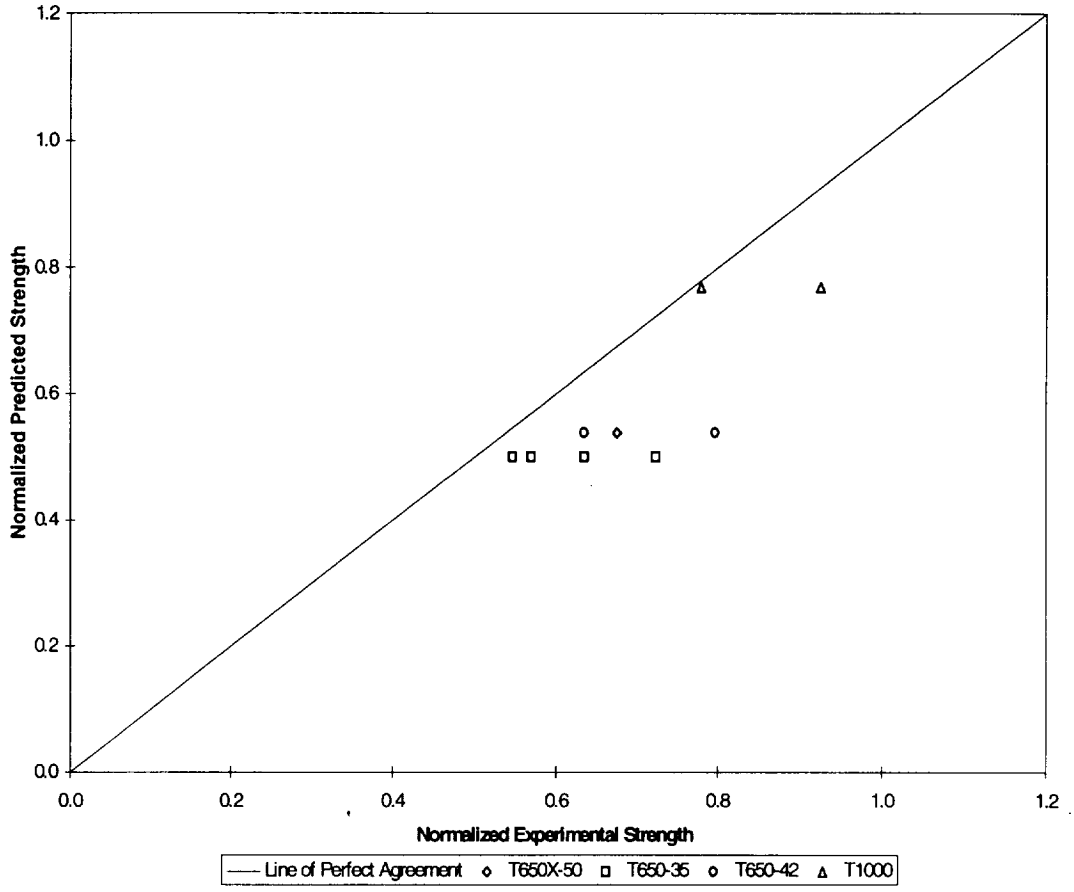

Figure 2.24. Comparison of predicted strength based on maximum stress concentration and experimentally measured values for composites containing four different graphite fibers.

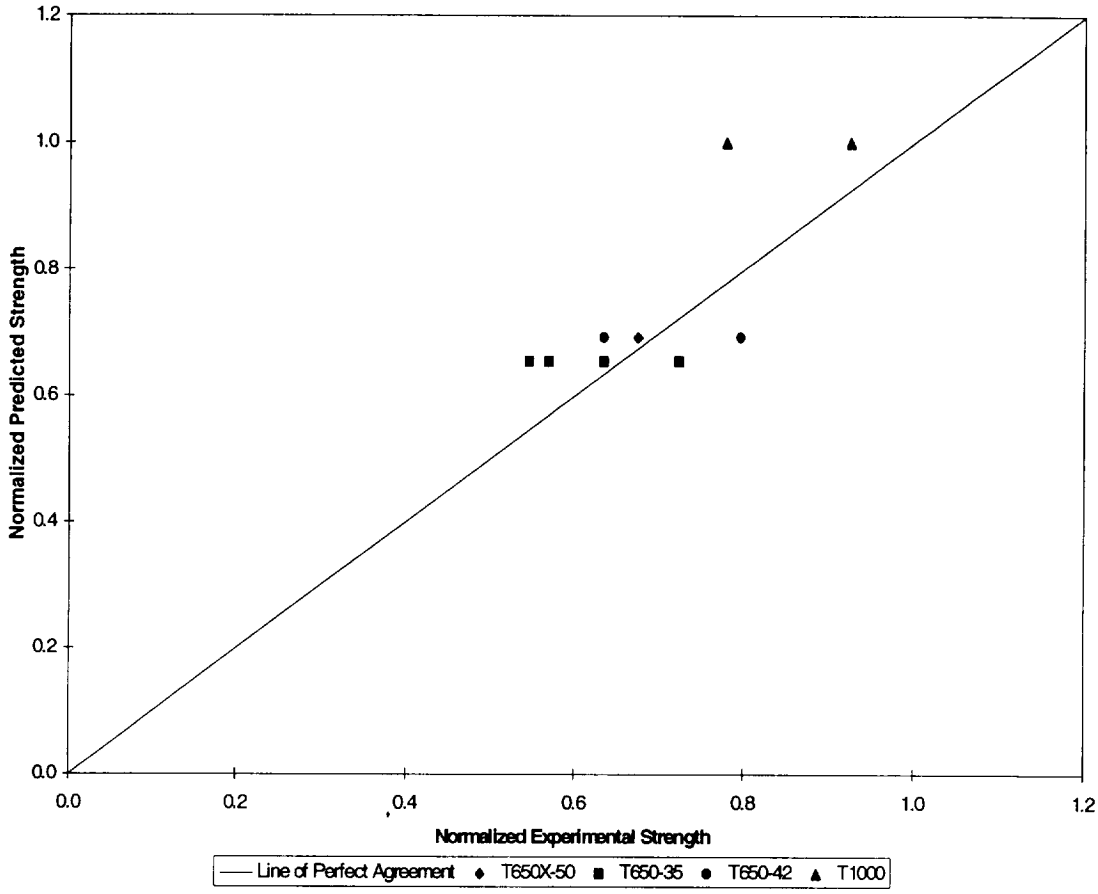

Figure 2.25. Comparison of predicted strength based on center stress concentration and experimentally measured values for composites containing four different graphite fibers.

3. Durability And Damage Tolerance Analysis In Composite Materials

The durability of composite materials, particularly the area of analytical modeling of damage and the resulting degradation in material properties, has received much attention in recent years [48]. Nevertheless, the prediction of the remaining strength and life in these inhomogeneous, anisotropic materials is inherently complicated--there are many different damage modes (such as delamination or matrix cracking) that may develop and interact before a final failure occurs. These damage modes, that occur before final failure, make it possible to design components from composite materials that are extremely damage tolerant. Due to this complex interaction of the damage modes, methods of analysis typically used for engineering metals which involve the propagation of a self-similar single crack cannot be used with composite materials. However, to use the damage tolerance composite materials possess to its fullest, we must have some method to predict the stiffness, strength, and life of these materials in differing environmental conditions. In this section, we consider the implementation of a kinetics-based approach to such a method using damage accumulation concepts. Such an approach is implemented using the critical element model proposed by Reifsnider and Stinchcomb [49].

3.1 Damage Accumulation Concepts

In the present analysis we will follow arguments presented by Reifsnider et al. [38] for damage accumulation in composites. We begin our analysis by postulating that remaining strength may be used as a damage metric. We next assume that the remaining strength may be determined (or predicted) as a function of load level and some form of generalized time. For a given load level, a particular fraction of life corresponds to a certain reduction in remaining strength. We claim that a particular fraction of life at a second load level is equivalent to the first if and only if it gives the same reduction in remaining

strength, as illustrated in Figure 3.1. In the case of Figure 3.1, time t_1 at an applied stress level S_a^1 is equivalent to time t_2 at stress level S_a^2 because it gives the same remaining strength. In addition, the remaining life at the second load level is given by the amount of generalized time required to reduce the remaining strength to the applied load level. In this way, the effect of several increments of loading may accounted for by adding their respective reductions in remaining strength. For the general case, the strength reduction curves may be nonlinear, so the remaining strength and life calculations are path dependent.

Our next step in the analysis is to postulate that normalized remaining strength (our damage metric) is an internal state variable for a damaged material system. This normalized remaining strength is based upon the selection of an appropriate failure criterion (such as maximum stress or Tsai-Hill) which is a scalar combination of the principal material strengths and applied stresses in the critical element. In this way we are able to consider a single quantity rather than the individual components of the strength tensor. We denote this failure function by *Fa*. We next construct a second state variable, the continuity [50], which we shall define to be *(1-Fa)* and denote by ψ. We shall attempt to define our remaining strength and life in terms of ψ. To do so, we assume that the kinetics are defined by a specific damage accumulation process for a particular failure mode, and assign different rate equations to each of the processes that may be present.

As an example, let us consider a common kinetic equation (a power law) such that

$$\frac{d\psi}{d\tau} = A\psi^j \tag{3.1}$$

where j is a material constant and τ is a generalized time variable defined by

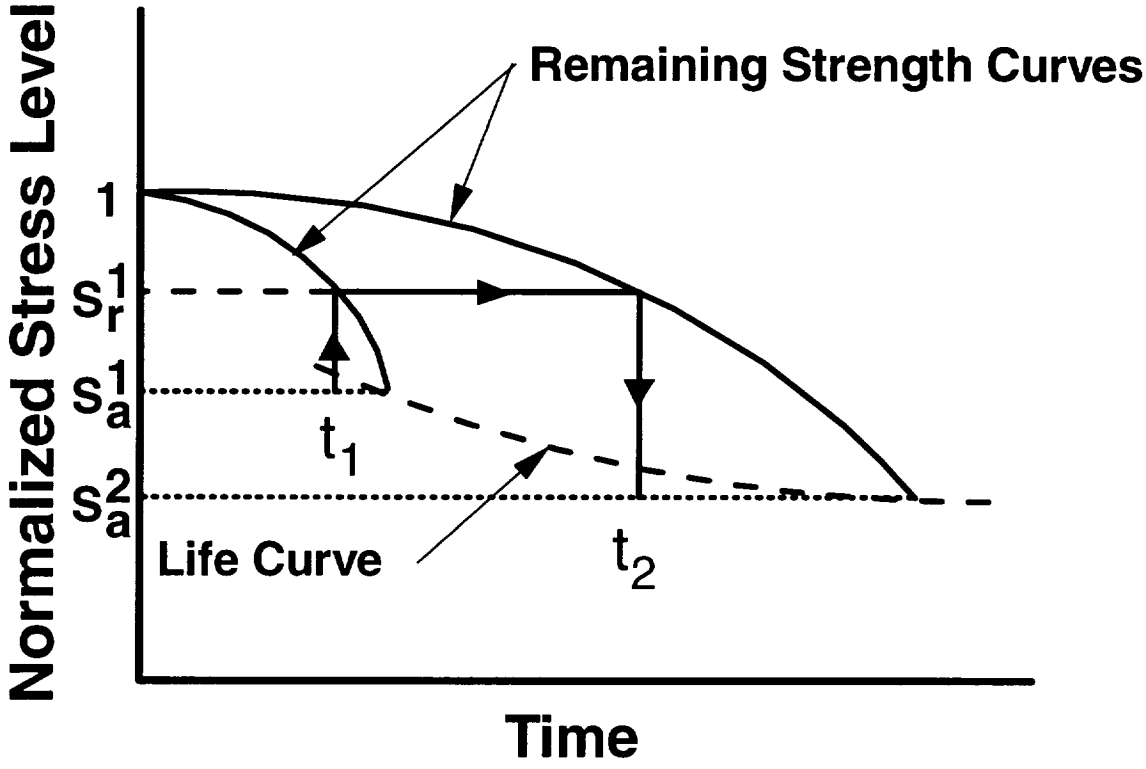

Figure 3.1.The use of remaining strength as a damage metric.

$$\tau = \frac{t}{\hat{\tau}} \tag{3.2}$$

and $\hat{\tau}$ is the characteristic time for the process at hand. This characteristic time could be a creep rupture life, a creep time constant, or even a fatigue life, in which case

$$\tau = \frac{n}{N} \tag{3.3}$$

where n is the number of fatigue cycles and N is the number of cycles to failure at the current applied loading conditions. Next we rearrange Equation (3.1) and integrate so that we have

$$\int_{\psi_0}^{\psi_i} d\psi = A \int_0^{\tau_i} (\psi(\tau))^j d\tau \tag{3.4}$$

If we set A=-*1* and j = *1*, we arrive at

$$\psi_i - \psi_0 = 1 - Fa_i - (1 - Fa_0) = -\Delta Fa = -\int_0^{\tau_i} (1 - Fa(\tau)) d\tau \tag{3.5}$$

Then we define our normalized remaining strength, *Fr* so that

$$Fr = 1 - \Delta Fa = 1 - \int_0^{\tau} (1 - Fa(\tau)) d\tau \tag{3.6}$$

In such a form, the failure condition is the point at which the remaining strength equals the applied load (Fr = Fa).

A special case of Equation (3.6) is that of fatigue loading at a constant amplitude in which

$$\tau = \frac{n}{N}$$
$$Fa = \frac{S_a}{S_{ult}} \tag{3.7}$$
$$Fr = \frac{S_r}{S_{ult}}$$

Substituting into Equation (3.6), we arrive at

$$\frac{S_r}{S_{ult}} = 1 - \left(1 - \frac{S_a}{S_{ult}}\right)\left(\frac{n}{N}\right) \tag{3.8}$$

This form is identical to that proposed by Broutman and Sahu [33] to explain the fatigue behavior of fiberglass.

If instead of the kinetic equation given in Equation (3.1), we use a different form given by

$$\frac{d\psi}{d\tau} = \psi j \tau^{j-1} \tag{3.9}$$

If we integrate Equation (3.9) from τ_1 to τ_2, we obtain

$$\psi_2 - \psi_1 = Fr_2 - Fr_1 = \Delta Fr = -\int_{\tau_1}^{\tau_2} (1 - Fa) j \tau^{j-1} d\tau \tag{3.10}$$

If we set τ_1 equal to zero and Fr_1 equal to unity, we arrive at the remaining strength as a function of generalized time

$$Fr = 1 - \int_{o}^{\tau} (1 - Fa(\tau)) j \tau^{j-1} d\tau \tag{3.11}$$

For the case in which *Fa* is constant, Equation (3.11) may be integrated analytically to yield

$$Fr = 1 - (1 - Fa)\tau^{j} \tag{3.12}$$

Equation (3.11) has been used with a great deal of success [35-38] for cases in which $Fa(\tau)$ is continuous. However, for cases in which $Fa(\tau)$ is not continuous (such as in the case of block loading)

we use a slightly modified approach based on the idea of remaining strength as a damage metric. To explain our implementation of these ideas, we will consider the case of block loading at a level Fa_1 for a generalized time τ_1 resulting in a remaining strength Fr. This loading is followed by loading at a level Fa_2. The question then is how to determine the equivalent amount of generalized time, τ_2^0, that would have been necessary to cause an equivalent amount of damage (reduction in residual strength) at the level Fa_2. We will call a time "pseudo-time" because it does not refer to actual time. Substituting into Equation (3.12) and using the idea of equivalent remaining strength, we obtain

$$Fr = 1-(1-Fa_1)\tau_1^{\,j} = 1-(1-Fa_2)(\tau_2^{\,0})^j \tag{3.13}$$

Equation (3.13) may then be solved for the pseudo-time to yield

$$\tau_2^{\,0} = \left(\frac{1-Fr}{1-Fa_2}\right)^{\frac{1}{j}} \tag{3.14}$$

In order to understand such a procedure, it may be helpful to consider a specific example such as that shown in Figure 3.2. This represents fatigue loading at an applied stress level of Fa_1 (with a corresponding characteristic number of cycles to failure N_1) for n_1 cycles followed by loading at a level Fa_2 (with a corresponding characteristic number of cycles to failure N_2) for Δn cycles. The number of pseudo-cycles, n_2^0, is given by

$$n_2^{\,0} = N_2\tau_2^{\,0} = \left(\frac{1-Fr}{1-Fa_2}\right)^{\frac{1}{j}} N_2 \tag{3.15}$$

Making use of Equation (3.10), the change in remaining strength, ΔFr, over the interval $(n_1, n_1+\Delta n)$ which corresponds to an interval $(n_2^{\,0}, n_2^{\,0}+\Delta n)$ is then given by

$$\Delta Fr = -(1-Fa_2)\left\{\left[\frac{n_2^{\,0}+\Delta n}{N_2}\right]^j - \left(\frac{n_2^{\,0}}{N_2}\right)^j\right\} \tag{3.16}$$

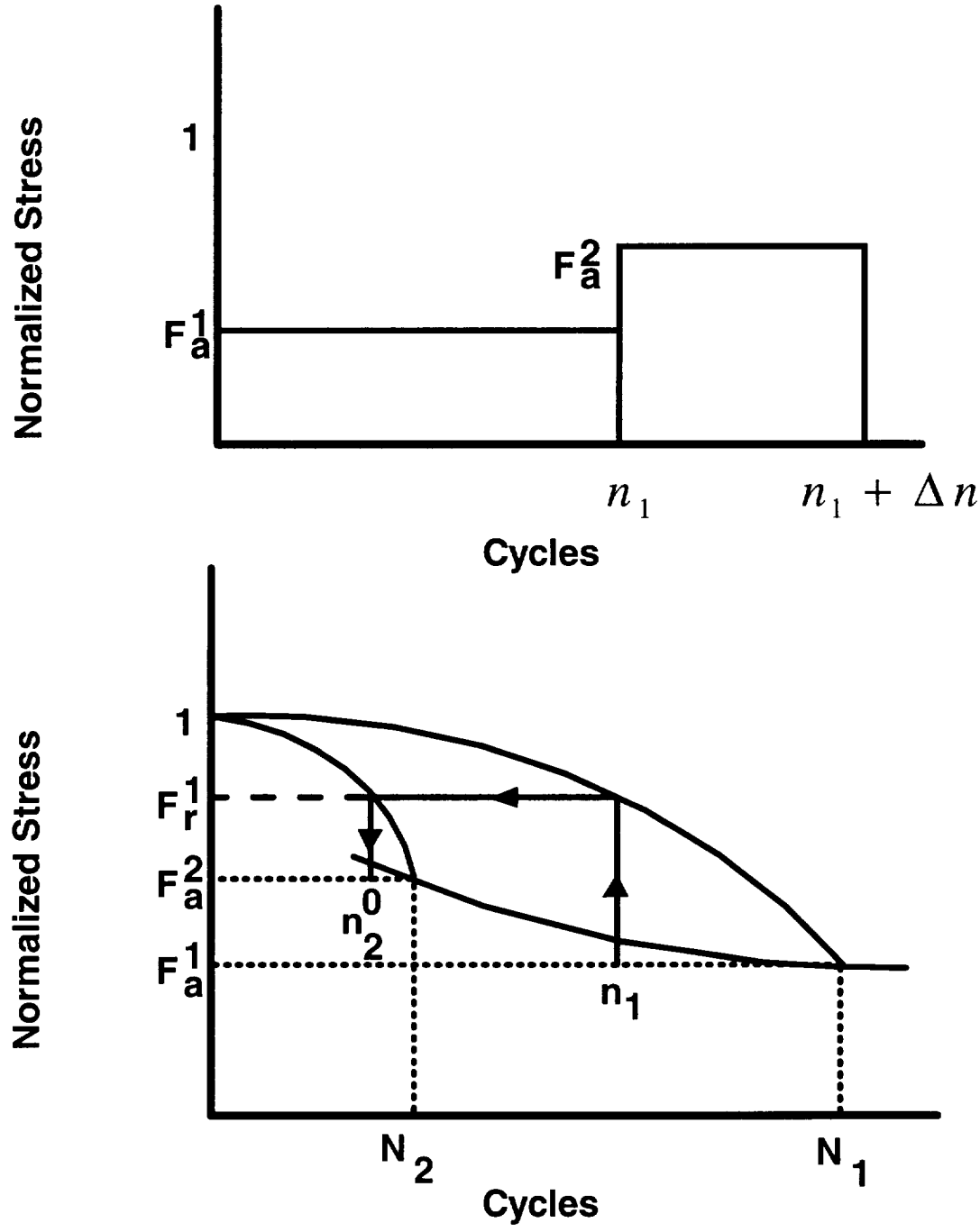

Figure 3.2. Calculation of equivalent ("pseudo") cycles for block loading.

In general, such an approach may be carried out for any number of blocks of loading having an applied stress level Fa_i so that the remaining strength is given by

$$Fr = 1 - \sum_{i=1}^{i=N_{blocks}} \Delta Fr_i \tag{3.17}$$

where N_{blocks} is the number of blocks of loading. This procedure has been recently been used with a great deal of success for ceramic composite materials [51] and also with polymeric composites [52].

3.2 Concepts of the Critical Element Model

Now our problem has been reduced to determining the inputs to either Equation (3.11) or Equation (3.17). To do so, we introduce the "critical element" concept [49]. The essentials of the critical element model are shown schematically in Figure 3.3. Such an approach is based upon the assumption that the damage associated with property degradation is widely distributed within the composite laminate. In addition, it is assumed that a representative volume can be chosen such that the state of stress in that volume is typical of all other volumes in the laminate, and that the details of stress distribution and damage accumulation in that volume are sufficient to describe the final failure resulting from a specific failure mode. Thus, it is possible to select different representative volume elements for different failure modes. We proceed by further dividing the representative volume into "critical" and "sub-critical" elements. The critical elements are selected in such a manner that their failure controls the failure of the representative volume and therefore (by definition of the representative volume) of the laminated component. The remainder of the elements in the representative volume are regarded as sub-critical because their failure does not cause failure of the of the representative volume and, therefore, of the component. Their failure (due to such events as cracking or delamination) does, however, lead to greater stresses in the critical element that contribute to the eventual failure of the component. As an example of such a failure process, we may consider the case of tensile fatigue failure of a cross-ply laminate. During the fatigue process, matrix cracks develop in the 90° plies. However, these cracks do not cause failure of the laminate. They do

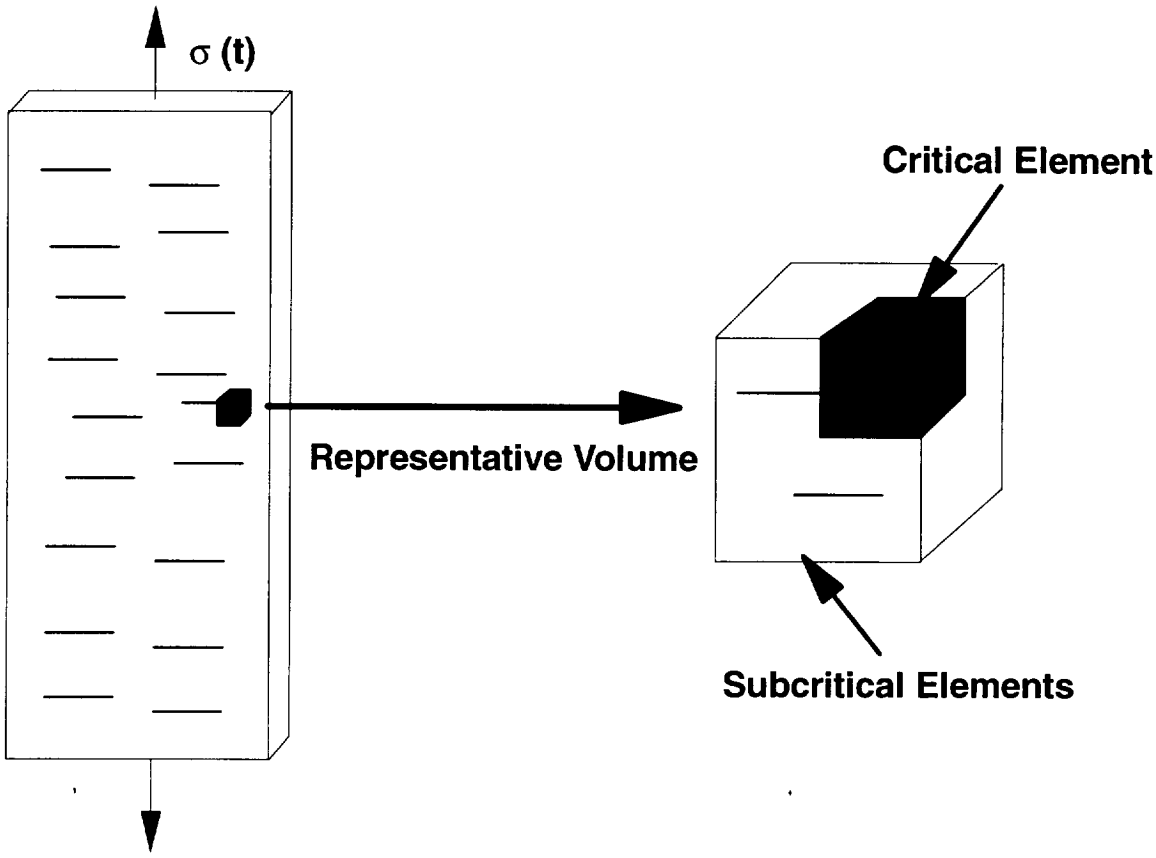

Figure 3.3. Illustration of the concepts involved in the critical element model.

increase the stress level in the 0° plies. But it is only when the 0° plies fail that the laminate fails. Thus, in this simple example, the 0° plies would correspond to the critical element and the 90° plies would correspond to the sub-critical element. This example takes into account only ply-level knowledge. The inclusion of micromechanical models (such as that for tensile strength) is readily accomplished within the framework of the model [39]. All of our calculations of remaining strength and life are then carried out within the critical element. The process used to calculate the remaining strength is given in Figure 3.4.

3.3 Validation Examples

In order to validate the remaining strength and life prediction scheme described above, a number of initial validations were performed. These validations were based upon experimental data taken from the literature which was then compared to the predicted values. The material used in the first two of these validations present study is the Aromatic Polymer Composite (APC-2) which is PolyEtherEtherKetone (PEEK) matrix reinforced with AS-4 carbon fibers. PEEK is a semi-crystalline polymer with a glass transition temperature of 144°C and a melting point of 335°C. Typical unidirectional properties of this material system are given in Table 3.1.

One of the principal reasons that this material system was chosen is that it has been well characterized experimentally. In particular, Picasso and Priolo [54] have characterized the unidirectional (0°) fatigue behavior of APC-2. This data were found to be well fit by a bi-linear form as follows:

Table 3.4. Mechanical properties of APC-2 composites [53].

QUANTITY	VALUE
E_1	19.4 msi (134 GPa)
E_2	1.29 msi (8.89 GPa)
G_{12}	0.74 msi (5.10 GPa)
ν_{12}	0.35
X_t	303 ksi (2090 MPa)
X_c	176 ksi (1210 MPa)
Y_t	11.6 ksi (80 MPa)
Y_c	40.6 ksi (280 MPa)
SS	11.6 ksi (80 MPa)

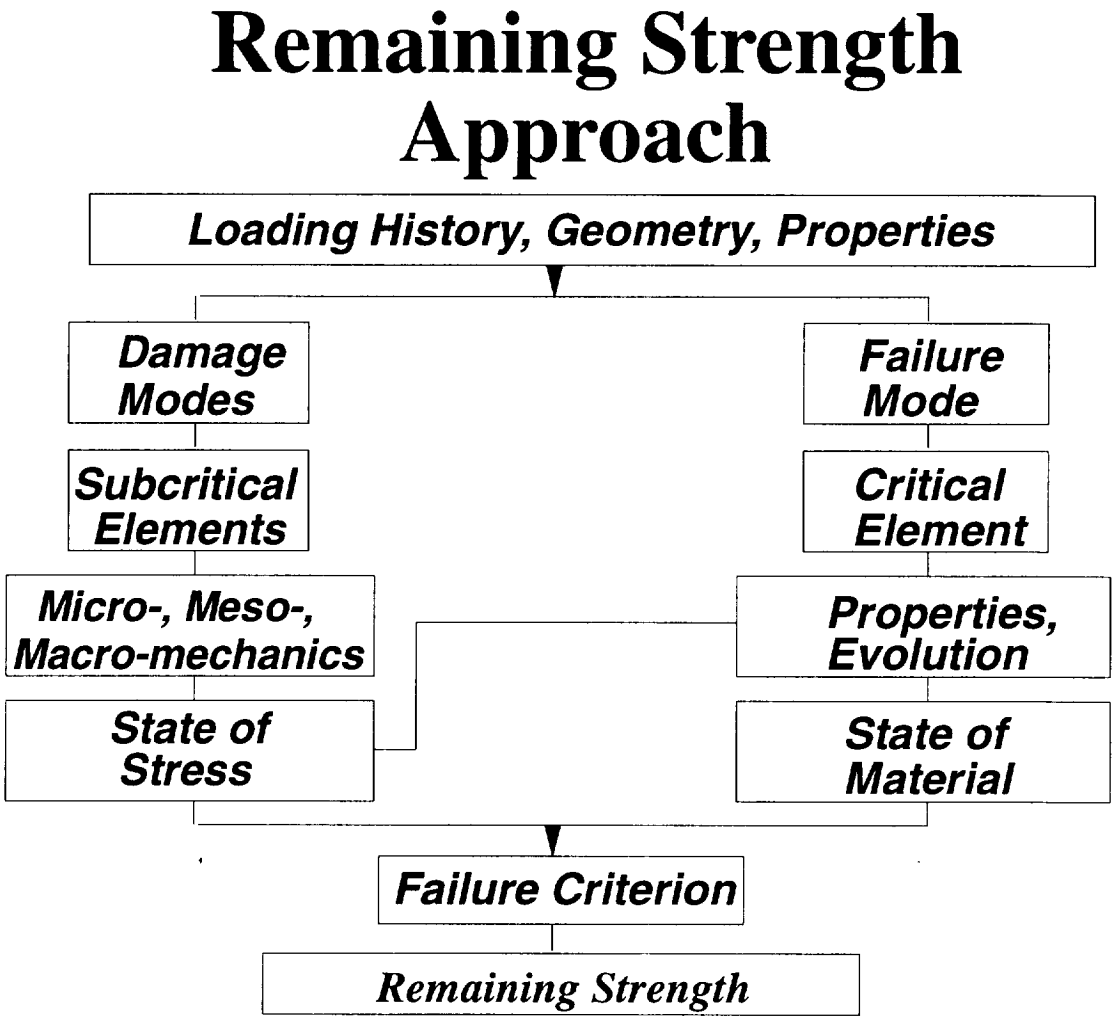

Figure 3.4. Flowchart of the approach used to calculate remaining strength.

$$\frac{S}{S_{ult}} = A_n + B_n \log N_f$$

$$\begin{aligned} A_n &= 1.312 \\ B_n &= -0.1818 \qquad N_f \leq 5982 \text{ cycles} \end{aligned} \tag{3.18}$$

$$\begin{aligned} A_n &= 0.7866 \\ B_n &= -0.0425 \qquad N_f > 5982 \text{ cycles} \end{aligned}$$

a comparison of the experimentally determined values and this fit is shown in Figure 3.5. Equation (3.18) can then be solved for N to obtain the characteristic time for the fatigue process to be used in Equation (3.3).

The validation data to be considered are that of Curtis [55], who studied the fatigue behavior of $[0/90/90/0]_s$ laminates of APC-2. These tests were conducted in load control at room temperature using sinusoidal loading at a frequency of 10Hz. Although the tests were conducted in load control, Curtis chose to present his data in terms of initial peak applied strain for comparison purposes with other materials. These initial peak applied strains were converted to applied stresses by use of classical lamination theory (CLT) for purposes of remaining strength and life predictions. 'Using solely the characteristic time information from Equation (3.18) and the critical element scheme illustrated in Figure 3.4, it is possible to determine the remaining strength as a function of applied stress level and cycles. With this information known, life prediction becomes a trivial task—the life is given by the point at which the remaining strength equals the maximum applied load. The results of such predictions are shown in Figure 3.6. We see that the agreement is quite good, although in most cases the experimental lives are less than the predicted ones. This is not surprising—the predicted lives are based upon the initial stiffness values given in Table 3.1. If the changes in stiffness in the 90 ° plies (subcritical element) due to matrix

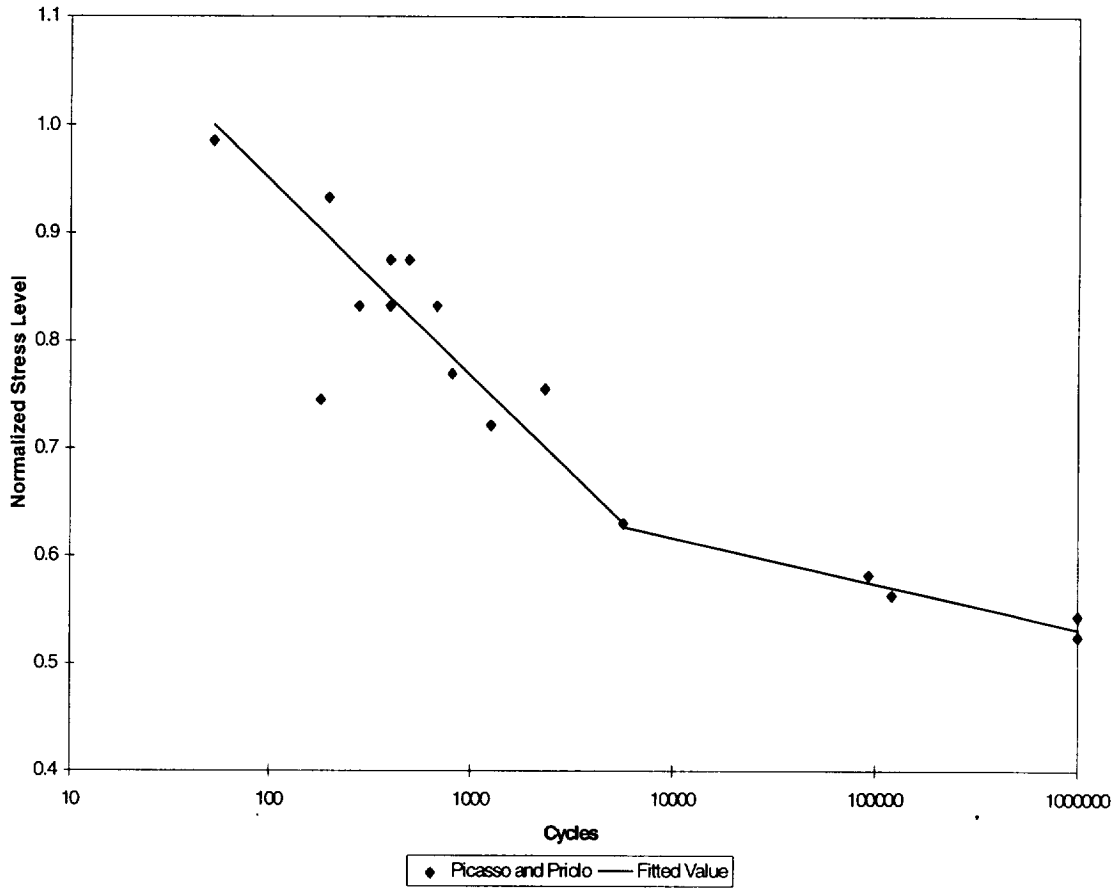

Figure 3.5. Comparison between measured and fitted fatigue lives for unidirectional APC-2 based on the data of Picasso and Priolo [54].

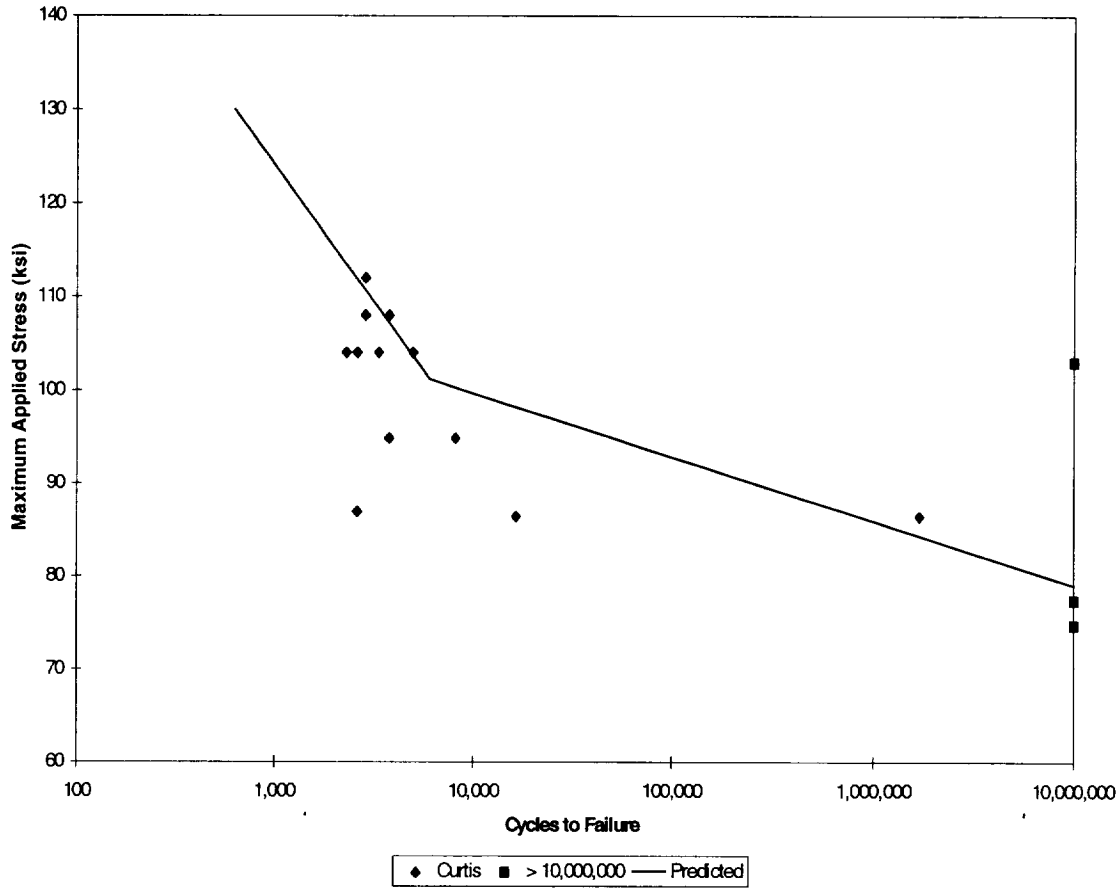

Figure 3.6. Comparison between predicted and measured fatigue lives for cross-ply APC-2 based on the data of Curtis [55].

cracking were included, the stress in the 0° plies (critical element) would be increased, leading to shorter predicted lives. However, the data of Curtis did not include such stiffness reduction information, and therefore it is not included in the modeling.

The next data to be considered are that of Simonds and Stinchcomb [56], who studied the fully reversed (R=-1) fatigue of $[(0/+45/90/-45)_s]_4$ APC-2 laminates containing a center hole. The laminates had dimensions of 4.75 in X 1.5 in (121 mm X 38.1 mm) and the hole was 0.375 in (9.5 mm) in diameter. The presence of the hole complicates the modeling somewhat. One initial approach would be to use the elastic stress concentration due to the hole to "knock-down" the laminate strength. However, experience has shown that such an approach leads to overly conservative estimates of notched strength. An two alternate approaches have been suggested by Whitney and Nuismer [57]. In one of these approaches, failure of the laminate is predicted to occur when the average stress over some characteristic distance, a_0, matches the unnotched laminate strength. We use this approach with one modification: rather than using the laminate strength and average laminate stress, the Whitney-Nuismer criterion is applied on a ply-level basis. Experience has also shown that this averaging distance, a_0, is typically on the order of the total laminate thickness. For the particular laminate used by Simonds and Stinchcomb, a value of a_0 = 0.178 in (4.52 mm) was found to well represent the quasi-static compressive strength. Using this information, along with the unidirectional S-N curve information from Picasso and Priolo, it was possible to predict fatigue lives for compression-controlled failure. The results are shown in Figure 3.7. The agreement is obviously quite excellent.

In addition to the number of cycles to failure information, Simonds and Stinchcomb also obtained residual strength measurements. These measurements may be directly compared to the predicted values from the analysis. An example of such a comparison is shown in Figure 3.8 for a maximum applied stress of 22.0

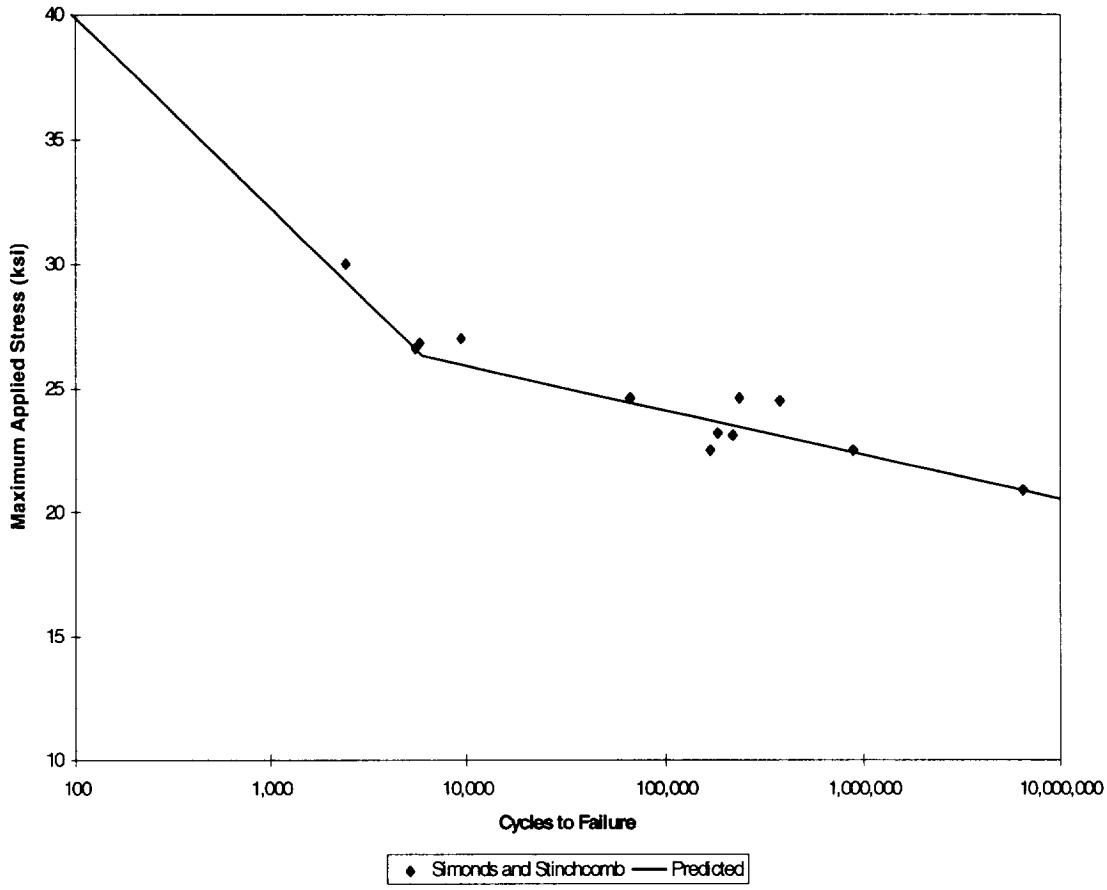

Figure 3.7. Comparison between predicted and measured fatigue lives for quasi-isotropic APC-2 based on the data of Simonds and Stinchcomb [56].

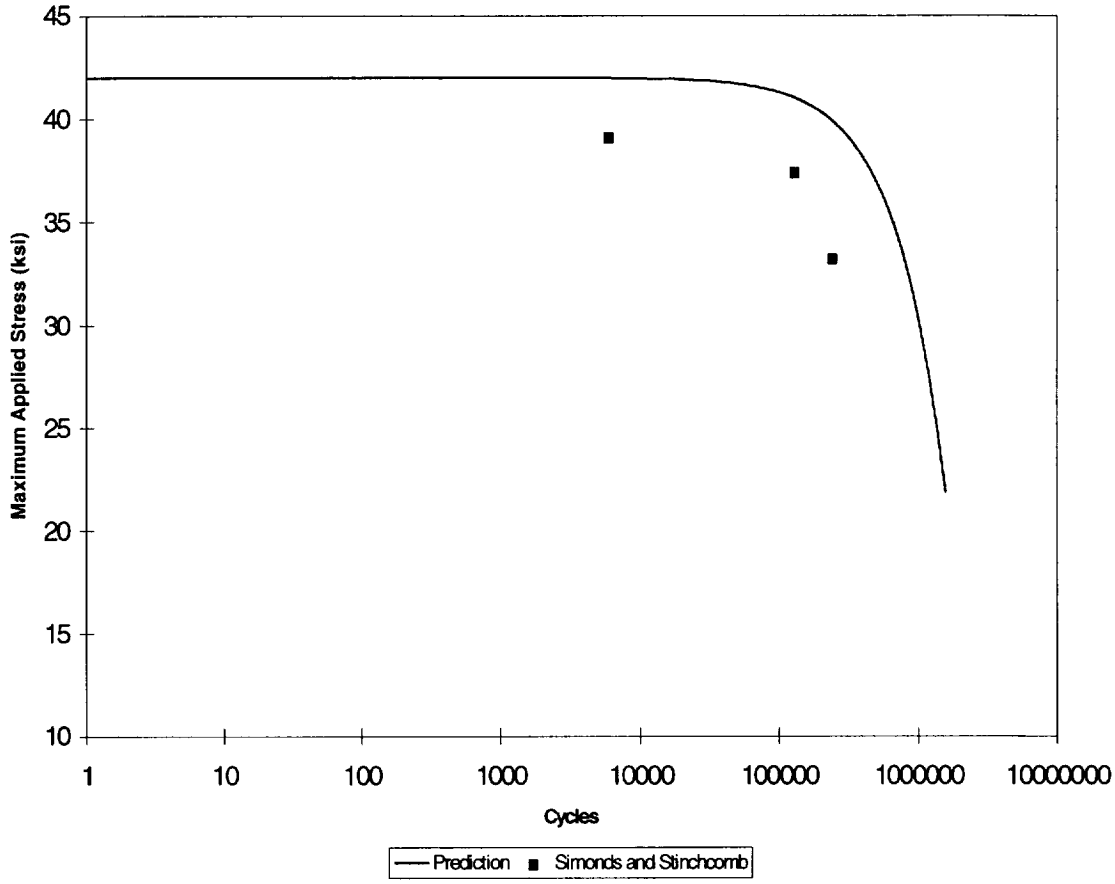

Figure 3.8. Comparison between predicted and measured remaining strength for quasi-isotropic APC-2 based on the data of Simonds and Stinchcomb [56].

ksi (151 MPa). The agreement here is also seen to be good, although the predicted remaining strength is always greater than the experimentally determined value.

4. Quasi-Static and Fatigue Behavior of Notched $[0/90]_{4s}$ APC-2

4.1 Experimental Techniques

4.1.1 Specimen Preparation

All the composite panels used in this study were fabricated from prepreg supplied by ICI. The panels were laid up in a 6" X 6" (15.25 cm X 15.25 cm) mold in a $[0/90]_{4s}$ stacking sequence. In an effort to evaluate the effect of the level of crystallinity of the matrix on the behavior of the composite, three different cooling rates were used to manufacture the panels: 10°C/min (the rate recommended by ICI), 5°C/min, and 1°C/min. After the panels were manufactured, they were examined ultrasonically using a C-scan technique. All the panels were determined to be of good quality, within the limits of the technique. Subsequent to the C-scan process, the panels were machined into 6" inch long by 1" wide specimens containing a 0.250" diameter center hole.

4.1.2 Quasi-Static Testing

These tests were conducted in an electro-hydraulic load frame with hydraulic wedge grips operated in load control using a grip pressure of 1200 psi. A loading rate of 200 lb/sec was used for all quasi-static tests This relatively high rate of loading (specimen failures occurred within 30 seconds) was chosen because the ultimate strength values obtained in the tests were to be used to determine load levels for the fatigue testing. During the tests, strain was measured by means of a 1" gage length extensometer centered over the hole. The knife edges of the extensometer were secured in V-notched aluminum tabs which had been bonded to the specimen surface. During the testing process, the extensometer output, as well as the load and stroke signals were recorded at a rate of 10 samples per channel per second using a computer controlled data acquisition system [52]. This was accomplished by sampling the data at 360 points per channel per second, and then averaging blocks of 36 points per channel. The failure load, determined by

the peak indicator of the load frame, was recorded for each of the specimens and used to determine the specimen's ultimate strength.

4.1.3 Fatigue Tests

The fatigue tests were performed in load control at 10 Hz (sinusoidal waveform) using a R-ratio of 0.1. Two fixed percentages of the average ultimate strength values from the quasi-static tests were used: 80.0% and 87.5%. These loads were chosen in an effort to provide a compromise between little (or no) damage development at lower load levels and uncontrollable, instantaneous or nearly instantaneous failure at high load levels. An extensometer was mounted across the hole in a manner identical to that used for the quasi-static tests. During the course of the experiment, maximum as well as minimum values of load, actuator displacement, and strain were recorded using a computer-controlled data acquisition system. This was accomplished by acquiring data at 1000 points per channel per second, dividing the data into discrete cycles, and storing only the maximum and minimum values [52]. Early experience with this material system suggested that fatigue failures would not occur in a period of 10^6 cycles, therefore the tests were interrupted after periods of 100, 10000, and 100000 cycles for damage analysis and residual strength testing.

4.1.4 Penetrant Enhanced Radiography

Penetrant enhanced radiography has proven to be a valuable tool for monitoring and evaluating damage development in composite laminates. This technique allows one to detect damage modes such as fiber failure, matrix cracking, longitudinal splitting, and delamination. Using radiography at different stages in the life of a specimen can provide particular insight into the mechanisms of damage development. The procedure for obtaining the penetrant enhanced used in this investigation radiograph involved several steps. First the specimen was removed from the load frame, and an X-ray opaque penetrant was applied liberally to the specimen surface. This penetrant—a zinc iodide solution—consisted of 60 grams of ZnI_2 mixed in 10 ml each of water, isopropyl alcohol, and Kodak Photo-Flo 200. As this penetrant is quite

corrosive, it was allowed to remain on the specimen for only two hours. After this period, the penetrant was removed from the surface of the specimen. The specimens were then placed flat on a sheet of Kodak M-5 double-sided emulsion film in the X-ray cabinet (Hewlett Packard 43805N Faxitron Series X-ray System) at a distance of 16 inches (40 cm) from the emitter. A trial-and-error process was used to determine that a 30 kVp voltage applied for a period of 30 seconds produced acceptable quality radiographs.

4.1.5 Strip Strain Gages and Residual Strength Testing

In an effort to quantify the relaxation of stress concentrations around the hole during the fatigue process, strip strain gages (Micro Measurements EP-08-045PG-120) were adhesively bonded to the surface of the specimens using a cyanoacrylate adhesive (M-Bond 200, also supplied by Micro Measurements). These gages were located along the specimen axis adjacent to the hole in a manner illustrated by Figure 4.1. In order to determine the initial strain distribution, gages were applied to several specimens before the specimens were fatigue loaded. The specimens were then ramped quasi-statically to a low load level (corresponding to a stress of approximately 4000 psi—28 MPa), and the resulting strain distribution was recorded. Subsequently, the specimens were fatigue loaded and the maximum as well as minimum strains experienced by each gage were recorded as a function of cycles. At the high strain levels employed during the fatigue tests, gage failure occurs quite rapidly. Therefore gages were applied to the specimens after the X-ray process was completed. This also was not entirely satisfactory, as bonding the gage to the surface after the dye penetrant used for the radiography had been applied proved to be difficult. As a result, for subsequent specimens the gages were bonded to the surface before any penetrant was applied. The specimens were then loaded quasi-statically to the same low stress level, 4000 psi (28 MPa), that was used prior to the fatigue process and the resulting strain distribution recorded. Next the specimens were removed from the load frame, penetrant applied, and X-rays taken. Finally, the specimens were placed in the load frame for residual strength testing. These residual strength tests were conducted in a manner identical to that used for the quasi-static tests.

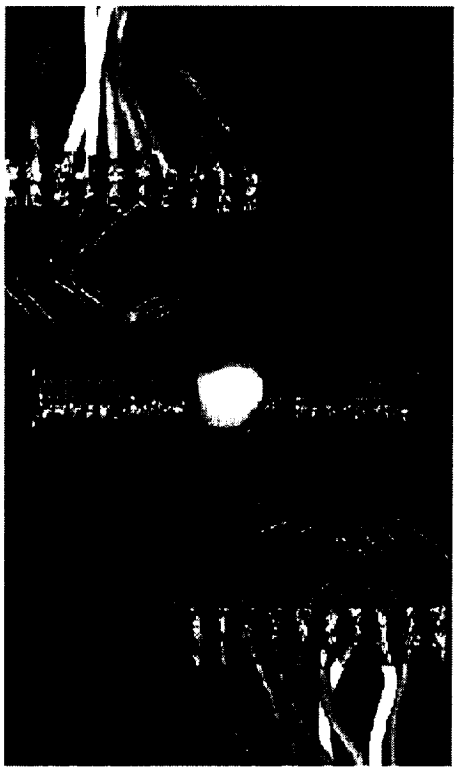

Figure 4.1. Strip strain gage placement along hole axis.

4.2 Experimental Results and Discussion

4.2.1 Quasi-Static Testing

Due to the amount of material available for testing, two specimens were tested for the cooling rate of 10°C/min, and one each for the cooling rates of 5°C/min and 1°C/min. The results of these tests are summarized in Table 4.1. It should be notched that the strength was calculated on the basis of a gross, rather than a net, section stress and that the strain values were the average strains measured by the extensometer over its gage length. Although it is certainly undesirable to draw a definitive conclusion from such a small data set, the cooling rate does not appear to significantly affect the quasi-static strength. There seems to be a great deal of scatter in the strain to failure and particularly in the modulus data, particularly in light of the agreement in the strengths. This discrepancy could perhaps be explained by misalignment of the extensometer tabs with respect to the hole. Examples of the failed specimens are shown in Figure 4.2. As expected the failures all occur at the location of maximum stress concentration due to the hole an proceed perpendicular to the loading direction.

4.2.2 Fatigue Testing

A total of eighteen specimens were tested (nine at each of the different load levels) for this investigation. Example normalized compliance curves based upon the extensometer strain measurements are shown in Figure 4.3. The data have been normalized to the compliance of the specimen during the first cycle. These data proved to be extremely reproducible. In addition to these measurements, observations of the surface of the specimen were made periodically during the test. In all of the specimens except for those six in which the test was stopped after 100 cycles, longitudinal splits emanating from both sides of the hole could be observed on the surface of the specimen with the naked eye. The rate of growth of these splits appeared to be proportional to the applied load level.

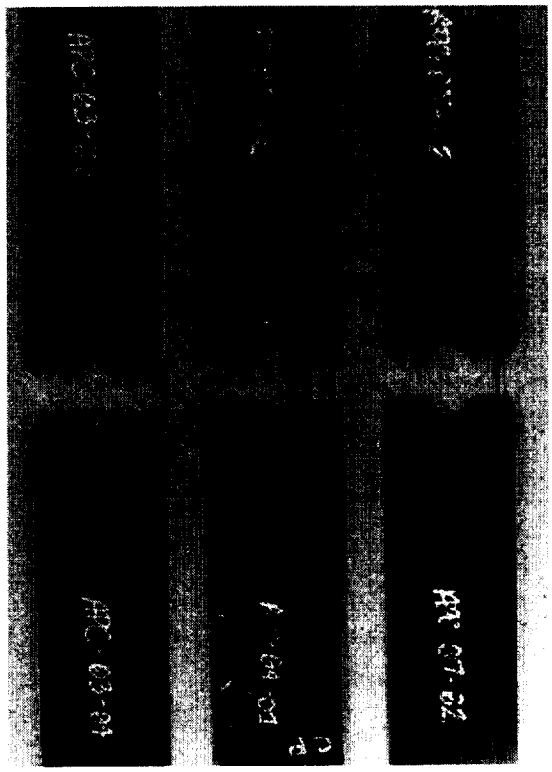

Figure 4.2. Failed cross-ply APC-2 quasi-static specimens.

Table 4.1. Notched quasi-static test results for APC-2 laminates having different cooling rates.

Specimen ID	Cooling Rate °C/Min	Notched Strength ksi (MPa)	Notched Strain to Failure %	Notched Modulus msi (GPa)
APC-03-04	10	55.6 (383)	0.941	6.11 (42.1)
APC-04-01	10	56.1 (387)	0.897	6.39 (44.1)
APC-07-02	5	57.5 (396)	0.962	6.09 (42.0)
APC-10-01	1	58.0 (400)	0.915	6.40 (44.1)

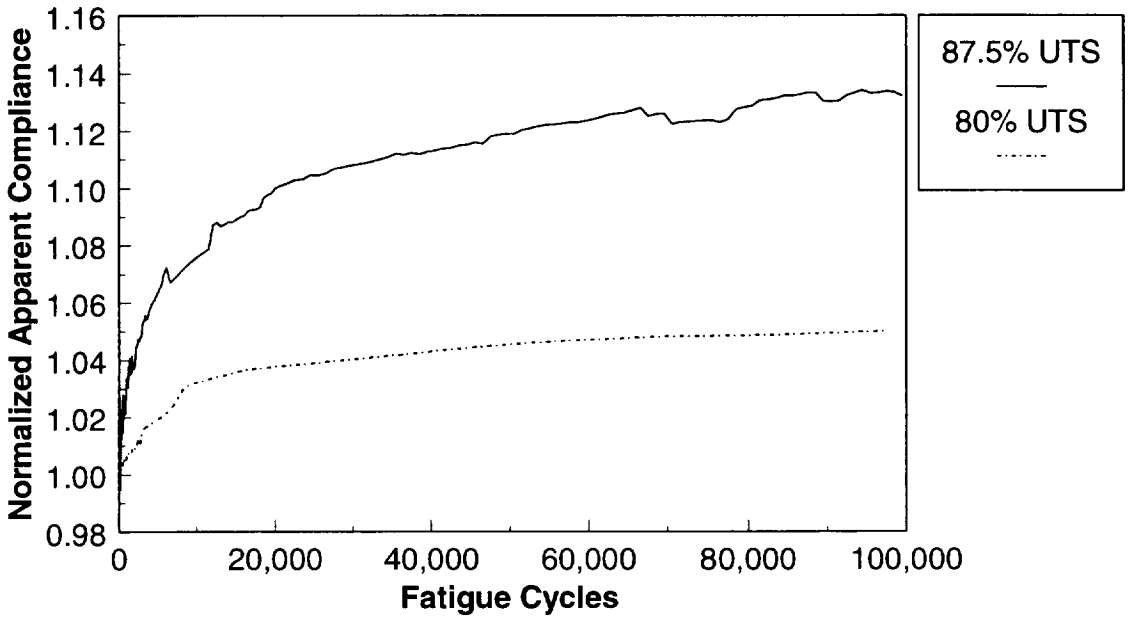

Figure 4.3. Normalized compliance meaured across the hole using an extensometer for APC-2 specimens fatigue at 87.5% and 80% of ultimate tensile strength.

4.2.3 Penetrant Enhanced Radiography

This technique proved to be useful for identifying features of the damage development, although there were some problems with its implementation. As mentioned previously, the penetrant was only allowed to remain on the specimen for two hours, and then groups of specimens (normally three) were radiographed simultaneously. During subsequent viewing of the X-rays, it became apparent that the amount detail that was observable in the radiographs was highly dependent upon the location of the specimens within the X-ray cabinet. In particular, matrix cracking was difficult to observe in the specimens which were not placed at the center of the cabinet, directly under the emitter. However, the longitudinal splits were always readily apparent, with the exception of the tests which were interrupted after 100 cycles at 80% of the ultimate strength. In this case, it appears that the splits are still in their initiation phase. Rather than being present on both sides of the hole and extending in both directions, there is only one split adjacent to the hole which extends in one direction. Radiographs of the specimens at different stages of life are shown in Figures 4.4 and 4.5 for 80% and 87.5% of ultimate strength, respectively. One interesting feature of the splits that can be observed it that they do not emanate from the location of the maximum tensile stress concentration. Rather, they begin a few degrees above and below this location.

Because these splits are readily identifiable in the radiographs (and also on the surface of the specimen during the test), it was hoped that the split length could be correlated with the reduction of the stress concentration due to the hole that is known to occur during the fatigue of composite materials. As a result, the individual split lengths for each of the specimens were measured. The results of such measurements are shown in Figure 4.6, along with the resulting curve fits. In view of the stress level dependence of the length of the splits, it is not surprising that the strains measured across the hole during the fatigue tests using the extensometer are greater at a given number of cycles for specimens fatigued at 87.5% UTS than specimens fatigued at 80% UTS.

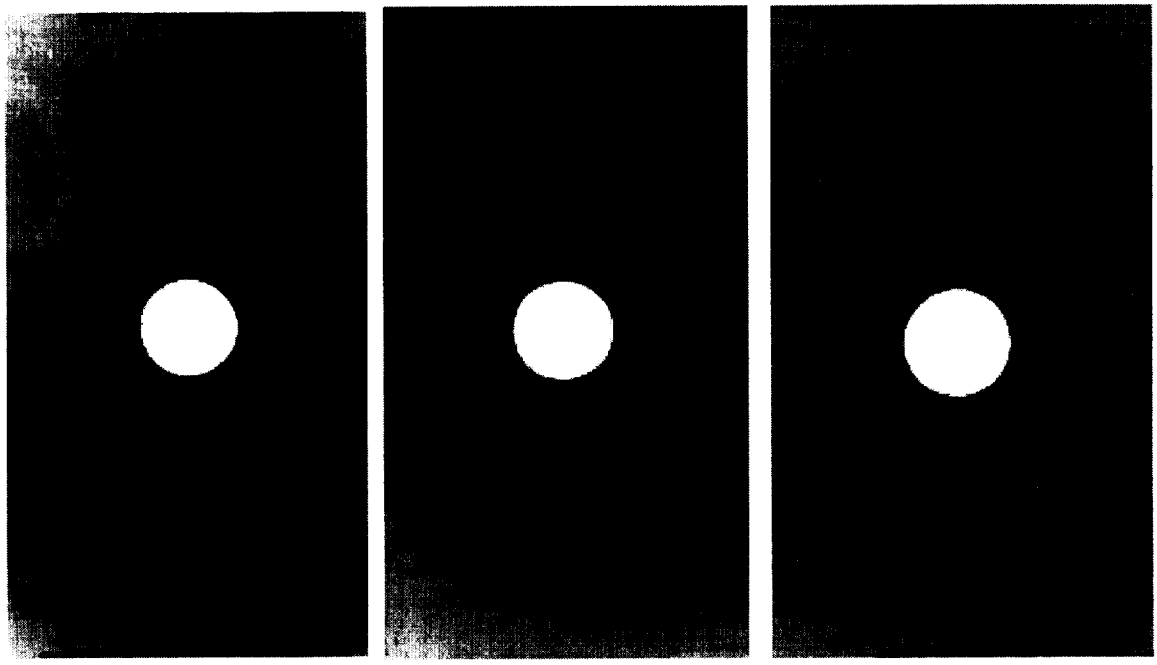

Figure 4.4. Radiographs of specimens fatigued at 80% of ultimate strength for 100, 10000, and 100000 cycles.

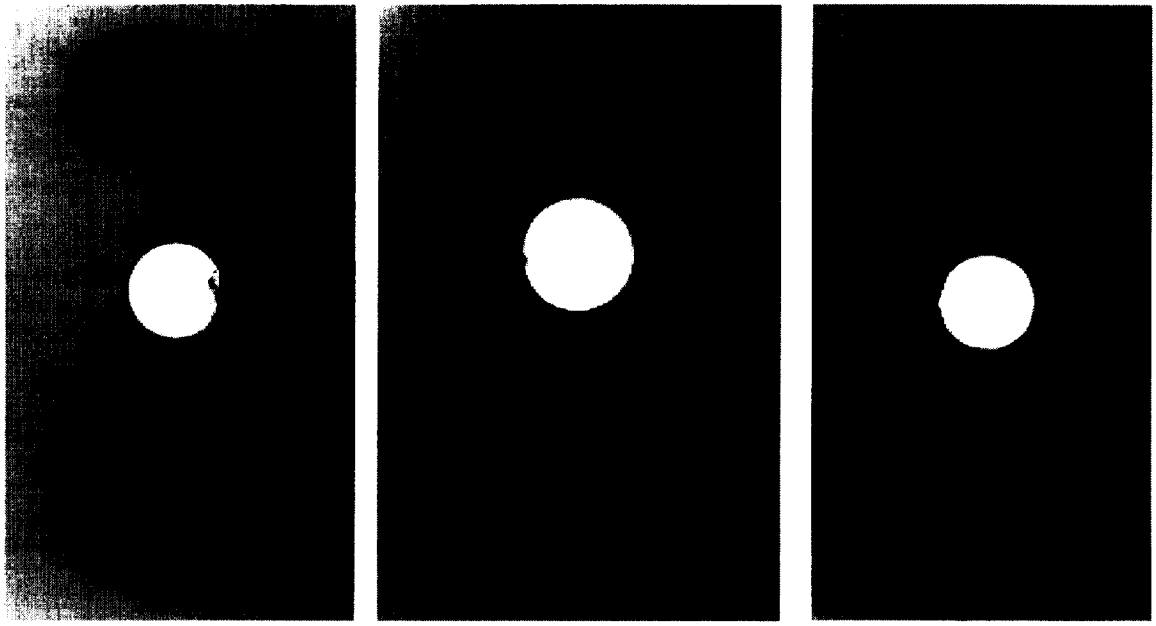

Figure 4.5. Radiographs of specimens fatigued at 87.5% of ultimate strength for 100, 10000, and 100000 cycles.

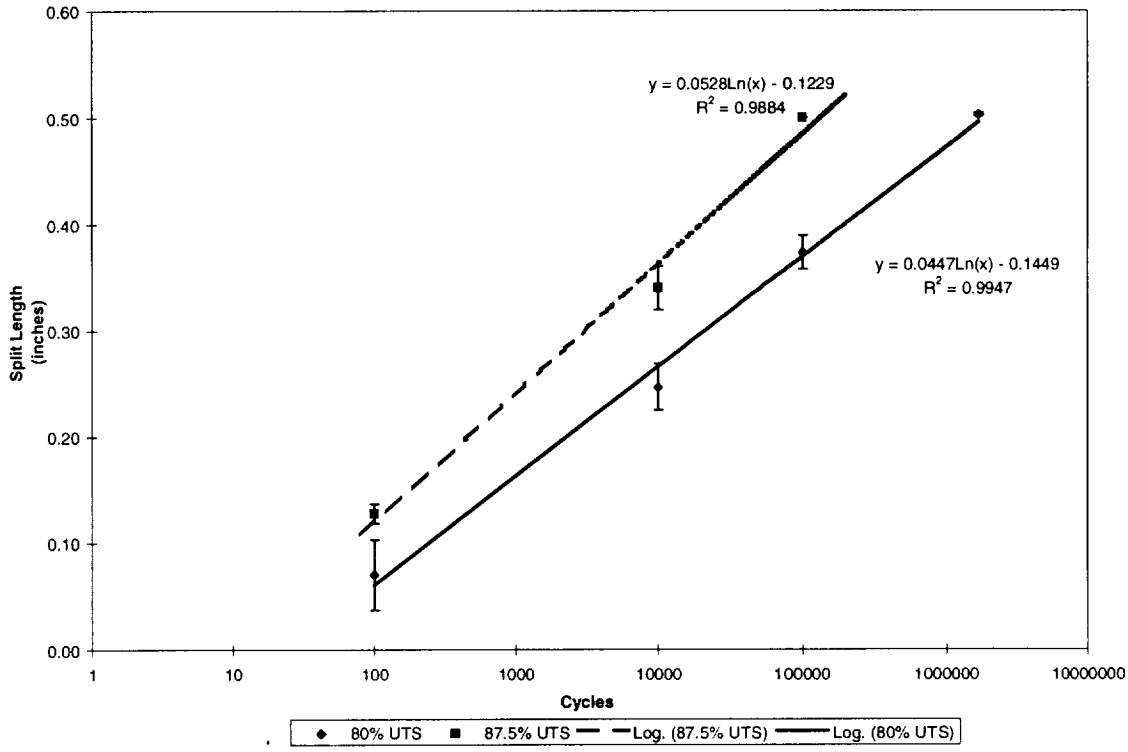

Figure 4.6. Longitudinal split length as a function of cycles for APC-2 laminates fatigued at 80% and 87.5% of ultimate tensile strength.

4.2.4 Strip Gage Results

Strain distributions near the hole were measured on three specimens before fatigue, and on at least two specimens at each of the different stages of life for the two stress levels. The results of these measurements are given in Table 4.2, where the strains have been obtained at each gage position at an applied stress level of approximately 4000 psi (28 MPa). In light of the statistical nature of the damage development process in composite materials and the difficulty in positioning the gages in a consistent manner, these measurements proved to be surprisingly reproducible. It should be noted that increases in strain (such as that for 100000 cycles at 80% of the ultimate strength) do not correspond with increases in *stress* as a result of increased specimen compliance with damage and a redistribution of the stresses. These ideas will be investigated during the analysis.

4.2.5 Residual Strength Results

After the radiography procedure and the strip strain gage tests, the residual strength tests were conducted. The results of these tests are summarized in Table 4.3. The residual strength values for this material system exhibit an interesting pattern. First there is an initial decrease in the residual strengths, followed by an increase. In addition to this interesting behavior, the specimen failures exhibited three modes of failure. In the first mode, the specimen failures appeared identical to those from the quasi-static tests (i.e. failures occurred along the axis of the hole in a line perpendicular to the axis of the applied load). In the second mode of failure, the failures occurred in a line perpendicular to the applied load, but in an offset location from the axis of the hole. The final mode of failure was a combination of the previous two. In this case the failure was antisymmetric to the loading axis. Examples of the failed specimens are shown in Figure 4.7. No direct correlation was observed, however, between the failure mode and the residual strength values. Note that the specimens which were fatigued 100000 cycles at 87.5% of the ultimate strength had consistently higher remaining strengths than those fatigued at 80% of the ultimate strength.

Table 4.2. Strip strain gage results for APC-2 laminates.

Specimen	Cooling Rate (°C/min)	Normalized Fatigue Stress Level	Applied Fatigue Cycles	Gage 1 (με)	Gage 2 (με)	Gage 3 (με)	Gage 4 (με)
APC-05-01	10	N/A	Before	884	567	526	496
APC-04-05	10	N/A	Before	815	540	494	469
APC-07-01	5	N/A	Before	775	498	456	422
APC-04-05	10	80%	100	833	545	504	480
APC-05-01	10	80%	100	888	562	520	495
APC-07-01	5	80%	100	783	490	449	414
APC-03-02	10	80%	10000	781	532	490	456
APC-06-02	5	80%	10000	687	481	449	408
APC-10-03	1	80%	10000	744	519	472	439
APC-03-01	10	80%	100000	901	544	493	452
APC-06-05	5	80%	100000	950	619	562	---
APC-10-02	1	80%	100000	940	599	517	479
APC-04-02	10	87.5%	100	892	582	531	504
APC-10-04	1	87.5%	100	873	570	520	493
APC-06-03	5	87.5%	10000	938	584	533	476
APC-07-04	5	87.5%	10000	921	586	537	491
APC-04-04	10	87.5%	100000	792	529	481	437
APC-06-04	5	87.5%	100000	827	568	523	475

Table 4.3. Residual strength results for APC-2 laminates.

Specimen	Cooling Rate (°C/min)	Normalized Fatigue Stress Level (%)	Fatigue Cycles	Residual Strength ksi (MPa)
APC-04-05	10	80	100	54.6 (376)
APC-05-01	10	80	100	55.4 (382)
APC-07-01	5	80	100	52.6 (363)
APC-03-02	10	80	10000	59.1 (407)
APC-06-02	5	80	10000	63.3 (436)
APC-10-03	1	80	10000	59.5 (410)
APC-03-01	10	80	100000	60.4 (416)
APC-06-05	5	80	100000	61.8 (426)
APC-10-02	1	80	100000	61.2 (422)
APC-04-02	10	87.5	100	54.5 (376)
APC-05-03	10	87.5	100	57.4 (396)
APC-10-04	1	87.5	100	56.9 (392)
APC-05-05	10	87.5	10000	64.1 (442)
APC-06-03	5	87.5	10000	57.4 (396)
APC-07-04	5	87.5	10000	64.9 (447)
APC-04-04	10	87.5	100000	69.2 (477)
APC-04-04	10	87.5	100000	67.2 (463)
APC-06-04	5	87.5	100000	68.7 (474)

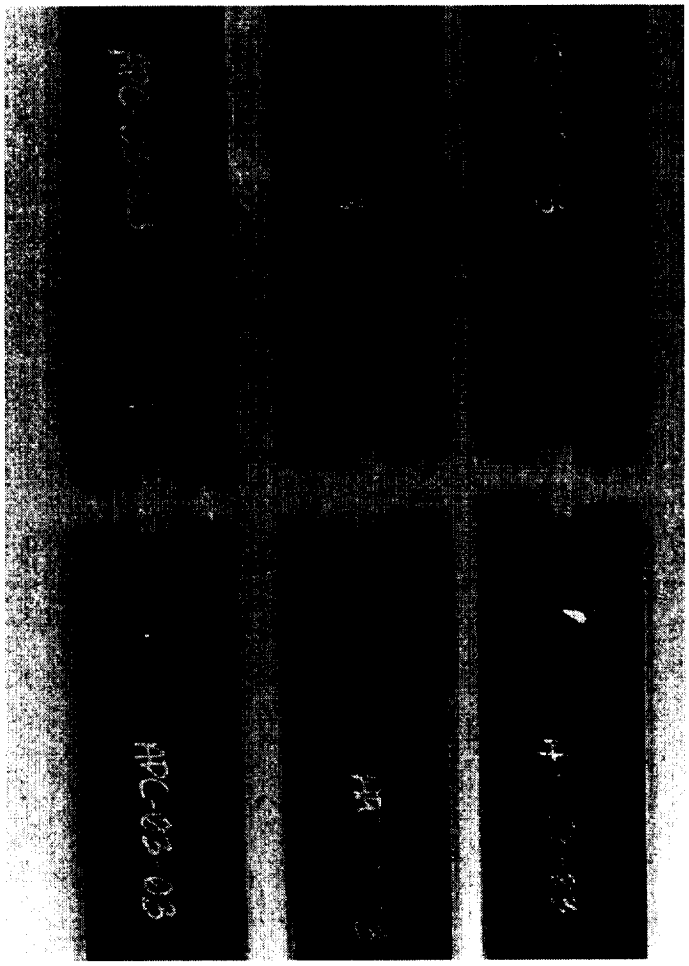

Figure 4.7. Cross-ply APC-2 specimens after residual strength testing exhibiting the three different failure modes.

4.3 Analysis Techniques

4.3.1 Notched Quasi-Static Strength

A reasonable approach to predicting/explaining the quasi-static strength of notched composite laminates would be to use the elastic stress concentration factor in conjunction with the unnotched material strengths. This approach suffers from two shortcomings: it requires that the unnotched strength of the laminate be known and it also gives overly conservative estimates of the notched strength. To overcome these difficulties, Reifsnider [28] has suggested applying the average stress criterion of Whitney and Nuismer [57] on a ply-level basis. Whitney and Nuismer's average stress criterion is given by

$$\sigma_0 = \frac{1}{d_0} \int_a^{a+d_0} \sigma_y(x,0)dx \tag{4.1}$$

where σ_0 is the unnotched strength of the laminate, a is the hole size, $\sigma_y(x, 0)$ is the stress along the hole axis, and d_0 is the averaging distance. This averaging distance may be viewed as a process zone over which the failure takes place. To apply this criterion on a ply-level basis for the $[0/90]_{4s}$ laminates, we proceed in the following manner. First, we calculate the material properties for an equivalent anisotropic laminate using classical lamination theory (CLT) in conjunction with the laminae properties and the laminate stacking sequence. Next, we use Lekhnitskii's [58] solution for an anisotropic plate containing a hole to evaluate the strain distribution for the anisotropic equivalent laminate when the applied laminate stress to S. The resulting strain distribution is then substituted back into CLT to calculate the average stress distribution in the 0° plies as follows

$$\overline{\sigma}_{ij} \equiv \frac{1}{d_0} \int_a^{a+d_0} \sigma_{ij}^{0^\circ}(x,0)dx \tag{4.2}$$

All that remains is the selection of an appropriate failure criterion. For 0° plies, we have found that a maximum stress criterion works well. Therefore, the averaging distance, d_0, is selected so that when the applied stress is equal to the failure stress determined experimentally, we have

$$\overline{\sigma}_{11}^{0^\circ} = \frac{1}{d_0}\int_{a}^{a+d_0} \sigma_{11}^{0^\circ}(x,0)dx = X_t \tag{4.3}$$

where X_t is the unidirectional tensile strength in the fiber direction. For the purposes of simplicity and notation, it has been assumed that the maximum value of this stress occurs along the hole axis (this may be easily verified). Equation (4.3) may be viewed as the defining equation for d_0.

The preceding analysis is based upon the assumption that the anisotropic equivalent plate may be used to represent the composite laminate. To validate whether such an assumption is validate, we can compare the resulting strain distribution measured using the strip strain gages to that predicted from by Lekhnitskii's solution. Such a comparison is shown in Figure 4.8 where the Lekhnitskii solution, which appears as the solid line, has been calculated on the basis of the material properties given in Table 3.1. At first, the comparison does not appear to be very good. There are two reasonable explanations for such an occurrence. First of all, the Lekhnitskii solution is for a hole in an infinite anisotropic plate; the situation here is that of a finite width plate (the total specimen width is only four times the hole diameter). In addition, the strain gages are not capable of measuring a point strain, but instead average over the gage section. In order to attempt to compare this measured average strain with the Leknitskii solution, the Leknitskii solution was averaged over the width of each gage (0.090 inches—2.3 mm). This average solution value is shown as the dotted line in Figure 4.8. It then becomes apparent that the anisotropic plate solution may be used, at least as an engineering approximation.

4.3.2 Notched Residual Strength Analysis

When the laminate is fatigue loaded, however, the situation is greatly complicated. As damage such as

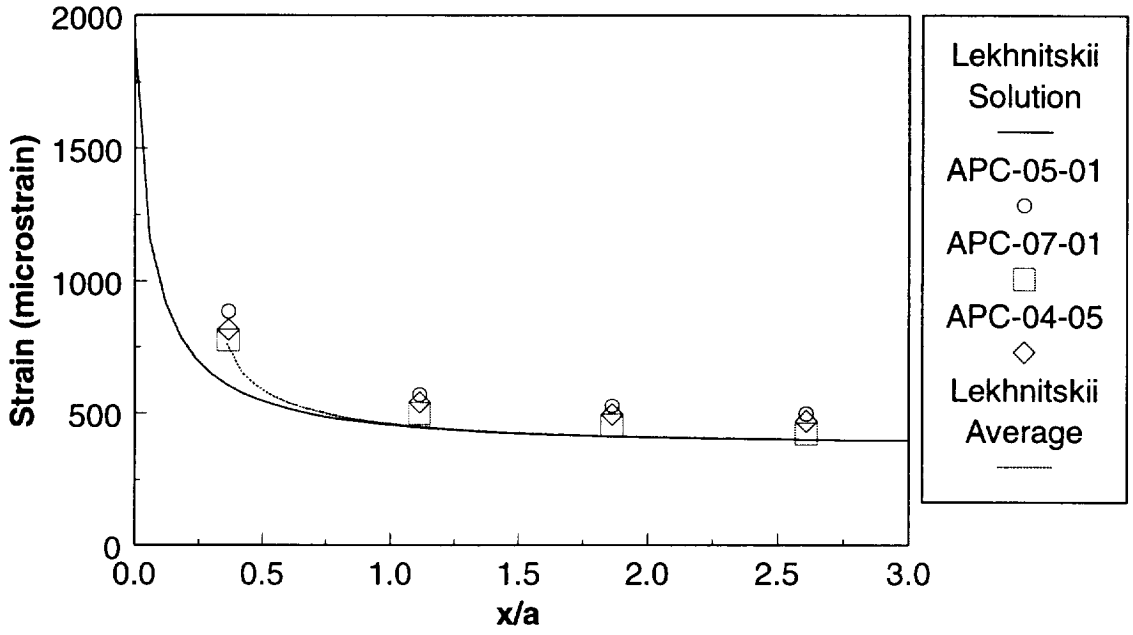

Figure 4.8. Comparison of predicted and measured axial strain as a function of position along the hole axis.

matrix cracking develops, the stiffness of the plies changes. Also, the development of the longitudinal splits reduces the stress concentration due to the notch by making the hole act more as ellipse than a circle. In addition, as the laminate is fatigued, the 0° plies begin to accumulate fiber fractures which lower the remaining strength of the plies. Developing an exact solution for the combined effects in an exact fashion would be a difficult, if not impossible, proposition. Instead an approximate approach is taken. This approach involves three steps:

1. Representing the change in off-axis ply stiffnesses (E_{22} and G_{12}) due to matrix cracking
2. Redistributing the stresses around the hole to account for the development of the longitudinal splits and a stress relaxation zone.
3. Calculating the effect of damage accumulation on the remaining strength of the 0 ° plies.

The first two steps were treated in a combined manner using the data from the strip gages. For ease of analysis, we assume that the normalized values for E_{12} and G_{12} can be represented in the form of

$$\frac{G_{12}(n)}{G_{12}(0)} = \frac{E_{22}(n)}{E_{22}(0)} = C - (C-1)(1+\alpha n)\exp(-\beta n) \qquad (4.4)$$

where n is the number of fatigue cycles and C, α, and β are fitting parameters. Such an expression can be used to take into account the stiffness reduction due to cycle-dependent matrix cracking. Now we need to account for the stress redistribution due to the presence of the longitudinal splits. This may be accomplished by representing the hole in the laminate by an "effective" elliptical hole having different dimensions than the actual hole. Because the splitting extends only in the direction of the applied load, we assume that the dimension of this hole axis may modified according to

$$b(n) = b_f + (a - b_f)\exp\left(-D\left(\frac{S}{S_{ult}}\right)^p n\right) \tag{4.5}$$

where b_f, D, and p are fitting constants and S_{ult} is the ultimate strength of the laminate.

The next step is to evaluate the fitting parameters C, α, β, b_f, D, and p. To do so we make use of the strip gage data. We attempt to fit the measured strain distributions after 100, 10000, and 100000 cycles of fatigue at the two stress levels to those predicted by the anisotropic plate solution using reduced off-axis stiffness values and an effective hole size. These fits are accomplished in a least-squares sense by comparing the predicted average strain across each gage to the measured values, as well as comparing the calculated total load supported by the section to the global applied load (the equilibrium condition). This results in an effective hole size and reduced values for the off-axis stiffnesses for each loading condition. These values are then fit to the forms given in Equations (4.4) and (4.5). The fitting parameters are subject to two constraints: at no point is the stiffness allowed to increase as a function of applied cycles nor is the effective hole size allowed to decrease at any point. The results of such a fitting process are compared to the experimental data for each of the different number of cycles and applied stress level in Figures 4.9-4.14. The agreement in most cases is good, with the greatest discrepancy occurring for the 10000 cycle data at 87.5% of ultimate strength. Although this process is far from ideal, it possible to obtain useful estimates of the stress distribution around the hole at any point in the life of the specimen.

Now we address the problem of reduction of residual strength due to the accumulation of fiber fractures. To calculate these changes in remaining strength, we shall make use of the analysis presented in the previous chapter. First, for a given applied fatigue load, we use Equations (4.2), (4.4), and (4.5) along with CLT and the Lekhnitskii solution to calculate the average stress state in the 0° plies. Next we apply

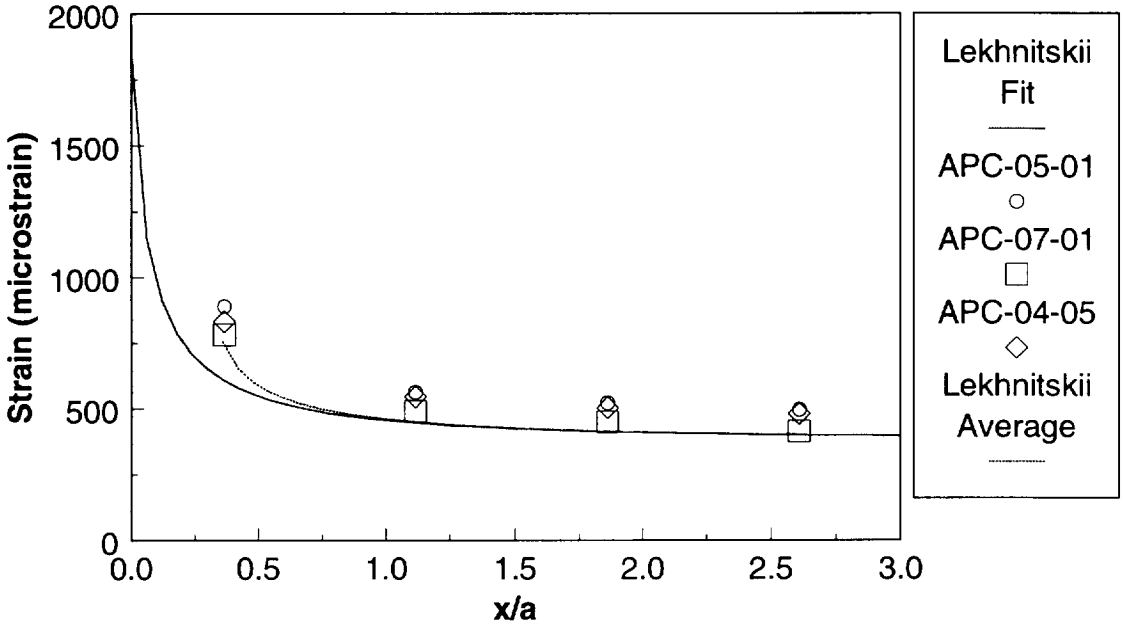

Figure 4.9. Comparison between the strip-strain gage measurements and the predictions based on the effective hole size for specimens fatigued 100 cycles at 80% of the ultimate strength.

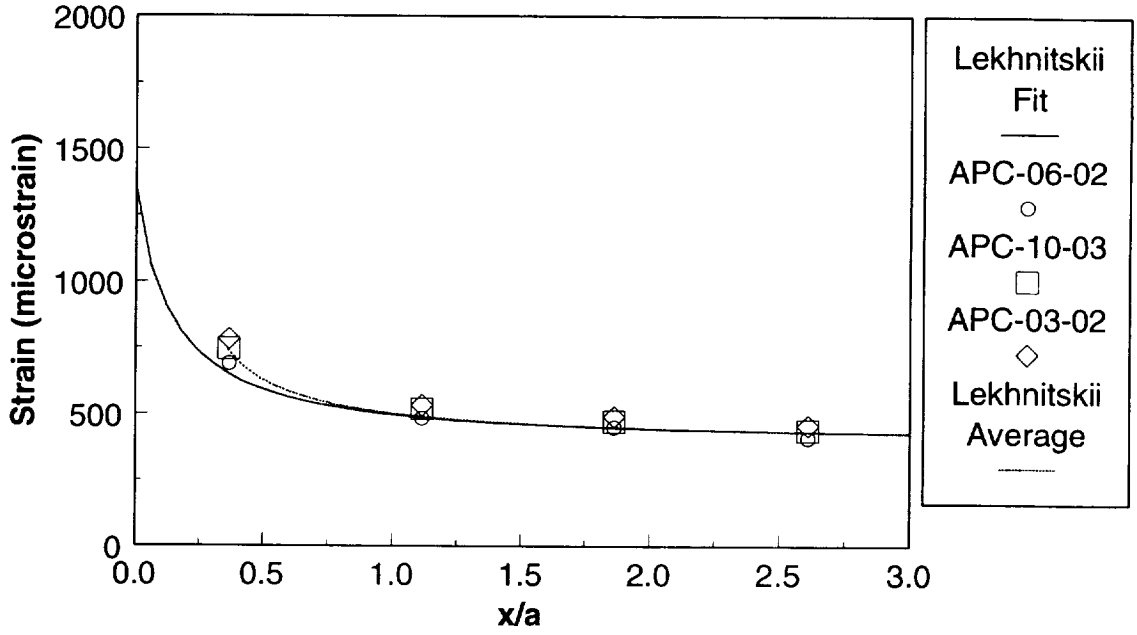

Figure 4.10. Comparison between the strip-strain gage measurements and the predictions based on the effective hole size for specimens fatigued 10000 cycles at 80% of the ultimate strength.

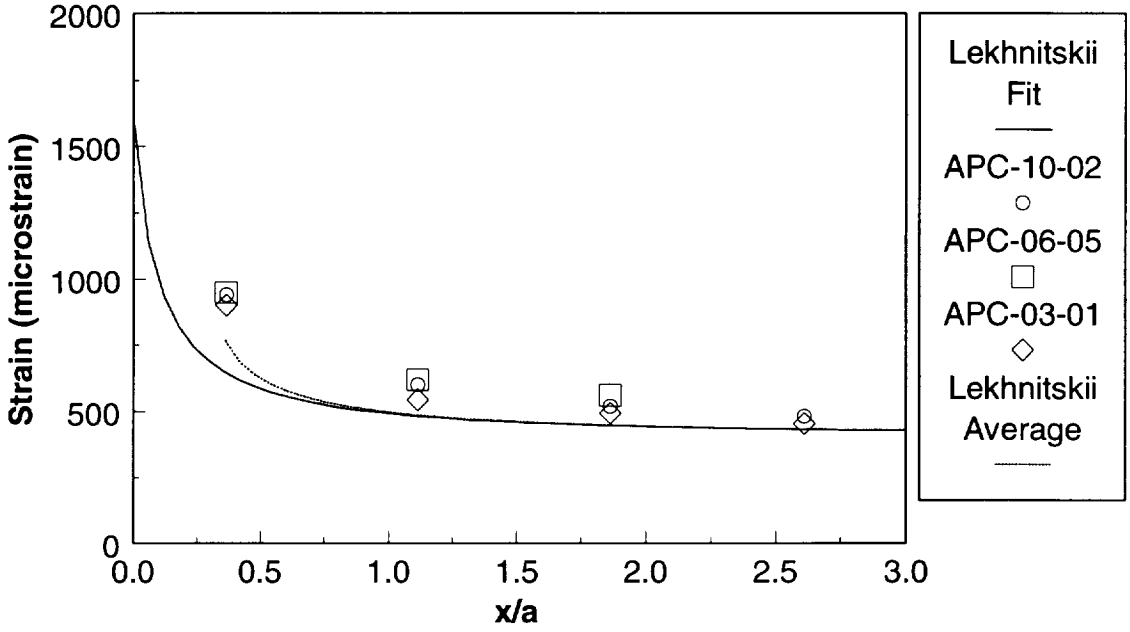

Figure 4.11. Comparison between the strip-strain gage measurements and the predictions based on the effective hole size for specimens fatigued 100000 cycles at 80% of the ultimate strength.

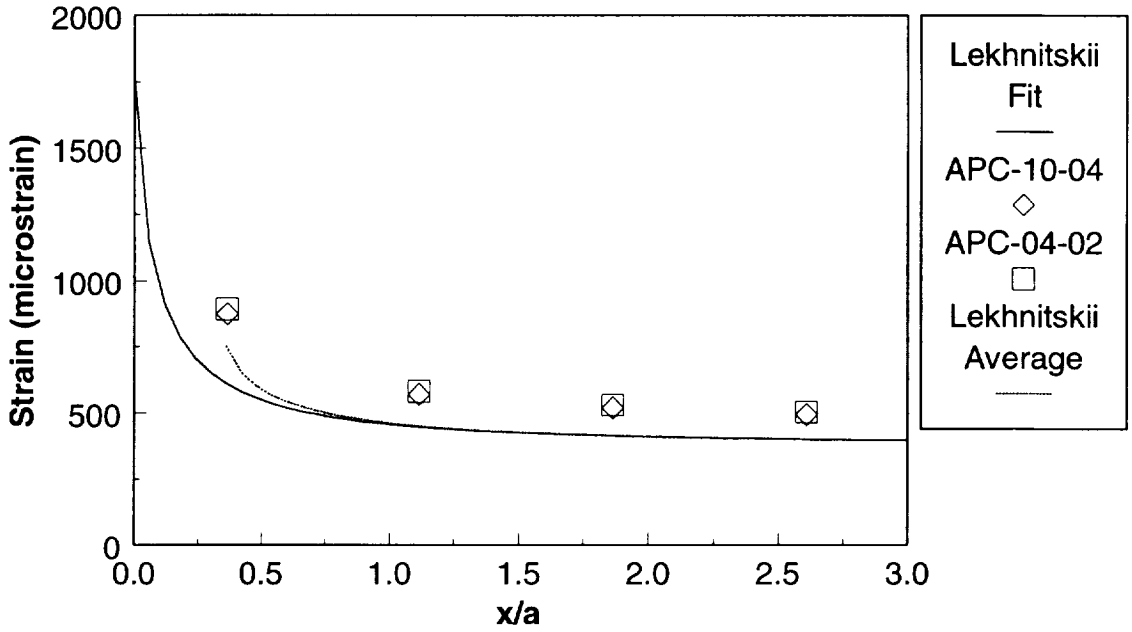

Figure 4.12. Comparison between the strip-strain gage measurements and the predictions based on the effective hole size for specimens fatigued 100 cycles at 87.5% of the ultimate strength.

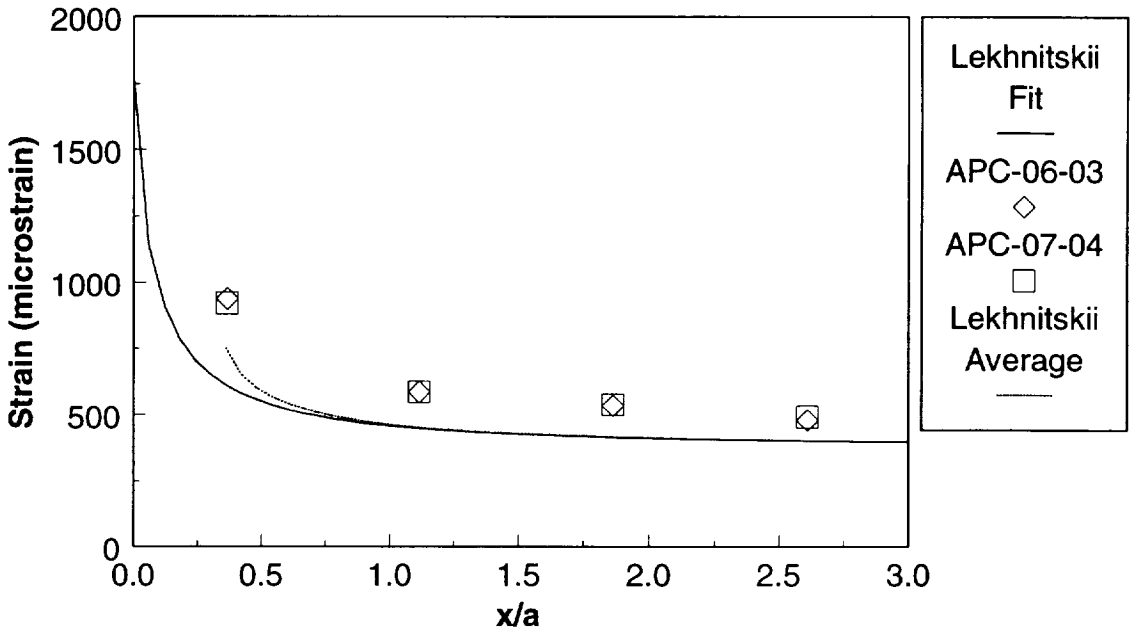

Figure 4.13. Comparison between the strip-strain gage measurements and the predictions based on the effective hole size for specimens fatigued 10000 cycles at 87.5% of the ultimate strength.

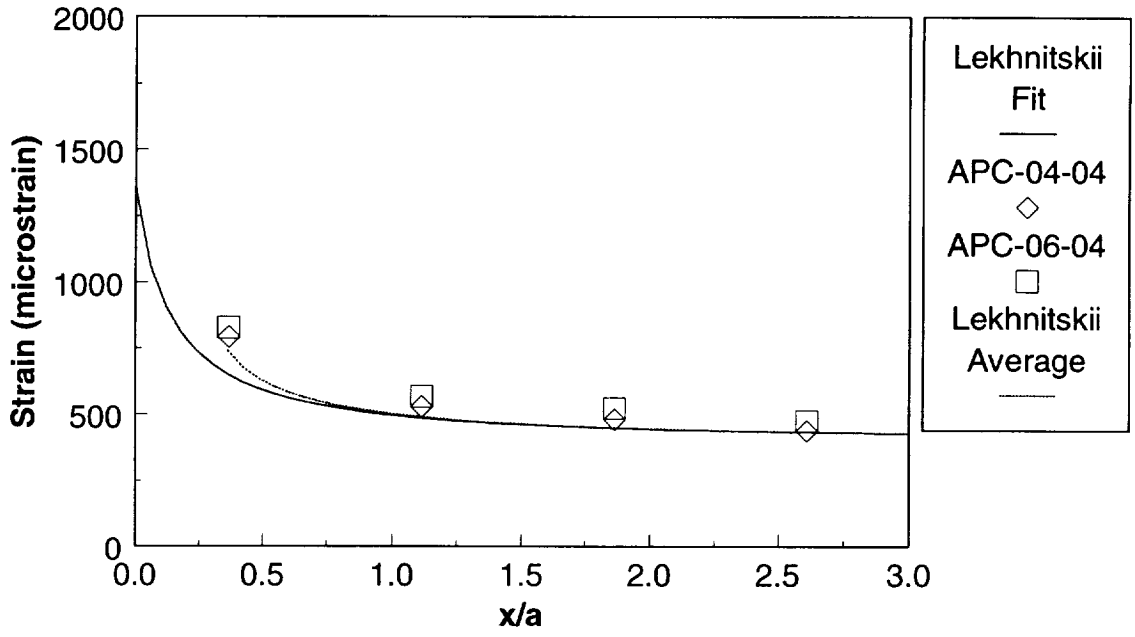

Figure 4.14. Comparison between the strip-strain gage measurements and the predictions based on the effective hole size for specimens fatigued 100000 cycles at 87.5% of the ultimate strength.

a maximum stress failure criterion, so that our failure function, Fa, is given by

$$Fa = \frac{\overline{\sigma}_{11}^{0^\circ}}{X_t} \tag{4.6}$$

Our normalized characteristic time, τ, for the fatigue process is given by

$$\tau = \frac{n}{N(Fa)} \tag{4.7}$$

where N may be determined by

$$N = 10^{\left(\frac{Fa - A_n}{B_n}\right)} \tag{4.8}$$

and the constants A_n and B_n for this material are given in Equation (3.18). Equations (4.6)-(4.8) may be substituted into Equation (3.11) to calculate the remaining strength of the critical element at any point during the life of the laminate. Ultimate failure of the laminate is predicted at the point which the normalized remaining strength of the critical element is equal to the value of the failure function in the critical element.

There is one final step required to relate the remaining strength of the critical element to the remaining strength of the laminate, S_r. This step is necessary to account for the redistribution of stresses within our representative volume element. To determine the remaining strength of the laminate (the value that could be measured experimentally) at any point during its lifetime from the remaining strength of the critical element, we use the following procedure. First we apply a unit stress to the laminate. Next, we apply Equation (4.6) to calculate the failure function at this point in the lifetime of the laminate. The remaining strength of the laminate is then given by

$$S_r(n) = \frac{Fr(n)}{Fa(n)\big|_{unit\ stress}} \tag{4.9}$$

This approach is correct so long as the failure function varies linear linearly with the applied stress (as is true for the maximum stress failure function).

The results of such a prediction, along with the experimental data, are shown in Figure 4.15. There are many interesting trends exhibited due to the three effects which determine the remaining strength of the laminate. If we first consider the prediction at for the loading at 80% of the ultimate strength we can understand these effects better. When the fatigue load is first applied, we begin to develop matrix cracks which reduce the stiffness of the off-axis plies and transfer load to the 0° plies. In addition, we begin to accumulate fiber fractures in the 0° plies. These two effects work together to decrease the strength of the laminate. At the same time, the development of the longitudinal splits works to reduce the stress in the 0° plies for a given applied laminate stress, thereby increasing the laminate strength. The combined effect is to produce the result seen in Figure 4.15—an initial decrease in remaining strength followed by a continuing increase in remaining strength.

For the case of loading at 87.5% of the ultimate strength, the behavior is even more complicated. For this situation, we see an initial decrease in remaining strength, followed by an increase, followed by a decrease, and then a subsequent increase in remaining strength. This complicated behavior is due to the events which control the remaining strength of the laminate all occurring at different rates.

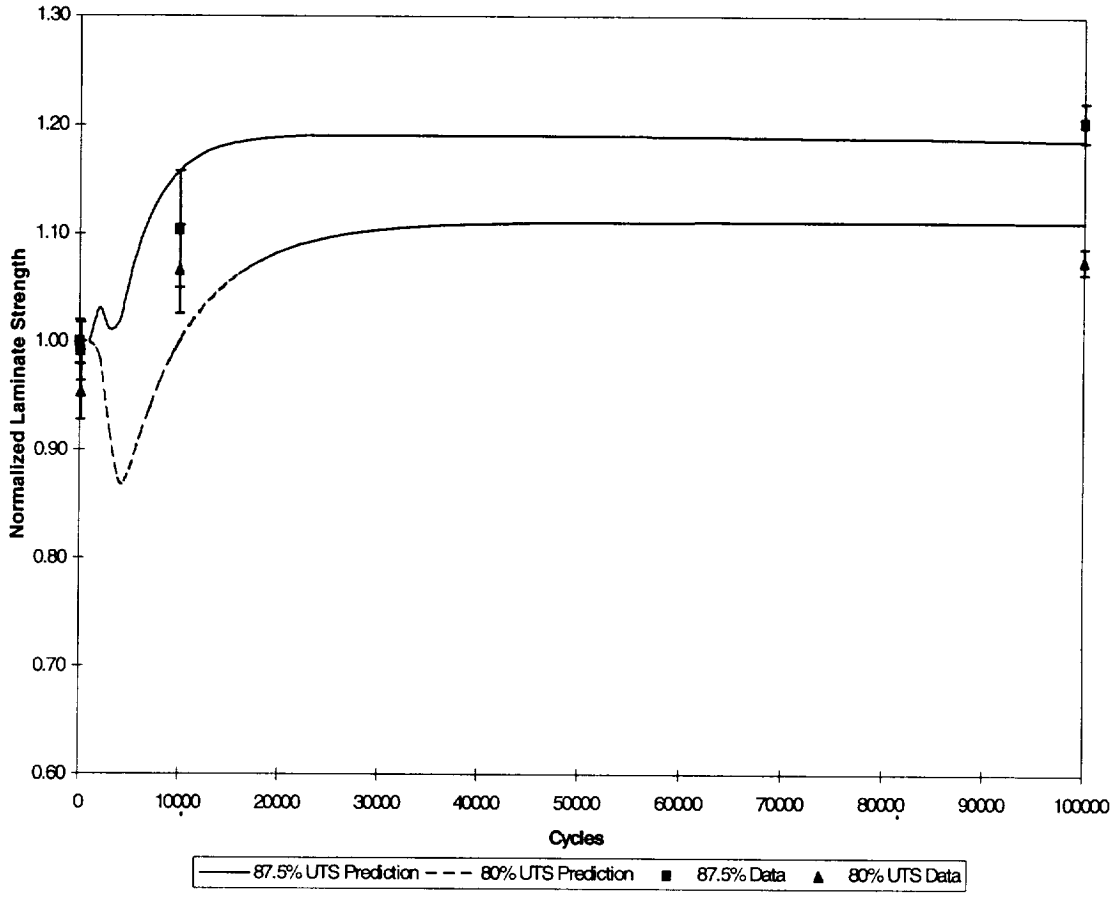

Figure 4.15. Comparison between predicted and measured remaining strength of cross-ply APC-2 laminates as a function of number of cycles.

5. Room Temperature and Elevated Temperature Characterization of IM7/K3B

All of the specimens used in this chapter consisted of IM7/K3B supplied by NASA Langley Research center. For purposes of discussion the material will be divided into three categories, or phases. The Phase I material was used for initial quasi-static baseline mechanical characterization. These specimens were of three different lay-ups ($[0]_{12}$, $[90]_{12}$, and $[\pm45]_{3s}$) and were designated for room temperature testing and for testing at 350°F (177°C). All Phase I specimens were tested in the dimensions supplied with the exception of the $[0]_{12}$ specimens designated for testing at 350°F (177°C). These specimens were supplied as 1" (2.54 cm) wide coupons, but were cut in half for ease of testing. This resulted in specimens having a nominal width of 0.48" (1.2 cm). The Phase II material consisted of $[0/\pm45]_{2s}$ specimens containing a 0.25" (0.635 cm) diameter center hole. These specimens were designated for baseline fatigue testing at room temperature and 350°F (177°C). The Phase III material was supplied in the form of a 12" X 24" (30.5 cm 61.0 cm) panel having a $[-45/0/45/90]_{2s}$ stacking sequence, which was subsequently cut into forty specimens. The nominal dimensions for all of the specimen types are given in Table 5.1.

After the material arrived at Virginia Tech, each of the specimens was ultrasonically C-scanned to determine its integrity. All specimens were determined to be defect free (within the limits of the technique) with the exception of a number of the $[0/\pm45]_{2s}$ specimens. Imperfections were noted in the C-scans and were also visible on the specimen surface. However, due to a shortage of material, these specimens were tested. Subsequent to the ultrasonic C-scan, the specimens were placed in an oven and allowed to soak for 120 hours at 120°C. The specimens were then allowed to cool to room temperature at a rate of 0.1°C per minute before being removed from the oven. This process was intended to serve two

Table 5.1. Nominal specimen dimensions for IM7/K3B material.

	Lay-Up	Room Temperature Specimens	Elevated Temperature (350°F—177°C) Specimens
Phase I Specimens	$[0]_{12}$	0.5" x 6.0" (12.7 mm x 152 mm)	0.48" x 8.0" (12.2 mm x 203 mm)
	$[90]_{12}$	1.0" x 6.0" (25.4 mm x 152 mm)	1.0" x 8.0" (25.4 mm x 203 mm)
	$[\pm 45]_{3s}$	0.5" x 6.0" (12.7 mm x 152 mm)	1.0" x 8.0" (25.4 mm x 203 mm)
Phase II Specimens	Notched $[0/\pm 45]_{2s}$	1.5" x 6.0" (38.1 mm x 152 mm) 0.25" (6.35 mm) Diameter Center Hole	1.5" x 8.0" (38.1 mm x 203 mm) 0.25" (6.35 mm) Diameter Center Hole
Phase III Specimens	Unnotched $[45/0/-45/90]_{2s}$	1.0" x 6.0" (25.4 mm x 152 mm)	1.0" x 6.0" (25.4 mm x 152 mm)
	Notched $[45/0/-45/90]_{2s}$	1.0" x 6.0" (25.4 mm x 152 mm) 0.25" (6.35 mm) Diameter Center Hole	1.0" x 6.0" (25.4 mm x 152 mm) 0.25" (6.35 mm) Diameter Center Hole

purposes: to remove any moisture that might have been absorbed during the C-scanning process and also to give the specimens as nearly an identical thermal history as possible.

5.1 Phase I Testing

5.1.1 Room Temperature Testing

5.1.1.1 Unnotched $[0]_{12}$ Specimens

These specimens were used to obtain 0° tensile strength (X_t) and stiffness (E_{11}) values at room temperature. End tabs—1.5" (38.1mm) long, 0.5" (12.7 mm) wide, and 0.1" (2.5mm) thick—formed from high-pressure glass/epoxy cross-plied laminates, were adhered to each specimen using 3M Scotch-Weld DP-420 (a high toughness, high peel and shear strength) adhesive. Prior to the bonding, the end tabs were sandblasted and the specimen ends were lightly sanded using 400 grit sandpaper to promote adhesion. A bondline of 0.007" (0.18 mm) was maintained by placing enameled wires in the adhesive. The adhesive was then cured at 50°C for 2 hours. After removing the specimens from the oven, one strain gage (Micro-Measurements CEA-06-250UN-350) was applied to each face of the specimen and was aligned with the loading axis using Micro-Measurements M-Bond 200 adhesive. All of the room temperature 0° tensile tests were performed in a 20 kip, electro-hydraulic, servo-controlled load frame with hydraulic wedge grips. To ensure that the gage length remained constant during from one specimen to the next, a number of controls were employed. First of all, a marks was made on each specimen edge 1.25" (31.8 mm) from the tabbed end of the specimen using a lead pencil. Then a second mark was made on the specimen 3.5" (88.9 mm) from the first mark. The specimen was then aligned in the load frame using a bead level so that the axis of loading corresponded with the specimen axis. Each of the pencil marks was aligned with the end of the grips, providing what was hoped to be a 3.5" (88.9 mm) gage section for each specimen. This was verified by using the LVDT readout of the load frame which had been zeroed at the gage length of the first specimen. In all cases, the LVDT readout was less than 0.05" (1.27 mm) when the specimen was gripped using a grip pressure of 1200 psi. The specimens were then

loaded to failure in a load-controlled test at a loading rate of 400 pounds per second. This relatively high rate of loading (corresponding to a stress rate of approximately 13 ksi per second) was chosen for two reasons. First of all, the material properties were to ultimately be used as inputs for the modeling of the 10 Hz fatigue behavior of laminated materials. Secondly, it was desirable to be able to make comparisons between the material behavior at room temperature and at the elevated temperature of 350°F (177°C), where viscoelastic effects could become important. The rate of loading chosen was selected to achieve specimen failures within approximately 30 seconds of initial loading.

During the test, the load and stroke signal outputs from the load frame as well as the two strain gage outputs were monitored using a computer controlled data acquisition system. Data were collected at a rate of 10 samples per channel per second. These data were saved as raw voltages for subsequent analysis by a spreadsheet. A regression analysis was performed on the resulting stress strain curves (one curve for each gage) up to a strain level of 0.5%. The peak detector on the load frame's digital display was used to capture the highest load achieved by the specimen during the test. This value was converted to a peak stress, which allowed the material strength to be well characterized.

5.1.1.2 Unnotched $[90]_{12}$ Specimens

These specimens were used to obtain 90° tensile strength (Y_t) and stiffness (E_{22}) values at room temperature. Specimen preparations were identical to those employed for the room temperature $[0]_{12}$ specimens. The specimens were then placed in the load frame in an identical manner to that described in the previous section, except that the grip pressure was 200 psi (the minimum allowed by the machine). The tests were then conducted in load control at a loading rate of 10 pounds per second. This loading rate was chosen for the same reasons detailed in the previous discussion. An identical procedure for data collection and reduction to that described in the previous section was followed.

5.1.1.3 Unnotched $[\pm 45]_{3s}$ Specimens

These specimens were used in an attempt to obtain lamina values for the shear strength (S) and stiffness (G_{12}) values at room temperature. The ASTM standardized method D-3518 [59] contains the following caution: "Although this test method can establish shear stress strain response well into the nonlinear region, the ultimate stress and strain values so obtained should be evaluated with caution." The standard suggests that such a test results in *lower* values for the material shear strength than would be obtained from a tube torsion test. Thus, the results from this test should result in a conservative estimate of the material properties.

An identical tabbing procedure was employed for the $[\pm 45]_{3s}$ specimens as for the $[0]_{12}$ room temperature specimens. Strain gages were applied in a different manner, however. Two gages (Micro-Measurements CEA-06-125UW-350) were adhered to each side of the specimen oriented with the specimen's principal axes (a total of four gages per specimen) using the M-Bond 200 adhesive. The gages were then connected in a bridge configuration as shown in Figure 5.1. When connected in this manner, the bridge output is then proportional γ_{12}, where

$$\gamma_{12} = \varepsilon_x - \varepsilon_y \tag{5.1}$$

and ε_x is the strain experienced by the specimen in the longitudinal direction, and ε_y is the strain experienced by the specimen in the transverse direction. The shear stress, τ_{12}, may then be determined by

$$\tau_{12} = \frac{P}{2wt} \tag{5.2}$$

where P is the applied load, w is the specimen width, and t is the specimen thickness. This wiring configuration has the advantage of being temperature compensated.

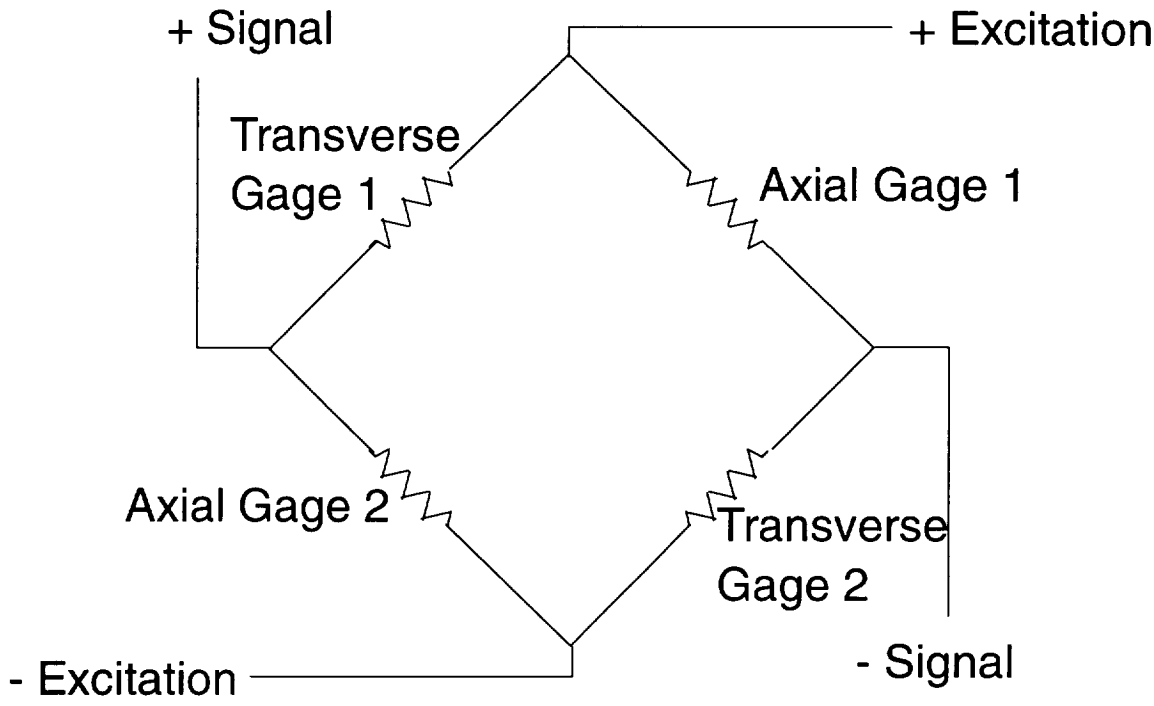

Figure 5.1. Bridge wiring for +/- 45 tensile specimens.

The specimens were placed in the load frame and secured with a grip pressure of 1000 psi. The specimens were then loaded to failure at a rate of 100 pounds per second. An identical procedure for data collection to that described in the section on room temperature testing of $[0]_{12}$ laminates was followed. The data were then analyzed according to Equations (5.1) and (5.2) so that a shear stress versus shear strain curve was obtained. The shear modulus was then calculated from the linear regression of this curve up to a shear strain level of 0.2%.

5.1.2 Elevated Temperature Testing

5.1.2.1 Unnotched $[0]_{12}$ Specimens

These specimens were used to obtain 0° tensile strength (X_t) and stiffness (E_{11}) values at 350°F (177°C). End tabs—1.5" (38.1mm) long, 0.5" (12.7 mm) wide, and 0.1" (2.5mm) thick--formed from high-pressure glass/epoxy cross-plied laminates, were adhered to each specimen using 3M Scotch-Weld DP-420 adhesive, an identical procedure to that used for the $[0]_{12}$ room temperature specimens. Prior to the bonding, the end tabs were sandblasted and the specimen end were lightly sanded using 400 grit sandpaper to promote adhesion. A bondline of 0.007" (0.18 mm) was maintained by placing wires in the bondline. The adhesive was then cured at 50°C for 2 hours. After removing the specimens from the oven, one strain gage (Micro-Measurements WK-06-250BG-350) was applied to each face of the specimen aligned with the loading axis using Micro-Measurements M-Bond 600 adhesive. The adhesive was cured according to the manufacturer's instructions for 2 hours at 120°C. Lead wires were attached to the gages' leads with high-temperature solder. Each of the gages was then wired in a full-bridge configuration and a shunt calibration performed. Temperature compensation was achieved by means of thermal dummies located inside the oven adjacent to the specimen. All of the elevated temperature 0° tensile tests were performed in a 20 kip, electro-hydraulic, servo-controlled load frame with hydraulic wedge grips. The elevated temperature was achieved in a convection oven located between the grips. In initial tests, the specimen temperature was monitored at three locations on the specimen surface well as at

one location in the oven. All readings were found to be within 4°F (2°C) of each other. Therefore, in subsequent tests only the internal oven temperature was monitored. To ensure that the gage length remained constant during from one specimen to the next, the controls used for the room temperature tests were repeated. The specimens were then loaded to failure in a load-controlled test at a loading rate of 400 pounds per second using a grip pressure of 1200 psi (identical to the room temperature tests). Subsequent data analysis was identical to that utilized for the room temperature tests.

5.1.2.2 Unnotched $[90]_{12}$ Specimens

These specimens were used to obtain 90° tensile strength (Y_t) and stiffness (E_{22}) values at elevated temperature. Specimen preparations were identical to those employed for the elevated temperature $[0]_{12}$ specimens with one major exception: no end tabs were used. The decision not to used end tabs was based on two factors. The first was that gage section failures were easily obtained in the room temperature $[90]_{12}$ tests. In addition, it was felt that at the elevated temperature the specimens would be even more likely to fail within the gage section. Sandpaper was placed on the ends of the specimen in a similar manner to that used for the $[0/\pm45]_{2s}$ tests at room temperature. The specimens were then placed in the load frame in an identical manner to that described in the previous section, except that the grip pressure was 200 psi (the minimum allowed by the machine). The tests were then conducted in load control at a loading rate of 10 pounds per second.

5.1.2.3 Unnotched $[\pm45]_{3s}$ Specimens

These specimens were used in an attempt to obtain lamina values for the shear strength (S) and stiffness (G_{12}) values at elevated temperature. Specimens were end tabbed in the manner described previously. A pair of gages (Micro-Measurements WK-06-125TM-350) were adhered to each side of the specimen oriented with the specimen's principal axes (a total of four gages per specimen) using the M-Bond 600 adhesive. The gages were then wired in a bridge configuration in a manner illustrated by Figure 5.1.

The specimens were placed in the load frame and secured with a grip pressure of 1000 psi and then loaded to failure at a rate of 100 pounds per second. An identical procedure for data collection to that described in the section on room temperature testing of $[0]_{12}$ laminates was followed. The data were then analyzed according to Equations (5.1) and (5.2). so that a shear stress versus shear strain curve was obtained. The shear modulus was then calculated from the linear regression of this curve up to a shear strain level of 0.2%.

5.2 Phase II Testing

5.2.1 Room Temperature Testing of Notched $[0/\pm45]_{2s}$ Specimens

5.2.1.1 Quasi-Static Testing

These specimens did not require the end tabs employed in the other room temperature tests. Instead, two layers of 100 grit sandpaper were wrapped lengthwise over each specimen end with the grit side inward. The sandpaper was held in place using a narrow strip of masking tape. In addition, aluminum V-notched extensometer tabs were adhered 1" (2.54 cm) apart, centered with respect to the hole, using as a thin layer of silicone rubber. The knife edges of the extensometer were then placed in the V-notches, and the extensometer secured to the specimen using rubber bands. The strain readings obtained in this manner could then be used in a semi-quantitative manner to monitor damage. The specimens were aligned in the load frame using a level so that 1.25" (3.18 cm) was in each grip and then gripped using a pressure of 2000 psi (14 MPa). The specimens were then loaded to failure at a rate of 500 pounds per second. During the loading process, the load signal, extensometer strain signal, and stroke signal were collected at a rate of 10 points per channel per second. The maximum load experienced by the specimen was determined using the peak detector on the digital display of the load frame.

5.2.1.2 Fatigue Testing

These specimens were prepared in an identical manner to those which were used for quasi-static testing. The fatigue tests were performed in load control at 10 Hz (sinusoidal waveform) with an R-ratio of 0.1. Two fixed percentages of the ultimate strength were employed: 70% and 80%. During the course of these

tests, maximum and minimum values of the load, actuator displacement, an extensometer strain were recorded in an identical manner to that used for the APC-2 fatigue specimens. Initial tests at the two load levels revealed that no failures could be expected within 1000000 cycles; therefore subsequent tests were interrupted for x-ray damage analysis, strip strain gage measurements (conducted in the same manner as those on the APC-2 specimens), and residual strength testing.

5.2.2 Elevated Temperature (350°F—177°C) Testing of Notched $[0/\pm45]_{2s}$ Specimens

5.2.2.1 Quasi-Static Testing

These specimens were prepared in an identical fashion to those used in the room temperature tests with one exception—no extensometer tabs were applied to the specimen (no extensometer measurements were made). The specimens were aligned in the load frame using a level so that 1.25" (3.18 cm) was in each grip and then gripped using a pressure of 2000 psi (14 MPa). The specimens were then loaded to failure at a rate of 500 pounds per second. During the loading process, the load signal and stroke signal were collected at a rate of 10 points per channel per second. The maximum load experienced by the specimen was determined using the peak detector on the digital display of the load frame.

5.2.2.2 Fatigue Testing

These specimens were prepared in an identical manner to those which were used for quasi-static testing. The fatigue tests were performed in load control at 10 Hz (sinusoidal waveform) with an R-ratio of 0.1. Two fixed percentages of the ultimate strength were employed: 70% and 80%. During the course of these tests, maximum and minimum values of the load and actuator displacement were recorded in an identical manner to that used for the room temperature fatigue specimens. Initial tests at the two load levels revealed that no failures could be expected within 250000 cycles; therefore subsequent tests were interrupted for x-ray damage analysis, strip strain gage measurements, and residual strength testing.

5.3 Phase III Testing of Unnotched and Notched $[45/0/-45/90]_{2s}$ Specimens

5.3.1 Quasi-Static Testing

Testing of these specimens proceeded along much the same lines as that of the Phase II specimens. The room temperature specimens were prepared by placing the V-notched extensometer tabs on the surface of the specimen and by securing two layers of 100 grit sandpaper on each end of the specimen with masking tape. The elevated temperature specimens were prepared in an identical fashion with the exception of the extensometer tabs. The specimens were aligned in the load frame so that 1" (2.54 cm) was in each grip and then gripped using a pressure of 1600 psi (11 MPa). The tests were then conducted in load control at a loading rate of 500 pounds per second. Data were recorded using the computer controlled data acquisition system.

5.3.2 Fatigue Testing

The specimens were prepared and gripped in a manner identical to the quasi-static specimens. The fatigue tests were then performed at 10 Hz in load control (R = 0.1) at two fixed percentages of the ultimate strength for each of the specimen types (notched and unnotched). The unnotched specimens were fatigued at 65% and 70% of their ultimate strengths, while the notched specimens were fatigued at 70% and 80% of their ultimate strengths. During the course of the tests, data were recorded in a manner identical to that employed for the Phase II fatigue tests. In addition, real-time measurements were made of the complex dynamic stiffness using a dynamic signal analyzer.

5.4 Experimental Results

5.4.1 Phase I Tests

The results from these tests are summarized in Table 5.2. The discussion which follows will attempt to point out important features which were observed during the course of the experimental investigation.

5.4.1.1 Unnotched $[0]_{12}$ Specimens

Photographs of representative failed room temperature and elevated temperature $[0]_{12}$ specimens are shown in Figure 5.2. In addition, representative stress-strain curves for these specimens at both temperatures are shown in Figure 5.3. One interesting feature of the experimental results for this loading condition is that the measured modulus at the elevated temperature is greater than that which was measured at room temperature. Such behavior is somewhat counter-intuitive. As the temperature is increased, we would expect the matrix stiffness to decrease, and therefore would expect to see a corresponding decrease in the composite stiffness. However, such is not the case. There are three plausible explanations for the behavior. One is that the differences are due solely to the statistical scatter in the data and are not really significant. A second possible explanation is that the differences are due to experimental error, particularly in the strain measurements at elevated temperature (as is evidenced by the increase in the scatter at the elevated temperature). However, every effort was made to minimize such errors, including the use of temperature compensation gages, as well as making use of back-to-back gages on each specimen. The third possible explanation is that the changes in modulus are evidence of some underlying change in the material behavior. There is some (albeit limited) support for such a conclusion—similar behavior has been observed by other researchers at elevated temperature (see, for example, the work of Fisher et al. [60]).

5.4.1.2 Unnotched $[90]_{12}$ Specimens

Photographs of representative failed room temperature and elevated temperature $[90]_{12}$ specimens are shown in Figure 5.4. In addition, representative stress-strain curves for these specimens at both temperatures are shown in Figure 5.5. In the case of these specimens, there were no surprises in the experimental behavior. As the temperature was increased, there was a decrease in the transverse stiffness and strength corresponding to the changes in the matrix properties at these temperatures.

Table 5.2. Results of Phase I tests on IM7/K3B laminates at room temperature and 350 °F (177°C).

Lay-up	Property	Room Temperature	350°F -177°C
$[0]_{12}$	E_{11}^t	24.3±0.3 msi (167±2 GPa)	25.7±1.5 msi (177±10 GPa)
	X_t	392±18 ksi (2700±120 MPa)	324±27 ksi (2230±190 MPa)
	ε_{11}^t	1.46±0.05%	1.13±0.10%
$[90]_{12}$	E_{22}^t	1.38±0.03 msi (9.51±0.18 GPa)	1.27±0.02 msi (8.76±0.14 GPa)
	Y_t	8.64±1.18 ksi (59.6±8.2 MPa)	5.15±0.42 ksi (35.5±2.9 MPa)
	ε_{22}^t	0.622±0.088%	0.408±0.035%
$[\pm 45]_{3s}$	G_{12}	0.721±0.043 msi (4.97±0.30 GPa)	0.610±0.039 msi (4.21±0.27 GPa)
	S	26.4±0.6 ksi (182±5 MPa)	17.1±0.5 ksi (118±4 MPa)

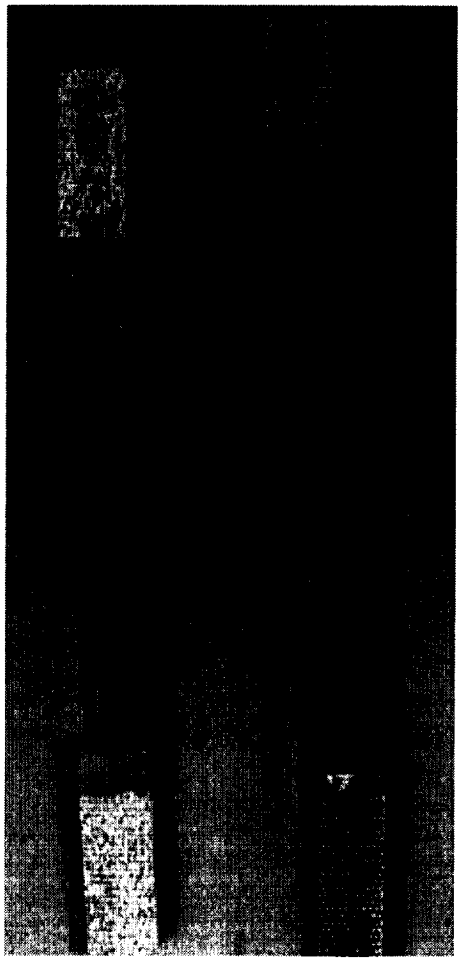

Figure 5.2. Failed $[0]_{12}$ tensile specimens from room temperature (left) and 350°F (177°C) tests (right).

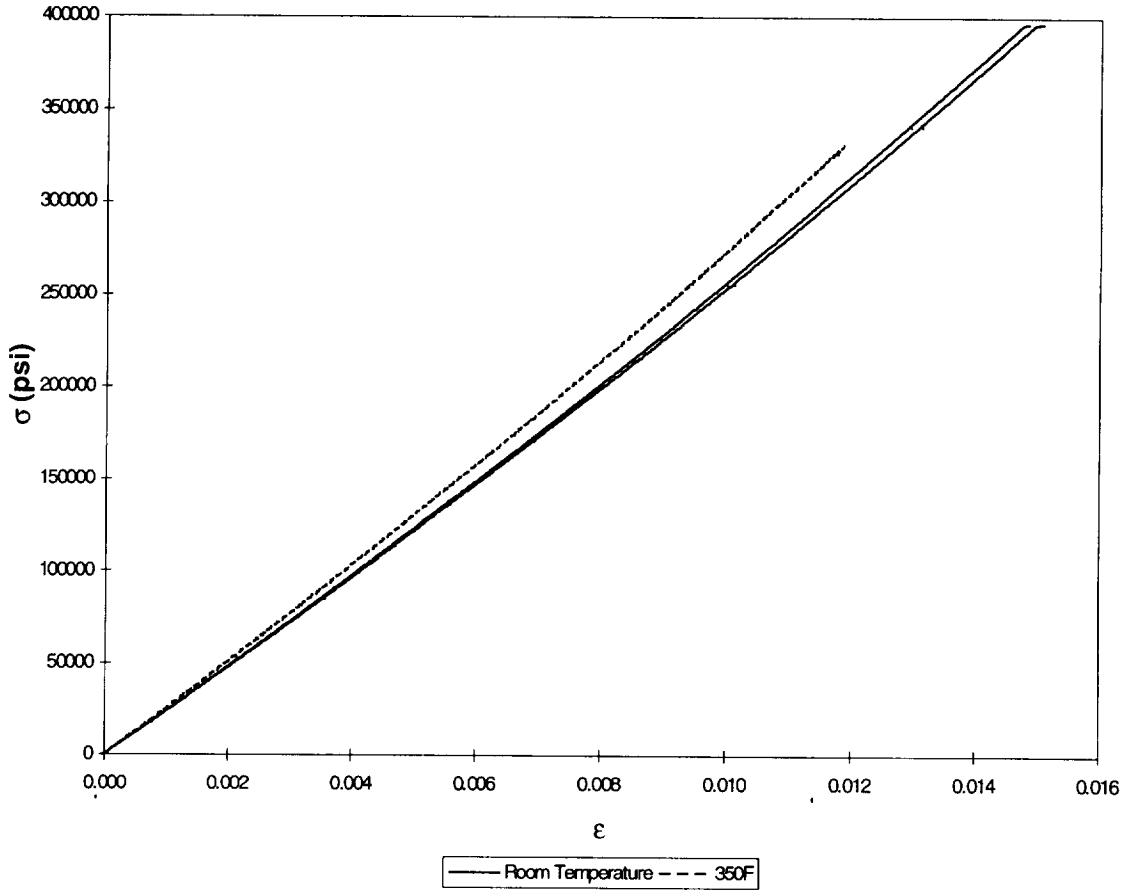

Figure 5.3. Stress-strain curves for $[0]_{12}$ laminates of IM7/K3B at room temperature and 350°F (177°C).

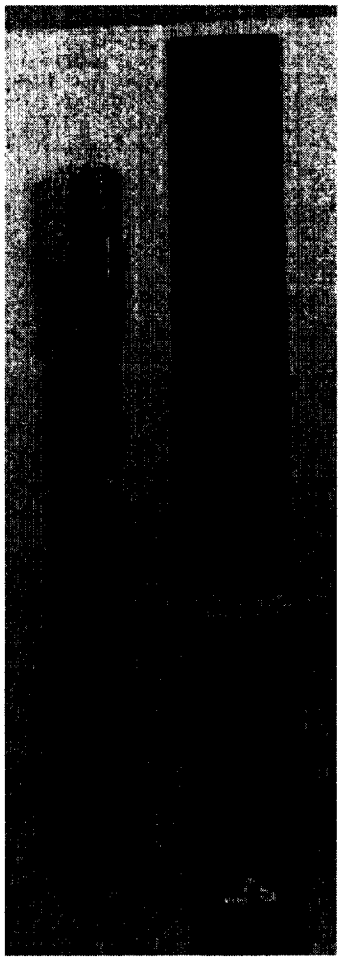

Figure 5.4. Failed $[90]_{12}$ tensile specimens from room temperature (left) and 350°F (177°C) tests (right).

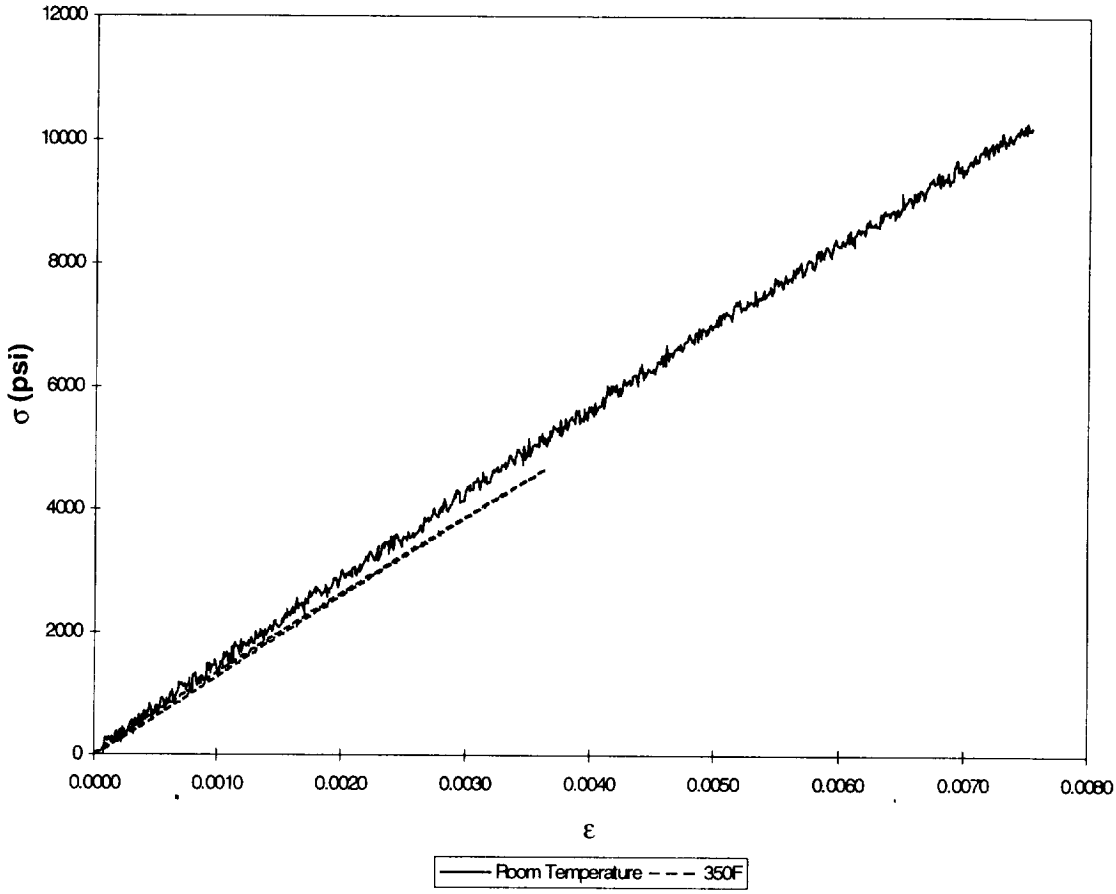

Figure 5.5. Stress-strain curves for $[90]_{12}$ laminates of IM7/K3B at room temperature and 350°F (177°C).

5.4.1.3 Unnotched $[\pm 45]_{3s}$ Specimens

Photographs of representative failed room temperature and elevated temperature $[\pm 45]_{3s}$ specimens are shown in Figure 5.6. These failures were characterized by substantial necking and scissoring, as is to be expected from the test. In addition, representative stress-strain curves for these specimens at both temperatures are shown in Figure 5.7. It was not possible to determine the strain-to-failure of these specimens because failure of the strain gages occurred before final failure of the specimens.

5.4.2 Phase II Tests

5.4.2.1 Quasi-Static Tests

Only two room temperature and two elevated temperature specimens were available for the quasi-static tests. The two strength values obtained for the room temperature specimens were 80.3 ksi (554 MPa) and 75.5 ksi (521 MPa), while the two elevated temperature strength values were 77.0 ksi (531 MPa) and 76.2 ksi (525 MPa). Representative specimens from the room temperature and elevated temperature tests are shown in Figure 5.8. In the case of the elevated temperature specimens, there was a great deal of delamination noted around the hole section for both specimens. This delamination appeared to involve only the surface 0° plies. The stress-strain plots from the room temperature tests are shown in Figure 5.9. The strain information for this plot is based upon the average strain measured across the hole, so it combines material behavior as well as geometry effects. Stress-strain plots for the elevated temperature specimens based upon the stroke measurements are shown in Figure 5.10.

5.4.2.2 Fatigue Tests

Characteristic stiffness curves from the room temperature specimens as a function of number of fatigue cycles and load level based upon the extensometer measurements are shown in Figure 5.11. The stiffness reduction curves from the extensometer are based on strain measurements taken over the hole section. Such measurements include both the effects of the stiffness reduction due to the cracking which occurs in the off-axis plies, as well as geometry effects in a local region. Stiffness reductions based upon the stroke

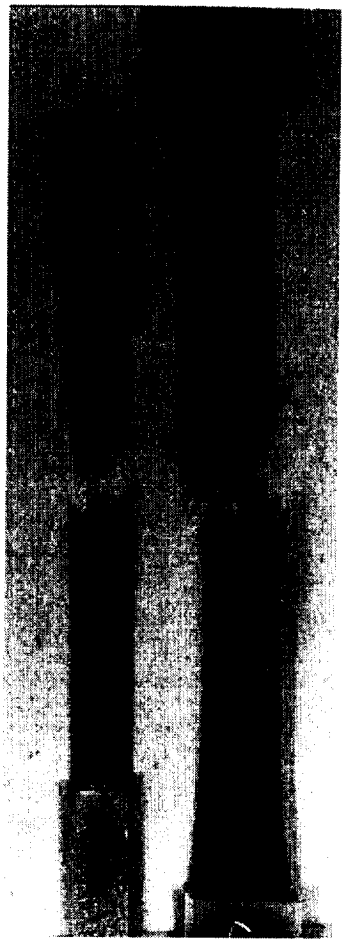

Figure 5.6. Failed $[\pm 45]_{3s}$ tensile specimens from room temperature (left) and 350°F (177°C) tests (right).

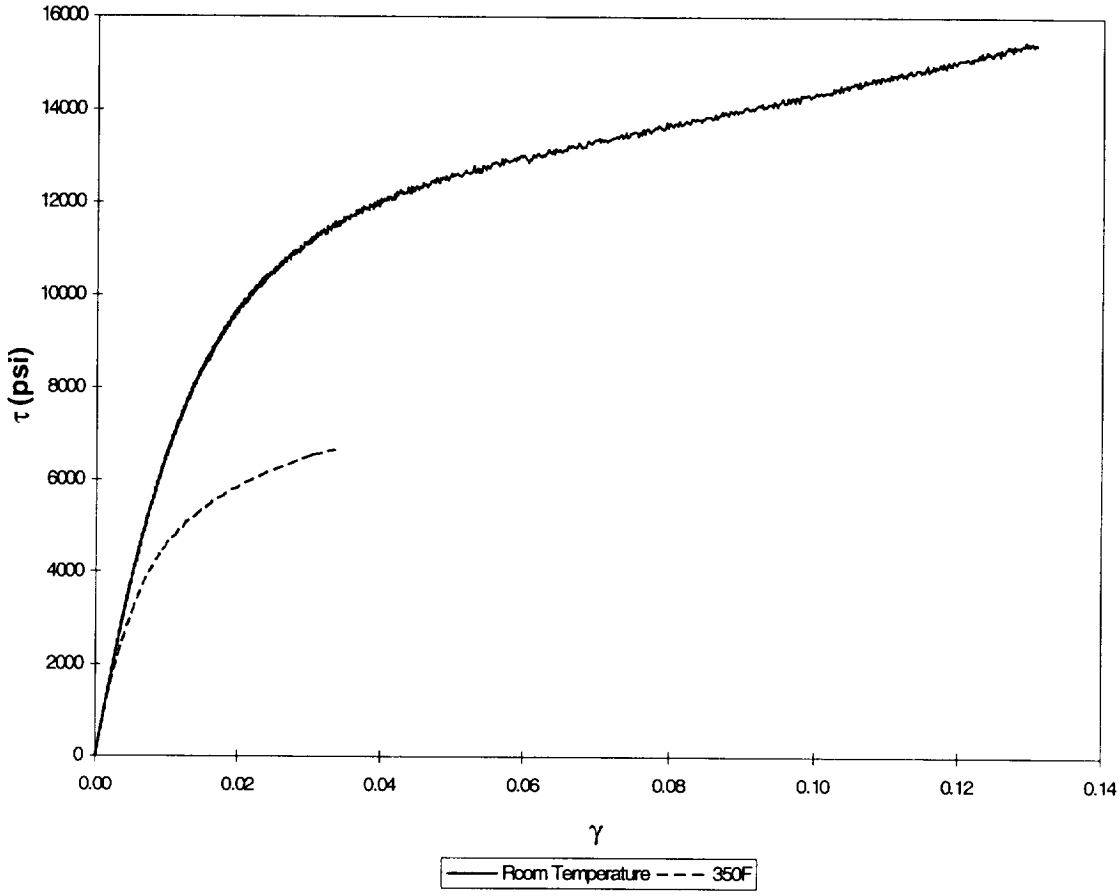

Figure 5.7. Shear stress-shear strain curves for $[\pm 45]_{3s}$ laminates of IM7/K3B at room temperature and 350°F (177°C).

Specimen failure does not occur at the final strain point shown in the plots.

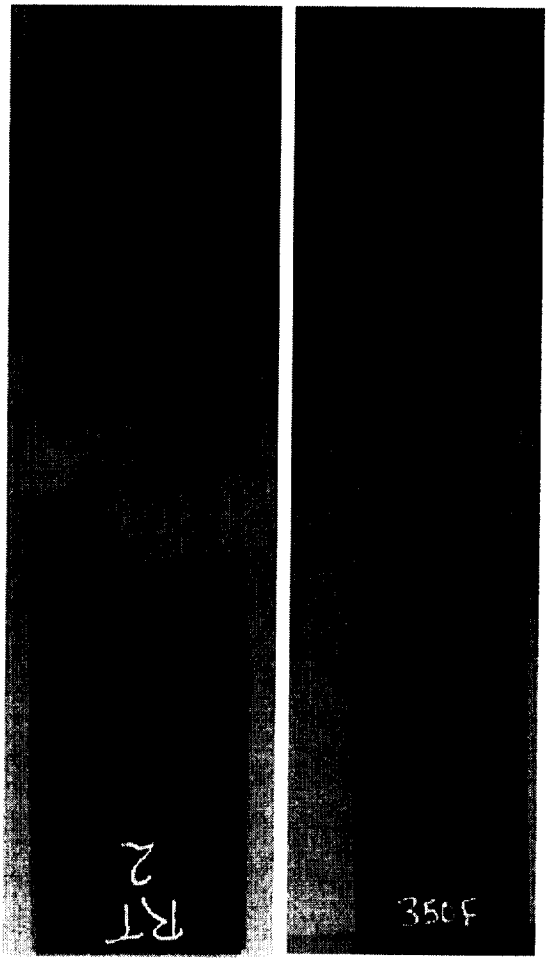

Figure 5.8. Failed notched $[0/\pm45]_{2s}$ tensile specimens from room temperature (left) and 350°F (177°C) (right) tests.

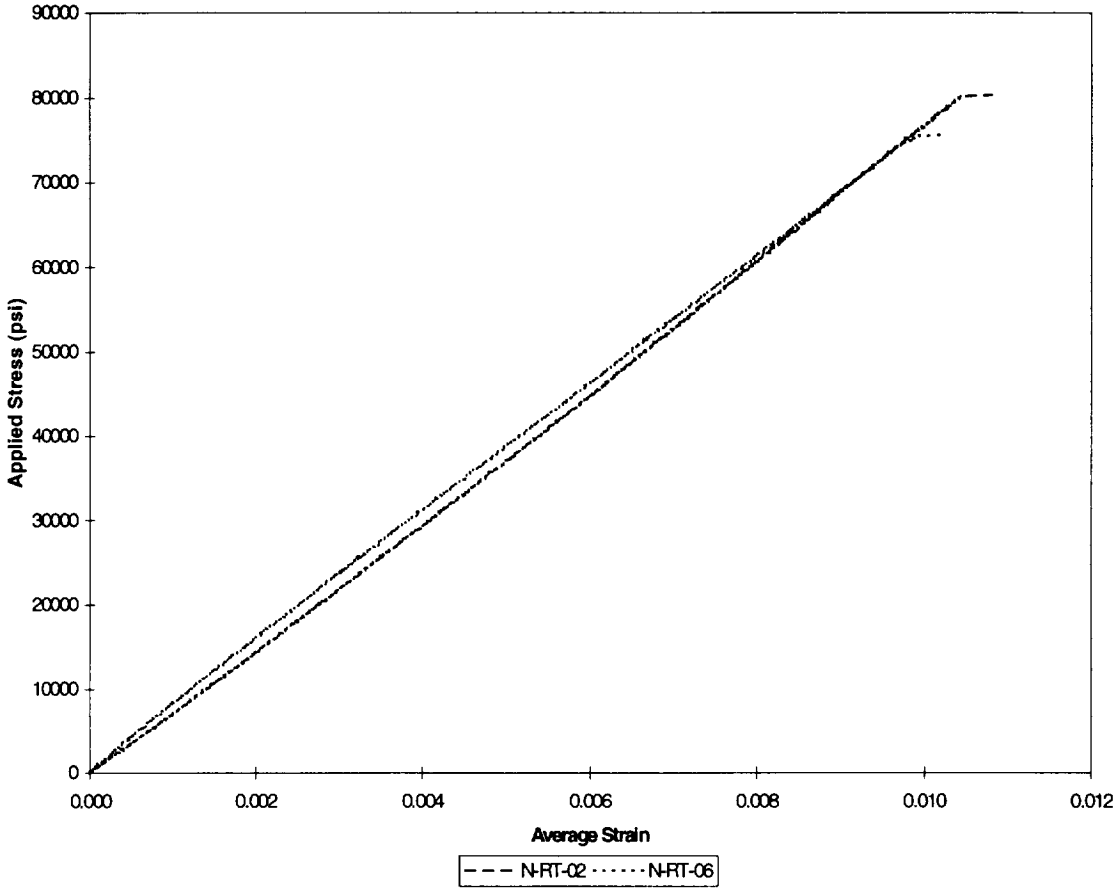

Figure 5.9. Stress-strain curves based on extensometer measurements for room temperature $[0/\pm45]_{2s}$ IM7/K3B laminates containing a center hole.

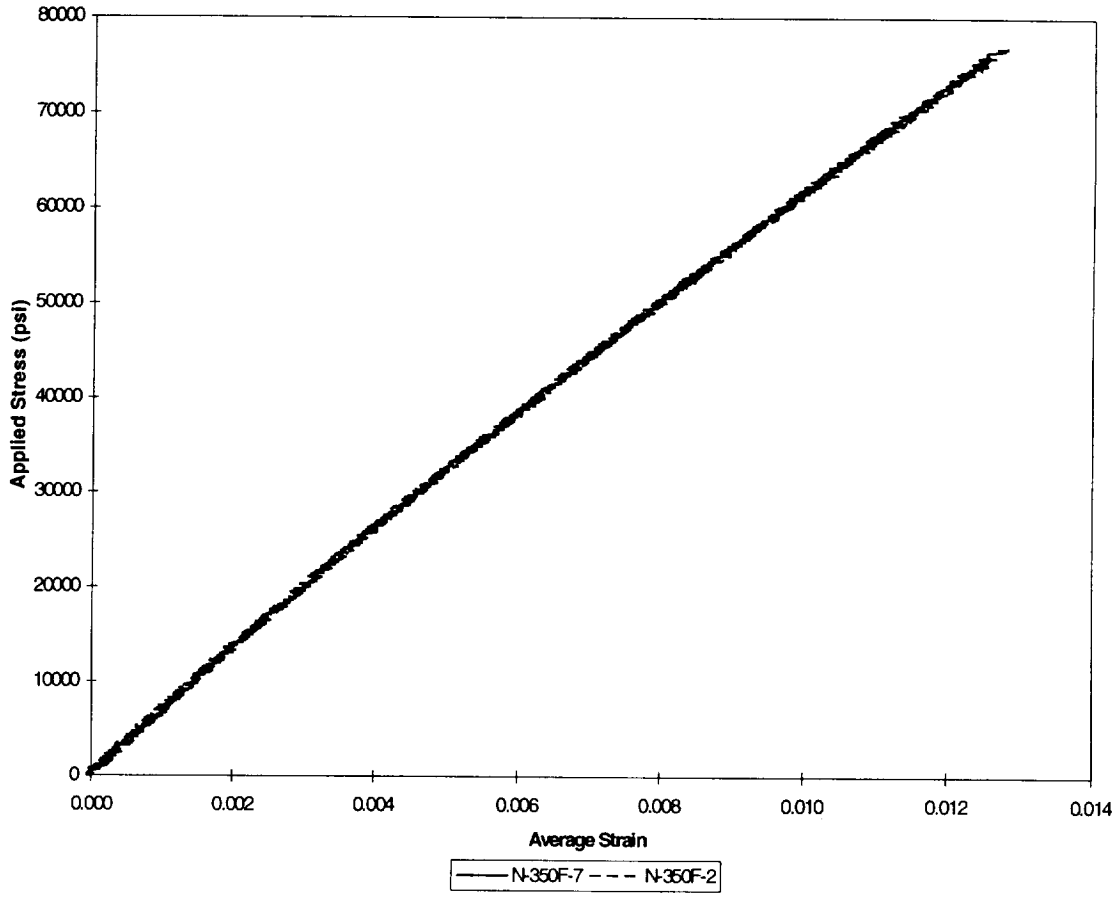

Figure 5.10. Stress-strain curves based on stroke measurements at 350°F (177°C) for $[0/\pm45]_{2s}$ IM7/K3B laminates containing a center hole.

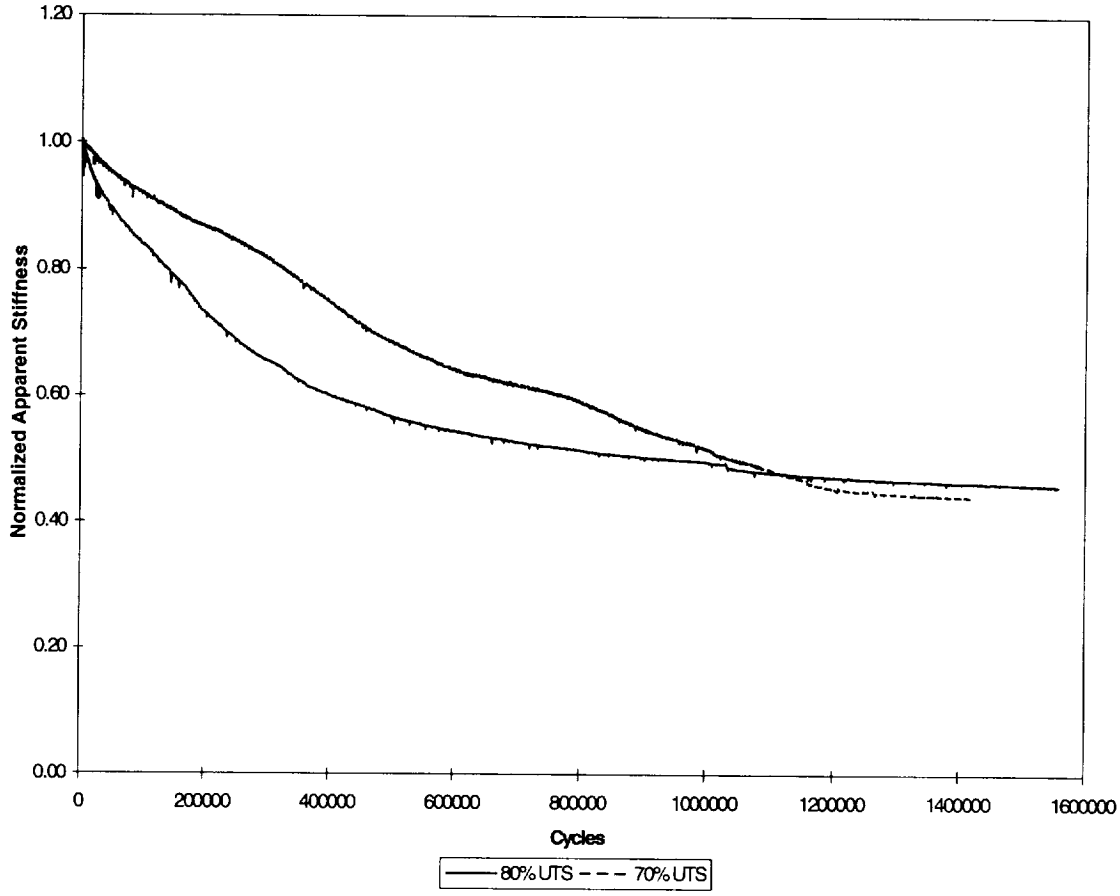

Figure 5.11. Fatigue stiffness reduction curves based on extensometer measurements at room temperature for $[0/\pm45]_{2s}$ IM7/K3B laminates containing a center hole.

measurements for the room temperature tests are shown in Figure 5.12. These stiffness reductions based upon the stroke measurements give a integrated material response over the gage section (3.5 inches—8.9 cm). Representative stiffness reduction curves for the specimens tests at 350°F (177°C) are shown in Figure 5.13, based upon the stroke measurements made over a gage length of 4.5 inches (11.4 cm). Both the room temperature and elevated temperature specimens were characterized by delamination of the surface 0° plies above the hole section, parallel to the axis of the applied load.

5.4.2.3 Penetrant Enhanced Radiography

This method proved to be a useful means of identical the processes of damage development during the fatigue process. Radiographs of the specimens fatigued at room temperature at 70% and 80% of ultimate tensile strength are shown in Figure 5.14 and Figure 5.15, respectively. If we first consider the radiographs of the specimens fatigued at 70% of ultimate strength, we notice that the damage development begins with the matrix cracks in the ±45° degree plies around the hole. In addition, the specimen which has been fatigued 10000 cycles at this load level has begun to develop the delaminations of the 0° plies above the hole section. This delamination continues to grow as the number of cycles increases, until it passes the location of the extensometer tabs. The pattern for the specimens fatigued at 80% of ultimate strength is similar, although the rate of development of the matrix cracking and the rate of delamination growth is greater.

Radiographs of the specimens fatigued at 350°F (177°C) at 70% and 80% of ultimate tensile strength are shown in Figure 5.16 and Figure 5.17, respectively. These radiographs show a similar pattern of damage development to that observed in the room temperature specimens, although the rates of development of the matrix cracking and the delaminations are greater.

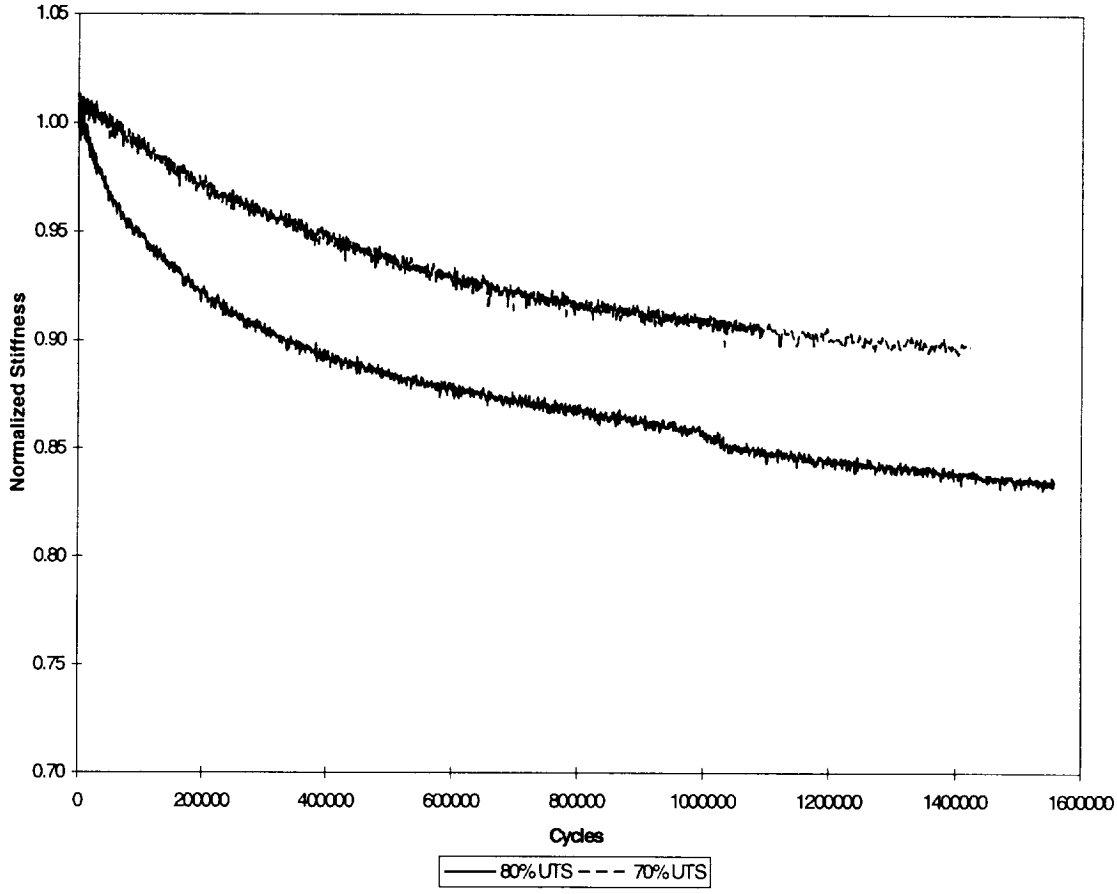

Figure 5.12. Fatigue stiffness reduction curves based on stroke measurements at room temperature for $[0/\pm45]_{2s}$ IM7/K3B laminates containing a center hole.

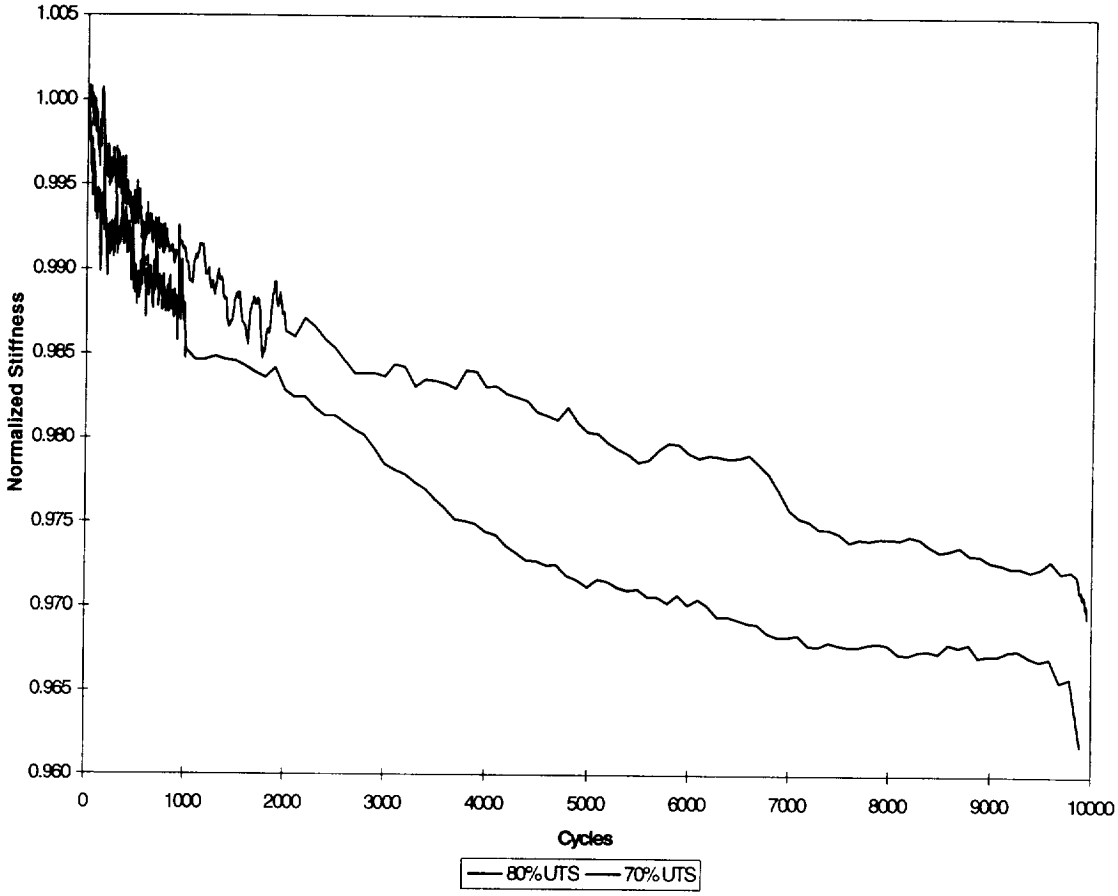

Figure 5.13. Fatigue stiffness reduction curves based on stroke measurements at 350°F (177°C) for $[0/\pm45]_{2s}$ IM7/K3B laminates containing a center hole.

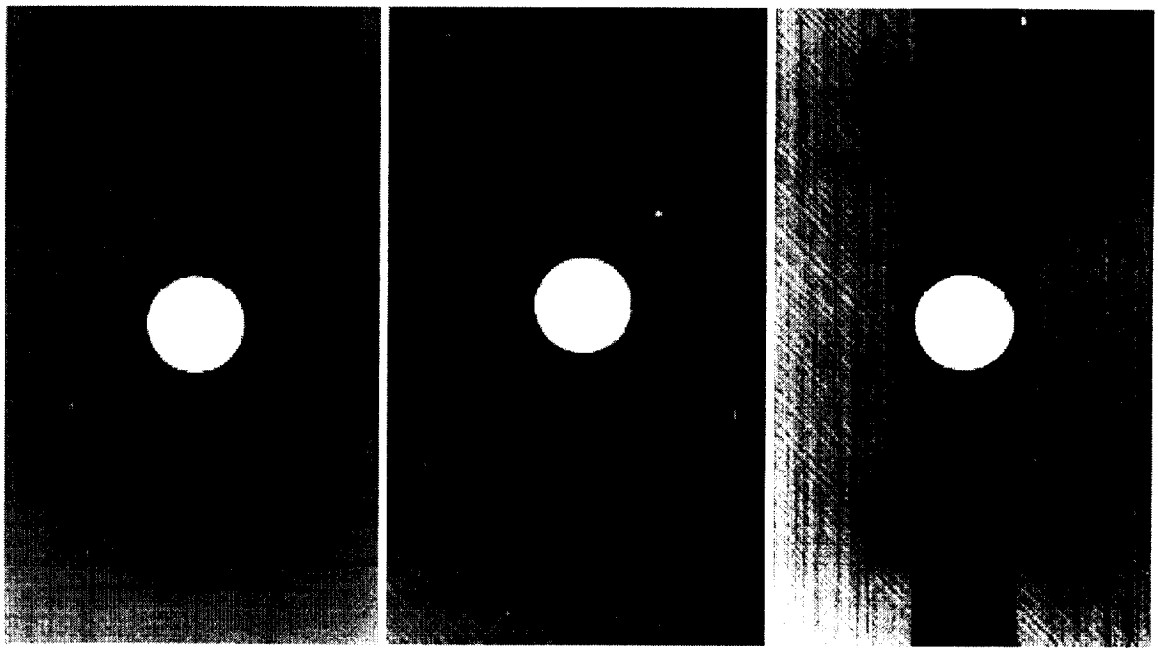

Figure 5.14. Penetrant-enhanced radiographs of $[0/\pm45]_{2s}$ laminates of IM7/K3B fatigued at room temperature at 70% of ultimate tensile strength after 10000 cycles (left), 260000 cycles (center) and 1430515 cycles (right).

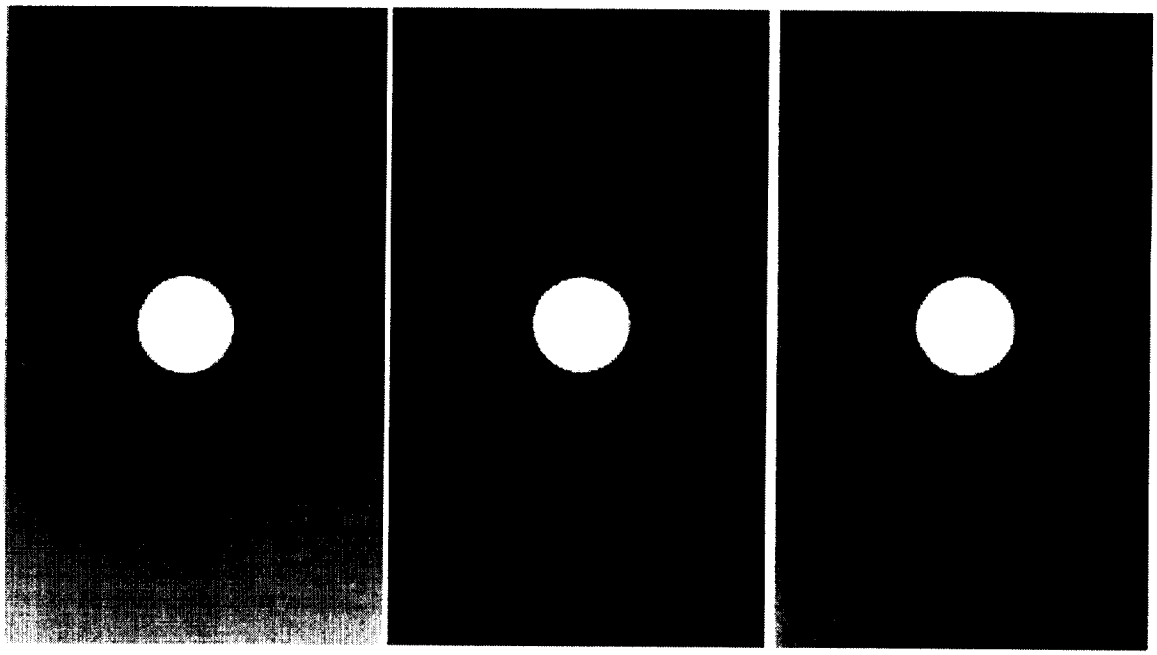

Figure 5.15. Penetrant-enhanced radiographs of $[0/\pm45]_{2s}$ laminates of IM7/K3B fatigued at room temperature at 80% of ultimate tensile strength after 10000 cycles (left), 280000 cycles (center) and 1560401 cycles (right).

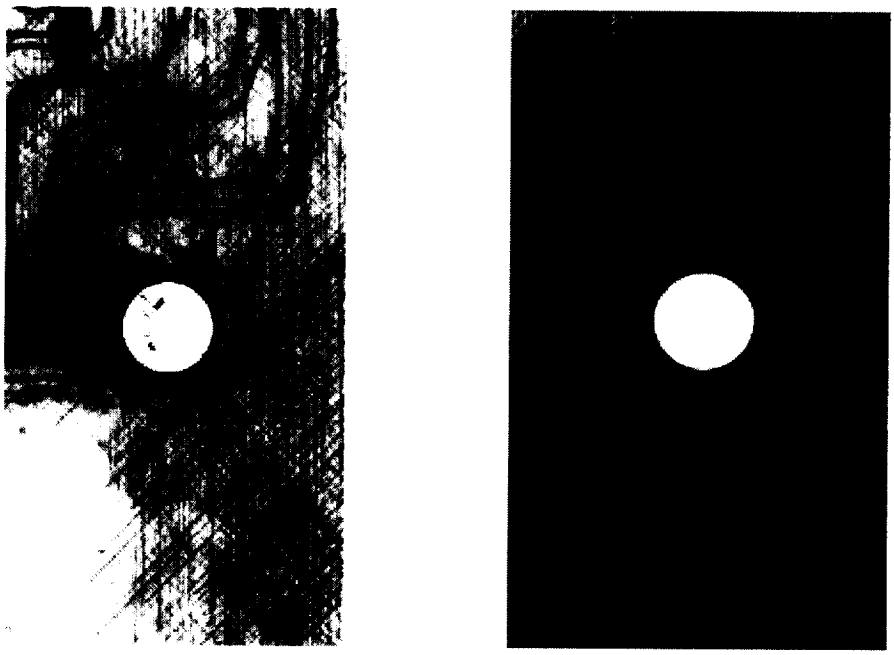

Figure 5.16. Penetrant-enhanced radiographs of $[0/\pm45]_{2s}$ laminates of IM7/K3B fatigued at 350°F (177°C) at 70% of ultimate tensile strength after 10000 cycles (left) and 224500 cycles (right).

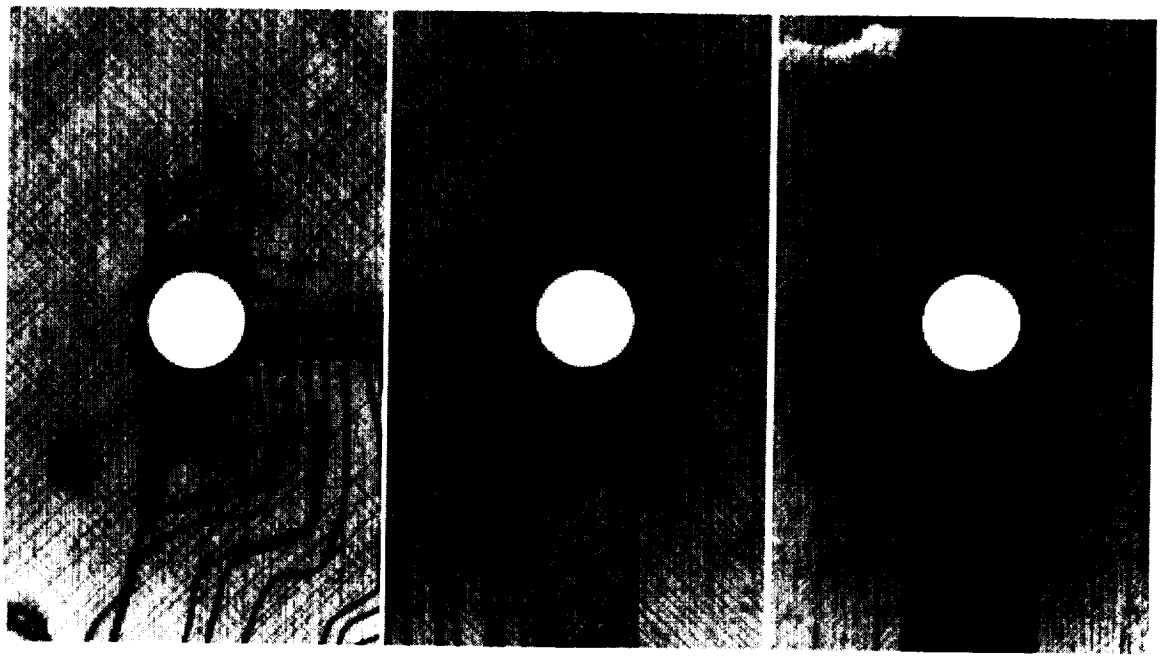

Figure 5.17. Penetrant-enhanced radiographs of $[0/\pm45]_{2s}$ laminates of IM7/K3B fatigued at 350°F (177°C) at 80% of ultimate tensile strength after 10000 cycles (left), 75000 cycles (center) and 224500 cycles (right).

5.4.2.4 Residual Strength Tests and Strip Strain Gage Measurements

Subsequent to the radiography process, measurements of the strain distribution around the hole after fatigue were taken in a manner identical to that employed for the APC-2 specimens. In the case of the elevated temperature specimens, it was not possible to make the strain distribution measurements at the test temperature (due to a lack of temperature compensation for the strain gages). Rather, it was necessary to make those measurements at room temperature. After these measurements were made, they were fit to the Lekhnitskii solution in a manner identical to that described in Section 4.3.2. The results of such a fitting process are shown in Figures 5.18-5.25.

After the strip strain gage measurements were made, residual strength tests were conducted. The results of these tests are summarized in Table 5.3. The room temperature specimens exhibit a behavior similar to that exhibited by the APC-2 specimens. There is an initial decrease in the laminate level residual strength initially, followed by a subsequent increase in the remaining strength. In the case of the elevated temperature specimens, no initial decrease in the residual strength is observed. In addition, there is one interesting behavior to be noted: at the highest number of cycles tested (224500), the remaining strength of the specimen fatigued at 80% of ultimate strength is greater than that of the specimen fatigued at 70% of ultimate strength. This behavior is not something that we would expect beforehand; we would expect the higher stress level to give us more damage and hence a lower residual strength. This behavior is not exhibited by the room temperature specimens.

5.4.2.5 Residual Strength Predictions

Using the results of the strip gage fits in conjunction with the techniques presented in Chapters 3 and 4, we are now ready to make predictions for the room temperature remaining strength of the Phase I material. The results of such a prediction are shown in Figure 5.26, along with the experimental data.

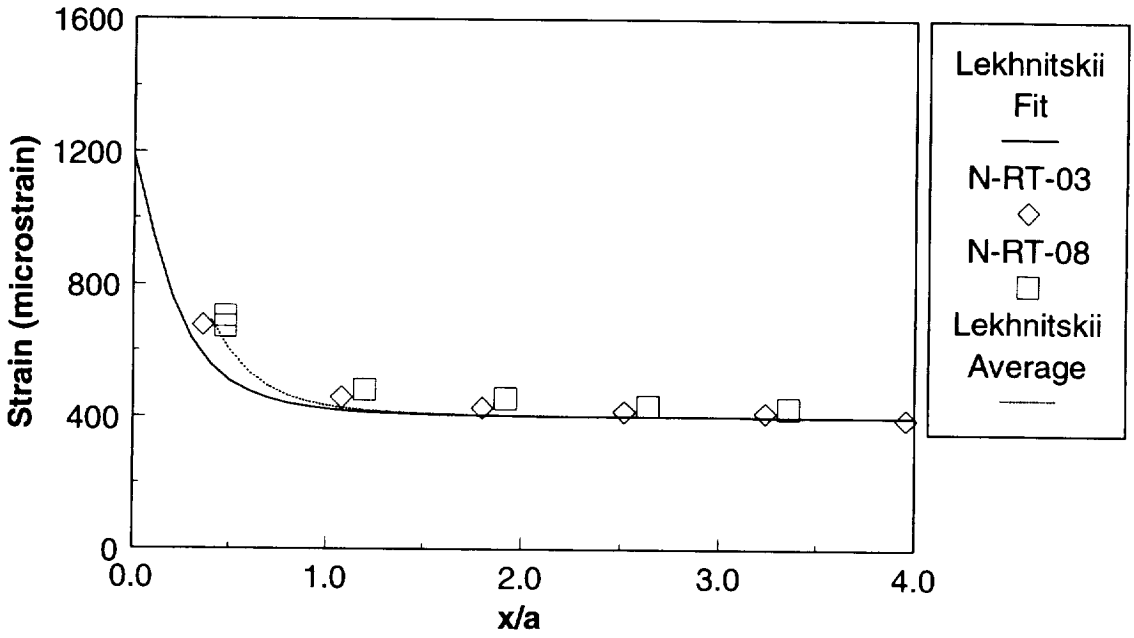

Figure 5.18. Comparison of predicted and measured axial strain as a function of position along the hole axis before fatigue.

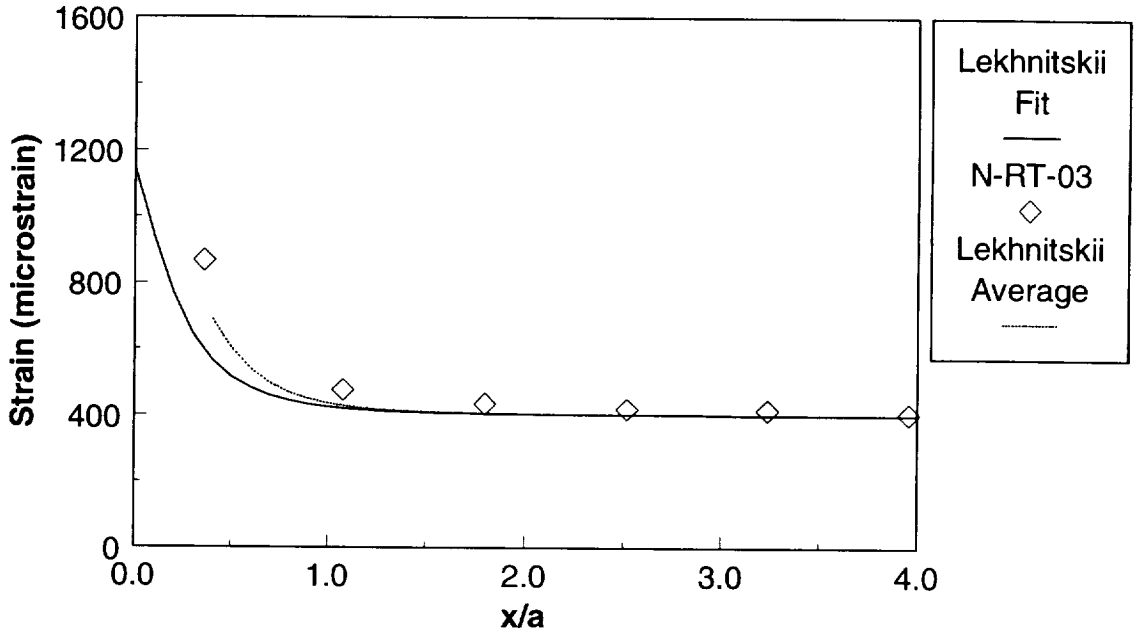

Figure 5.19. Comparison between the strip-strain gage measurements and the predictions based on the effective hole size for a specimen fatigued 10000 cycles at room temperature at 70% of ultimate strength.

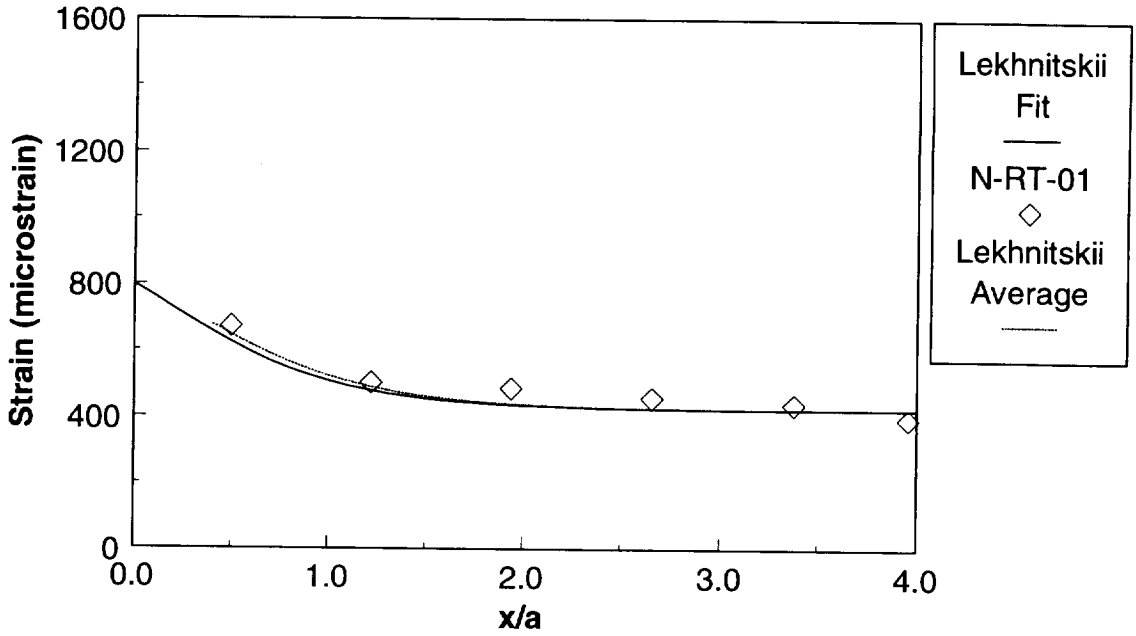

Figure 5.20. Comparison between the strip-strain gage measurements and the predictions based on the effective hole size for a specimen fatigued 260000 cycles at room temperature at 70% of ultimate strength.

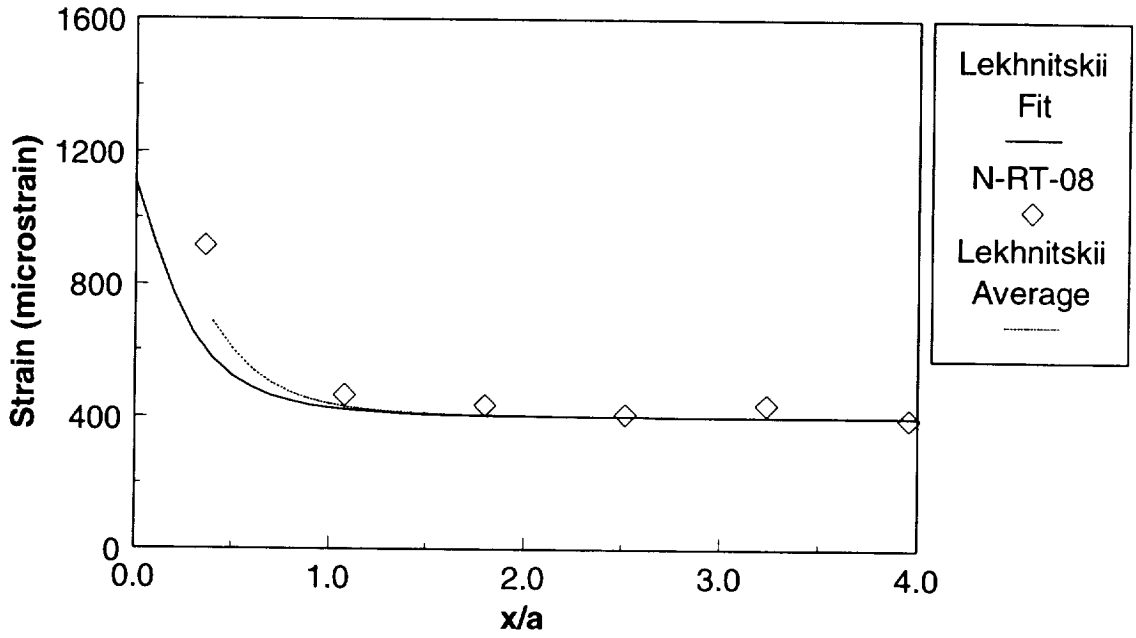

Figure 5.21. Comparison between the strip-strain gage measurements and the predictions based on the effective hole size for a specimen fatigued 10000 cycles at room temperature at 80% of ultimate strength.

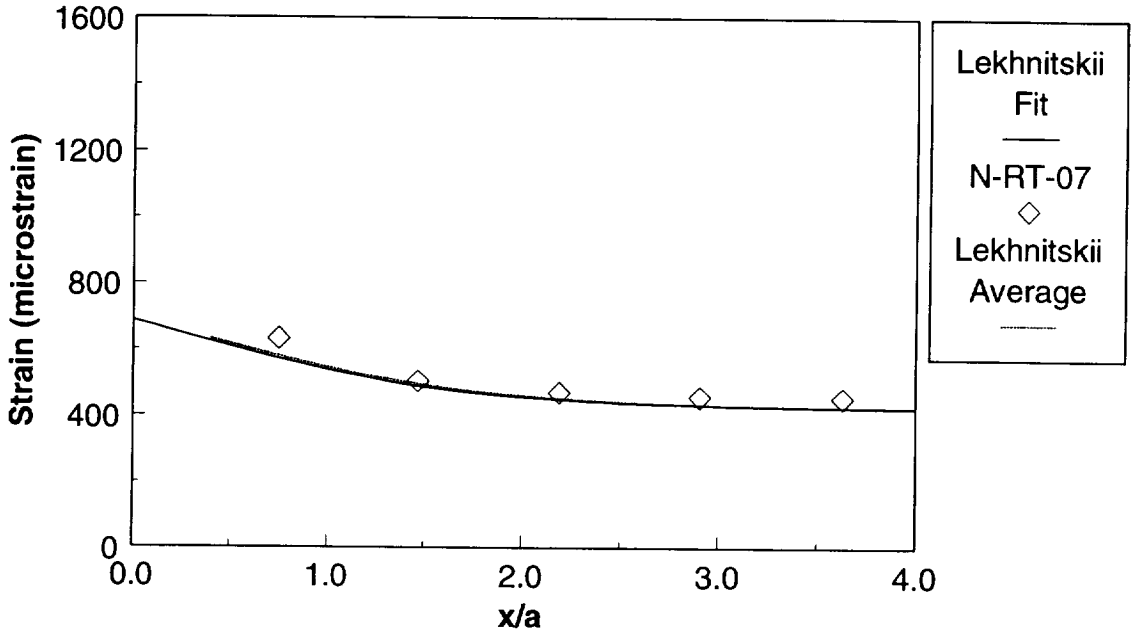

Figure 5.22. Comparison between the strip-strain gage measurements and the predictions based on the effective hole size for a specimen fatigued 280000 cycles at room temperature at 80% of ultimate strength.

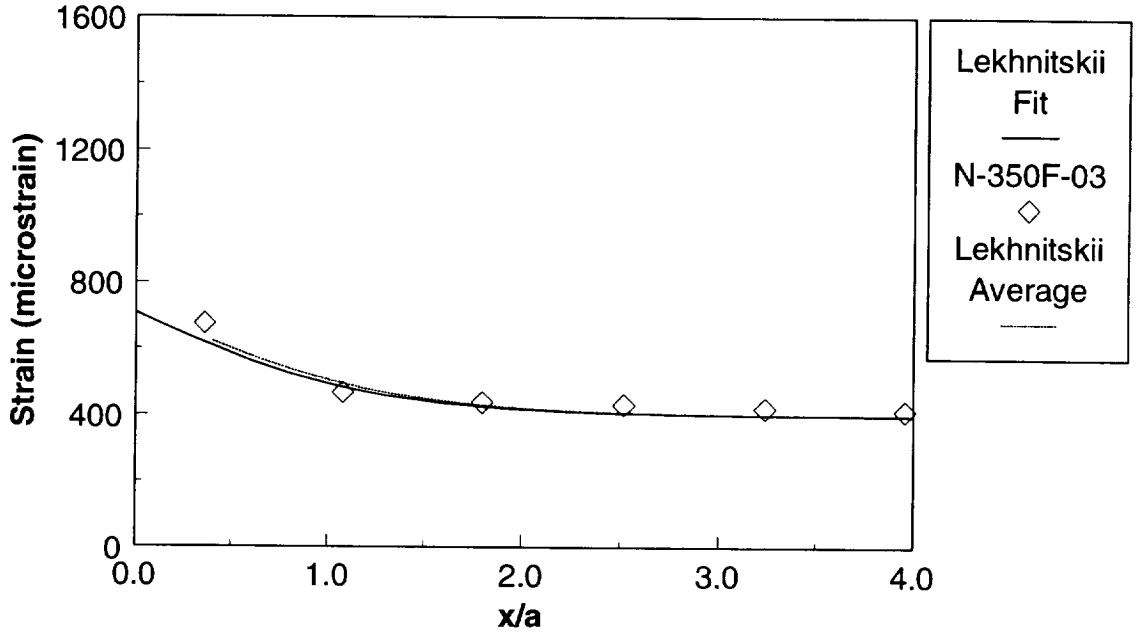

Figure 5.23. Comparison between the strip-strain gage measurements and the predictions based on the effective hole size for a specimen fatigued 10000 cycles at 350°F (177°C) at 70% of ultimate strength.

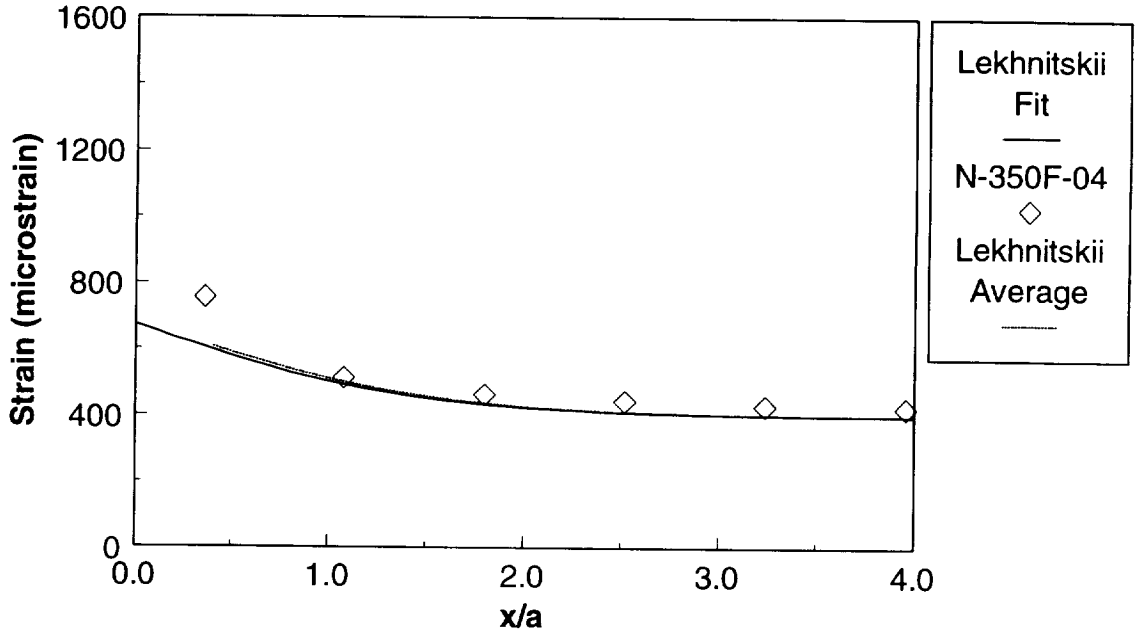

Figure 5.24. Comparison between the strip-strain gage measurements and the predictions based on the effective hole size for a specimen fatigued 10000 cycles at 350°F (177°C) at 80% of ultimate strength.

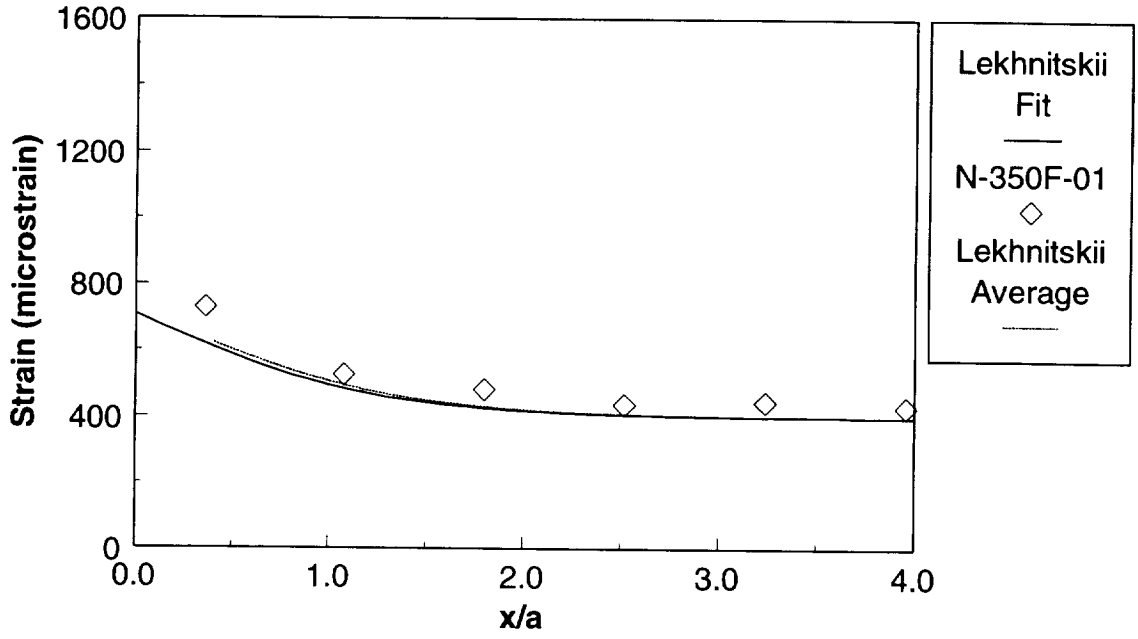

Figure 5.25. Comparison between the strip-strain gage measurements and the predictions based on the effective hole size for a specimen fatigued 10000 cycles at 350°F (177°C) at 80% of ultimate strength.

Table 5.3. Residual strength results for $[0/\pm45]_{2s}$ IM7/K3B laminates containing a center hole.

Specimen	Test Temperature	Normalized Fatigue Stress Level (%)	Fatigue Cycles	Residual Strength ksi (MPa)
N-RT-03	Room	70	10000	74.2 (512)
N-RT-01	Room	70	260000	84.9 (585)
N-RT-05	Room	70	1430515	105 (723)
N-RT-08	Room	80	10000	72.6 (501)
N-RT-07	Room	80	28000	94.3 (650)
N-RT-04	Room	80	1560401	94.4 (651)
N-350F-03	350°F (177°C)	70	10000	83.7 (577)
N-350F-05	350°F (177°C)	70	224500	90.7 (625)
N-350F-04	350°F (177°C)	80	10000	85.8 (591)
N-350F-01	350°F (177°C)	80	75000	98.8 (681)
N-350F-01	350°F (177°C)	80	224500	104 (715)

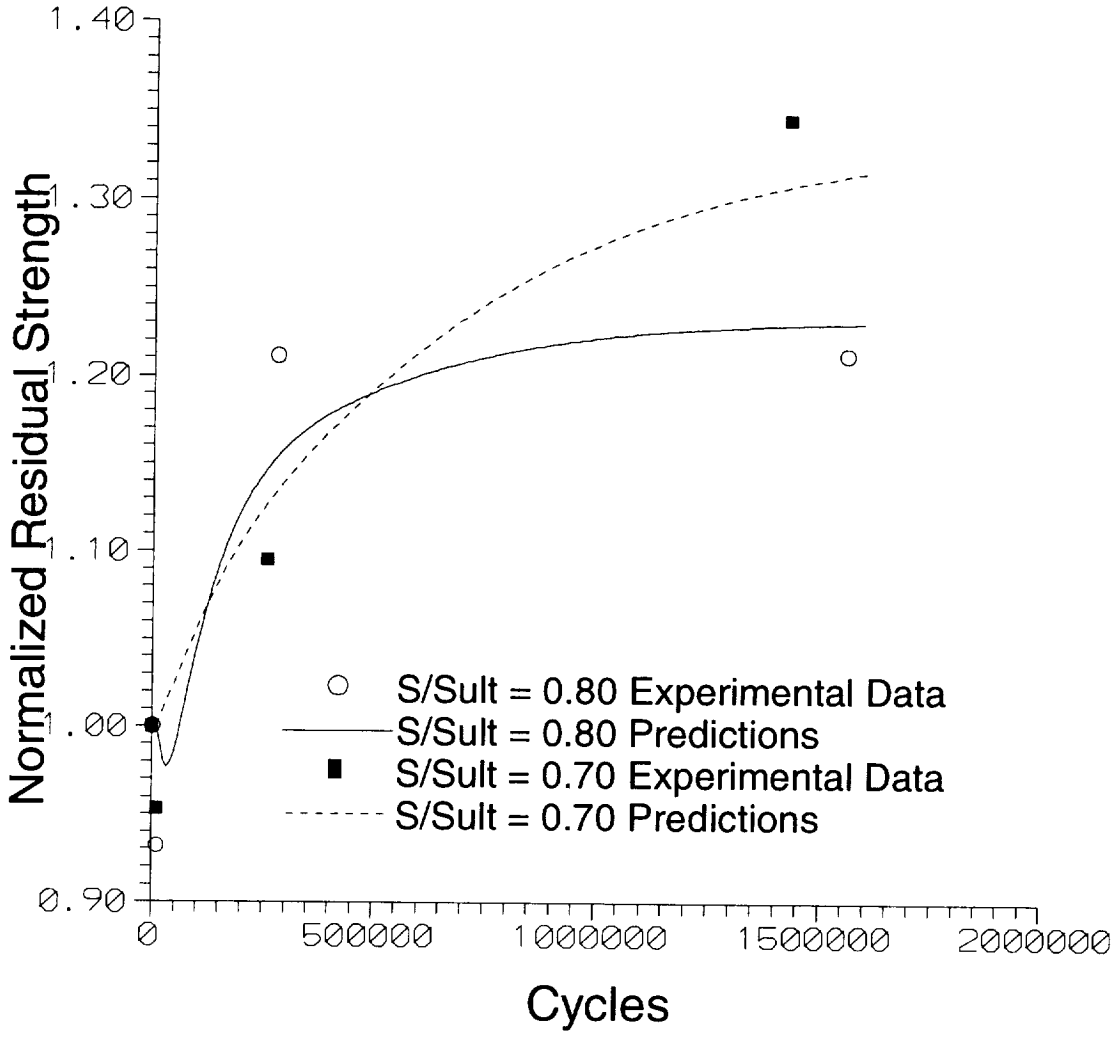

Figure 5.26. Comparison between measured and predicted remaining strength as a function of fatigue cycles and applied stress level at room temperature for $[0/\pm45]_{2s}$ laminates of IM7/K3B containing a center hole.

These features include the initial decrease followed by an increase in the remaining strength of the laminates fatigued at 80% of the ultimate strength. The model is unable to predict the initial decrease in the remaining strength of the laminates fatigued at 70% of the ultimate strength, although it does do a reasonable job of recovering the long-term behavior.

The remaining strength prediction at 350°F (177°C) requires additional information—the viscoelastic behavior of the off-axis plies at temperature. To include such an effect, the stress relaxation modulus of a $[\pm 45]_{3s}$ laminate was measured at 350°F (177°C). This data were then fit to the same functional form used to represent the change in the off-axis stiffness values due to fatigue behavior:

$$\frac{E(t)}{E(0)} = C - (C-1)(1+\alpha t)\exp(-\beta t) \tag{5.3}$$

where t is the total elapsed time. Such a fit is shown in Figure 5.27. Using this information, it is then possible to make predictions of the residual strength of the $[0/\pm 45]_{2s}$ laminates at 350°F (177°C). Such predictions are shown in Figure 5.28. The agreement is quite good, and the model is able to predict that the remaining strength of the specimens fatigue at 80% of ultimate strength is greater than those fatigued at 70% of ultimate strength.

5.4.3 Phase III Tests

5.4.3.1 Quasi-Static Tests

Only two room temperature and two elevated temperature specimens were available for the unnotched and notched quasi-static tests. The two strength values obtained for the unnotched room temperature specimens were 146.4 ksi (1010 MPa) and 140.9 ksi (971 MPa), while the two strength values obtained for the unnotched elevated temperature specimens were 132.6 ksi (914 MPa) and 124.8 ksi (860 MPa).

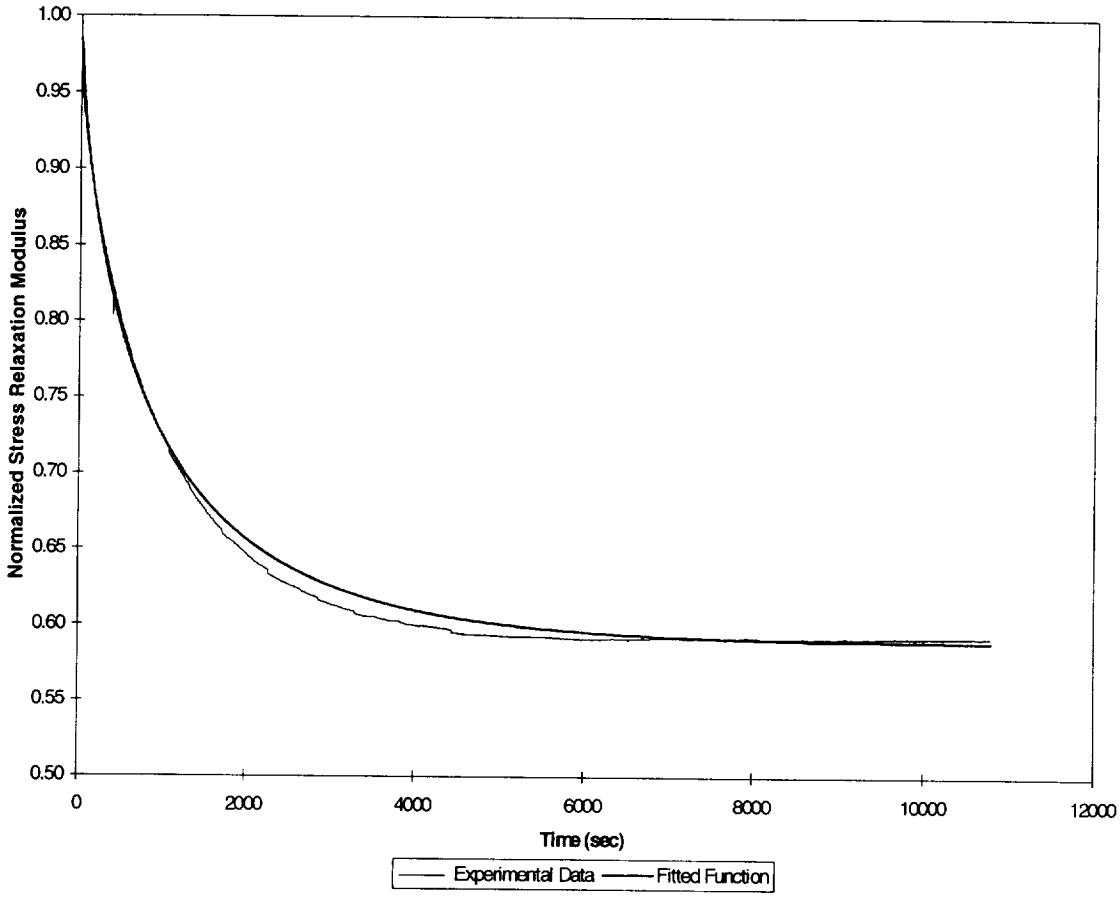

Figure 5.27. Comparison between measured and fitted stress relaxation modulus for $[\pm 45]_{3s}$ IM7/K3B at 350°F (177°C).

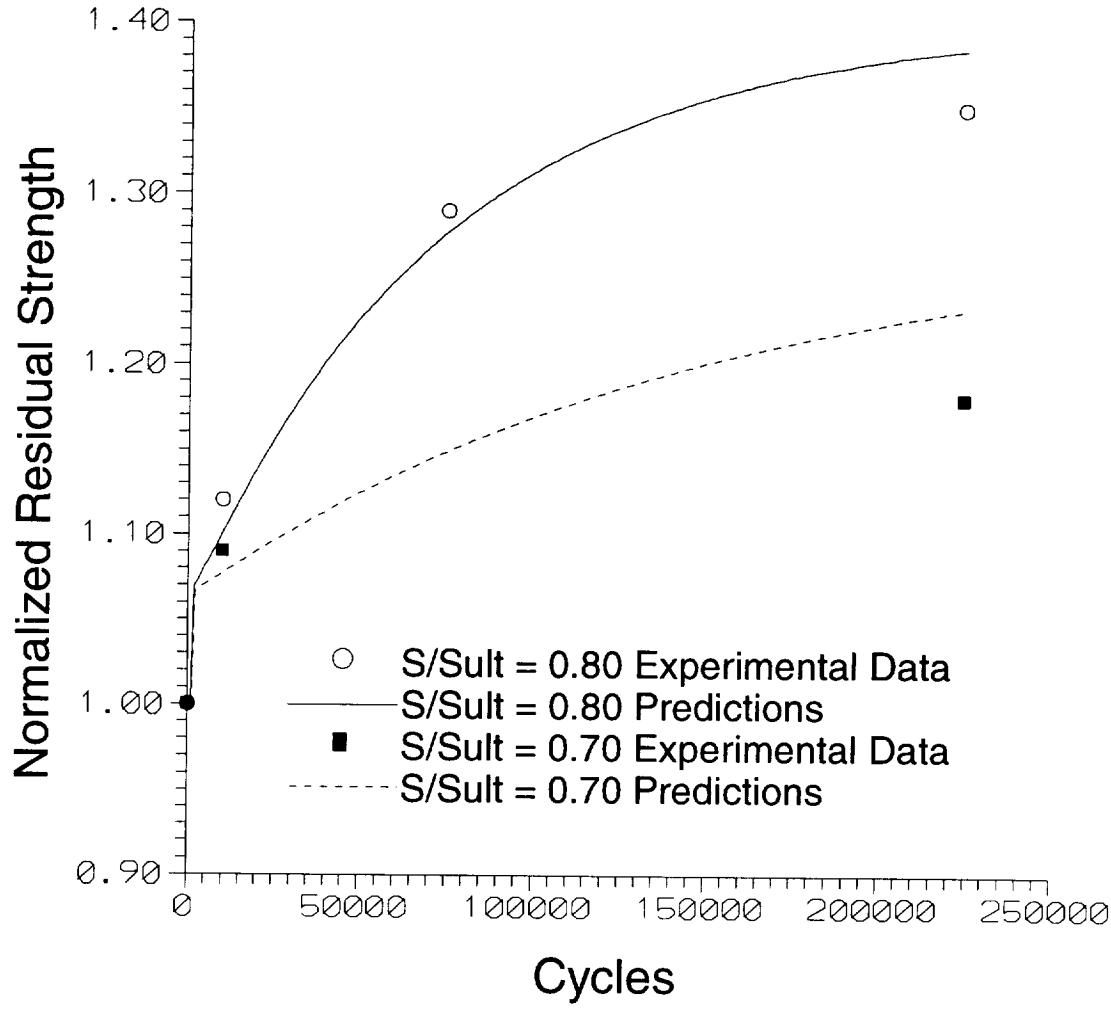

Figure 5.28. Comparison between measured and predicted remaining strength as a function of fatigue cycles and applied stress level 350°F (177°C) for $[0/\pm45]_{2s}$ laminates of IM7/K3B containing a center hole.

Representative stress-strain curves for the room temperature tests are shown in Figures 5.29 and 5.30, and those for the elevated temperature tests are shown in Figure 5.31. The two strength values obtained for the notched room temperature specimens were 62.2 ksi (429 MPa) and 60.8 ksi (419 MPa), while the two strength values obtained for the notched elevated temperature specimens were 59.9 ksi (413 MPa) and 59.0 ksi (407 MPa). Representative stress-strain curves for the tests are shown in Figures 5.32 and 5.33, and for the elevated temperature tests in Figure 5.34. Because the room temperature and elevated temperature specimens have identical gage lengths, it is possible to make direct comparisons between the room temperature data and the elevated temperature data (i.e. Figure 5.30 may be compared to Figure 5.31 and Figure 5.33 may be compared to Figure 5.34). From these data, we can see why it way necessary to use the average stress criterion given by Equation (4.3) to determine the strength of the laminates containing a hole. If we had used the elastic stress concentration for the quasi-isotropic laminate (k=3.0), we would have estimated the strength of the notched room temperature laminate to be approximately 48 ksi—an error of over 25%.

5.4.3.2 Fatigue Tests

During the course of the fatigue tests of the Phase III materials, real-time measurements were made of the storage modulus and the phase lag based upon the load and the stroke signal for the specimens. Elahi et al. [61] have published work which details the development of this scheme for use with composite materials. The technique is essentially a Dynamic Mechanical Analysis (DMA) on a full-scale (rather than reduced) specimen. In the case of the elevated temperature tests, it offers the advantage of being a totally non-contact measurement. As such, it was hoped that the test could shed light on difference in material behavior at room temperature and at 350°F (177°C).

As this technique is still under development, and is being continually refined, most of the results will be confined to the presentation of the data itself. We begin by considering the room temperature fatigue of

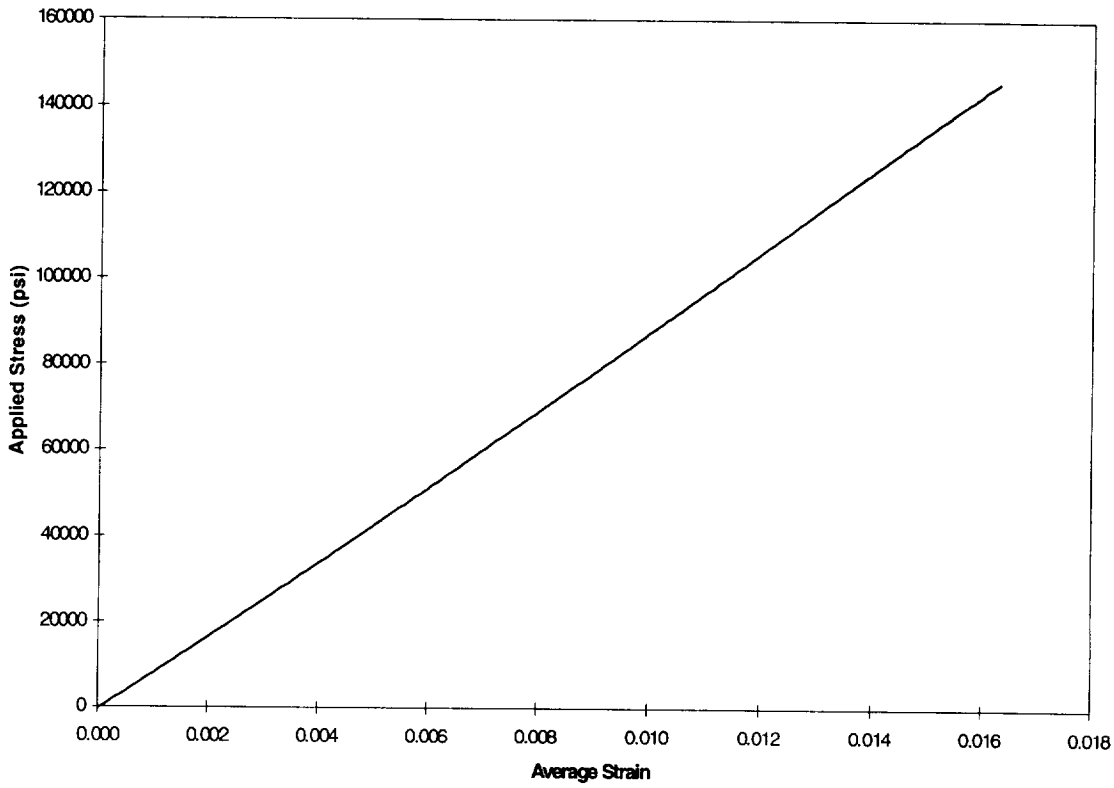

Figure 5.29. Representative stress-strain curve based on extensometer measurements for room temperature tests of $[45/0/-45/90]_{2s}$ IM7/K3B laminates without a center hole.

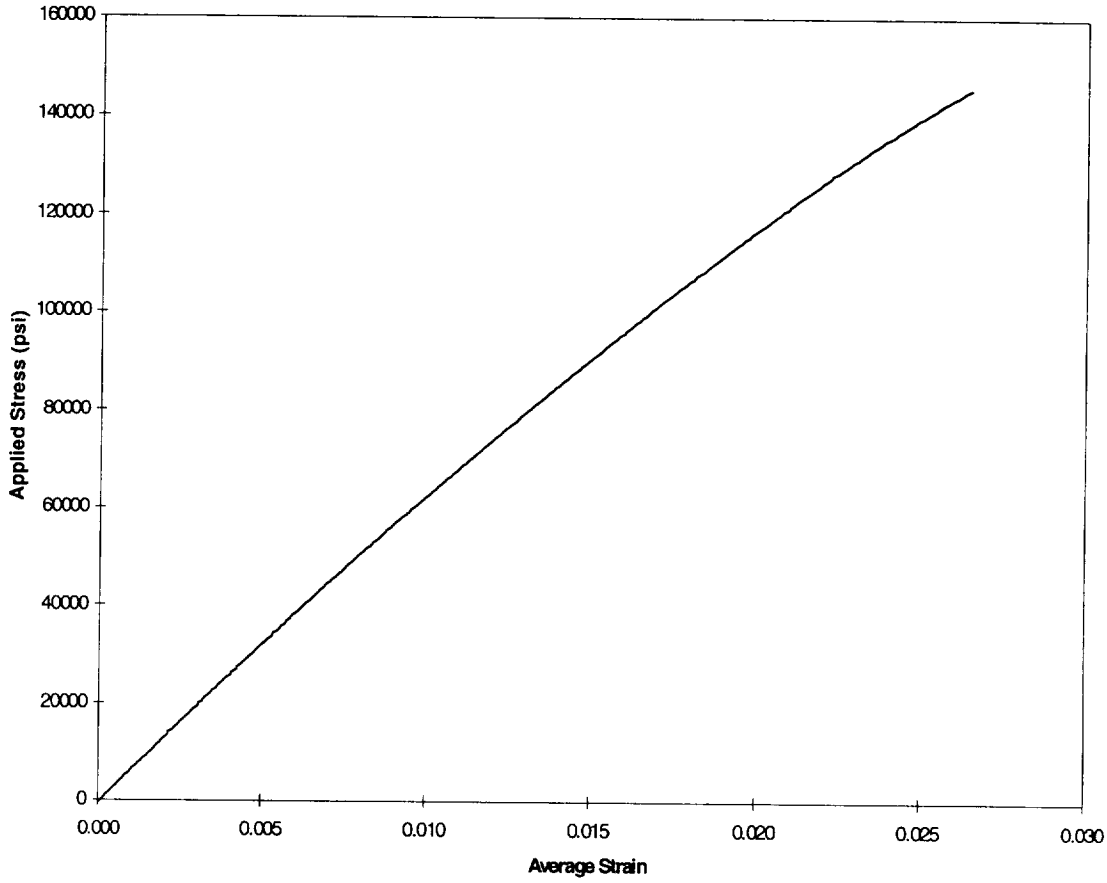

Figure 5.30. Representative stress-strain curve based on stroke measurements for room temperature tests $[45/0/-45/90]_{2s}$ IM7/K3B laminates without a center hole.

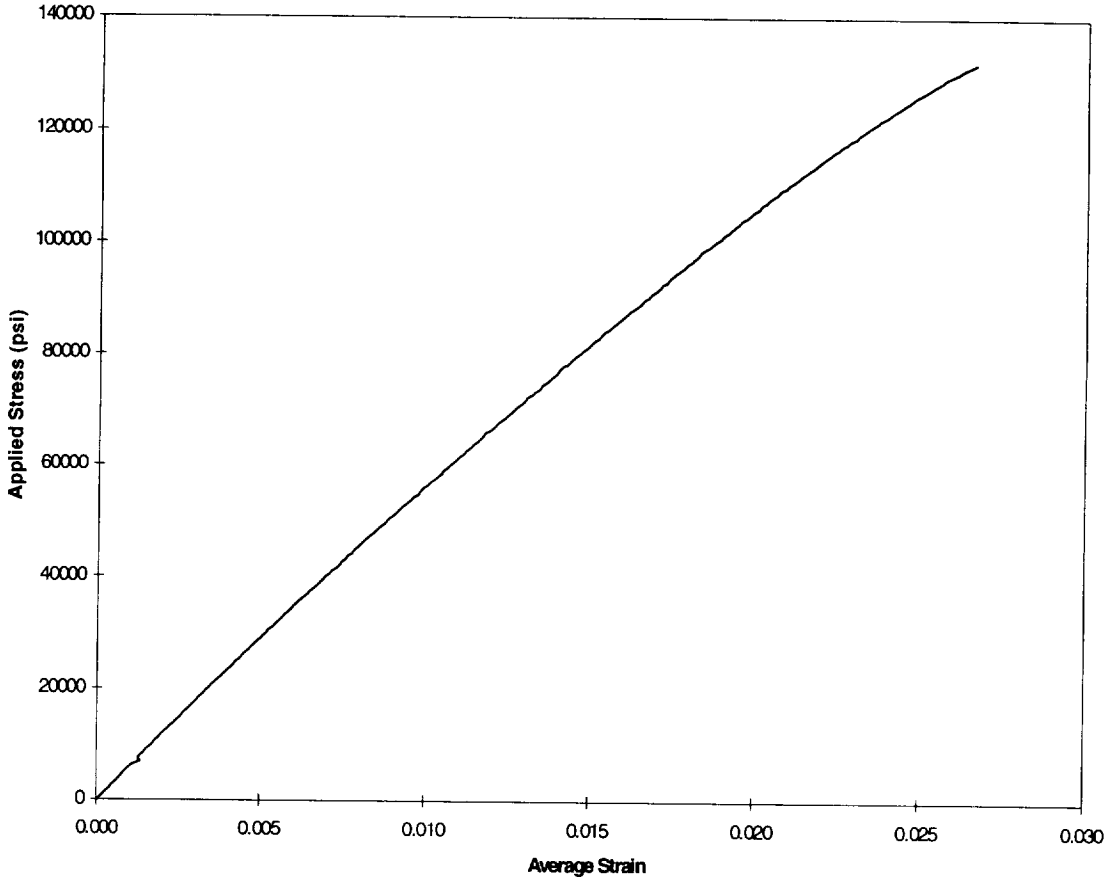

Figure 5.31. Representative stress-strain curve based on stroke measurements for 350°F (177°C) tests of $[45/0/-45/90]_{2s}$ IM7/K3B laminates without a center hole.

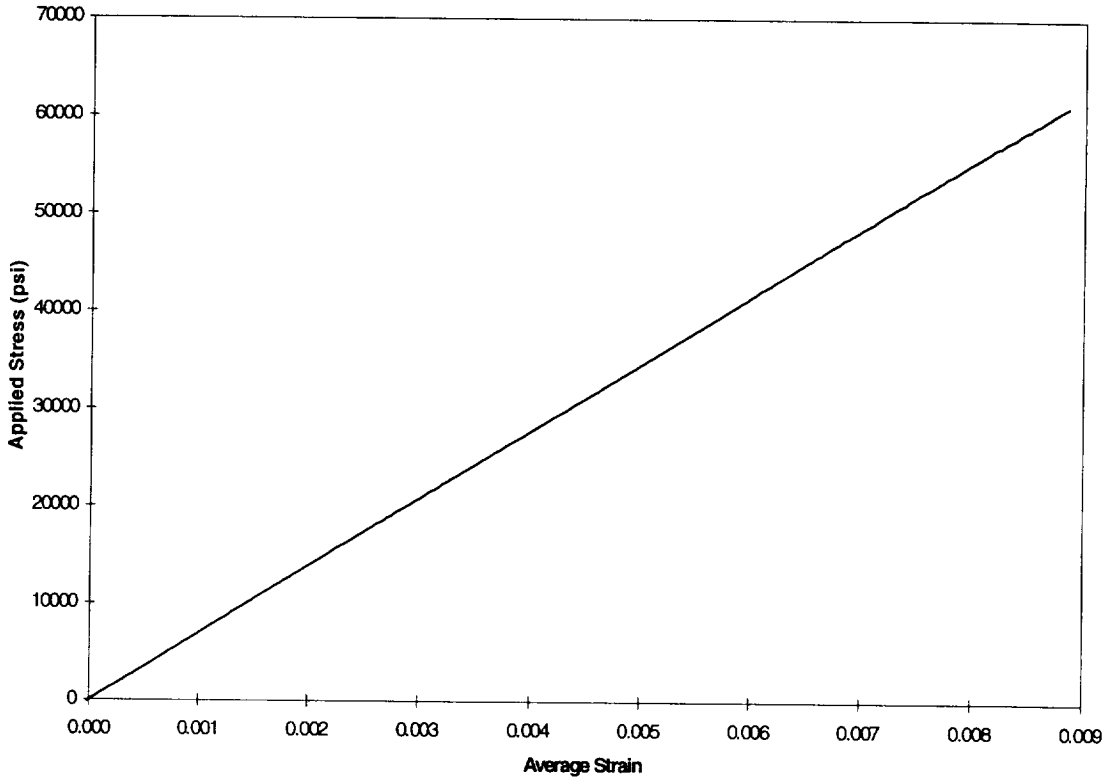

Figure 5.32. Representative stress-strain curve based on extensometer measurements for room temperature tests of $[45/0/-45/90]_{2s}$ IM7/K3B laminates with a center hole.

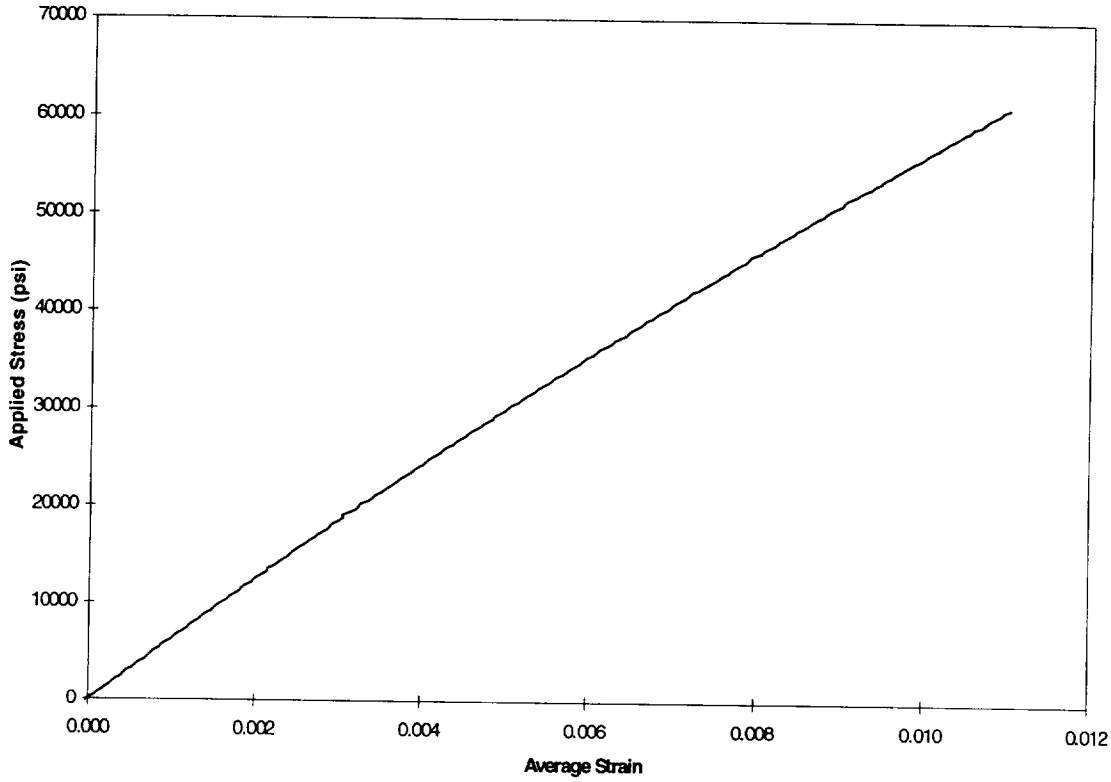

Figure 5.33. Representative stress-strain curve based on stroke measurements for room temperature tests of $[45/0/-45/90]_{2s}$ IM7/K3B laminates with a center hole.

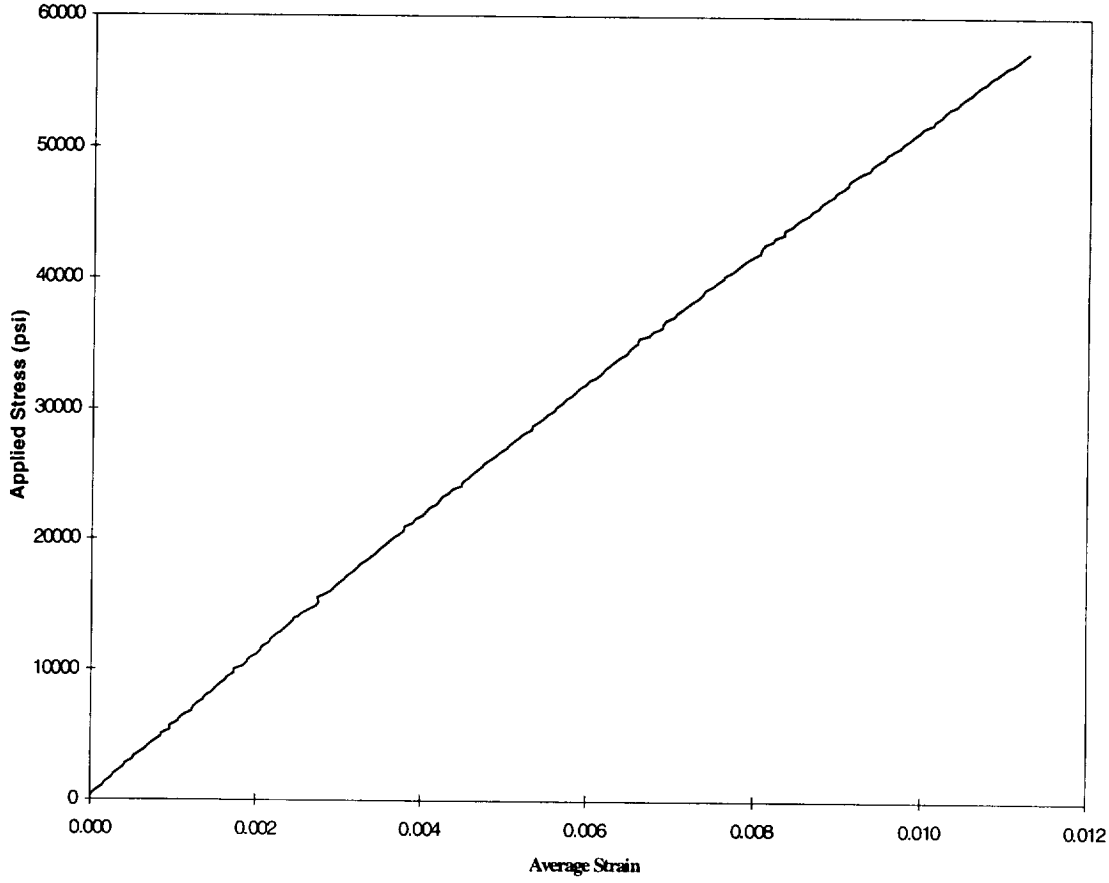

Figure 5.34. Representative stress-strain curve based on stroke measurements for 350°F (177°C) tests of $[45/0/-45/90]_{2s}$ IM7/K3B laminates with a center hole.

the unnotched $[45/0/-45/90]_{2s}$ specimens. The dynamic storage modulus and phase lag for those specimens which were fatigued at 65% of ultimate strength are shown in Figure 5.35 and Figure 5.36, respectively. Those specimens which failed during the course of the fatigue test have the number of cycles to failure noted, while those specimens which had the fatigue tests interrupted are labeled with the number of cycles at which this interruption occurred. Similar plots for those specimens which were fatigued at 70% of ultimate strength are shown in Figure 5.37 and Figure 5.38. If we compare the results in Figure 5.35 and Figure 5.37, we see that there is little difference in the dynamic storage modulus as a function of cycles at the two load levels. However, if we compare the results in Figure 5.36 and Figure 5.38, we see that there is almost always a greater phase lag as a function of cycles, suggestion a greater rate of dissipation of energy.

We next consider the fatigue of the unnotched $[45/0/-45/90]_{2s}$ specimens at 350°F (177°C). The dynamic storage modulus and phase lag for those specimens which were fatigued at 65% of ultimate strength are shown in Figure 5.39 and Figure 5.40, respectively. Similar plots for those specimens which were fatigued at 70% of ultimate strength are shown in Figure 5.41 and Figure 5.42. In the case of the elevated temperature specimens there is no apparent difference in either the storage modulus or the phase lag between the two load levels. However, there is a greater phase lag than was observed in the room temperature specimens, suggesting a greater rate of dissipation of energy. This is not surprising in view of the viscoelastic nature of the matrix material, which dissipates more energy under dynamic loading as the temperature approaches its glass transition temperature (approximately 245°C for K3B). One feature of interest is that in all cases the data appeared to be very reproducible.

Now we may consider the response of the notched $[45/0/-45/90]_{2s}$ specimens at room temperature. The dynamic storage modulus and phase lag for those specimens which were fatigued at 70% of ultimate

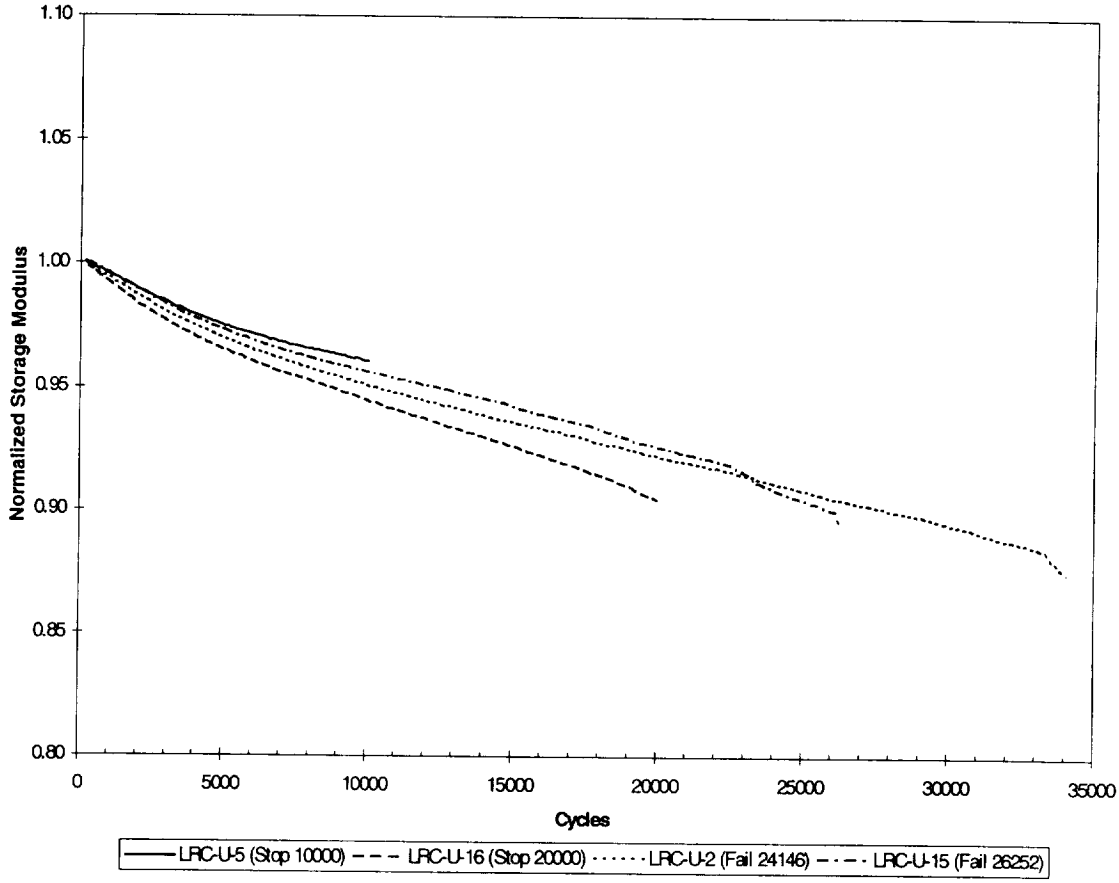

Figure 5.35. Normalized dynamic storage modulus measurements for room temperature fatigue tests at 65% of ultimate strength for $[45/0/-45/90]_{2s}$ IM7/K3B laminates without a center hole.

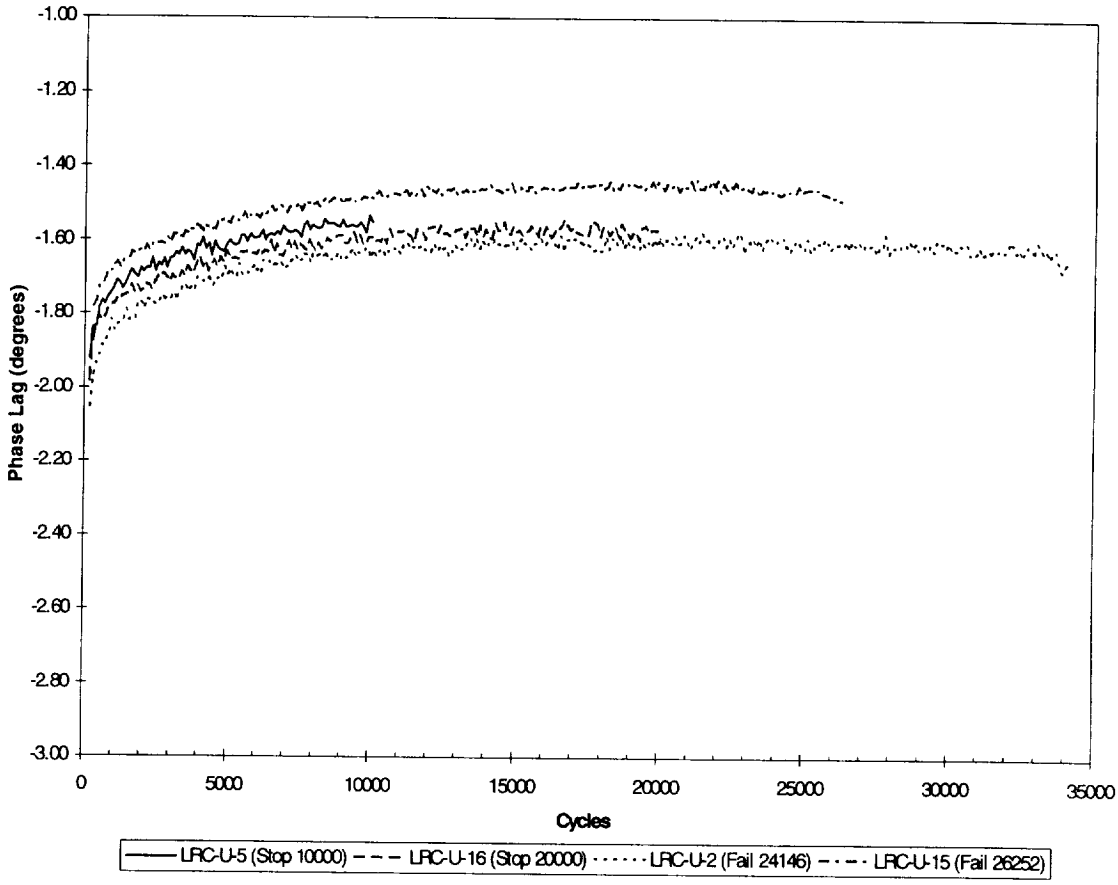

Figure 5.36. Phase lag measurements for room temperature fatigue tests at 65% of ultimate strength for $[45/0/-45/90]_{2s}$ IM7/K3B laminates without a center hole.

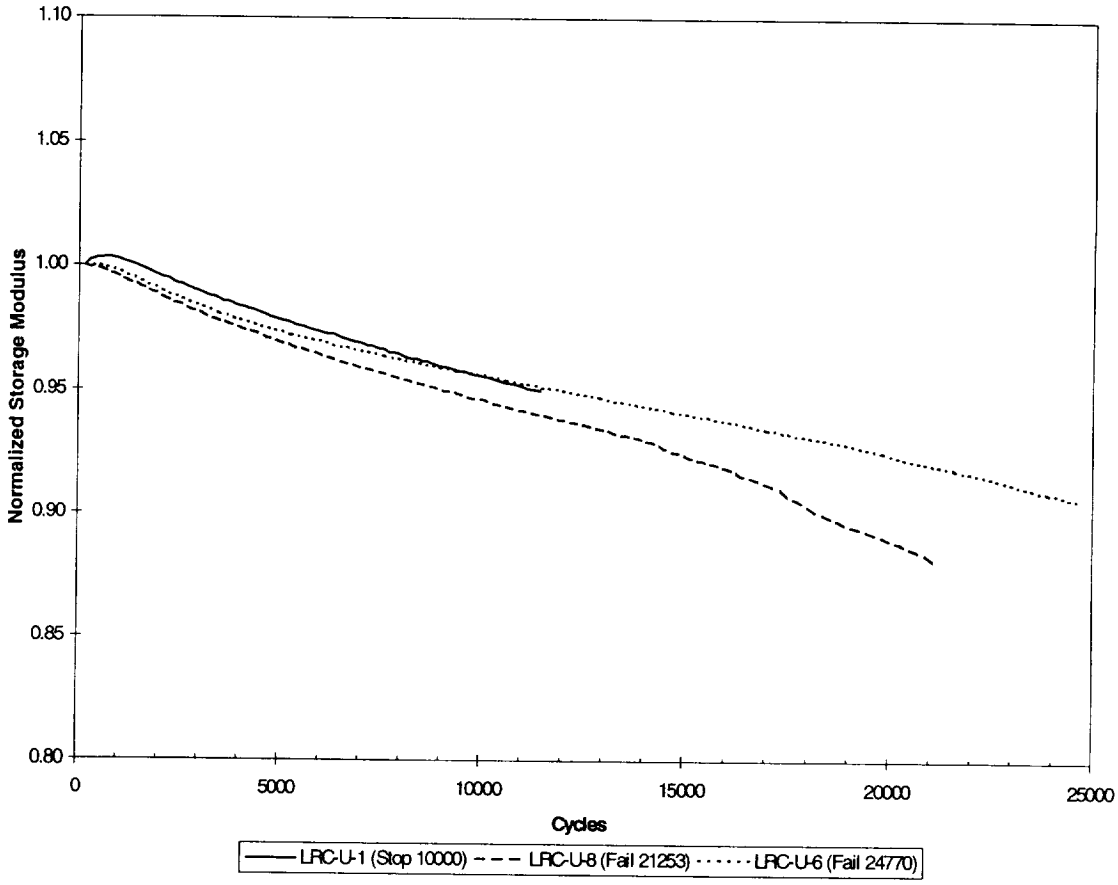

Figure 5.37. Normalized dynamic storage modulus measurements for room temperature fatigue tests at 70% of ultimate strength for $[45/0/-45/90]_{2s}$ IM7/K3B laminates without a center hole.

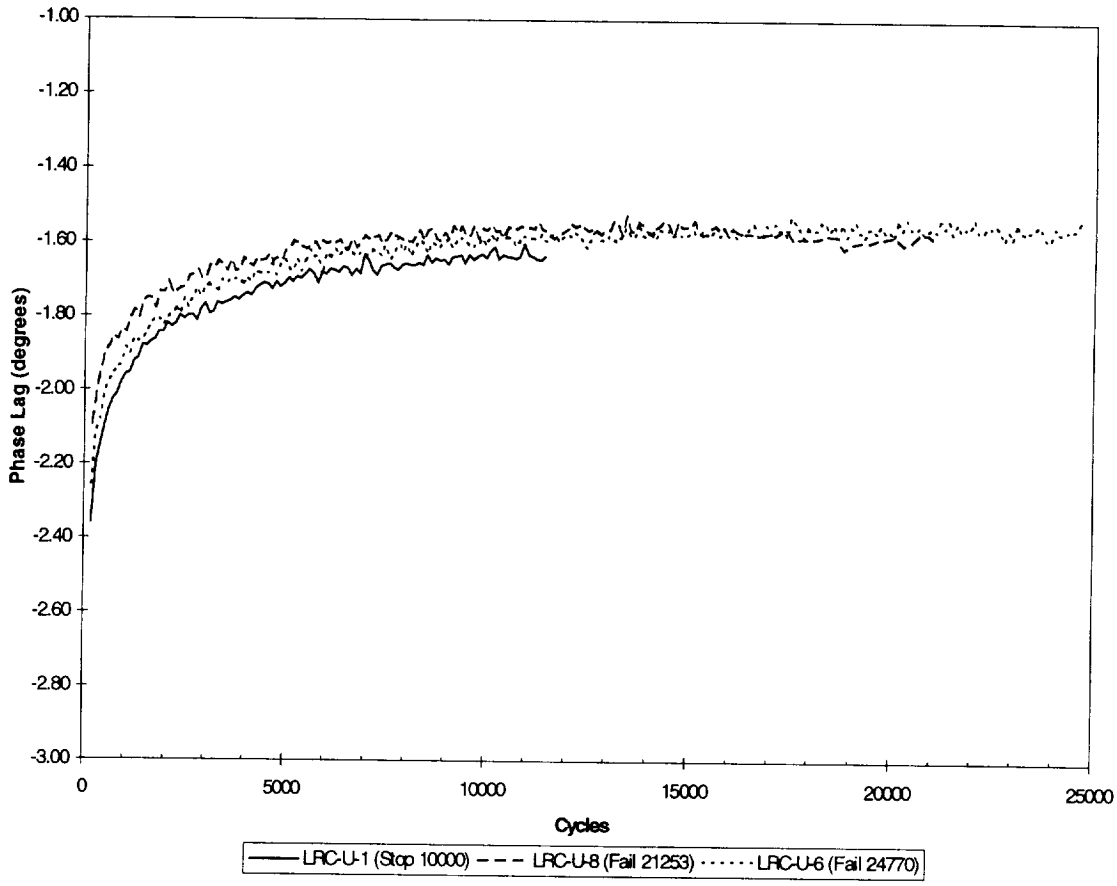

Figure 5.38. Phase lag measurements for room temperature fatigue tests at 70% of ultimate strength for $[45/0/-45/90]_{2s}$ IM7/K3B laminates without a center hole.

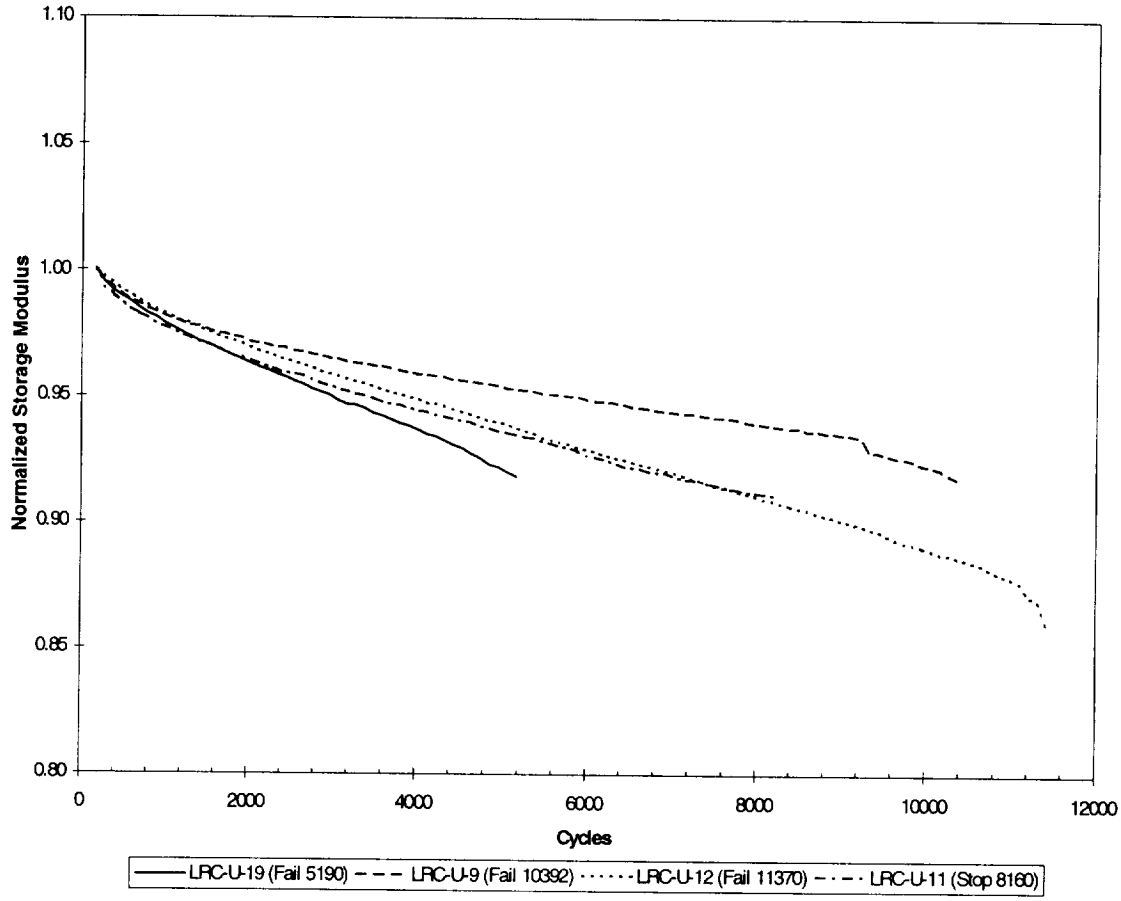

Figure 5.39. Normalized dynamic storage modulus measurements for 350°F (177°C) fatigue tests at 65% of ultimate strength for $[45/0/-45/90]_{2s}$ IM7/K3B laminates without a center hole.

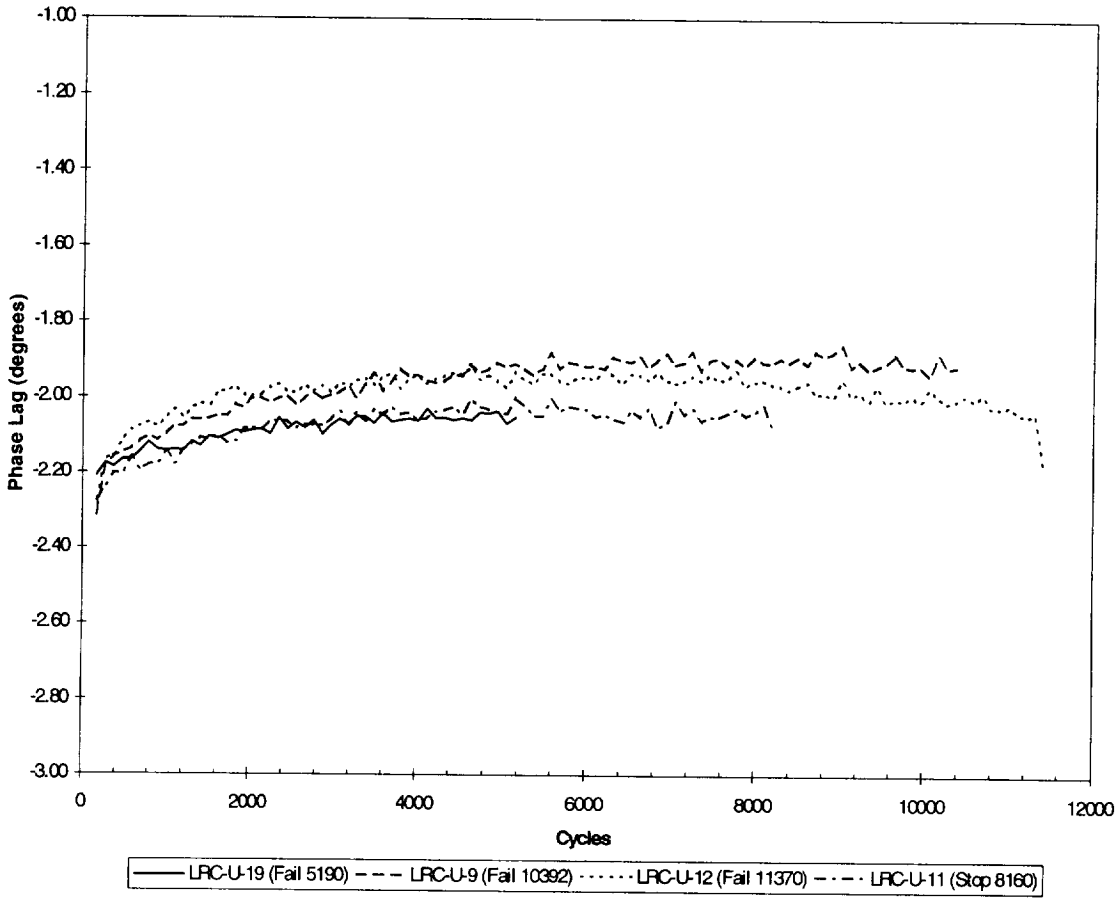

Figure 5.40. Phase lag measurements for room temperature fatigue tests at 65% of ultimate strength for $[45/0/-45/90]_{2s}$ IM7/K3B laminates without a center hole.

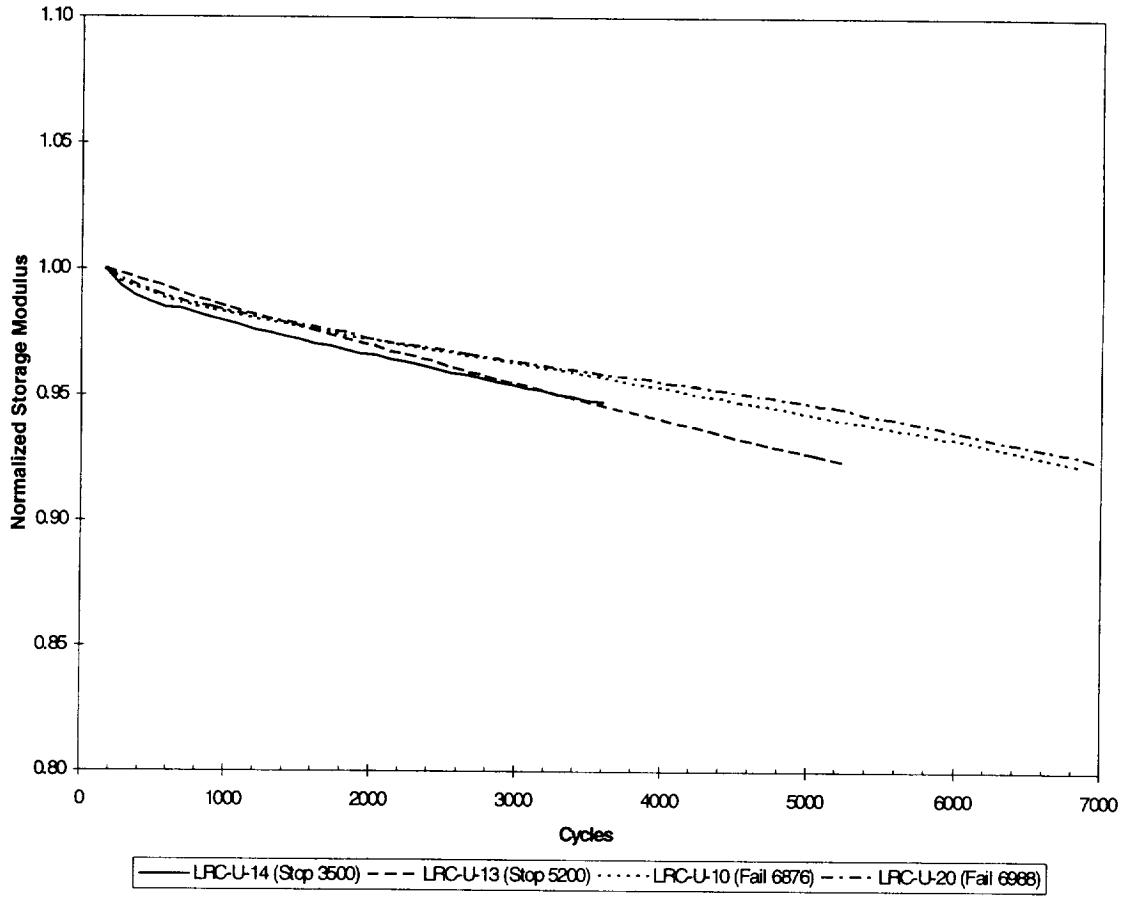

Figure 5.41. Normalized dynamic storage modulus measurements for 350°F (177°C) fatigue tests at 70% of ultimate strength for $[45/0/-45/90]_{2s}$ IM7/K3B laminates without a center hole.

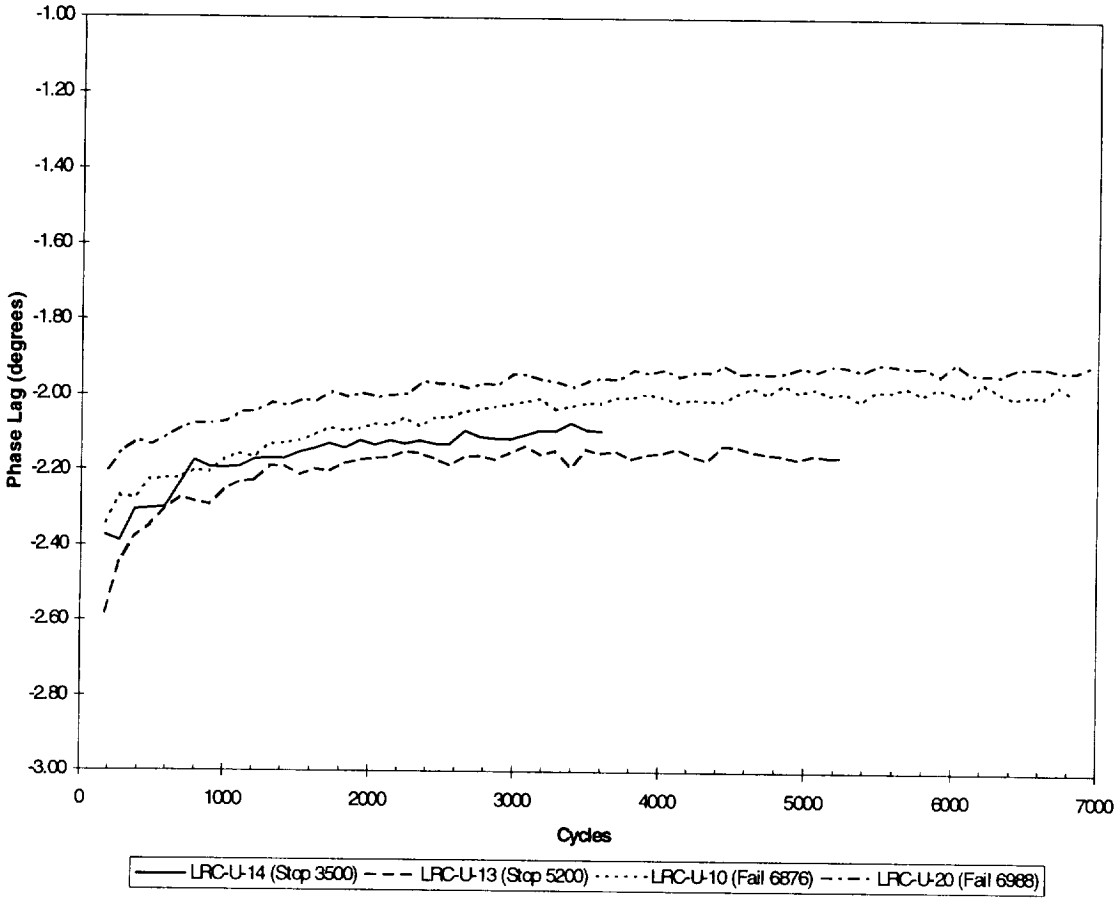

Figure 5.42. Phase lag measurements for 350°F (177°C) fatigue tests at 70% of ultimate strength for $[45/0/-45/90]_{2s}$ IM7/K3B laminates without a center hole.

strength are shown in Figure 5.43 and Figure 5.44, respectively. Similar plots for those specimens which were fatigued at 80% of ultimate strength at room temperature are shown in Figure 5.45 and Figure 5.46. In this case the repeatability is not as good as it was for the unnotched specimens. Specimen LRC-N-11 which was fatigued at 70% of ultimate strength, and specimen LRC-N-19 which was fatigued at 80% of ultimate strength have behaviors which are different from the other specimens which were fatigued at corresponding load levels. No explanation for this behavior is available at the present time.

Finally, we may consider the behavior of the notched $[45/0/-45/90]_{2s}$ specimens which were fatigued at 350°F (177°C). The dynamic storage modulus and phase lag for those specimens which were fatigued at 70% of ultimate strength are shown in Figure 5.47 and Figure 5.48, respectively. Corresponding plots for those specimens which were fatigued at 80% of ultimate strength at 350°F (177°C) are shown in Figure 5.49 and Figure 5.50. Once again, there is one specimen (LRC-N-4—fatigued at 70% of ultimate strength) whose behavior differs from the other specimens of its type.

5.4.3.3 Penetrant Enhanced Radiography

Radiographs of the unnotched specimens fatigued at room temperature at 65% and 70% of ultimate tensile strength are shown in Figure 5.51 and Figure 5.52, respectively. If we first consider the radiographs of the specimens fatigued at 65% of ultimate strength, we notice that the damage development begins with the matrix cracks in the all the plies. In the specimen which was stopped after 10000 cycles, we may see the beginnings of the edge delamination. This delamination continues to grow inward as the number of cycles increases, as can be see in the specimen which was stopped after 20000 cycles. Only a single specimen fatigued at 70% of ultimate strength was stopped before failure occurred. The radiograph of this specimen is shown in Figure 5.52 after 10000 cycles. The pattern of damage development is similar to those specimens which were fatigued at 65% of ultimate strength, although the delamination growth is more advanced than in the specimen which was fatigued 10000 cycles at 65% of ultimate strength.

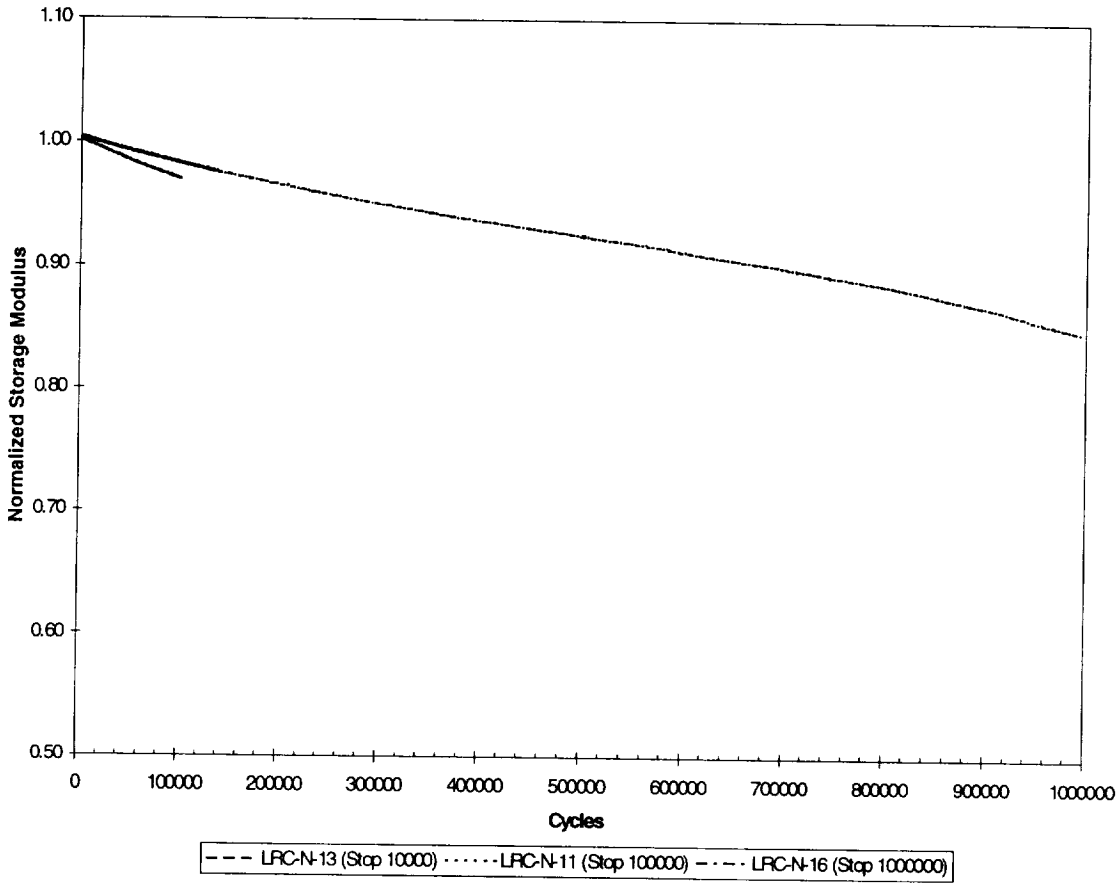

Figure 5.43. Normalized dynamic storage modulus measurements for room temperature fatigue tests at 70% of ultimate strength for $[45/0/-45/90]_{2s}$ IM7/K3B laminates with a center hole.

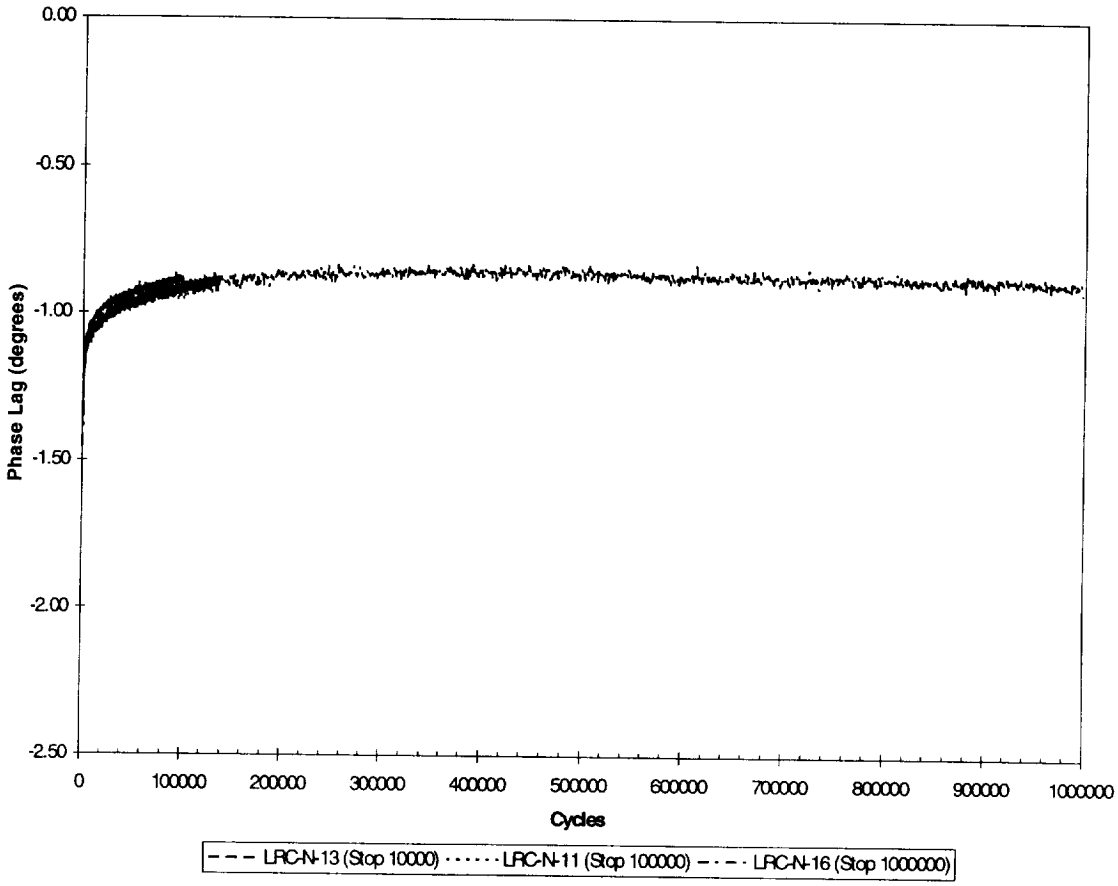

Figure 5.44. Phase lag measurements for room temperature fatigue tests at 70% of ultimate strength for $[45/0/-45/90]_{2s}$ IM7/K3B laminates with a center hole.

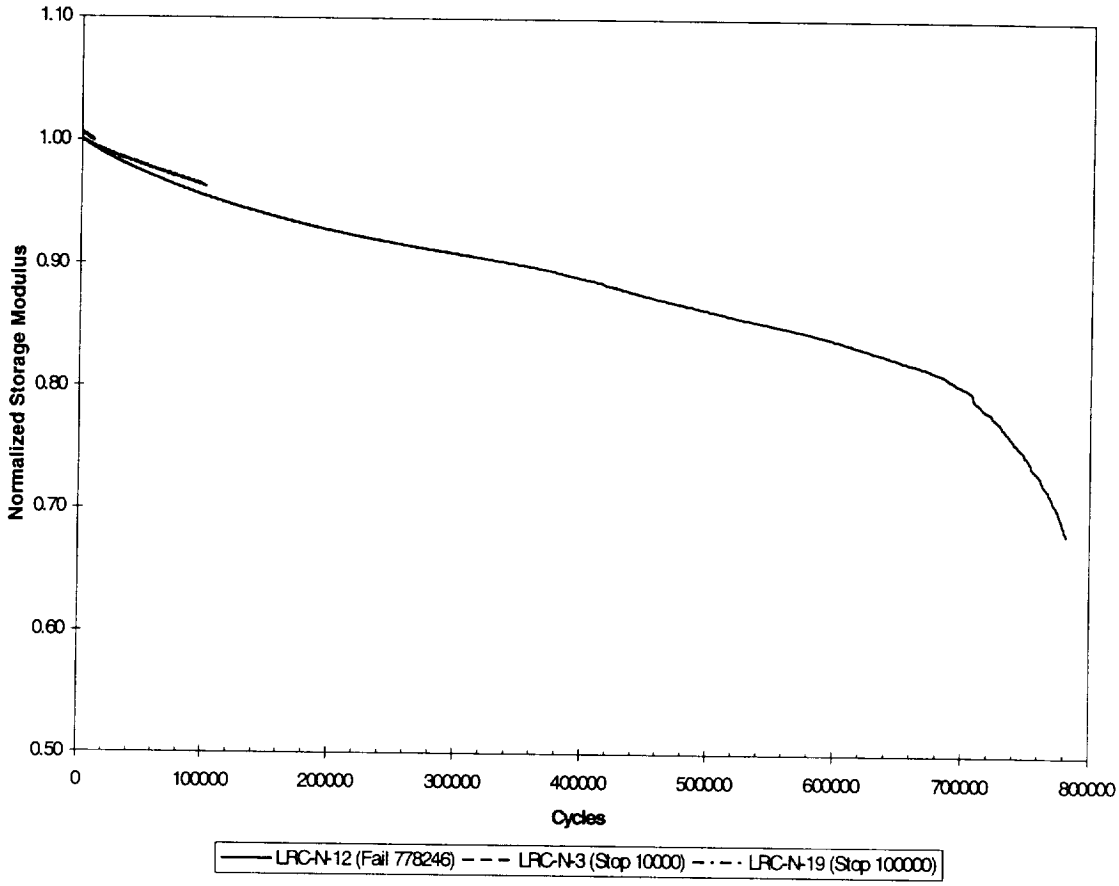

Figure 5.45. Normalized dynamic storage modulus measurements for room temperature fatigue tests at 80% of ultimate strength for $[45/0/-45/90]_{2s}$ IM7/K3B laminates with a center hole.

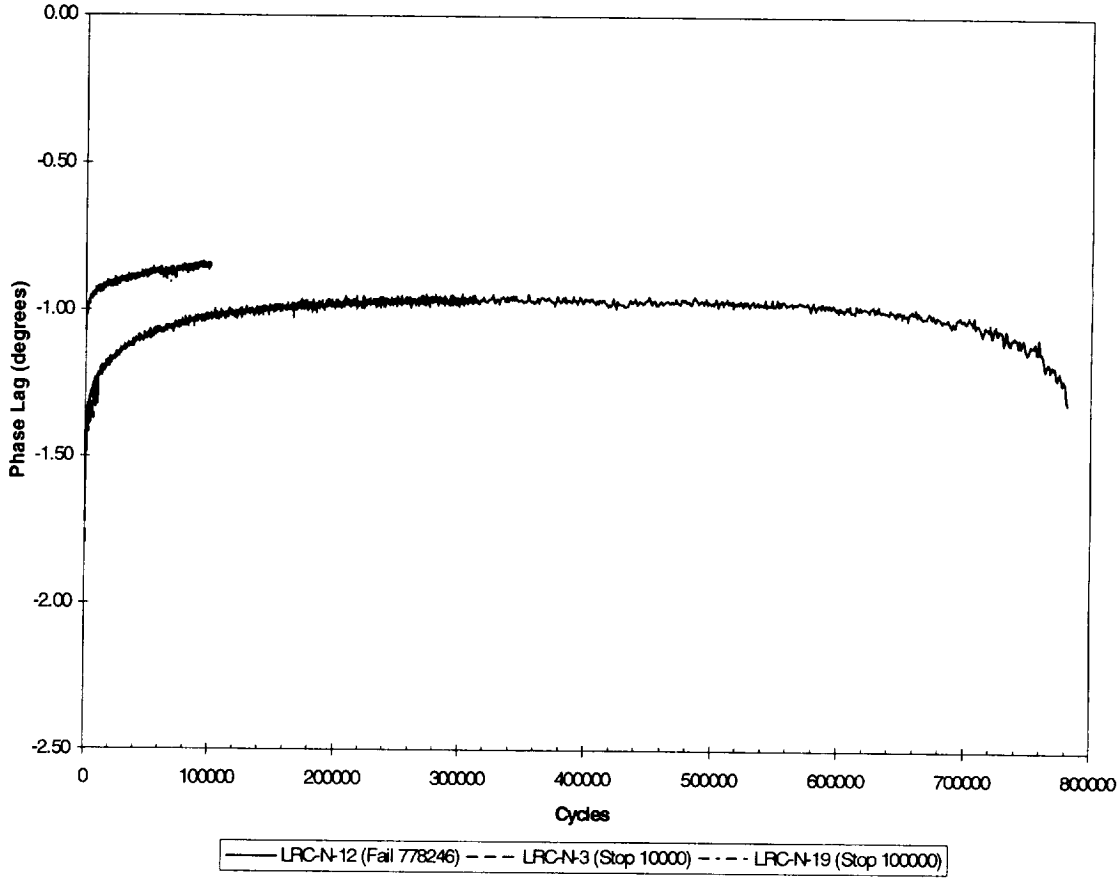

Figure 5.46. Phase lag measurements for room temperature fatigue tests at 80% of ultimate strength for $[45/0/-45/90]_{2s}$ IM7/K3B laminates with a center hole.

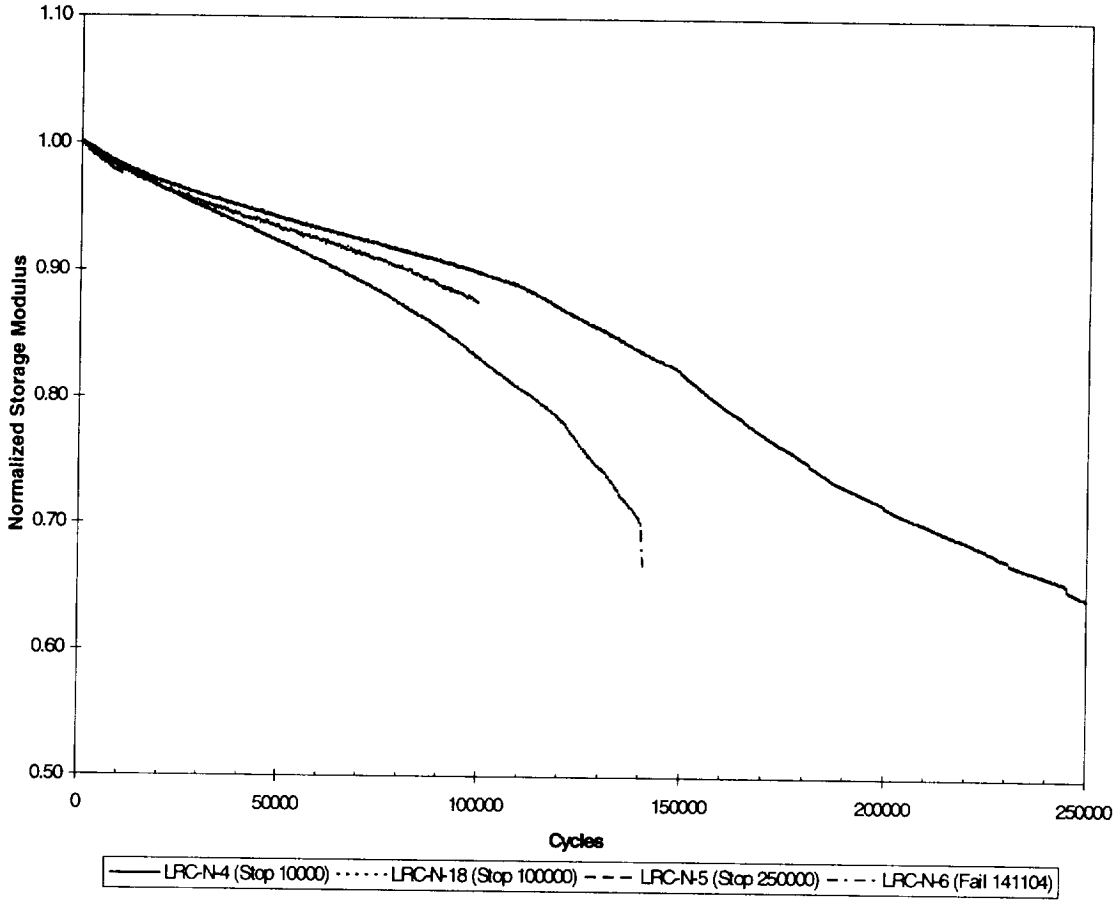

Figure 5.47. Normalized dynamic storage modulus measurements for 350°F (177°C) fatigue tests at 70% of ultimate strength for $[45/0/-45/90]_{2s}$ IM7/K3B laminates with a center hole.

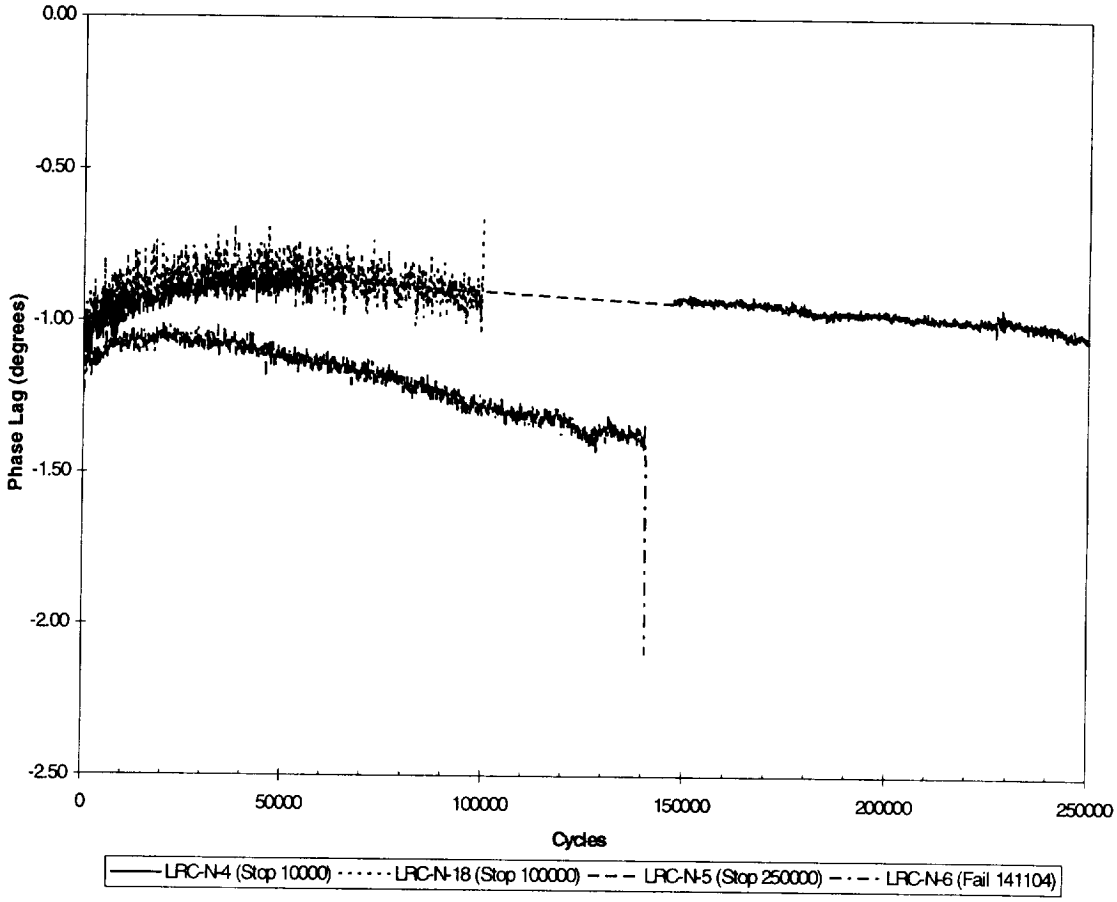

Figure 5.48. Phase lag measurements for350°F (177°C) fatigue tests at 70% of ultimate strength for $[45/0/-45/90]_{2s}$ IM7/K3B laminates with a center hole.

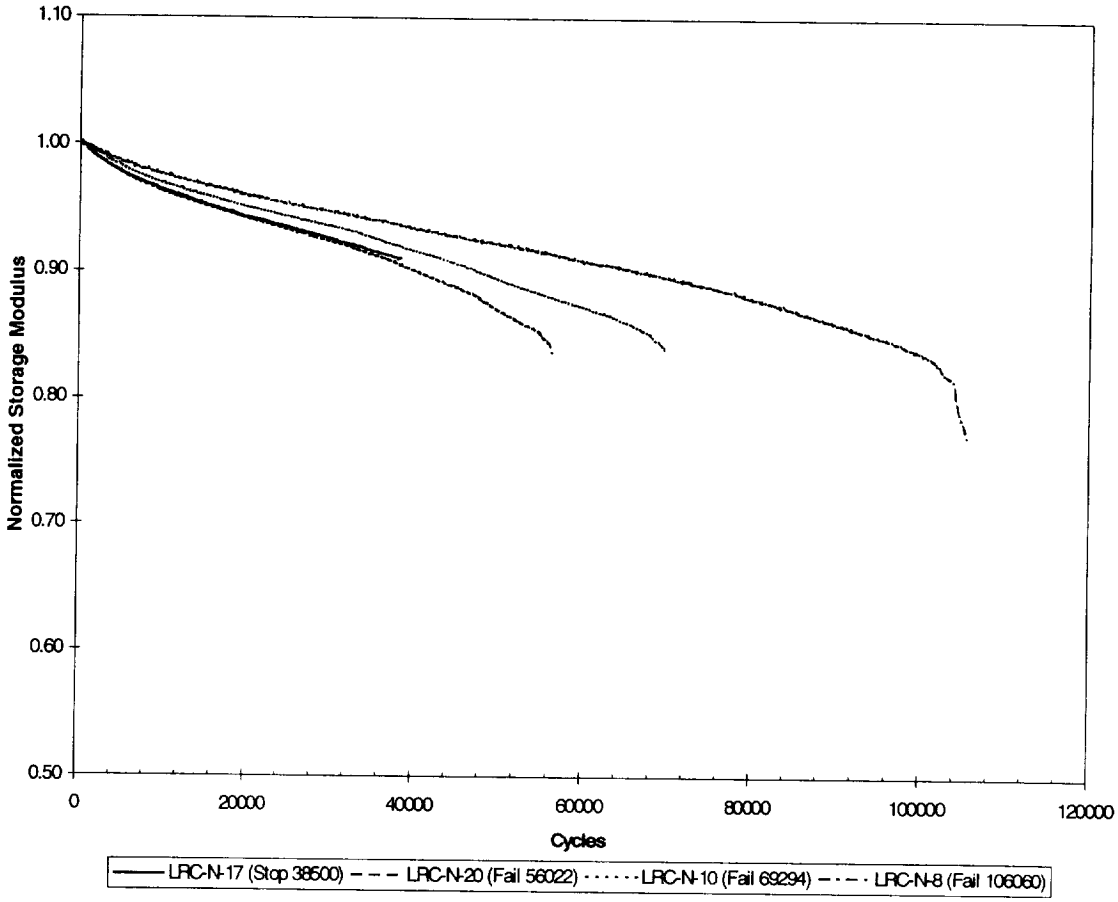

Figure 5.49. Normalized dynamic storage modulus measurements for 350°F (177°C) fatigue tests at 80% of ultimate strength for $[45/0/-45/90]_{2s}$ IM7/K3B laminates with a center hole.

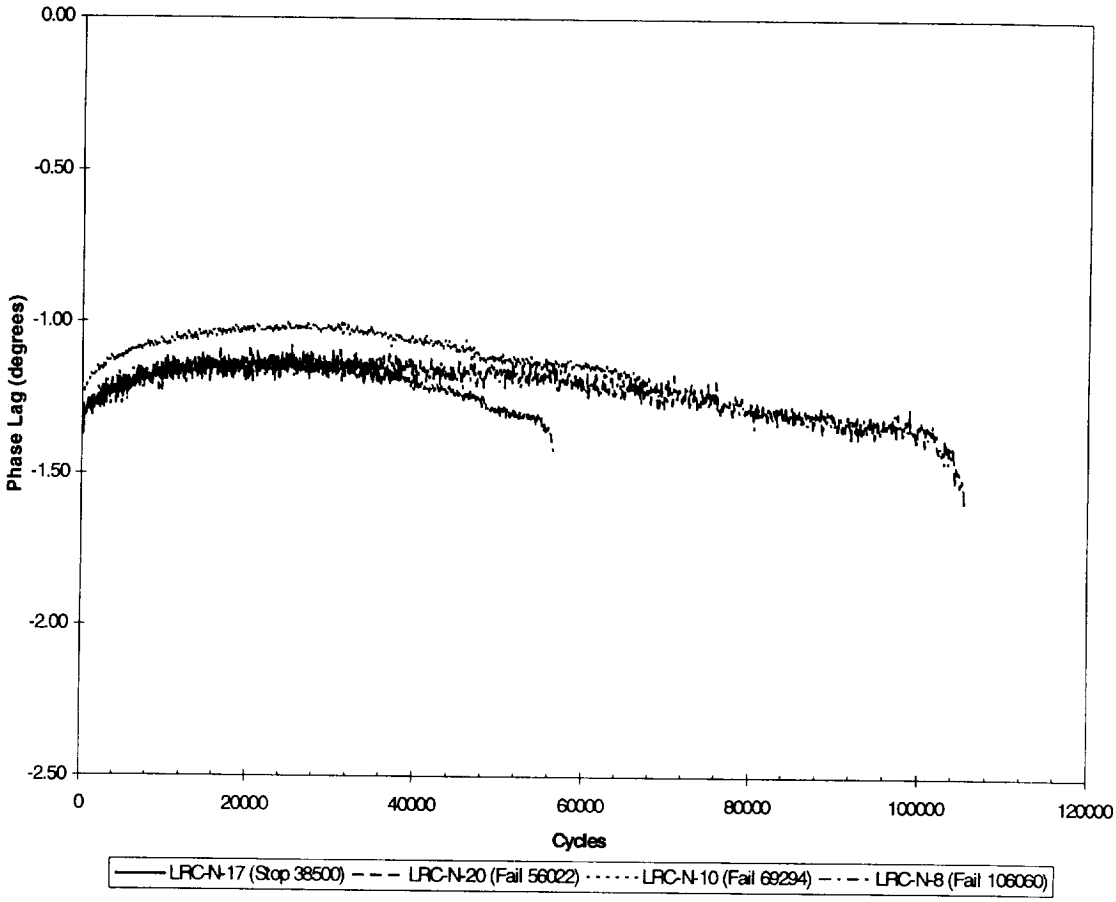

Figure 5.50. Phase lag measurements for 350°F (177°C) fatigue tests at 70% of ultimate strength for $[45/0/-45/90]_{2s}$ IM7/K3B laminates with a center hole.

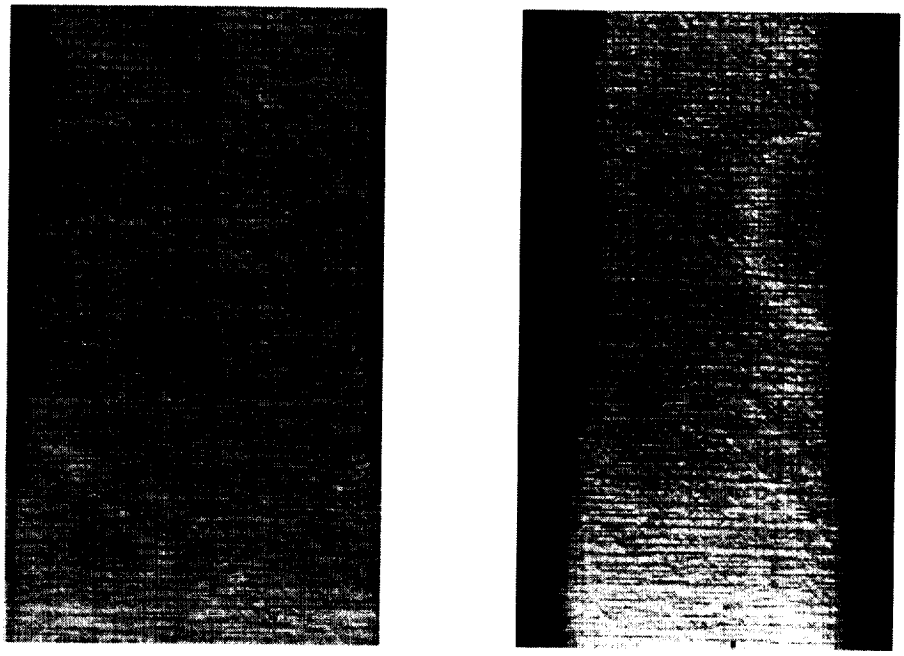

Figure 5.51. Penetrant-enhanced radiographs of unnotched $[45/0/-45/90]_{2s}$ laminates of IM7/K3B fatigued at room temperature at 65% of ultimate tensile strength after 10000 cycles (left) and 20000 cycles (right).

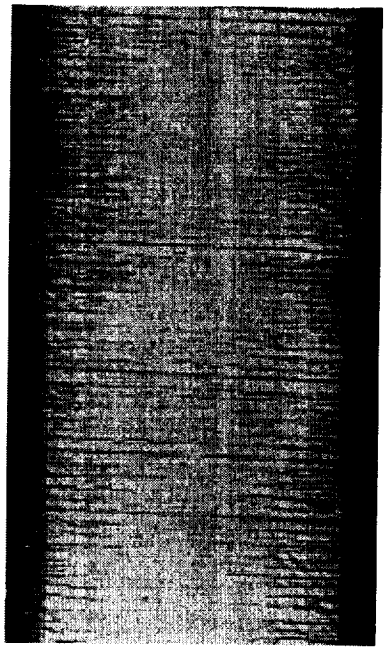

Figure 5.52. Penetrant-enhanced radiograph of an unnotched $[45/0/-45/90]_{2s}$ laminate of IM7/K3B fatigued at room temperature at 70% of ultimate tensile strength after 10000 cycles.

Radiographs of the unnotched specimens fatigued at 350°F (177°C) at 65% and 70% of ultimate tensile strength are shown in Figure 5.53 and Figure 5.54, respectively. These radiographs show a similar trend to that from the notched $[0/\pm45]_{2s}$ laminates: as the temperature is increased, the damage modes appear to remain the same as in the room temperature specimens, although the rate at which the damage develops is increased.

Now we may consider the radiographs of the notched specimens. Radiographs of the notched specimens fatigued at room temperature at 70% and 80% of ultimate strength are shown in Figure 5.55 and Figure 5.56, respectively. From the radiographs of the specimens fatigued at 70%, we may see that the damage development begins with the development of the matrix cracks. After this damage has developed, delaminations begin to form around the hole. Rather than developing and growing above the hole section parallel to the loading direction as in the $[0/\pm45]_{2s}$ specimens, this delamination grows in the transverse direction. In Figure 5.56, we see the beginning of the development of the edge delamination in the specimen in which the test was stopped after 100000 cycles.

Radiographs of the notched specimens fatigued at 350°F (177°C) at 70% and 80% of ultimate strengths are shown in Figure 5.57 and Figure 5.58. In the specimen which was stopped after 10000 cycles, we can see the fully-saturated matrix cracking, the beginning of the delamination around the hole, and the initiation of the delaminations around the edge. In the specimen which was stopped after 100000 cycles, we can see that the delamination around the hole has connected with the edge delamination. This can be seen more clearly in the radiograph of the specimen which was fatigued 38500 cycles at 80% of ultimate strength (Figure 5.58).

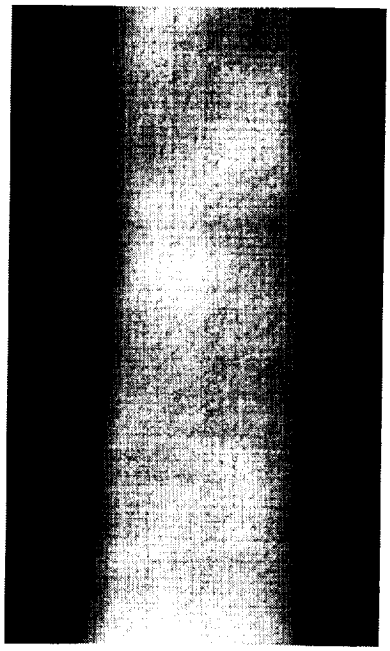

Figure 5.53. Penetrant-enhanced radiograph of an unnotched $[45/0/-45/90]_{2s}$ laminate of IM7/K3B fatigued at 350°F (177°C) at 65% of ultimate tensile strength after 8160 cycles.

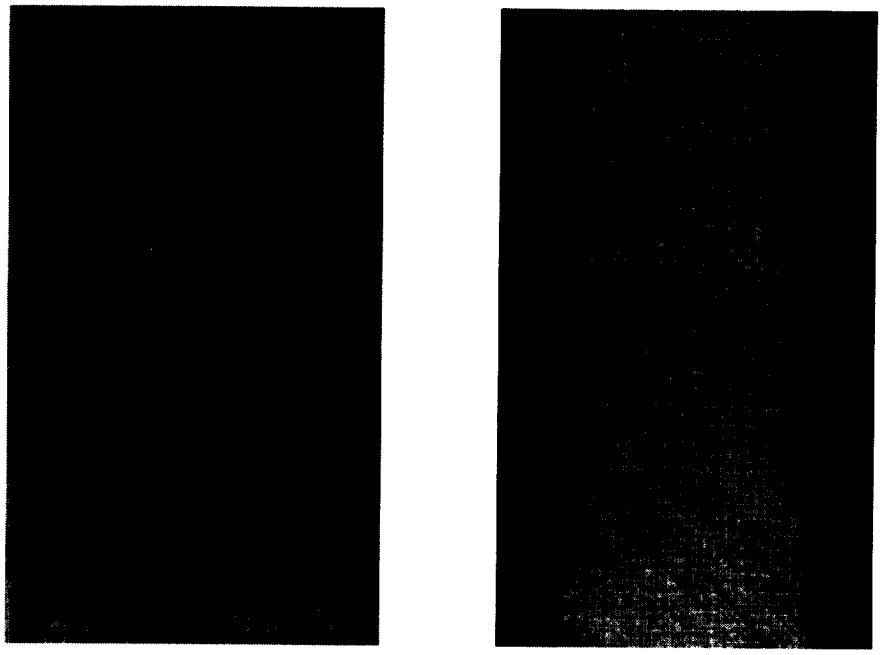

Figure 5.54. Penetrant-enhanced radiographs of unnotched $[45/0/-45/90]_{2s}$ laminates of IM7/K3B fatigued at 350°F (177°C) at 70% of ultimate tensile strength after 3500 cycles (left) and 5200 cycles (right).

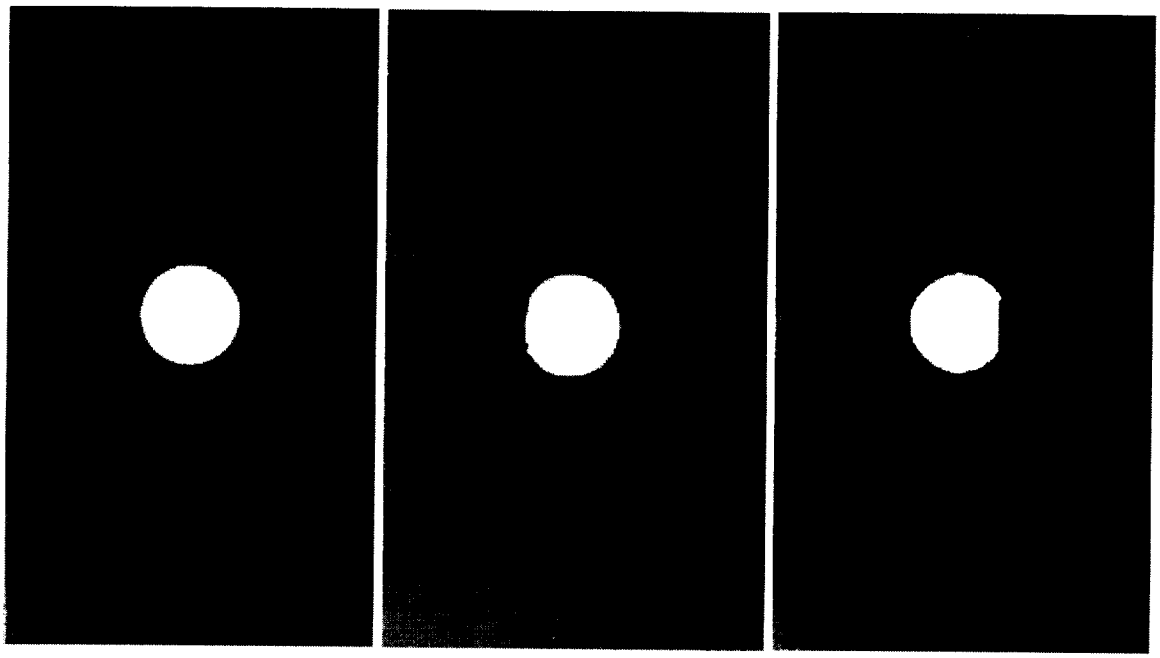

Figure 5.55. Penetrant-enhanced radiographs of notched $[45/0/-45/90]_{2s}$ laminates of IM7/K3B fatigued at room temperature at 70% of ultimate tensile strength after 1000 cycles (left), 10000 cycles (center) and 100000 cycles (right).

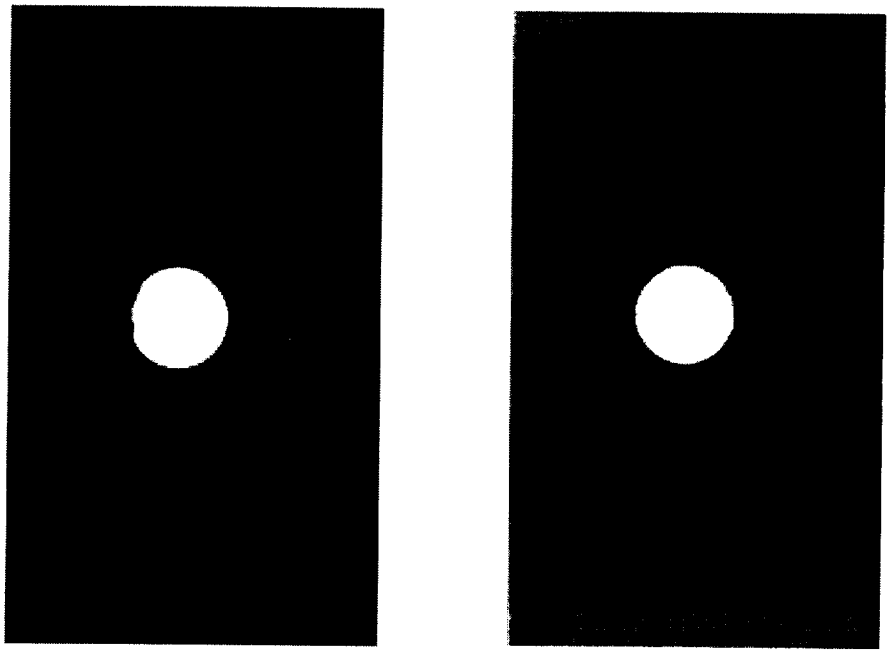

Figure 5.56. Penetrant-enhanced radiographs of notched $[45/0/-45/90]_{2s}$ laminates of IM7/K3B fatigued at room temperature at 80% of ultimate tensile strength after 10000 cycles (left) and 100000 cycles (right).

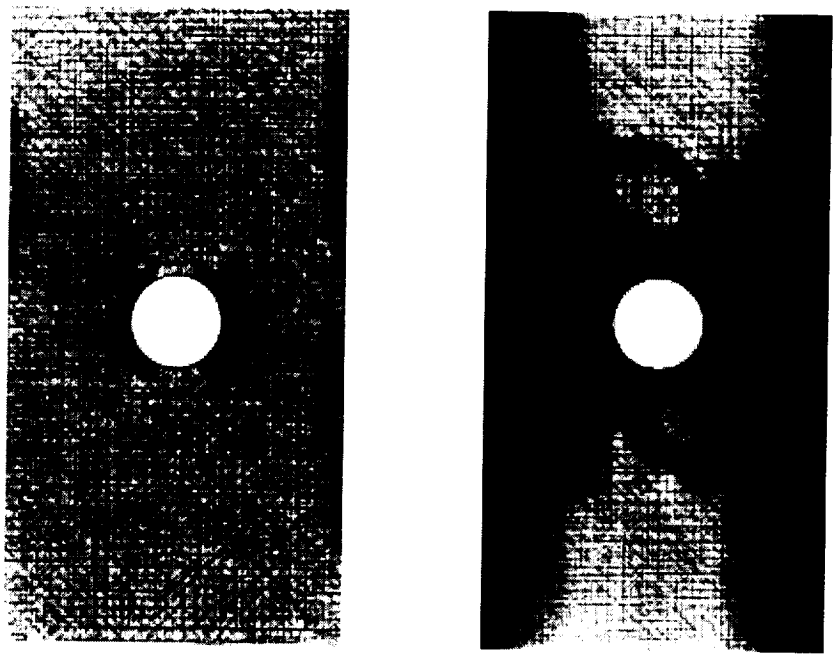

Figure 5.57. Penetrant-enhanced radiographs of notched $[45/0/-45/90]_{2s}$ laminates of IM7/K3B fatigued at 350°F (177°) at 70% of ultimate tensile strength after 10000 cycles (left) and 100000 cycles (right).

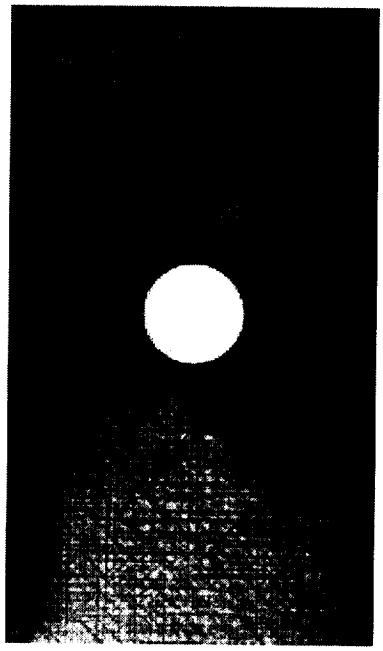

Figure 5.58. Penetrant-enhanced radiograph of an notched $[45/0/-45/90]_{2s}$ laminate of IM7/K3B fatigued 350°F (177°C) at 80% of ultimate tensile strength after 38500 cycles.

5.4.3.4 Residual Strength Measurements

The residual strength values for the Phase III specimens were obtained in two different manners. In the case of the specimens in which fatigue failure occurred, the residual strength at the number of cycles at which failure occurred was taken to be the maximum applied fatigue load. In the case in which the fatigue tests were interrupted, residual strength tests were conducted in a manner identical to that utilized in the quasi-static tests. The residual strength results for the unnotched $[45/0/-45/90]_{2s}$ laminates are summarized in Table 5.4. Considering the normal scatter which is expected in fatigue data, these data are extremely consistent. In fact, the strength values appear to be monotonically decreasing from their initial value to the value at which failure occurs. Such is not the case for the notched $[45/0/-45/90]_{2s}$ laminates. The remaining strength results for these specimens are summarized in Table 5.5. The remaining strength values in this case have a complicated behavior. Such a behavior is not surprising, however, in view of the complicated damage states which were observed in the radiographs.

5.4.3.5 Residual Strength Predictions

In the case of the unnotched specimens, the prediction of the remaining strength during the fatigue process is much more straightforward than the predictions made for the notched $[0/90]_{4s}$ APC-2 laminates and the $[0/\pm45]_{2s}$ IM7/K3B laminates. In this case, it is only necessary to represent the stiffness reduction of the plies due to the matrix cracking and the delamination. This is accomplished by using the stiffness reduction measured during the fatigue tests in conjunction with CLT to fit the off-axis stiffness values to the form given in Equation (4.4). The remaining strength may then be calculated in the manner described in Chapter 3. The results of such a prediction for the unnotched room temperature specimens are shown in Figure 5.59. The analysis does seem to do a reasonable job of predicting the remaining strength, although it does appear that it over-predicts the number of cycles to failure (the point at which the applied stress equals the remaining strength) at 65% of ultimate strength. Corresponding results for the 350°F (177°C) tests are shown in Figure 5.60. The agreement for the specimens which were fatigued at 70% of

Table 5.4. Residual strength results for unnotched $[45/0/-45/90]_{2s}$ laminates of IM7/K3B.

Specimen	Normalized Stress Level	Test Temperature	Fatigue Cycles (†Fatigue Failure)	Residual Strength
LRC-U-15	65	Room	26252†	93.4 ksi (644 MPa)
LRC-U-2	65	Room	34146†	93.4 ksi (644 MPa)
LRC-U-5	65	Room	10000	127 ksi (876 MPa)
LRC-U-16	65	Room	20000	94.0 ksi (648 MPa)
LRC-U-9	65	350°F (177°C)	10392†	83.7 ksi (577 MPa)
LRC-U-12	65	350°F (177°C)	11370†	83.7 ksi (577 MPa)
LRC-U-19	65	350°F (177°C)	5190†	83.7 ksi (577 MPa)
LRC-U-11	65	350°F (177°C)	8160	116 ksi (800 MPa)
LRC-U-4	70	Room	15412†	101 ksi (693 MPa)
LRC-U-8	70	Room	21253†	101 ksi (693 MPa)
LRC-U-6	70	Room	24770†	101 ksi (693 MPa)
LRC-U-1	70	Room	10000†	118 ksi (814 MPa)
LRC-U-10	70	350°F (177°C)	6876†	90.1 ksi (621 MPa)
LRC-U-20	70	350°F (177°C)	6988†	90.1 ksi (621 MPa)
LRC-U-14	70	350°F (177°C)	3500	116 ksi (798 MPa)
LRC-U-18	70	350°F (177°C)	5200	105 ksi (726 MPa)

Table 5.5. Residual strength results for notched $[45/0/-45/90]_{2s}$ laminates of IM7/K3B.

Specimen	Normalized Stress Level	Test Temperature	Fatigue Cycles (†Fatigue Failure)	Residual Strength
LRC-N -2	70	Room	1000	63.1 ksi (435 MPa)
LRC-N-13	70	Room	10000	60.3 ksi (416 MPa)
LRC-N-11	70	Room	100000	65.3 ksi (450 MPa)
LRC-N-16	70	Room	999993	58.8 ksi (405 MPa)
LRC-N-6	70	350°F (177°C)	141104†	41.6 ksi (287 MPa)
LRC-N-4	70	350°F (177°C)	10000	64.9 ksi (447 MPa)
LRC-N-18	70	350°F (177°C)	100000	61.9 ksi (427 MPa)
LRC-N-5	70	350°F (177°C)	250000	55.2 ksi (381 MPa)
LRC-N-2	80	Room	537537†	61.5 ksi (424 MPa)
LRC-N-12	80	Room	778246†	61.5 ksi (424 MPa)
LRC-N-3	80	Room	10000	63.7 ksi (439 MPa)
LRC-N-19	80	Room	100000	66.4 ksi (458 MPa)
LRC-N-8	80	350°F (177°C)	106060†	47.6 ksi (328 MPa)
LRC-N-20	80	350°F (177°C)	56022†	47.6 ksi (328 MPa)
LRC-N-10	80	350°F (177°C)	69294†	47.6 ksi (328 MPa)
LRC-N-17	80	350°F (177°C)	38500	60.7 ksi (419 MPa)

ultimate strength is excellent, although once again the analysis appears to slightly over-predict the life at 65% of ultimate strength.

In the case of the notched laminates, it had been hoped that the same techniques which had been applied to the $[0/\pm45]_{2s}$ laminates could be used again. However, this did not prove possible due to the delaminations which grew perpendicular to the loading directions. As a result of these delaminations, it was not possible to use the strip strain gages to make accurate strain measurements.

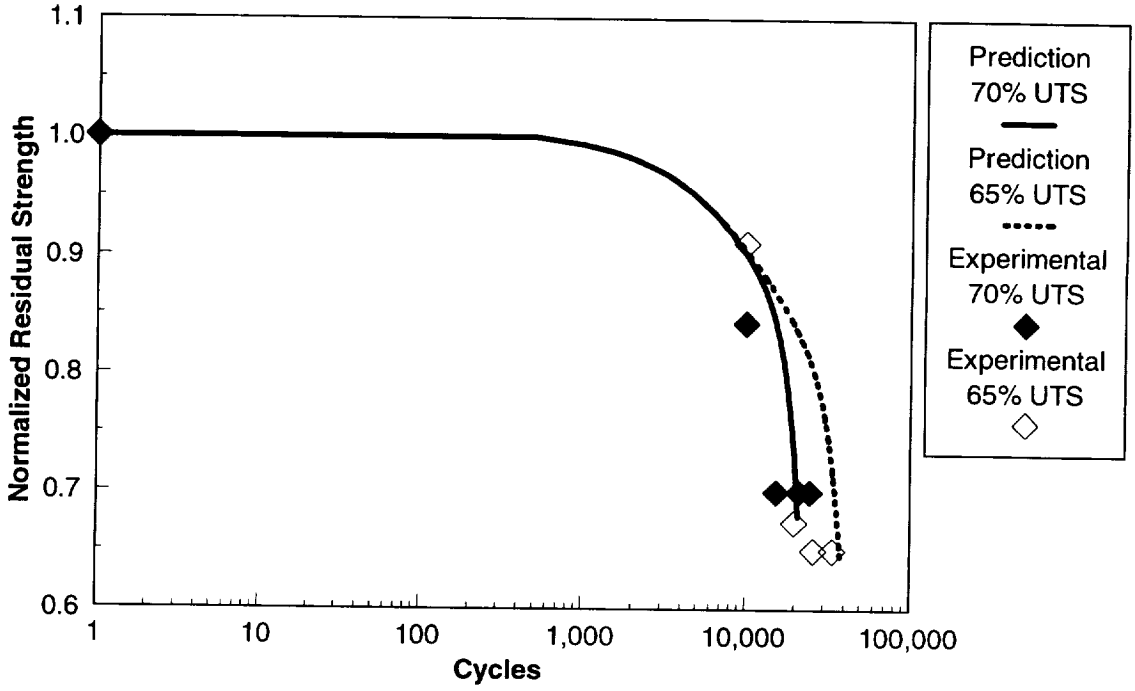

Figure 5.59. Comparison of predicted and measured remaining strength for unnotched $[45/0/-45/90]_{2s}$ specimens fatigued at room temperature.

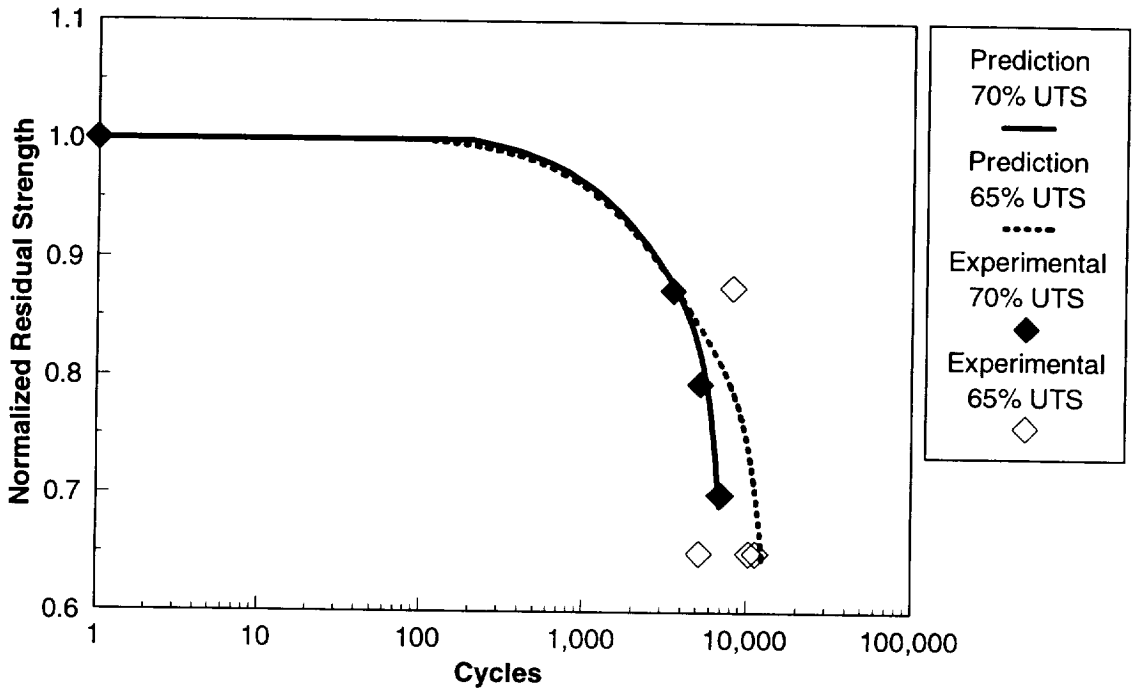

Figure 5.60. Comparison of predicted and measured remaining strength for unnotched $[45/0/-45/90]_{2s}$ specimens fatigued at 350°F (177°C).

6. Summary and Conclusions

The purpose of this chapter is to bring together the results from the previous sections as succinctly as possible. In order to do so, the organization of this chapter will follow along the same lines as that used for the previous chapters.

6.1 Introduction and Literature Review

6.1.1 Micromechanical Modeling of Tensile Strength

- A number of exact solutions exist for determining the stress state around a penny-shaped crack in a single, homogenous material under a variety of loading conditions. There are few exact solutions for the problem of a penny-shaped crack in a heterogeneous material which could be applied directly to a composite material.

- There are, however, a number of approximate solutions for determining the stress state in a composite material surrounding a broken fiber. The majority of these solutions are based upon shear-lag type assumptions.

- Two new models [25, 26] provide approximations of the stress state surrounding broken fibers without the need for the shear lag assumptions.

- The knowledge of the stress state around broken fibers in a unidirectional composite is necessary for statistical prediction of the composite tensile strength.

6.1.2 Estimation of Residual Strength and Fatigue Life

- Models used to predict fatigue lives may be divided into three classes: residual strength degradation, modulus degradation, and damage tolerance approaches [30]. Most life prediction methods for polymeric composite materials are based upon residual strength degradation approaches.

- It has been suggested [29] that a universal fatigue damage model needs to meet four requirements:

  a) It should explain fatigue phenomena at an applied stress level.

  b) It should explain fatigue phenomena for an overall applied stress range

     i) During a cycle at a high applied stress level the material should be more damaged than that at a low applied stress level.

     ii) If it is true that failure occurs at each maximum applied stress level, then the final damage (damage just before failure) at a low applied stress level should be larger than that at a high applied stress level.

  c) It should explain multi-stress level fatigue phenomena.

  d) It is desirable to establish the fatigue damage model without an S-N curve.

- One of the first cumulative damage approaches based upon remaining strength was presented in [33], in which the remaining strength of the laminate was assumed to vary linearly with fatigue cycles.

- One cumulative damage approach which has achieved a great deal of success [35-38] involves the use of a "critical element" model along with a nonlinear damage accumulation model.

Accurate attempts to model either the tensile strength or the fatigue life of composite materials should include the role of the interphase.

6.2 Strength Prediction in Unidirectional Composite Materials

- A exact elasticity solution was developed for a penny-shaped crack in an N-phase composite material. This solution was used in conjunction with a geometry approximation to estimate the stress concentrations due to fiber fractures.

- The stress concentrations due to these fiber fractures were then used to estimate the tensile strength of a unidirectional composite material based upon the model presented in [7].

- Because the exact solution is subject to a number of limitations, an approximate solution [26] was used to better estimate the stress concentrations due to multiple fiber fractures in a graphite/polymeric composite.

- These stress concentrations were then used to estimate the tensile strength of unidirectional composites as the matrix stiffness was varied. Such a situation would arise physically if the temperature were varied.

- Predicted tensile strengths were compared to measured strengths for composites containing a number of different fibers, with reasonable agreement.

- Although none of the models specifically included the role of the interphase, it could be readily included in the stress analysis. However, it any analysis which includes the interphase should also includes the interphase should also include paths of crack propagation (i.e. whether a fiber fracture leads to an axial debond, a matrix crack, or neither). Such work is currently underway [62].

6.3 Durability and Damage Tolerance Analysis in Composite Materials

- An analysis was presented based on the work in [38] for predicting the remaining strength of composites subjected to cyclic loading conditions.

- Modifications were made to the analysis to include the effect of changing stress levels. The modifications make use of the idea of remaining strength as a damage metric, and the definition of an equivalent time ("pseudo-time").

- The analysis has been used to predict lifetimes of composite materials subjected to fatigue loads. These predictions have been compared to experimental data with good agreement.

6.4 Quasi-Static and Fatigue Behavior of Notched $[0/90]_{4s}$ APC-2

- Three different cooling rates were considered (10°C/min, 5°C/min, and 1°C/min). These were not found to have an effect on the composite behavior.

- Specimens were fatigue loaded (10 Hz, R=0.1) at 80% and 87.5% of the ultimate strength. No fatigue failures occurred within 100000 cycles at these load levels.

- Fatigue tests were interrupted for damage analysis and remaining strength tests. The damage analysis revealed the growth of longitudinal splits around the hole section. It was surmised that the growth of these splits reduced the stress concentration around the hole to a level at which fatigue failure would not occur (at least within practical numbers of cycles).

- Strip strain gages were used to quantify the changes in stress distribution around the hole. These measurements were used to approximate the stress state based upon an "effective" hole size along with reduced stiffness properties based upon the solution in [58]. Phenomenological models were used to represent the changes in the effective hole size and stiffness properties.

- The approximate stress state was used in the cumulative damage model to estimate the remaining strength of the composites. These values were compared to the experimental data.

6.5 Room Temperature and Elevated Temperature Characterization of IM7/K3B

- Characterization tests were conducted at room temperature and 350°F (177°C). These tests included $[0]_{12}$ tension tests, $[90]_{12}$ tension tests, and $[\pm 45]_{3s}$ tension tests to determine baseline mechanical properties. One interesting finding was that the value for E_{11} measured at 350°F (177°C) was greater than that measured at room temperature.

- Fatigue tests (R=0.1) were conducted at various stress levels on unnotched $[45/0/-45/90]_{2s}$, notched $[45/0/-45/90]_{2s}$, and notched $[0/\pm45]_{2s}$ laminates at the two temperatures.

- Radiographs of the specimens indicated that the damage modes present in the materials at the two temperatures were the same. However, the rate of damage development and growth was greater at the elevated temperature.

- Strip gage measurements were made of the strain distributions around the hole in damaged and undamaged laminates for the $[0/\pm45]_{2s}$ stacking sequence. An effective hole size was estimated based upon these measurements and reduced stiffness properties.

- Phenomenological models were used to represent the stiffness reduction (for notched and unnotched laminates) as well as the effective hole size (for $[0/\pm45]_{2s}$ laminates).

- Residual strength measurements were made at the two temperatures. These values were compared to predicted values for the notched $[0/\pm45]_{2s}$ specimens and the unnotched $[45/0/-45/90]_{2s}$ specimens based upon the cumulative damage model. These results were compared to the experimental data.

- No prediction were made for the notched $[45/0/-45/90]_{2s}$ because the delaminations made measurements of the strain gradients around the hole using the strip strain gages impossible.

6.6 Recommendations

A great deal of work still remains to be done in these areas. Among areas that I believe merit consideration are the following:

- Considering the role of the interphase in the path of crack propagation around fiber fractures in composite materials. This would also require including the effect of axial debonds and matrix cracks in the stress analysis used for strength predictions.

- A number of the relations used to represent the material behavior were phenomenological rather than mechanistic. As such, their applicability is limited to the special cases for which they were developed.

- The fatigue tests demonstrated that the rate of damage development is greater at the higher temperatures. Now an explanation is needed as to why this is the case.

7. References

1. Madhukar, M. S. and Drzal, L. T. "Fiber-Matrix Adhesion and Its Effect on Composite Mechanical Properties: I. Inplane and Interlaminar Shear Behavior of Graphite/Epoxy Composites," *Journal of Composite Materials*, Volume 25 (1991), pp. 932-957.
2. Madhukar, M. S. and Drzal, L. T. "Fiber-Matrix Adhesion and Its Effect on Composite Mechanical Properties: II. Longitudinal (0°) and Transverse (90°) Tensile and Flexure Behavior of Graphite/Epoxy Composites," *Journal of Composite Materials*, Volume 25 (1991), pp. 958-991.
3. Swain, R. E. *Role of the Fiber/Matrix Interphase on the Static and Fatigue Behavior of Polymeric Matrix Composite Laminates.* PhD Dissertation, Virginia Polytechnic Institute and State University. (1992).
4. Chang, Y. S., Lesko, J. J., Case, S. W., Dillard, D. A., and Reifsnider, K. L. "The Effect of Fiber-Matrix Interphase Properties on the Quasi-Static Performance of Thermoplastic Composites," *Journal of Thermoplastic Composite Materials*, Volume 7 (1994), pp. 311-324.
5. Lesko, J. J. *Interphase properties and their effects on the compression mechanics of polymeric composites.* PhD Dissertation, Virginia Polytechnic Institute and State University. (1994).
6. Gao, Z., Reifsnider, K. L., and Carman, G. P. "Strength prediction and optimization of composites with statistical fiber flaw distributions," *Journal of Composite Materials,* Volume 26, pp. 1678-1705.
7. Batdorf, S. B. "Tensile strength of unidirectional reinforced composites--I," *Journal of Reinforced Plastics and Composites,* Volume 1 (1982), pp.153-176.
8. Sneddon, I. N. "The distribution of stress in the neighborhood of a crack in an elastic solid," *Proceedings of the Royal Society of London,* A 187 (1946), pp. 229-260.
9. Collins, W. D. "Some axially symmetric stress distributions in elastic solids containing penny-shaped cracks. I. Cracks in an infinite solid and a thick plate," *Proceedings of the Royal Society of London,* A 266 (1962), pp. 359-386.

10. Keer, L. M. "A class of non-symmetrical punch and crack problems," *Quarterly Journal of Mechanics and Applied Mathematics,* Volume 17 (1964), pp. 423-436.

11. Green, A. E. and Zerna, W. *Theoretical Elasticity,* Clarendon Press, Oxford,.(1960).

12. Smith, F. W., Kobayashi, A. S. and Emery, A. F. "Stress intensity factors for penny-shaped cracks. Part I--infinite solid," *Journal of Applied Mechanics,* (1967), pp. 947-952.

13. Guidera, J. T. and Lardner, R. W. "Penny-shaped cracks," *Journal of Elasicity,* Volume 5 (1975), pp. 59-73.

14. Lardner, R. W. and Tupholme, G. E. "A note on arbitrarily loaded penny-shaped cracks in hexagonal crystals," *Journal of Elasticity,* Volume 6 (1976), pp. 221-224.

15. Sneddon, I. N. and Tait, R. J. "The effect of a penny-shaped crack on the distribution of stress in a long circular cylinder," *International Journal of Engineering Science*, Volume 1 (1963), pp. 391-409.

16. Dhaliwal, R. S., Singh, B. M., and Rokne, J. "Penny-shaped crack in an infinite elastic cylinder bonded to an infinite elastic material surrounding it," *International Journal of Engineering Science,* Volume 17 (1979), pp. 1245-1255.

17. Cox, H. L. "The elasticity and strength of paper and other fibrous materials," *British Journal of Applied Physics,* Volume 3 (1952), pp. 72-79.

18. Rosen, B. W. "Fiber composite materials," *American Society of Metals,* Chapter 3 (1964), pp. 37-75.

19. Whitney, J. M. and Drzal, L. T. "Axisymmetric stress distribution around an isolated fiber fragment," *ASTM STP 937* (1987), pp. 179-196.

20. Hedgepeth, J. M. and Van Dyke, P. "Local stress concentrations in imperfect filamentary composite materials," *Journal of Composite Materials,* Volume 1 (1967), pp. 294-309.

21. Carman, G. P., Lesko, J. J., and Reifsnider, K. L. "Micromechanical analysis of fiber fracture," *Composite Materials: Fatigue and Fracture, ASTM STP 1156* (1993), pp. 430-452.

22. Fajardo, A. B. *Stress Concentration Measurements in a Composite Macro-Model Containing Fiber Fracture,* Senior Project Report, Engineering Science and Mechanics Department, Virginia Polytechnic Institute and State University, (1992).

23. Case, S. W., Carman, G. P., Lesko, J. J., Fajardo, A. B., and Reifsnider, K. L. "Fiber fracture in unidirectional composites," *Journal of Composite Materials,* Volume 29 (1995), pp. 208-228.

24. Kaw, A. K. and Jadhav, D. "Axisymmetric response of a cracked fiber in matrix," *Theoretical and Applied Fracture Mechanics,* Volume 21 (1994), pp. 197-206.

25. McCartney, L. N. "Stress transfer mechanics for multiple perfectly bonded concentric cylinder models of unidirectional composites," National Physical Laboratory Report DMM(A)129, (1993).

26. Pagano, N. J. "Axisymmetric micromechanical stress fields in composites," Proceedings IUTAM Symposium on Local Mechanics Concepts in Composite Materials, Blacksburg, VA, (1991).

27. Harlow, D. G. and Phoenix, S. L. "Probability distributions for the strength of composite materials I: two-level bounds," *International Journal of Fracture*, Volume 17 (1981), pp. 347-372.

28. Reifsnider, K. L. Class notes--ESM 6104. Department of Engineering Science and Mechanics, Virginia Polytechnic Institute and State University, (1994).

29. Hwang, W. and Han, K. S. "Cumulative damage models and multi-stress fatigue life prediction," *Journal of Composite Materials,* Volume 20 (1986), pp. 125-153.

30. Liu, B. and Lessard, L. B. "Fatigue and damage tolerance analysis of composite laminates: stiffness loss, damage modelling, and life prediction," *Composites Science and Technology,* Volume 51 (1994), pp. 43-51.

31. Huston, R. J. "Fatigue life prediction in composites," *International Journal of Pressure Vessels and Piping,* Volume 59 (1994), pp. 131-140.

32. Poursartip, A., Ashby, M. F., and Beaumont, P. W. R. "Damage accumulation during fatigue of composites," *Scripta Metallurgica,* Volume 16 (1982), pp. 601-606.

33. Broutman, L. J. and Sahu, S. "A new damage theory to predict cumulative fatigue damage in fiberglass reinforced plastics," *Composite Materials: Testing and Design (Second Conference), ASTM STP 497,* American Society for Testing and Materials (1972), pp. 170-188.

34. Hashin, Z. and Rotem, A. "A cumulative damage theory of fatigue failure," *Materials Science and Engineering,* Volume 34 (1978), pp. 147-160.

35. Reifsnider, K., Case, S. and Xu, Y. "A micro-kinetic approach to durability analysis: the critical element method," Keynote address, International Conference on Durability of Composite Material Systems, July 17-20, 1995, in press.

36. Reifsnider, K., Iyengar, N., Case, S. and Xu, Y. "Kinetic Mehods for Durability and Damage Tolerance Design of Composite Components," Keynote Address, Conference on Composite Materials, Japan Society for Mechanical Engineers, June 26, 1995, Tokyo.

37. Reifsnider, K., Lesko, J., and Case, S. "Kinetic Methods for Prediction of Damage Tolerance of High Temperature Polymer Composites," Composites '95: Recent Advances in Japan and the United States, I. Kimpara, H. Miyairi, and N. Takeda, Ed., Proceedings Japan-U.S. CCM-VII, Kyoto, 1995. pp. 49-55.

38. Reifsnider, K., Iyengar, N., Case, S. and Xu, Y. "Damage tolerance and durablitity of fibrous material systems: a micro-kinetic approach," Short Course, Free University of Brussels, March 8-9, 1995. To be published in book form 1996.

39. Subramanian, S., Reifsnider, K. L., and Stinchcomb, W. W. "A cumulative damage model to predict the fatigue life of composite laminates including the effect of a fibre-matrix interphase," *International Journal of Fatigue*, Volume 17 (1995), pp. 343-351.

40. Erdélyi, A. (ed.). *Tables of Integral Transforms,* Volume 2, McGraw-Hill, New York (1954).

41. Pagano, N. J. and Tandon, G. P. "Elastic response of multi-directional coated-fiber composites," *Composite Science and Technology*, Volume 33 (1988), pp. 273-293.

42. Carman, G. P. *Micromechanics of Finite Length Fibers in Composite Materials.* PhD Dissertation, Virginia Polytechnic Institute and State University. (1991).

43. Press, W. H., Teukolsky, S. A., Vetterling, W. T., and Flannery, B. P. *Numerical Recipes in FORTRAN: The Art of Scientific Computing,* Second Edition, Cambridge University Press, Cambridge, U. K. (1992).

44. Nedele, M. R. and Wisnom, M. R. "Stress concentration factors around a broken fibre in a unidirectional carbon fibre-reinforced epoxy," *Composites*, Volume 25 (1994), pp. 549-557.

45. Beck, A. R. and Yen, A. "Development of ultralightweight materials," Fourth Interim Technical Report, Air Force Contract Number F33615-88-C-5447, May 1989.

46. Beck, A. R. and Yen, A. "Development of ultralightweight materials," Fifth Interim Technical Report, Air Force Contract Number F33615-88-C-5447, August 1989.

47. Beck, A. R. and Yen, A. "Development of ultralightweight materials," Sixth Interim Technical Report, Air Force Contract Number F33615-88-C-5447, November 1989.

48. Vellios, L., Kostopoulos, V., and Paipetis, S. A. "Fatigue effect on the dynamic properties of CFRP composites," *Advanced Composites Letters,* Volume 3 (1994), pp. 145-150.

49. Reifsnider, K. L. and Stinchcomb, W. W. "A critical element model of the residual strength and life of fatigue-loaded composite coupons," *Composite Materials: Fatigue and Fracture, ASTM STP 907,* Edited by H. T. Hahn, ASTM, Philadelphia (1986), 298-303.

50. Kachanov, L. M. *Introduction to continuum damage mechanics.* Martinus Nijhoff Publishers, Boston. (1986).

51. Reifsnider, K., Case, S., and Iyengar, N. "Recent advances in composite damage mechanics," European Space Agency, (1996).

52. Halverson, H. G. *Improving Fatigue Life Predictions: Theory and Experiment on Unidirectional and Crossply Polymer Matrix Composites.* MS Thesis, Virginia Polytechnic Institute and State University, (1996).

53. Vure, N. R. S. *Effect of Cooling Rate and Stacking Sequence on the Fatigue Behavior of Notched Quasi-Isotropic APC-2 Laminates.* MS Thesis, Virginia Polytechnic Institute and State University, (1993).

54. Picasso, B. and Priolo, P. "Damage assessment and life prediction for graphite-PEEK quasi-isotropic composites," *American Society of Mechanical Engineers, Pressure Vessels and Piping Division (Publication) PVP v 146.* Published by ASME, New York, (1988), pp. 183-188.

55. Curtis, P. T. "An investigation of the mechanical properties of improved carbon fibre composite materials," RAE Technical Report 86021, Royal Aircraft Establishment, (1986).

56. Simonds, R. A. and Stinchcomb, W. W. "Response of notched AS4/PEEK laminates to tension/compression loading," *Advances in Thermoplastic Matrix Composite Materials, ASTM STP 1044,* G. M. Newaz, Ed., American Society for Testing and Materials, Philadelphia, (1989), pp. 133-145.

57. Whitney, J. M. and Nuismer, R. J. "Stress fracture criteria for laminated composites containing stress concentrations," *Journal of Composite Materials*, Volume 8, (1974), pp. 253-265.

58. Lekhnitskii, S. G. *Anisotropic Plates.* S. W. Tsai and T. Cheron, translators, Gordon and Breach, (1968).

59. ASTM Standard D 3518/D 3518 M. "Standard practice for in-plane shear and stress-strain response of unidirectional polymer matrix composites," *Annual Book of ASTM Standards,* Volume 03.01, (1991), pp. 148-152.

60. Fisher, J. M., Palazotto, A. N., and Sandhu, R. S. "A study of failure characteristics in thermoplastic composite material at 250°F (121°C)," *Journal of Composites Technology & Research*, JCTRER, Vol. 13, No. 3, Fall 1991, pp. 152-160.

61. Elahi, M., Razvan, A., Reifsnider, K. "Characterization of composite materials dynamic response using load/stroke frequency response measurement," presented at the *ASTM Fourth Symposium on Composite Materials: Fatigue and Fracture,* Indianapolis, Indiana, May 1991.

62. Private communication with Ari Caliskan, May 1996.